Department of Physics
The Blackett Laboratory
Imperial College London
SW7 2AZ

Investigating the impact of non-local parallel transport in tokamak edge plasmas

Dominic Power

Submitted in part fulfilment of the requirements for the degree of
Doctor of Philosophy of Imperial College, July 4, 2023

Abstract

The thin region of plasma at the edge of a tokamak, as the boundary condition to the confined plasma in the core, plays an oversized role in the performance of such devices. As such, the topic of exhaust physics is central to the ongoing effort to make magnetically confined fusion a viable approach to clean energy generation. A defining feature of this edge plasma, called the scrape-off layer (SOL), is a large temperature gradient in the direction parallel to the magnetic field. Large temperature drops are probably crucial to avoid excessive heat loads to the solid components which make up the walls of the device. However, their presence means that classical transport models, which assume the plasma is at or close to local thermodynamic equilibrium (LTE) and which are used widely in SOL modelling, can lose their predictive power [1–3]. The aim of this thesis is to investigate the extent of this effect in detail by performing kinetic simulations of parallel transport in SOL plasmas, with a focus on the electrons. There is an emphasis on quantifying the modelling uncertainties that exist in classical ('fluid') approaches to SOL simulations by performing self-consistent comparisons between kinetic and fluid models.

To do this, the one-dimensional SOL kinetic code SOL-KiT has been used [4]. By extending the capabilities of this code, reducing its computational expense, and developing a standalone atomic physics code (all of which are described), it has been possible to study electron kinetics in a range of conditions relevant to current and future tokamaks. A number of distinct investigations have been performed. Firstly, it has been shown that fluid models are in fact very good at capturing the transfer of energy between ions and electrons in SOL plasmas. Secondly, it is demonstrated that a kinetic treatment leads to significant differences in parallel conductive heat transport and behaviour at the wall boundary, both of which contribute to modified temperature profiles. A set of simple scaling laws for these effects has been proposed. Finally, the effect of non-LTE electrons on plasma-atomic physics has been investigated. Here, strongly enhanced reaction rates due to the form of the electron velocity distribution have been observed, but this effect is largely reversed when considered alongside the modified temperature profiles.

Acknowledgements

This work has been made possible by the unconditional support of Amy, my family, and my friends.

I wish to thank Stefan Mijin. This thesis is greatly indebted to the countless productive discussions we have had, and his enthusiasm for the topic has been a source of inspiration.

I would like to thank Robert Kingham for his expert guidance as supervisor. The shape of my research has been vastly improved by his sense of perspective. Thanks also to Fulvio Militello as co-supervisor, our conversations during the initial period of my PhD were enlightening.

I would like to thank the many others with whom I have shared many illuminating conversations throughout the PhD, which has inevitably percolated into the work, in particular Mike Kryjak, Abi Anthony, David Moulton, Mike Wigram, Ben Dudson, Sarah Newton, Kevin Verhaegh, Ryoko Osawa, and others.

Dedication

To Richard.

'Knowing interestingly is always a risky business'

Bruno Latour

The role of the author

The work presented here has been performed with input from and discussions with colleagues from several institutions, most notably Imperial College London and the United Kingdom Atomic Energy Authority. However, this thesis is a presentation of original work, and I am the sole author.

Much of the work in this thesis has made use of the code SOL-KiT. This was originally developed by Stefan Mijin, but has since been upgraded by myself to carry out the investigations which are presented. The SIKE code was entirely developed by myself.

Parts of this thesis are based on manuscripts which have been published. These have been written with input from the co-authors, but I am the first author. References have been provided for these manuscripts.

Declaration

I hereby declare that, unless otherwise acknowledged, all material used and information reported in this thesis is entirely original.

Dominic Power

July 4, 2023

The copyright of this thesis rests with the author. Unless otherwise indicated, its contents are licensed under a Creative Commons Attribution-Non Commercial 4.0 International Licence (CC BY-NC). Under this licence, you may copy and redistribute the material in any medium or format. You may also create and distribute modified versions of the work. This is on the condition that: you credit the author and do not use it, or any derivative works, for a commercial purpose. When reusing or sharing this work, ensure you make the licence terms clear to others by naming the licence and linking to the licence text. Where a work has been adapted, you should indicate that the work has been changed and describe those changes. Please seek permission from the copyright holder for uses of this work that are not included in this licence or permitted under UK Copyright Law.

Contents

List of Tables

List of Figures

Chapter 1

Introduction

The source and availability of energy has been a key driver of societal development in the long run of human history [5]. Most recently, the industrial revolution followed by rapid globalisation has relied on large scale extraction of fossil fuel energy sources: coal, oil and gas are sufficiently abundant and energy dense to facilitate energy-intensive activites such as manufacturing, long-distance travel and heating, all of which are associated with increases in quality of life. As such, total energy consumption in wealthy countries, supplied primarily by fossil fuels, has increased rapidly in recent centuries. For countries which underwent this transition first, such as the United Kingdom, energy consumption has plateaued in recent years (see Figure 1.1). However, many nations across the world remain on an upward trajectory, and global energy consumption is likely to continue to increase for the foreseeable future [6]. This state of affairs is not compatible with the fact that burning fossil fuels drives unsustainable changes to the climate via the release of carbon dioxide, nor with the fact that fossil fuel reserves are finite. Of those finite reserves left in the ground, it has been estimated that 60% of oil and gas and 90% of coal should be considered unextractable if internationally-agreed levels of global warming are to be avoided [7].

The leading candidates to replace fossil fuel energy sources are nuclear fission, as well as renewable sources such as wind, solar, tidal, geothermal, etc. Nuclear fission is hindered by issues with radioactive waste products, limited uranium supplies and public perceptions of its

safety. At present, the most viable renewable energy sources are solar and wind. For both of these, there are concerns over the availability of raw materials, storage, and transmission. Of more long-term significance however is the issue of energy density, which is set by fundamental physics constraints. Wind and solar power have comparatively low energy density, which puts an upper limit on the power consumption density (i.e. the power consumption per person multiplied by the population density) which they can support. This is shown in Figure 1.1, where we can see that the power consumption density of countries like the United Kingdom is already close to the generating capacity for wind and, to a lesser extent, solar farms. For the UK, with a modern consumption density of around $1\mathrm{W/m^2}$, renewables are unlikely to be able to meet demand without constructing very large farms (and associated infrastructure) or importing from less densely-populated countries. This does not preclude renewables from playing an important role in the transition away from fossil fuels, but it does highlight the need for research into alternative, long-term solutions.

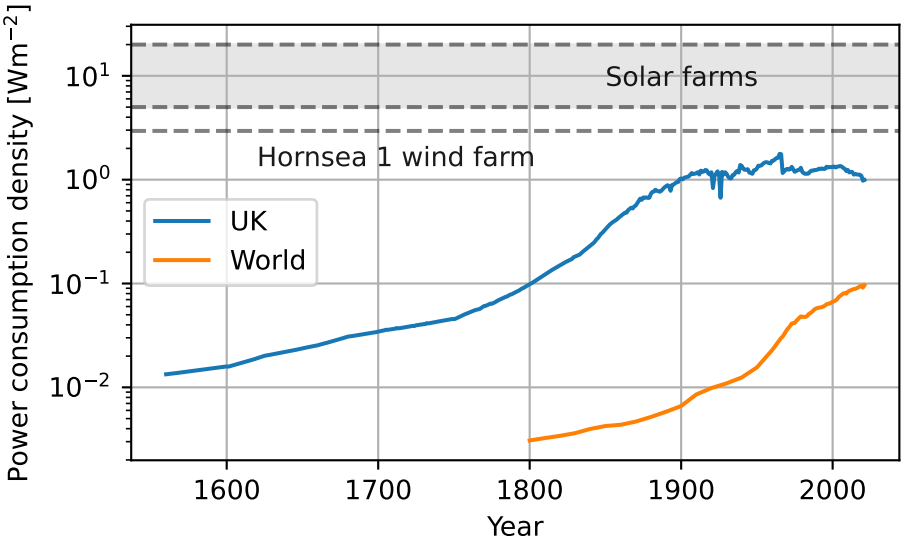

Figure 1.1: Power consumption density (= power consumption per capita × population density) over time for the UK and the globe. The horizontal lines show the power generation density for the Hornsea wind farm and solar farms (the range is due to differences in solar capacity depending on climate, latitude, efficiency, etc.). Data from [8], [9] and [10].

Nuclear fusion, where energy is released during the nuclear reaction in which light atomic nuclei fuse to create a heavier nucleus, may represent a solution to this dilemma. Like renewable energy sources and nuclear fission, no carbon dioxide is produced. It has a number of other advantages beyond this:

- The energy density of the fuel is high, being several million times higher than the stored chemical energy in fossil fuels. A building-sized fusion device could produce a gigawatt of power [11], consuming fuel at a rate of around a kilogram per day. By contrast, the Hornsea 1 wind farm, with an output of 1.2 GW, is spread over 407 square kilometres, and a 1 GW coal power station uses around 10,000 tonnes of fuel per day.

- The fuel source is abundant. Deuterium and tritium, isotopes of hydrogen, are used in most fusion designs. Deuterium is abundant in seawater; lithium, from which tritium can be derived, is found in both ore deposits and seawater. Both are available in quantities which could meet the energy demands from the entire planet for at least thousands of years [9].

- Nuclear fusion will not produce any long-lived, high activity radioactive waste [12]. Radioactive waste that is produced is predicted to be safe enough to recycle or reuse within 100 years.

- There is no risk of a fission-style meltdown, at least within conventional approaches to fusion. The primary challenge with fusion is initiating and sustaining the reaction, and the amount of fuel in the reactor at any one time is small (enough for only a few seconds of operation).

Gaining the ability to extract useful quantities of energy from a controlled nuclear fusion reaction would therefore be a transformative achievement. However, this remains an unsolved problem, with both scientific and engineering challenges which first need to be overcome. These problems typically stem from the need to achieve very high temperatures, often hotter than in the sun's core, in any proposed fuel source in order to achieve a high number of fusion reactions. Containing such a high temperature substance, while simultaneously avoiding the destruction of the reactor and extracting more energy than is put in to achieve these temperatures, is a challenge.

The current leading approaches to fusion are differentiated by the method used to confine the hot fuel. At the temperatures required, electrons dissociate from atoms and fusion fuel becomes

a plasma, with qualitatively different behaviour to a neutral gas. Confinement of this fuel is challenging, but vital to ensure that particles stay hot and do not escape faster than they can react. This is typically done using either magnetic fields, or by accelerating the fuel in an implosion such that its inertia does the job of confinement. There have been significant recent advances in inertial confinement fusion experiments [13], and there is considerable effort going into designing a roadmap towards fusion power plants based on magnetic confinement fusion [14]. ITER is a magnetically confined fusion device currently under construction in France. ITER will demonstrate several key aspects of a fusion power plant, including a long-pulse burning thermonuclear plasma, tritium fuel breeding, and several important engineering technologies related to control, diagnostics and safety [15]. See Figure 1.2 for a diagram of the ITER tokamak. This project, along with DEMO [16] and several others [17–20], represent serious attempts to solve the many challenges posed by attempting to harness fusion for energy using magnetic confinement.

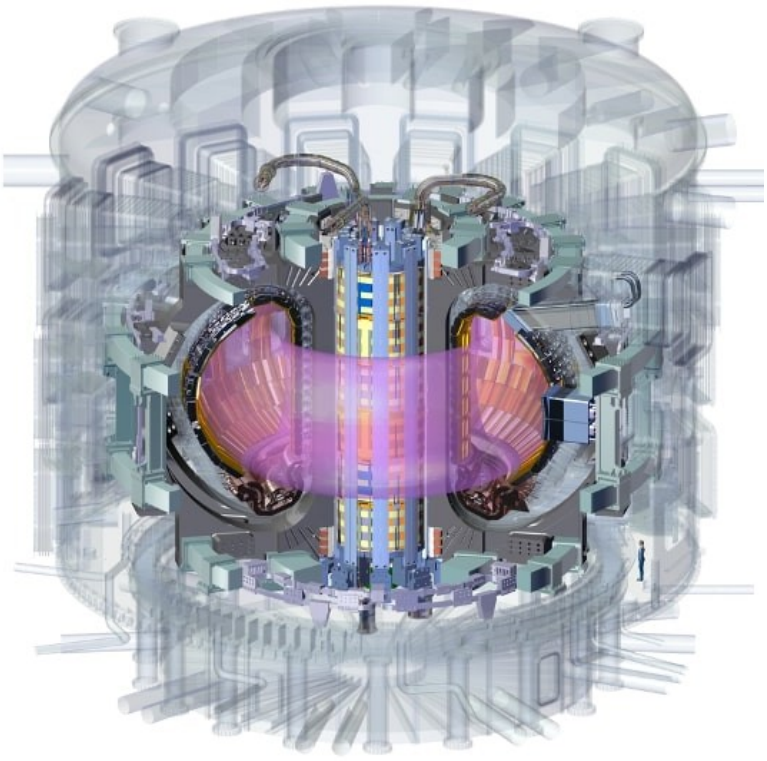

Figure 1.2: Diagram of the ITER tokamak. Key components can be seen such as the central solenoid, vacuum chamber, main plasma (pink), exhaust region (bottom of the vacuum chamber) and structural supports. Source: `https://www.iter.org/album/Media`.

1.1 Nuclear fusion

Nuclear fusion of deuterium and tritium releases an alpha particle and a neutron,

$$ {}^{2}_{1}\mathrm{D} + {}^{3}_{1}\mathrm{T} \rightarrow {}^{4}_{2}\mathrm{He} + \mathrm{n}, \tag{1.1} $$

where ${}^{2}_{1}\mathrm{D}$ is a deuterium nucleus with 1 neutron and 1 proton, and so on. The total binding energy of the products is less than that of the reactants, meaning energy is released in this reaction in the form of kinetic energy. For this reaction, 17.6 MeV is shared approximately 1:4 between the alpha particle and the neutron. Other fusion reactions with a net release of energy are

$$ {}^{2}_{1}\mathrm{D} + {}^{2}_{1}\mathrm{D} \rightarrow {}^{3}_{2}\mathrm{He} + n, \tag{1.2a} $$

$$ {}^{2}_{1}\mathrm{D} + {}^{2}_{1}\mathrm{D} \rightarrow {}^{3}_{1}\mathrm{T} + {}^{1}_{1}\mathrm{H}, \tag{1.2b} $$

$$ {}^{2}_{1}\mathrm{D} + {}^{3}_{2}\mathrm{He} \rightarrow {}^{4}_{2}\mathrm{He} + {}^{1}_{1}\mathrm{H}. \tag{1.2c} $$

The cross-sections for these reactions are shown in Figure 1.3a. It is clear that D-T (deuterium-tritium) fusion has the highest peak cross-section at the lowest energy, making it the favoured candidate for controlled fusion experiments. The D-T cross-section peaks around 100 keV, which is eminently achievable in modern particle accelerators. However, accelerating deuterons into a stationary tritium target turns out to be impractical due to energy losses to collisions with electrons in the target. Instead, we may heat a D-T mixture to a plasma and use the thermal energy of the particles to achieve fusion. This approach is viable because any population of particles in thermal equilibrium will have a distribution of particle energies, with a non-negligible fraction having much higher energy than the average. This means temperatures much lower than 100 keV can yield a significant reaction rate, as shown in Figure 1.3b.

The alpha particles from fusion are produced with 3.5 MeV of kinetic energy. In a D-T plasma heated to fusion-relevant temperatures, the alpha particles can deposit some energy back into the plasma via Coulomb collisions, acting as a heating source which can counteract losses. The

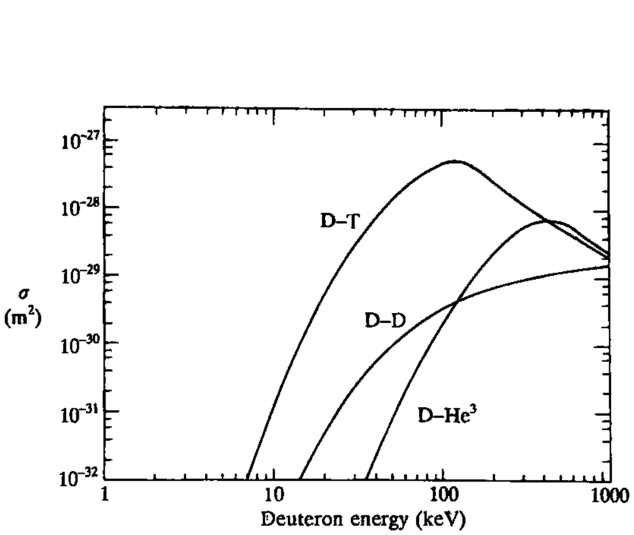

(a) Cross-sections of various fusion reactions as a function of the incident deuterium nucleus.

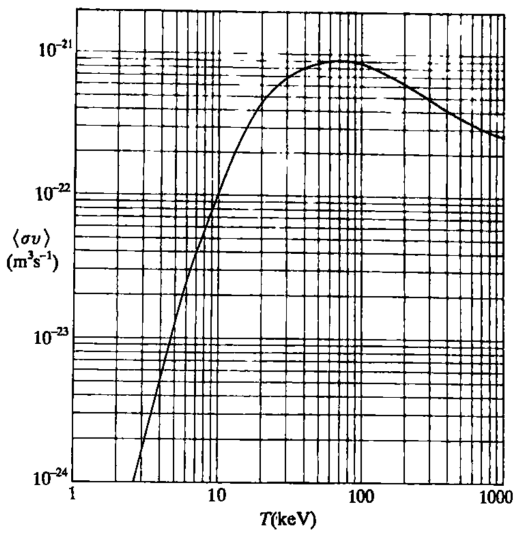

(b) Reaction rate for D-T fusion as a function of temperature.

Figure 1.3: Figures reproduced from [21].

power balance is therefore

$$P_H + P_\alpha = P_L, \tag{1.3}$$

where P_H is the external heating power, P_α is the alpha heating and losses are represented by P_L. When $P_\alpha > P_L$, the external heating used to heat the plasma initially can be removed, the plasma temperature can be self-sustained and we have reached 'ignition'. We can write this ignition condition [21, 22] in terms of the plasma density n, temperature T and energy confinement time τ_E ($= W/P_L$, where W is the total energy content of the plasma),

$$nT\tau_E > 3 \times 10^{21} \text{ m}^{-3}\text{keVs}. \tag{1.4}$$

This quantity $nT\tau_E$ highlights the importance of all three of temperature, density and confinement in achieving ignition. A measure of success in fusion experiments is the ratio

$$Q = P_{fus}/P_H, \tag{1.5}$$

where P_{fus} is the fusion power, i.e. the thermonuclear power produced in fusion reactions. Variations on this parameter include an accounting of the efficiencies involved in both applying external heating to the plasma and extracting usable energy from it. In the DT reaction (1.1),

the 3.5 MeV given to the alphas is about 20% of the total 17.6MeV of energy released per reaction, such that $Q \simeq 5P_\alpha/P_H$. This means $Q = 1$ (break-even) is reached when the alpha heating reaches around 20% of the external heating power. Under ignition conditions (1.4) and with external heating turned off, Q as defined in (1.5) goes to infinity. However, this is not a requirement for a fusion power plant, and $Q > 1$ can be achieved without reaching ignition.

As discussed, the two main approaches to controlled fusion in the lab are magnetic confinement fusion (MCF) and inertial confinement fusion (ICF). In MCF, particular configurations of magnetic fields can lead to high confinement times, $\tau_E \sim 0.1$ s, and relatively low plasma pressures ($p = nT$) are used. In MCF experiments, a finite $Q > 1$ can in principle be sustained for many confinement times with a constant input of external heating power. On the other hand, ICF is a pulsed scheme where very short confinement times are achieved, $\tau_E \sim 10^{-10}$ s, but much higher plasma pressures help to produce fusion-relevant conditions (including ignition). Experimental progress in the value of $nT\tau_E$ achieved in experiments since the late 1960s is shown in Figure 1.4.

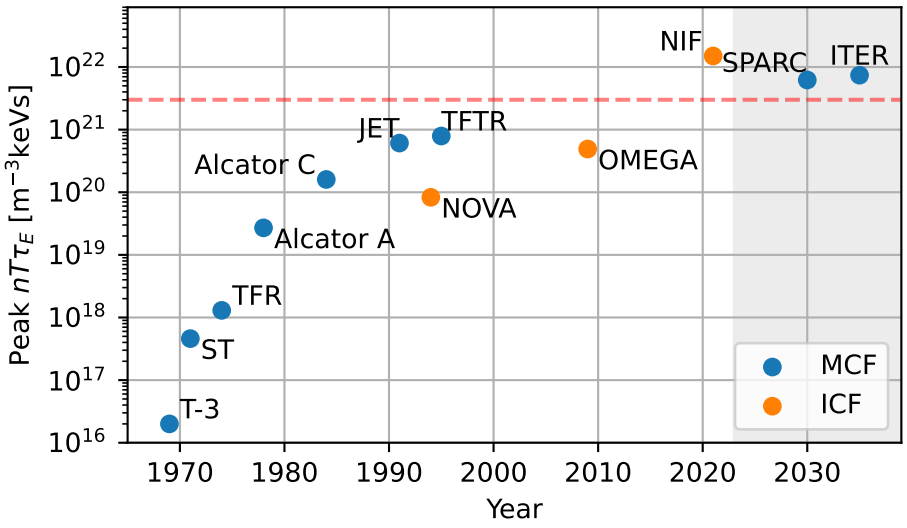

Figure 1.4: Achieved and predicted values of (peak) $nT\tau_E$ in experiments over time. The red dashed horizontal line is $nT\tau_E = 3 \times 10^{21}$ m^{-3}keVs. Points in the shaded grey region (SPARC and ITER) are predicted values for devices currently under construction. Data obtained from [23] and [13].

1.2 Magnetic confinement fusion

Confinement of a gaseous plasma using magnetic fields relies on the Lorentz force, which aids confinement in two ways. Firstly by causing plasma particles to orbit around the magnetic field lines, inhibiting cross-field transport; secondly by exerting a net force on the plasma which may counteract any forces acting to reduce confinement, such as pressure gradients.

A practical attempt at magnetic confinement may start with a cylindrical plasma with a magnetic field along the axis of the cylinder, inhibiting transport radially outwards. By also driving a current in the plasma, we can create a poloidal component to the magnetic field, which exerts a force radially inwards to counteract the outward force from the pressure gradient between the plasma and the surrounding vacuum. By joining the ends together a torus-shaped plasma is created, with helical field lines (shown in Figure 1.5). This very simple outline forms the basis of magnetic confinement in tokamaks. An alternative approach is to create helical magnetic field lines using magnetic coils only, without inducing a plasma current. See Figure 1.6 for a comparison. Such a device is called a stellarator, and avoids some of the complications and instabilities associated with plasma currents in tokamaks, but inherits issues related to precise control of the magnetic field to yield good confinement properties. Here, we focus on the tokamak as the more developed method of plasma magnetic confinement at present, although much of the physics is common to both configurations.

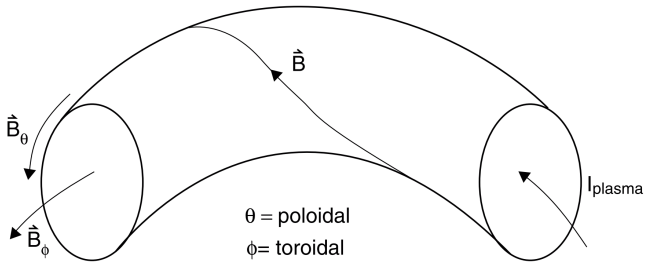

Figure 1.5: Simple diagram showing the magnetic field lines used for confinement in a tokamak. Reproduced from [24].

Present-day conventional tokamaks such as JET (Oxfordshire, UK), DIII-D (California, USA), and KSTAR (Daejon, South Korea), have a major radius of $1-3$ m and minor radius around half that. The magnetic field strength in the core is $2-5$ T, the plasma current is $2-4$ MA and

the external heating power is a few tens of MW. During operation, the core ion temperatures peak at up to around 9 keV ($\sim 10^8$ K). The ITER tokamak is designed to have more than double the major radius of JET, with a total plasma volume nearly an order of magnitude larger. The magnetic field strength will be similar to that in present-day devices as this is limited by the technology used in the field coils. However, there is active research into alternatives which may offer higher field strengths and so better confinement in a smaller device. Examples are the ARC and ST80-HTS tokamaks, which will employ high temperature superconducting magnets to achieve core field strengths over 10 T in devices similar in size to current tokamaks.

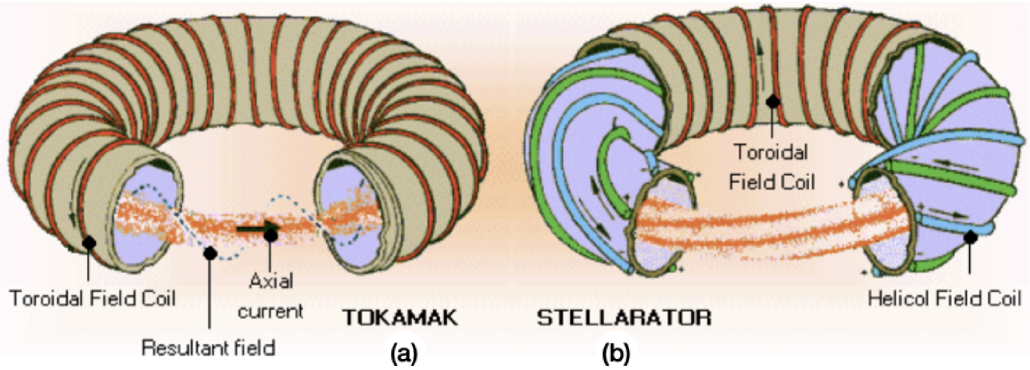

Figure 1.6: Diagram of a tokamak (left) and a stellarator (right). Figure reproduced from [25].

1.3 Exhaust physics

Magnetic confinement of a plasma in a tokamak implies the existence of some surrounding structure housing the magnetic field coils, structural supports, diagnostics, etc (this can be seen in the ITER diagram in Figure 1.2). Therefore, the torus-shaped plasma in a tokamak will not exist in an isolated vacuum, and some degree of plasma contact with a solid surface is inevitable. As it turns out, magnetic confinement cannot completely eliminate this region of plasma-surface interaction, and in fact some amount is desirable and necessary. This is because, firstly, we can see from the D-T reaction (1.1) that Helium 'ash' will build up in the fuel mixture. As charged particles, these will be confined to some extent by the same methods we are using to confine the fuel, and having some mechanism of removing the ash is vital to prevent fuel dilution. Secondly, ideal reactor conditions would involve steady-state (or quasi-steady-sate)

operation at a constant temperature, in contrast to the pulsed operation envisaged in ICF schemes. Therefore, excess heat needs to be manageably removed from the system. With these considerations in mind, we see that some kind of exhaust region is necessary for the removal of both particles and energy from a tokamak. Significant research effort is devoted to this exhaust region, and it is a highly complex area of tokamak design. In Figure 1.7, a rendering of the exhaust region as designed for the ITER tokamak is shown.

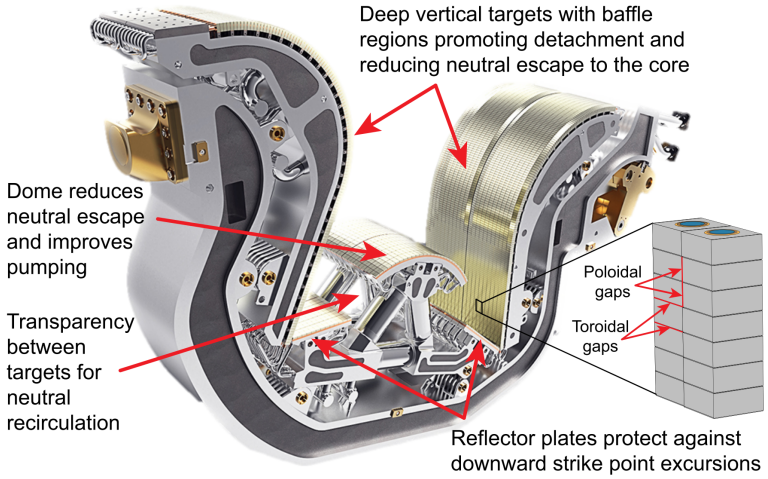

Figure 1.7: Diagram of the exhaust region designed for ITER, reproduced from [26].

A tokamak plasma can be divided into two regions, the core and the edge. Plasma in the core is well-confined by the magnetic field configuration described in the previous section: magnetic field lines here either close in on themselves or ergodically map out closed surfaces, and plasma particles gyrate in tight orbits about these field lines and transport off of them is minimal. The edge region is formed, by definition, by any solid surface which intersects the magnetic field lines and renders them 'open'. This is often called the scrape-off layer (SOL). If core confinement were perfect, the edge region would be a vacuum. However, this is never the case in practice and the core region leaks plasma slowly into the SOL, which is then transported towards a solid surface primarily along the direction parallel to the magnetic field lines. It is this edge plasma and region of plasma-surface interaction which makes up the tokamak exhaust.

Tokamak edge plasmas are characterised by supersonic flows towards the solid surfaces, steep temperature gradients, large discrepancies in temporal and length scales in different directions, surface interactions, the presence of several plasma species with distinct transport properties,

and a vast and complex array of atomic and molecular physics processes. As well as this, edge perturbations known as edge-localised modes (ELMs) and filaments result in time-varying sources of particles and energy into the edge. Because of this, quantitative predictions of edge plasma performance in current and future devices is highly challenging. A key quantity is the value of the heat flux delivered to the walls of the device - if this exceeds the material constraints, then the wall material can degrade and enter the plasma, causing critical confinement losses. Replacing wall materials after each discharge is also operationally difficult as well as expensive. Therefore, there is a need for a greater understanding of the physics determining the transport of particles and energy from the core to the walls via the edge, where transport in the direction parallel to the magnetic fields is dominant. This will enable better predictions in tokamak experiments, and permit experimentalists to utilise any available control parameters to minimise or manage issues related to this exhaust region.

1.4 Theory and modelling in tokamak edge plasmas

Accurate models of the plasma edge in tokamaks are essential for predicting reactor performance. However, the physics governing the behaviour of these plasmas is multi-faceted and difficult to model [27]. In general, models which contain a sufficient degree of fidelity do not have analytical solutions, and so numerical solutions must be found. This is a challenge because a huge range of length and temporal scales are relevant (see Figure 1.8), from the electron orbit about the magnetic field ($\sim 10^{-5}$m, 10^{-11}s) to the parallel length of magnetic field lines connecting solid surfaces ($\sim 10^{2}$m) and the evolution of macroscopic plasma features ($\sim 10^{-1}$s). The physics of plasmas is also highly non-linear, where tight coupling exists between important phenomena. This is most clearly demonstrated by the electromagnetic field, where plasma flows drive fields which exert forces back on the plasma.

Plasmas are very well-described by kinetic equations, which are derived using a statistical treatment of the equations of motion for all the charged particles in a plasma. They detail the time evolution of a probability distribution function in the phase space made up of position

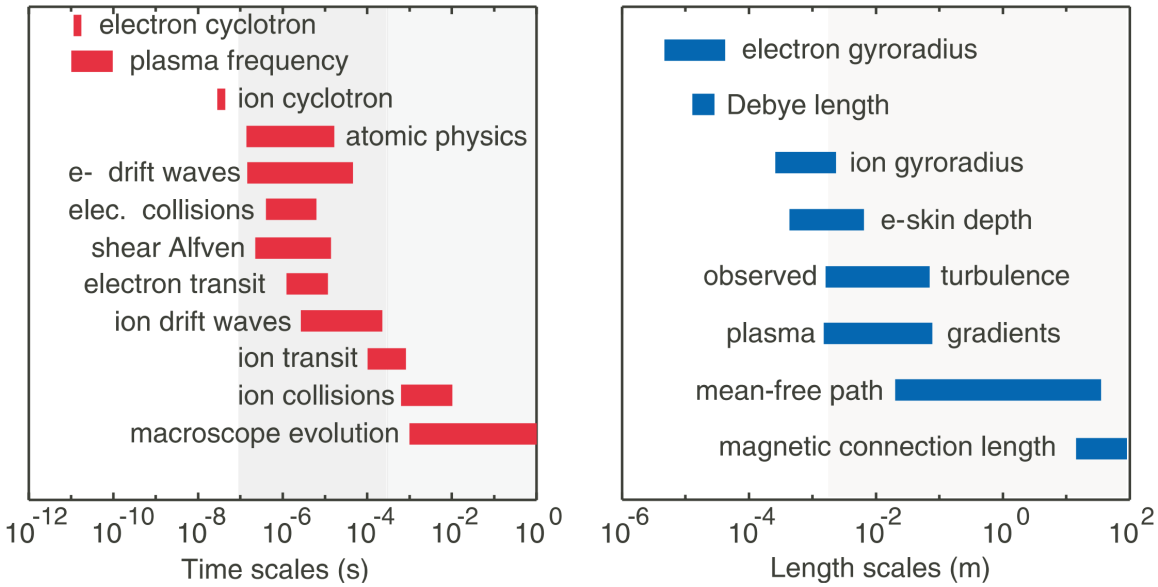

Figure 1.8: A summary of relevant length and temporal scales in scrape-off layer plasmas. Figure reproduced from [28].

and velocity or momentum. Variations on the kinetic equation stem from the treatment of collisions. Long-range Coulomb collisions between charged plasma particles can often safely be ignored at high temperatures because the cross-section decreases with energy, but at lower temperatures or higher densities they will have an effect on the distribution function which can be likened to a drag term and a diffusion term in velocity space. When neutral particles are present in the plasma, short-range Boltzmann collisions describing inelastic processes such as ionization may also be important.

The core challenge of modelling SOL plasmas with kinetic equations is in the fact that plasma conditions range from nearly collisionless in the region close to the core, to highly collisional and partially ionized (such that neutral particles are present) close to the walls. This means that these collision terms are important, but in general they take integro-differential forms and are thus expensive to compute. In addition, the high dimensionality of kinetic equations (7 in total: time, three spatial dimensions and three velocity dimensions) make numerical solutions to relevant problems intractable, and analytical solutions are rare.

A solution to this problem is offered by averaging over the velocity space dimensions, yielding a set of equations which describe the behaviour of macroscopic fluid quantities such as density, flow speed and temperature. While analytical solutions to fluid models remain elusive, they

are typically amenable to computation. However, averaging over velocity space in this way represents a loss of information: to avoid an infinite hierarchy of equations, a closure must be applied at some point by assuming some form of the distribution function. A common choice is to assume the distribution is at or close to a Maxwellian,

$$f(v) = n\left(\frac{m}{2\pi kT}\right)^{3/2} \exp\frac{-mv^2}{2kT}, \tag{1.6}$$

where for a given species of plasma particle (e.g. electrons), v is the velocity magnitude, n is the local density, T is the temperature, m is the particle's mass and k is Boltzmann's constant. This choice is natural since collisions between particles in plasmas act to push the plasma towards local thermodynamic equilibrium (LTE) and Maxwellian distributions, but this means that fluid models rely on sufficiently high collisionality to be valid. In practice, this means there is an assumption that the mean free path of plasma particles, λ, is short relative to some length scale of interest, L (for example the plasma dimensions), i.e. $\lambda/L \ll 1$. When this condition is not met, local plasma behaviour can depend on spatially distant conditions and so the behaviour may be termed 'non-local'. Non-local plasma effects are coincident with a strong departure from Maxwellian-distributed particles, highlighting that a kinetic treatment is necessary to capture this behaviour. As such, the term kinetic is used synonymously with non-local in this context. For a plasma consisting of electrons and ions, the greater mobility of the electrons (due to their small mass) and their importance in plasma-atomic reactions in the SOL means that kinetic effects in the electrons may be particularly relevant.

The presence of certain phenomena can push the plasma far from LTE and drive kinetic effects. Some examples are: time-varying sources of particles or energy into the edge such as ELMs and filaments; steep temperature gradients, where velocity-dependent particle mean free paths can result in local energy transport which depends on distant plasma conditions; inelastic collisions with atomic particles (including impurity species), which can deplete or seed high energy particle populations; and plasma-surface interactions, which act to truncate distribution functions above some threshold velocity leading to anisotropies. All of these phenomena are present in SOL plasmas, but for fluid models to be invalid the necessary condition of low

collisionality must also be met. Crucially, the hot edge plasma adjacent to the core can have very long mean free paths relative to the parallel distance along the SOL, so it is plausible that this is indeed the case. However, a defining feature of tokamak edge plasmas is that collisionality varies significantly along the parallel direction, increasing to high collisionality in the cool, dense plasma close to the walls. There is therefore a competition between drivers of kinetic effects in SOL plasmas and collisions, which act to localise the plasma behaviour and ensure fluid models are appropriate. Accordingly, there is an open question as to the validity of some aspects of fluid models of SOL plasmas, in particular in relation to transport in the parallel direction, and there is a clear motivation to compare predictions from kinetic models with fluid treatments.

This question is more pressing for future devices under design and construction, since the collisionality range spanned in the edge plasmas will be larger. We can define a collisionality parameter [24]

$$\nu_u^* = L/\lambda_u \simeq 10^{-16} L n_u / T_u^2,$$

where λ_u is the Coulomb mean free path of SOL plasma particles upstream, i.e. close to the core plasma, L is the length parallel to the magnetic field of the SOL from surface to surface in m, n_u is the upstream plasma density in m^{-3} and T_u its temperature in eV. Both n_u and T_u are controllable in tokamak experiments to some extent, depending largely on conditions on the core, so we can use ν_u^* to assess SOL conditions that result from a given tokamak experiment. Given that collisionality will be high close to the walls (a result of the required low temperatures there), $\nu_u^* \ll \nu_{wall}^*$, and that pressure is approximately constant in a given SOL flux tube and therefore collisionality increases monotonically along the SOL in the parallel direction between the core and the wall, then ν_u^* is a good proxy for the collisionality range of a given SOL plasma. Figure 1.9 shows how ν_u^* varies in current tokamaks and is expected to vary in future tokamaks as a result of differences in the values of L, n_u and T_u. It is clear that a different plasma regime will be accessed in future devices, and it is not obvious that fluid plasma models will be able to capture these collisionality ranges accurately.

The need for improved understanding and modelling of plasma transport in the SOL is demon-

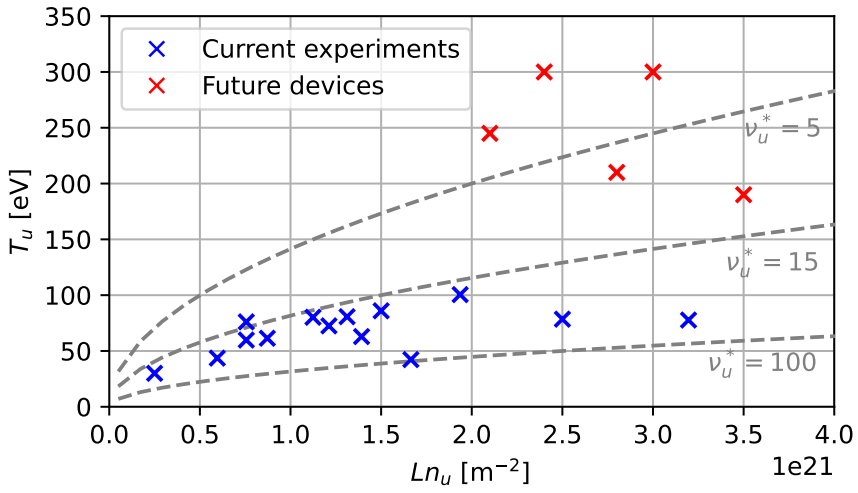

Figure 1.9: Plot of the range of Ln_u and T_u which are accessed in current tokamak experiments and in future planned devices. Also shown are some contours of constant collisionality parameter ν_u^*. Data for current experiments (DIII-D and JET) from [29, 30] and estimates for future experiments (ITER, DEMO and SPARC) from [31–33]

strated by discrepancies in experimental observations compared to predictions. An example comes from modelling with SOLPS-ITER [34], which is a widely-used edge plasma code for modelling of tokamak experiments where the plasma is modelled as a fluid and the neutral particles are modelled kinetically. Agreement between SOLPS-ITER and experiments is generally good, although this relies on post-hoc fitting of cross-field diffusive fluxes, meaning its predictive capacity is limited somewhat. Moreover, discrepancies often exist in plasma conditions close to the walls, with lower temperatures and higher densities predicted compared to experimental observations [35]. This is closely related to the neutral pressure, where discrepancies have been seen in a recent code comparison with experiments on the TCV tokamak by Wensing et al. [36]. In Figure 1.10, reproduced from this paper, we see various unsuccessful attempts to resolve differences in the measured divertor neutral pressure by making changes to the modelling approach. It has been suggested [1, 37] that non-local transport in the direction parallel to the magnetic field may be at the root of such differences. Differences from classical predictions have also been observed experimentally in measurements of conditions at the plasma-surface interface [38].

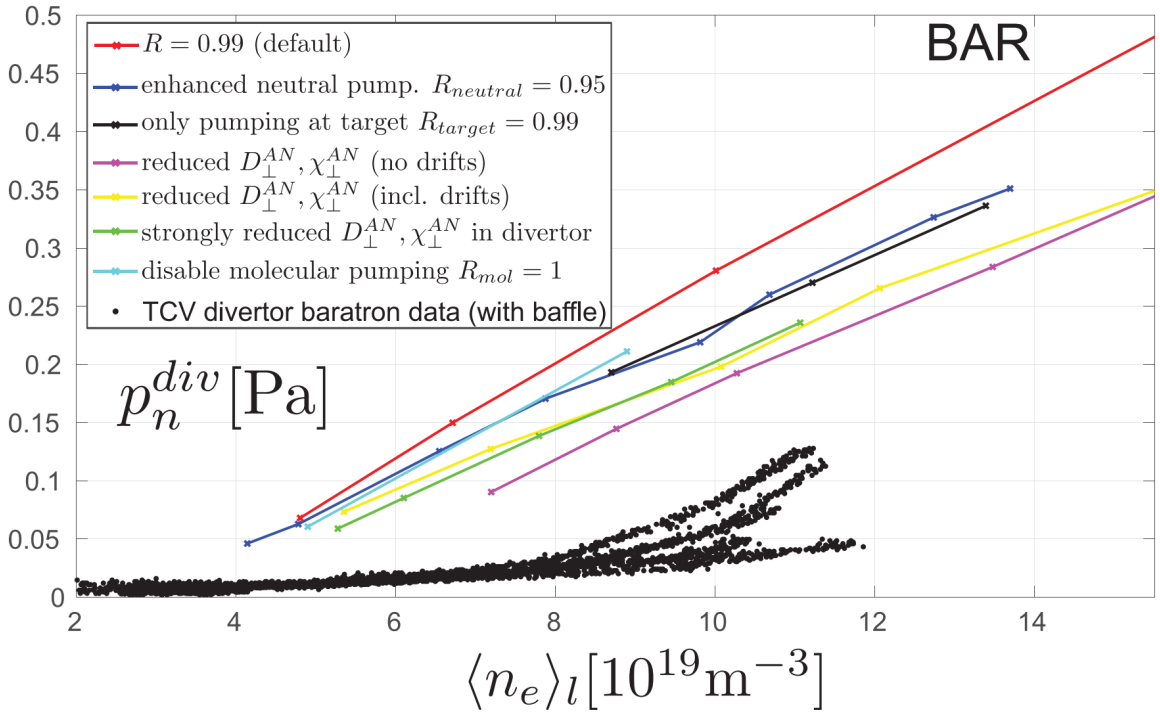

Figure 1.10: Attempts to resolve the discrepancy in divertor neutral pressure p_n^{div} as measured in experiments on the TCV tokamak and SOLPS-ITER simulations, while varying the line-averaged electron density $\langle n_e \rangle_l$. Figure reproduced from [36].

1.5 Research outline

Having motivated the task of seeking greater understanding of plasma transport processes in the edge plasma of tokamaks, and with particular reference to a kinetic treatment of the electron parallel transport, here we will now discuss the approach to attempting to answer some of these questions.

Chapter 2: Background

Here, we will work through the theoretical background required to carry out novel investigations of plasma transport in the SOL. A general overview of plasma transport will be presented, starting from a kinetic description and working towards a fluid description as is used in much plasma modelling today. Specific physics related to the SOL will be presented, along with some key insights gained from simplified analytical models. Plasma-atomic physics is discussed along with methods used to handle the large number of atomic processes involved. Finally, there will

be a discussion of non-local transport followed by a review of the current state of the field.

Chapter 3: Numerical modelling

The investigations in this work have been carried out using the plasma transport code SOL-KiT [4], which is briefly outlined. The studies with this code presented later have required upgrades to the physics model in SOL-KiT, and these will be discussed here and benchmarked. These extensions relate to the models used for ions and neutral particles in SOL-KiT, as well as a method of reducing the number of collision operators which need to be evaluated. In addition, a standalone atomic physics code, SIKE, has been developed to study kinetic effects in plasma-impurity reaction rates. This will also be described and benchmarked.

Chapter 4: Electron-ion energy transfer

An investigation into kinetic effects in electron-ion energy transfer in SOL plasmas is presented, both in steady-state and transient regimes. This chapter has been adapted from a paper published in the European Physical Journal Plus [39]. Results from this study inform the direction of the subsequent investigations.

Chapter 5: Scaling laws for kinetic effects in scrape-off layer plasmas at equilibrium

Another investigation carried out with SOL-KiT was motivated by the desire to understand the region of parameter space in which kinetic effects are and are not important in SOL plasmas. From this, a set of scaling laws have been observed which predict the magnitude of kinetic effects seen in simulations, which can be used as corrections to a fluid model. The results from this study have been submitted to Nuclear Fusion for publication, and are currently under review.

Chapter 6: Kinetic effects in plasma-impurity reaction rates

Given that impurities play such an important role in the scrape-off layer and tokamak performance more generally, there is a need to include them in our models. An initial investigation has been carried out and presented here, which looks into the presence of kinetic effects in plasma-impurity reaction rates, where it is natural to expect that modified electron velocity distribution functions and temperature profiles may change predictions for impurity radiation in SOL plasmas.

Chapter 7: Conclusions

The main conclusions of this body of work will be presented and discussed. Limitations will also be discussed, along with some further research questions which have been raised in the course of this study.

Chapter 2

Theoretical background

Plasmas exhibit an array of complex behaviour which is qualitatively different from that of neutral gases. This is despite the fact that, at a microscopic level, the physics governing their behaviour is similar. The key difference is the importance of the electromagnetic fields, which influence and are influenced by the motion of the charged plasma particles.

The primary and most general question we are interested in in this thesis is that of transport, which is to ask how macroscopic quantities move within and around a system containing a plasma. This question is crucial in tokamak plasmas, where there is an enormous change in conditions over just a few metres between the core and the walls. Understanding and predicting the flux of quantities such as mass and energy, driven by such steep gradients (as well as sources and sinks), is central to being able to create a sustained and controlled fusion reaction in the lab.

We may start a description of plasma transport from a macroscopic (fluid) viewpoint, which is intuitive, or a microscopic (kinetic) viewpoint, which is precise. In this thesis we are concerned with plasmas where theories in terms of fluid quantities are useful, but may miss important physics that only a kinetic treatment can capture. Because of this, a fluid transport theory relevant to the scrape-off layer will be developed by first starting with a description of the particle kinetics of plasmas. There will be an outline of the atomic physics which is relevant to partially ionized tokamak plasmas, as well as some discussion of the distinct phenomena missed

by fluid treatments of the scrape-off layer. Finally, a literature review of fluid and kinetic approaches to modelling tokamak edge plasmas will be presented.

Although the discussion presented here will start from a general perspective, we are primarily interested in electron kinetics in this work due to their significant role in scrape-off layer transport, and so the focus will progressively lean towards that direction. The role of ion kinetics will be discussed in Section 2.8.

2.1 Some basic plasma physics

A neutral gas with atomic number Z which has been ionized to form a plasma can be considered as a sea of electrons with charge $q_e = -e$, and ions with charge $q_i = Ze$, all of which are free to move independently and where the net electric charge is close to zero. If we were to place an additional positively charged particle somewhere in the plasma, it would attract electrons and repel ions so that the additional charge is locally neutralized. Under the assumptions of Boltzmann-distributed particles and particle energies dominated by kinetic energy rather than electrostatic potential energy, it can be shown [40] that the electrostatic potential ϕ around the particle is $\phi(r) \propto r^{-1}\exp(-r/\lambda_D)$, where r is the distance from the additional charge and λ_D is the Debye length,

$$\lambda_D = \left(\frac{\epsilon_0 kT}{n_e e^2}\right)^{1/2}, \tag{2.1}$$

where ϵ_0 is the vacuum permittivity, k is Boltzmann's constant, n_e is the electron density and T is the plasma temperature. So the electrostatic potential varies over a length scale set by λ_D, meaning that the additional charge is effectively screened beyond a sphere with radius approximately equal to λ_D. The number of particles in a Debye sphere is

$$N_D = \frac{4\pi}{3}\lambda_D^3 n_e, \tag{2.2}$$

where $N_D \gg 1$ is required due to assumptions made for Debye shielding theory to be valid. Such a plasma is called 'weakly coupled'. For a weakly coupled plasma, Debye shielding predicts

that random fluctuations will not produce charge imbalances over distances greater than λ_D and so the plasma is said to be quasineutral, $n_e = Zn_i$, where n_i is the ion density.

Another fundamental parameter is the plasma frequency, ω_{pe}, which is related to the speed at which the electronic shielding process described above occurs. If we were to displace a slab of electrons in the plasma some distance, their equation of motion in the electric field which arises from this displacement describes simple harmonic motion with a frequency

$$\omega_{pe} = \left(\frac{n_e e^2}{m_e \epsilon_0} \right)^{1/2}. \tag{2.3}$$

In the presence of a magnetic field, plasma electrons and ions will gyrate about the field lines at a frequency which depends on their charge-to-mass ratio, q/m, and the strength of the magnetic field, B. The Larmor frequency is thus

$$\Omega = \frac{qB}{m}. \tag{2.4}$$

The radius of this orbit depends also on the magnitude of the velocity component of the particle which is perpendicular to the magnetic field, $v_\perp$, so the Larmor radius is defined

$$r_L = \frac{v_\perp}{\Omega}. \tag{2.5}$$

Typically, the shortest time and length scales in plasmas are related to the plasma frequency and the electron Larmor radius. It is also useful to relate the Coulomb collision times and mean free paths of the different plasma species, since they are fundamental to understanding many important aspects of plasma transport. Coulomb collisions will be discussed in detail later in this chapter, but a simple estimate of the collisional mean free path is

$$\lambda \simeq 10^{16} \frac{T^2}{n}, \tag{2.6}$$

for temperature in eV and density in m^{-3}, where the values for both electron-electron and

ion-ion collisions are similar. The collision time is

$$\tau = \frac{v}{\lambda} \tag{2.7}$$

for some velocity v, which we may estimate with the thermal velocity, $v_{th} = \sqrt{2kT/m}$. Because of their much smaller mass, the thermal velocity of electrons is larger and so their collision time is typically shorter than the ions.

2.2 The kinetic equation

There are several ways of arriving at the kinetic equation. Here, a brief derivation of the Vlasov equation via the Klimontovitch equation is presented (following a similar approach to that presented by Swanson [41]), and it is the Vlasov equation which is referred to as 'the kinetic equation' here.

The starting point is a collection of N_0 plasma particles of species α, where the position of the i^{th} particle is $\mathbf{x}_i(t)$ and its velocity is $\mathbf{v}_i(t)$. The number density function, which describes the location of all particles in the 6-dimensional phase space made up of the position and velocity coordinates, is then

$$N_\alpha(\mathbf{x}, \mathbf{v}, t) = \sum_{i=1}^{N_0} \delta\left[\mathbf{x} - \mathbf{x}_i(t)\right] \delta\left[\mathbf{v} - \mathbf{v}_i(t)\right]. \tag{2.8}$$

To describe the plasma as a whole, we can sum over all species α (where α may be electrons or any of the ion species present) to define a total number density function,

$$N(\mathbf{x}, \mathbf{v}, t) = \sum_{\alpha} N_\alpha(\mathbf{x}, \mathbf{v}, t).$$

Integrating this equation over a small phase space volume gives the number of particles in that volume, but the resulting function is not smooth due to (2.8) being made up of delta functions. This will be dealt with shortly.

The evolution of the particle positions in time is

$$\frac{\partial \mathbf{x}_i}{\partial t} = \mathbf{v}_i, \tag{2.9}$$

and the velocities evolve due to the Lorentz force (assuming no other forces are acting on the particles),

$$\frac{\partial \mathbf{v}_i}{\partial t} = \mathbf{F}_i/m_\alpha = q_\alpha \left(\mathbf{E}^m(\mathbf{x}_i, t) + \mathbf{v}_i \times \mathbf{B}^m(\mathbf{x_i}, t)\right)/m_\alpha, \tag{2.10}$$

where q_α is the electric charge of particles of species α and m_α is their mass. The electric and magnetic fields, $\mathbf{E}^m$ and $\mathbf{B}^m$, are the electric and magnetic fields experienced by particle i due to all other particles as well as any externally applied fields. These are described by Maxwell's equations,

$$\nabla \cdot \mathbf{E}^m(\mathbf{x}, t) = \rho/\epsilon_0, \tag{2.11a}$$

$$\nabla \cdot \mathbf{B}^m(\mathbf{x}, t) = 0, \tag{2.11b}$$

$$\nabla \times \mathbf{E}^m(\mathbf{x}, t) = -\frac{\partial \mathbf{B}^m(\mathbf{x}, t)}{\partial t}, \tag{2.11c}$$

$$\nabla \times \mathbf{B}^m(\mathbf{x}, t) = \mu_0 \mathbf{j}^m(\mathbf{x}, t) + \frac{1}{c^2}\frac{\partial \mathbf{E}^m(\mathbf{x}, t)}{\partial t}, \tag{2.11d}$$

where $\rho = \sum_\alpha q_\alpha \int N_\alpha d\mathbf{v}$ and $\mathbf{j} = \sum_\alpha q_\alpha \int \mathbf{v} N_\alpha d\mathbf{v}$ are the charge and current densities respectively, μ_0 is the vacuum permeability and c is the speed of light.

To see how N_α evolves in time, we take the time derivative, noting that

$$\frac{\partial}{\partial t}\delta\left[\mathbf{r} - \mathbf{x}_i(t)\right]\delta\left[\mathbf{v} - \mathbf{v}_i(t)\right] = -\frac{\partial \mathbf{x}_i}{\partial t}\cdot\nabla\delta\left[\mathbf{x} - \mathbf{x}_i(t)\right] - \frac{\partial \mathbf{v}_i}{\partial t}\cdot\nabla_{\mathbf{v}}\delta\left[\mathbf{v} - \mathbf{v}_i(t)\right]. \tag{2.12}$$

Therefore, noting also that $\frac{\partial \mathbf{v}_i}{\partial t}$ is given by the Lorentz force (2.10), we have

$$\begin{aligned}\frac{\partial N_s}{\partial t} = &-\sum_i^{N_0} \mathbf{v}_i \cdot \nabla\delta\left[\mathbf{x} - \mathbf{x}_i(t)\right]\delta\left[\mathbf{v} - \mathbf{v}_i(t)\right] \\ &-\sum_i^{N_0} \frac{q_s}{m_s}\left(\mathbf{E}^m + \mathbf{v}_i \times \mathbf{B}^m\right)\cdot\nabla_{\mathbf{v}}\delta\left[\mathbf{x} - \mathbf{x}_i(t)\right]\delta\left[\mathbf{v} - \mathbf{v}_i(t)\right],\end{aligned} \tag{2.13}$$

from which which we can arrive at the Klimontovitch equation,

$$\begin{aligned}\frac{\partial N_\alpha}{\partial t} &= -\sum_i^{N_0} \mathbf{v}\cdot\nabla\delta\left[\mathbf{x}-\mathbf{x}_i(t)\right]\delta\left[\mathbf{v}-\mathbf{v}_i(t)\right] \\ &\quad -\sum_i^{N_0}\frac{q_\alpha}{m_\alpha}\left(\mathbf{E}^m+\mathbf{v}\times\mathbf{B}^m\right)\cdot\nabla_{\mathbf{v}}\delta\left[\mathbf{x}-\mathbf{x}_i(t)\right]\delta\left[\mathbf{v}-\mathbf{v}_i(t)\right] \\ &= -\mathbf{v}\cdot\nabla N_\alpha - \frac{q_\alpha}{m_\alpha}\left(\mathbf{E}^m+\mathbf{v}\times\mathbf{B}^m\right)\cdot\nabla_{\mathbf{v}}N_\alpha,\end{aligned} \tag{2.14}$$

by letting $\mathbf{v}_i \to \mathbf{v}$ (since the Dirac deltas will only be non-zero when $\mathbf{v} = \mathbf{v}_i$).

At this point, N_α is not smooth and solving (2.14) requires detailed knowledge of the positions and velocities of all particles. A more useful equation can be obtained by averaging over a small phase space volume $\Delta V = \Delta x\Delta y\Delta z\Delta v_x\Delta v_y\Delta v_z$, giving the probability distribution function

$$f_\alpha(\mathbf{x},\mathbf{v}) = \frac{N_\alpha(\mathbf{x}<\mathbf{x_i}<\mathbf{x}+\Delta\mathbf{x},\mathbf{v}<\mathbf{v_i}<\mathbf{v}+\Delta\mathbf{v})}{\Delta V}. \tag{2.15}$$

The precise value of N_α can then be written as a sum of the average and deviation from the average,

$$N_\alpha = f_\alpha + \delta N_\alpha, \tag{2.16}$$

and similarly for the electric and magnetic fields,

$$\mathbf{E}^m = \mathbf{E} + \delta\mathbf{E}^m \tag{2.17a}$$

$$\mathbf{B}^m = \mathbf{B} + \delta\mathbf{B}^m \tag{2.17b}$$

We can now insert these expressions into the Klimontivitch equation (2.14) and take the average values of all quantities (denoted by $\langle ...\rangle$), making use of the fact that $\langle\delta N_\alpha\rangle = 0$, etc. to yield a general kinetic equation

$$\frac{\partial f_\alpha}{\partial t} + \mathbf{v}\cdot\nabla f_s + \frac{q_\alpha}{m_\alpha}(\mathbf{E}+\mathbf{v}\times\mathbf{B})\cdot\nabla_{\mathbf{v}}f_\alpha = -\frac{q_\alpha}{m_\alpha}\left\langle(\delta\mathbf{E}^m+\mathbf{v}\times\delta\mathbf{B}^m)\cdot\nabla_{\mathbf{v}}\delta N_\alpha\right\rangle. \tag{2.18}$$

The left hand side here describes the average (macroscopic) behaviour, while the right hand

side here describes the effect of microscopic deviations of the electric and magnetic fields, or Coulomb collisions. If we ignore collisions on the basis that the relative effect of fluctuations is small providing the number of particles in the averaging volume is large, then we get the Vlasov equation,

$$\frac{\partial f_\alpha}{\partial t} + \mathbf{v} \cdot \nabla f_s + \frac{q_\alpha}{m_\alpha}(\mathbf{E} + \mathbf{v} \times \mathbf{B}) \cdot \nabla_{\mathbf{v}} f_\alpha = 0. \tag{2.19}$$

Along with Maxwell's equations for the average fields $\mathbf{E}$ and $\mathbf{B}$, with the charge and current densities defined $\rho = \sum_\alpha q_\alpha \int f_\alpha d\mathbf{v}$ and $\mathbf{j} = \sum_\alpha q_\alpha \int \mathbf{v} f_\alpha d\mathbf{v}$, we now have a solvable equation set.

It is possible to reformulate the distribution function, and the kinetic equation as a whole, as a series solution in terms of spherical harmonics in velocity space [42], where we start by shifting from Cartesian coordinates in velocity space, $\mathbf{v} = (v_x, v_y, v_z)$, to spherical coordinates, (v, θ, ϕ), where v is the velocity magnitude, and θ and ϕ are the polar and azimuthal angular coordinates respectively. We can then write the distribution function as

$$f_\alpha(\mathbf{v}) = f_\alpha(v, \theta, \phi) = \sum_{l=0}^{\infty} \sum_{m=-l}^{l} f_l^m(v) P_l^{|m|}(\cos\theta) e^{im\phi},$$

where $P_l^{|m|}$ are the associated Legendre polynomials. This is particularly useful for the electrons in moderately collisional scenarios and where the electric field is not too strong, as the distribution can then be viewed as being mostly spherically symmetric with some corrections. What's more, spherical harmonics are eigenfunctions of the scattering operator for collisions between electrons and heavy particles. The kinetic equation then becomes a series of equations for the coefficients $f_l^m(v)$, and so offers a physically meaningful method of dimensionality reduction providing the series is truncated at some point. See Section 3.1.1 and Appendix A.1 for more details.

2.3 Collisions

In deriving the Vlasov equation (2.19), we have assumed that plasma particles only interact with other particles via electromagnetic fields from macroscopic, collective motion, over distances greater than the Debye length. Short range encounters (i.e. collisions) do occur however, both between charged particles and between charged and neutral particles. In general, the effect of collisions is to cause the phase space position of particles to jump over timescales which are short compared to the undisturbed motion of the particle. As such, they can be seen as sources/sinks of the distribution function in phase pace, such that we can write the more general kinetic equation,

$$\frac{\partial f_\alpha(t,\mathbf{r},\mathbf{v})}{\partial t} + \mathbf{v}\cdot\nabla f_\alpha(t,\mathbf{r},\mathbf{v}) + \mathbf{a}\cdot\nabla_{\mathbf{v}} f_\alpha(t,\mathbf{r},\mathbf{v}) = \sum_\beta C_{\alpha,\beta}(f_\alpha, f_\beta), \tag{2.20}$$

where $C_{\alpha,\beta}$ is the collision operator for collisions between species α and β, which in general is a function of the distributions of both species types.

Collisions of plasma particles with neutrals are akin to billiard ball collisions, where the mediating potential is short-range and the deflection angle may be large. On the other hand, collisions between charged species via the Coulomb force are dominated by small, grazing collisions [41]. We use distinct formalisms to treat each interaction type but both start from the Boltzmann integral, which will be presented first before presenting the Fokker-Planck collision operator for Coulomb collisions. The discussion in this section is largely adapted from material contained in [40–44].

2.3.1 Boltzmann collision operator

We want to determine the effect on the distribution function of collisions between particles of species α and β. We will once again avoid providing a mathematically rigorous derivation here, instead providing a simplified outline for brevity. See e.g. [45,46] for a more detailed discussion. We will consider binary collisions where the initial velocities are $\mathbf{v}_\alpha^i$, $\mathbf{v}_\beta^i$ and final velocities are

$\mathbf{v}_\alpha^f$, $\mathbf{v}_\beta^f$, which interact via the potential $V(r)$ where r is their relative position. The form of the potential at this stage is unimportant, only that it depends of relative position only. The relative velocity is

$$\mathbf{v}_{rel}^i = \mathbf{v}_\alpha^i - \mathbf{v}_\beta^i, \tag{2.21}$$

which changes in direction but not magnitude during an elastic collision, so that $v_{rel}^i = v_{rel}^f = v_{rel}$.

In a time δt, the change in the number of particles of species α in a given phase space volume element $d\mathbf{r}d\mathbf{v}$ around the coordinates $(\mathbf{r}, \mathbf{v})$ due to collisions is

$$\begin{aligned} C_{\alpha,\beta} d\mathbf{r}d\mathbf{v}\delta t &= \delta f_\alpha(t, \mathbf{r}, \mathbf{v}) d\mathbf{r}d\mathbf{v} \\ &= (\text{collisions involving particles with velocity } \mathbf{v}_\alpha^f) \\ &\quad - (\text{collisions involving particles with velocity } \mathbf{v}_\alpha^i), \end{aligned} \tag{2.22}$$

i.e. there is a gain of particles into $d\mathbf{v}$ from particles of species α with $\mathbf{v}_\alpha^f$, and a loss of particles out of $d\mathbf{v}$ from particles with $\mathbf{v}_\alpha^i$. To determine each of these terms on the right hand side, we define the impact parameter b, which is the distance of closest approach if there is no interaction, and the deflection angle χ, which is uniquely determined by b. See Figure 2.1a. The azimuthal angle, ϕ, is measured relative to the orientation of the x-axis, although this decision is usually arbitrary as the collision parameters of interest are typically independent of ϕ.

To proceed, we will have to assume that no correlations exist between incident particles; a plausible but consequential leap which is responsible for introducing an arrow of time into the kinetic equation.

For the first term in (2.22), the number of particles of species β which can interact is given by their density at ($\mathbf{r}$,$\mathbf{v}_\beta^i$) around $d\mathbf{v}_\beta^i$, multiplied by the spatial volume element swept in time δt (see Figure 2.1b), which is $v_{rel}\delta t d\phi b db$, integrated over all possible initial velocities $\mathbf{v}_\beta^i$, impact parameters b and azimuthal angles ϕ. Multiplying by the number of particles of species α at ($\mathbf{r}$,$\mathbf{v}_\alpha^i$) around $d\mathbf{v}_\alpha^i$ therefore gives the total number of collisions,

$$\delta t d\mathbf{r} d\mathbf{v}_\alpha^i \int d\mathbf{v}_\beta^i \int d\phi \int b db f_\alpha(\mathbf{v}_\alpha^i) f_\beta(\mathbf{v}_\beta^i) v_{rel}, \tag{2.23}$$

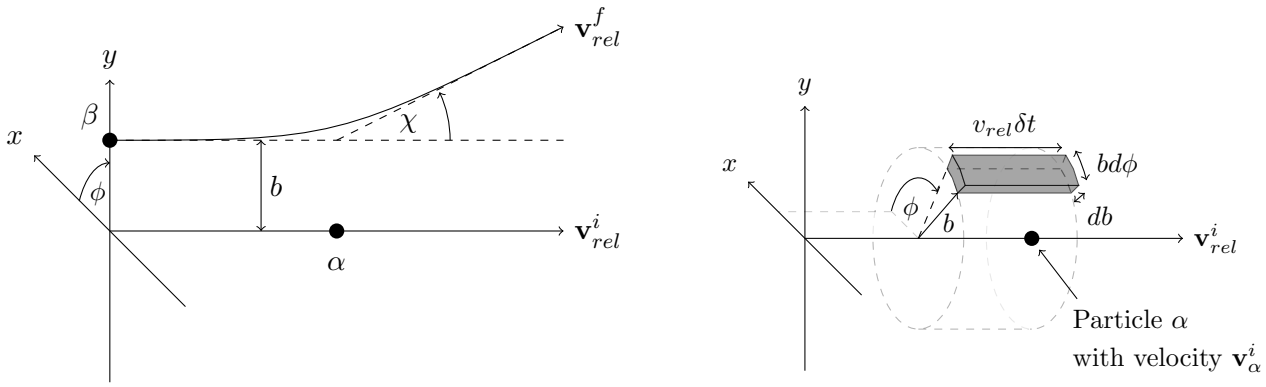

(a) Collision geometry. We orient along the $\mathbf{v}^i_{rel}$ direction, and are primarily interested in scattering angle χ rather than the orientation of the x-y plane.

(b) Volume element, where we can integrate over all b and ϕ to get the number of particles (of species β) which can interact with a particle of species α around $d\mathbf{v}^i_\alpha$.

Figure 2.1: Diagrams showing the setup for this heuristic derivation of the Boltzmann collision integral.

where we have dropped the $t, \mathbf{r}$ dependence in f_α and f_β to simplify the notation. With similar arguments, the loss term in (2.22) is

$$\delta t d\mathbf{r} d\mathbf{v}^f_\alpha \int d\mathbf{v}^f_\beta \int d\phi \int b db f_\alpha(\mathbf{v}^f_\alpha) f_\beta(\mathbf{v}^f_\beta) v_{rel}. \tag{2.24}$$

We now use the fact that the determinant of the Jacobian on coordinate transformation from $\mathbf{v}^i_\alpha$, $\mathbf{v}^i_\beta$ to $\mathbf{v}^f_\alpha$, $\mathbf{v}^f_\beta$ is 1, meaning that $d\mathbf{v}^i_\alpha d\mathbf{v}^i_\beta = d\mathbf{v}^f_\alpha d\mathbf{v}^f_\beta$. Furthermore, given we are free to choose the volume element $d\mathbf{v}$ at which we are evaluating the effect of collisions, we may set $d\mathbf{v} = d\mathbf{v}^i_\alpha$ in (2.22) and arrive at a typical form of the Boltzmann collision integral,

$$C_{\alpha,\beta} = \left(\frac{\delta f_\alpha(\mathbf{v}^i_\alpha)}{\delta t} \right) = \int d\mathbf{v}^i_\beta \int d\phi \int b db v_{rel} \left[f_\alpha(\mathbf{v}^f_\alpha) f_\beta(\mathbf{v}^f_\beta) - f_\alpha(\mathbf{v}^i_\alpha) f_\beta(\mathbf{v}^i_\beta) \right].$$

The differential cross-section, $\sigma(v_{rel}, \chi)$, is defined in terms of the impact parameter, b, and the scattering angle, χ,

$$\sigma(v_{rel}, \chi) = \frac{b}{\sin\chi} \left| \frac{\partial b}{\partial \chi} \right|,$$

which allows us to rewrite the collision integral as a function of $\sigma(v_{rel}, \chi)$ and an integral over

solid angle $d^2\Omega$,

$$C_{\alpha,\beta}(\mathbf{v}_\alpha^i) = \int d\mathbf{v}_\beta^i \int d^2\Omega v_{rel}\sigma(v_{rel},\chi)\left[f_\alpha(\mathbf{v}_\alpha^f)f_\beta(\mathbf{v}_\beta^f) - f_\alpha(\mathbf{v}_\alpha^i)f_\beta(\mathbf{v}_\beta^i)\right]. \tag{2.25}$$

This Boltzmann collision operator is hard to deal with in practice: it gives the kinetic equation an integro-differential form, while also being non-linear in f_α. However, the general form presented here is a useful starting point for developing more tractable collision terms which can be used in kinetic modelling of plasmas. For example, for electrons colliding with heavy ions or neutral particles (where the mass ratio is at least a few thousand), the collision is characterised by an angular deflection and a small transfer of kinetic energy. This means we can put $\mathbf{v}_\beta^i \simeq \mathbf{v}_\beta^f$ in (2.25) and, given the distribution of the heavy scatterers looks like a delta function to the electrons, $f_\beta \simeq n_\beta\delta(0)$ with β referring to some heavy species, we can eliminate the dependence on f_β entirely to yield a simplified operator,

$$C_{\alpha,\beta}(\mathbf{v}_\alpha^i) = n_\beta \int d^2\Omega v_{rel}\sigma(v_{rel},\chi)\left[f_\alpha(\mathbf{v}_\alpha^f) - f_\alpha(\mathbf{v}_\alpha^i)\right].$$

Appendix A.2 will outline a method, along similar lines and employing the spherical harmonic expansion, of treating the Boltzmann collision operator for electrons which is amenable to computation. For collisions between particles with equal mass however, such simplifications are not possible. Some processes do still offer some opportunities for streamlining (2.25) though. One SOL-relevant example is the charge exchange reaction, where a plasma ion collides with a neutral particle and their identities are swapped. Here, we can assume $\mathbf{v}_\alpha^i \simeq \mathbf{v}_\beta^f$ and $\mathbf{v}_\beta^i \simeq \mathbf{v}_\alpha^f$, and a cross-section which has no angular dependence, $\int d^2\Omega\sigma(v_{rel},\chi) = \sigma_{tot}(v_{rel})$, to obtain the simplified operator,

$$C_{\alpha,\beta}(\mathbf{v}_\alpha^i) = f_\beta(\mathbf{v}_\alpha^i)\int d\mathbf{v}_\beta^i v_{rel}\sigma_{tot}f_\alpha(\mathbf{v}_\alpha^i) - f_\alpha(\mathbf{v}_\alpha^i)\int d\mathbf{v}_\beta^i v_{rel}\sigma_{tot}f_\beta(\mathbf{v}_\beta^i).$$

Situations where such simplifying assumptions cannot be made, for example in collisions between like species in plasmas, have in part motivated the development of other approaches, discussed in the next section.

2.3.2 Fokker-Planck collision operator

For Coulomb collisions, especially between like particles, the Boltzmann collision operator is not optimal. It has been developed for binary, short-range collisions, but for charged particles in a plasma there are $\sim 10^3$ particles within a Debye length. As such, Coulomb collisions in plasmas are long-range compared to the mean inter-particle spacing, and involve interactions between many particles. Furthermore, the overall effect of Coulomb interactions is dominated by small-angle deflections, which is due to the relative weakness of the electrostatic potential between interacting particles compared to their thermal energy. Strong interactions, where the scattering angle is large, are rare [41]. This all suggests an alternative approach may be appropriate.

The primary challenge with the Boltzmann collision operator (2.25) is that, for it to be useful, we need to be able to relate the final velocities on the right hand side to the initial velocities. The distinct nature of Coulomb collisions in plasmas offers a way forward. We will retain the definitions and collision geometry of the previous section, see equation (2.21) and Figure 2.1. Under the assumption that small angular deflections dominate, we can write

$$\mathbf{v}_\alpha^f = \mathbf{v}_\alpha^i + \Delta\mathbf{v} + \mathcal{O}(\chi^3)$$

and drop the $\mathcal{O}(\chi^3)$ term, where

$$\Delta\mathbf{v} = \frac{m_\beta}{m_\alpha + m_\beta}\left[\chi v_{rel}(\cos\phi\hat{\mathbf{x}} + \sin\phi\hat{\mathbf{y}}) - \frac{1}{2}\chi^2\mathbf{v}_{rel}^i\right].$$

By inserting this into (2.25), an operator appropriate for Coulomb interactions between all species in a plasma can be obtained. Doing so yields the Landau form of the Fokker-Planck collision operator [41]. This is somewhat involved, so instead here we provide a simpler approach.

We start by considering a distribution function at time t, $f_\alpha(t, \mathbf{v}-\Delta\mathbf{v})$, where a particle changes velocity by $\Delta\mathbf{v}$ after a time Δt. If we propose the existence of some function $p(\mathbf{v}, \Delta\mathbf{v})$, which

gives the probability for a particle at $\mathbf{v}$ to change velocity by $\Delta\mathbf{v}$, then we can write

$$f_\alpha(t+\Delta t,\mathbf{v}) = \int f_\alpha(t,\mathbf{v}-\Delta\mathbf{v})p(\mathbf{v}-\Delta\mathbf{v},\Delta\mathbf{v})d(\Delta\mathbf{v}),$$

meaning we have arrived at $f_\alpha(t+\Delta t,\mathbf{v})$ by considering all possible velocity changes $\Delta\mathbf{v}$, weighted by their probability. If we Taylor expand both the left hand side and the integrand on the right hand side, we can get this expression in terms of functions evaluated at t and $\mathbf{v}$ rather than Δt and $\mathbf{v}-\Delta\mathbf{v}$,

$$\begin{aligned} f_\alpha(t,\mathbf{v}) + \Delta t\frac{\delta f_\alpha(t,\mathbf{v})}{\delta t} + ... \\ = \int d(\Delta\mathbf{v})\left(f_\alpha(t,\mathbf{v})p(\mathbf{v},\Delta\mathbf{v}) - \Delta\mathbf{v}\cdot\frac{\partial(f_\alpha p)}{\partial\mathbf{v}} + \frac{1}{2}\Delta\mathbf{v}\Delta\mathbf{v} : \frac{\partial^2(f_\alpha p)}{\partial\mathbf{v}\partial\mathbf{v}} + ...\right), \end{aligned}$$

where the $\frac{\delta f}{\delta t}$ notation on the left signifies that we are considering the change in f_α only due to collisions. For clarity, $\Delta\mathbf{v}\cdot\frac{\partial}{\partial\mathbf{v}} = \sum_i \Delta v_i\frac{\partial}{\partial v_i}$ and $\Delta\mathbf{v}\Delta\mathbf{v} : \frac{\partial}{\partial\mathbf{v}} = \sum_{i,j}\Delta v_i\Delta v_j\frac{\partial^2}{\partial v_i\partial v_j}$ for $i,j\in\{x,y,z\}$. Now, we can drop terms of order Δt^2 and higher from the left hand side, but we have to include terms up to $\Delta\mathbf{v}\Delta\mathbf{v}$ on the right hand side due to collisions being treated as a random walk process, where the magnitude of $\Delta\mathbf{v}$ and $\Delta\mathbf{v}\Delta\mathbf{v}$ both scale with Δt. We can simplify further by using the fact that p is a probability distribution and so integrates to one,

$$\int p(\mathbf{v},\Delta\mathbf{v})d(\Delta\mathbf{v}) = 1,$$

and by defining the average changes in $\Delta\mathbf{v}$ and $\Delta\mathbf{v}\Delta\mathbf{v}$ in a time Δt,

$$\langle\Delta\mathbf{v}\rangle = \int\frac{\Delta\mathbf{v}p(\mathbf{v},\Delta\mathbf{v})}{\Delta t}d(\Delta\mathbf{v}), \tag{2.26a}$$

$$\langle\Delta\mathbf{v}\Delta\mathbf{v}\rangle = \int\frac{\Delta\mathbf{v}\Delta\mathbf{v}p(\mathbf{v},\Delta\mathbf{v})}{\Delta t}d(\Delta\mathbf{v}), \tag{2.26b}$$

we arrive at the Fokker-Planck equation,

$$\frac{\delta f_\alpha(t,\mathbf{v})}{\delta t} = -\frac{\partial}{\partial\mathbf{v}}\cdot\left(f_\alpha\langle\Delta\mathbf{v}\rangle\right) + \frac{1}{2}\frac{\partial^2}{\partial\mathbf{v}\partial\mathbf{v}} : \left(f_\alpha\langle\Delta\mathbf{v}\Delta\mathbf{v}\rangle\right). \tag{2.27}$$

This equation describes the change in the distribution function due to frequent small-angle Coulomb collisions between charged particles. It can be shown [40] that the first term here produces a deceleration on particles undergoing Coulomb collisions, while the second term acts to spread out a narrow beam in velocity space. Accordingly, the Fokker-Planck equation is often said to constitute a drag and diffusion in velocity space.

Equation (2.27) does not yet tell us how to actually compute the effect of Coulomb collisions on a distribution function, since we do not know the form of $p(\mathbf{v}, \Delta\mathbf{v})$. The derivation of analytical forms for $\langle\Delta\mathbf{v}\rangle$ and $\langle\Delta\mathbf{v}\Delta\mathbf{v}\rangle$ is somewhat involved so only the final results are presented here, see [41] for details. The result is that, for collisions between species α and a (charged) scattering species β, we get

$$\langle\Delta\mathbf{v}\rangle_{\alpha,\beta} = \Gamma_{\alpha,\beta}\frac{\partial\mathcal{H}_\beta}{\partial\mathbf{v}}, \tag{2.28a}$$

$$\langle\Delta\mathbf{v}\Delta\mathbf{v}\rangle_{\alpha,\beta} = \Gamma_{\alpha,\beta}\frac{\partial^2\mathcal{G}_\beta}{\partial\mathbf{v}\partial\mathbf{v}}, \tag{2.28b}$$

where we now have a few quantities to define. $\mathcal{H}$ and $\mathcal{G}$ are the Rosenbluth potentials, which depend only on the scattering species β,

$$\mathcal{H}_\beta(\mathbf{v}) = \frac{m_\beta}{\mu}\int\frac{f_\beta(\mathbf{v}')}{|\mathbf{v}-\mathbf{v}'|}d\mathbf{v}', \tag{2.29a}$$

$$\mathcal{G}_\beta(\mathbf{v}) = \int f_\beta(\mathbf{v}')\,|\mathbf{v}-\mathbf{v}'|\,d\mathbf{v}'. \tag{2.29b}$$

The constant $\Gamma_{\alpha,\beta}$ is

$$\Gamma_{\alpha,\beta} = \frac{q_\alpha^2 q_\beta^2 \ln\Lambda_{\alpha,\beta}}{4\pi\varepsilon_0^2 m_\alpha^2}, \tag{2.30}$$

where $\ln\Lambda$ is the Coulomb logarithm. A key step in deriving these terms, which is also responsible for the Coulomb logarithm appearing in them, involves a consideration of the range of impact parameters b over which we must integrate to evaluate the number of collisions, as in the Boltzmann collision integral (see Figure 2.1). Because of the long-range nature of the Coulomb force, this integral diverges if we try to integrate over all possible impact parameters (or similarly, all scattering angles χ). Instead, we recognise that the Debye length puts an upper limit on the impact parameter, since the Coulomb potential from a scattering particle

is shielded beyond that distance. We can also apply a lower limit by recalling that grazing collisions dominate over large deflections. The Coulomb logarithm then becomes

$$\ln \Lambda_{\alpha,\beta} = \ln \left(\frac{\lambda_D}{b_{min}} \right), \tag{2.31}$$

where b_{min} is the impact parameter yielding a deflection of $\chi = 90°$, which can be calculated in terms of plasma parameters and the masses of the colliding species [47]. $\ln \Lambda$ varies slowly with all parameters due to the logarithm and typically $\ln \Lambda \simeq 10 - 20$; the case where $\ln \Lambda$ approaches unity implies some assumptions on which plasma transport theory rely (such as $N_D \gg 1$) may no longer be valid.

With this, we can write explicitly the usual form of the Fokker-Planck collision operator in terms of the Rosenbluth potentials,

$$C^{FP}_{\alpha,\beta} = \Gamma_{\alpha,\beta} \left\{ -\frac{\partial}{\partial \mathbf{v}} \cdot \left(f_\alpha \frac{\partial \mathcal{H}_\beta}{\partial \mathbf{v}} \right) + \frac{1}{2} \frac{\partial^2}{\partial \mathbf{v} \partial \mathbf{v}} : \left(f_\alpha \frac{\partial^2 \mathcal{G}_\beta}{\partial \mathbf{v} \partial \mathbf{v}} \right) \right\}, \tag{2.32}$$

with $\Gamma_{\alpha,\beta}$, $\mathcal{H}_\beta$ and $\mathcal{G}_\beta$ defined in equations (2.29) and (2.30), and where f_α is evaluated at $(t, \mathbf{r}, \mathbf{v})$. When appearing on the right hand side of the Vlasov equation (2.19), we are able to treat a rich variety of plasmas where conditions mean collisions between plasma particles may be important (both between like particles and different species). This is called the Vlasov-Fokker-Planck (VFP) equation. When also combined with the Boltzmann collision operator (2.25), sometimes referred to (rather clunkily) as the Vlasov-Fokker-Planck-Boltzmann equation, we may treat partially-ionized plasmas where the presence of neutrals also plays an important role in the plasma dynamics. Throughout this thesis, 'the kinetic equation' refers to this general equation which includes the effect of both Fokker-Planck and Boltzmann collisions.

2.4 Moments of the distribution function

From the definition of the distribution function (**??**), the number of particles of species α in an infinitesimal box in phase space is $f_\alpha(t, \mathbf{r}, \mathbf{v}) d\mathbf{r} d\mathbf{v}$. It follows therefore that the spatial variation

of the particle density can be obtained by integrating out the velocity-dependence,

$$n_\alpha(t, \mathbf{r}) = \int f_\alpha(t, \mathbf{r}, \mathbf{v}) d\mathbf{v}, \tag{2.33}$$

where the limits of integration are over all possible values of v_x, v_y and v_z, from $-\infty$ to $+\infty$. Similarly, we can evaluate the weighted average of any velocity-dependent quantity of interest ϕ,

$$\langle \phi \rangle = \frac{1}{n_\alpha} \int \phi f_\alpha(t, \mathbf{r}, \mathbf{v}) d\mathbf{v}, \tag{2.34}$$

where ϕ may be a scalar, vector or arbitrary-rank tensor made of direct products of velocity vectors. In equation (2.33), $\phi = 1$ has been used. Such quantities are referred to as moments of the distribution function.

In studying plasma transport, we are frequently interested in quantities like the flow velocity,

$$\langle \mathbf{v} \rangle = \mathbf{u}_\alpha = \frac{1}{n_\alpha} \int \mathbf{v} f_\alpha(t, \mathbf{r}, \mathbf{v}) d\mathbf{v}, \tag{2.35}$$

the pressure tensor,

$$\langle m_\alpha n_\alpha \mathbf{v}\mathbf{v} \rangle = \underline{\underline{\mathbf{p}}}_{\alpha,tot} = m_\alpha \int \mathbf{v}\mathbf{v} f_\alpha(t, \mathbf{r}, \mathbf{v})_\alpha d\mathbf{v}, \tag{2.36}$$

and the total energy flux,

$$\left\langle \frac{1}{2} m_\alpha n_\alpha v^2 \mathbf{v} \right\rangle = \mathbf{q}_{\alpha,tot} = \frac{1}{2} m_\alpha \int v^2 \mathbf{v} f_\alpha(t, \mathbf{r}, \mathbf{v}) d\mathbf{v}. \tag{2.37}$$

Clearly, these four moments (2.33 - 2.37) are already useful macroscopic plasma parameters. For example the charge density is related to the number density, $\rho_\alpha = q_\alpha n_\alpha$, and the current density is related to the flow velocity, $\mathbf{j}_\alpha = q_\alpha n_\alpha \mathbf{u}_\alpha$. However, it is often helpful to go further by defining the 'peculiar' velocity,

$$\mathbf{w} = \mathbf{v} - \mathbf{u}_\alpha,$$

such that $\langle \mathbf{w} \rangle = 0$, to allow us to distinguish between contributions to transport phenomena from intrinsic ('random') and bulk ('mean') motion.

With this we can calculate the intrinsic and bulk contributions to the total energy density,

$$W_\alpha = \left\langle \frac{1}{2} m_\alpha n_\alpha v^2 \right\rangle = \frac{1}{2} m_\alpha n_\alpha \langle w^2 + u_\alpha^2 + 2\mathbf{w}\cdot\mathbf{u}_\alpha \rangle = \frac{3}{2} n_\alpha k T_\alpha + \frac{1}{2} m_\alpha n_\alpha u_\alpha^2 \tag{2.38}$$

with the definition of temperature as $kT_\alpha = \frac{1}{3} m_\alpha \langle w^2 \rangle$ and $\langle \mathbf{w}\cdot\mathbf{u} \rangle = 0$. Furthermore, we can rewrite the total pressure tensor (2.36),

$$\underline{\underline{\mathbf{p}}}_{\alpha,tot} = m_\alpha \int (\mathbf{w}+\mathbf{u}_\alpha)(\mathbf{w}+\mathbf{u}_\alpha) d\mathbf{v} = \underline{\underline{\mathbf{p}}}_\alpha + m_\alpha n_\alpha \mathbf{u}_\alpha \mathbf{u}_\alpha = p_\alpha \underline{\underline{\mathbf{I}}} + \underline{\underline{\boldsymbol{\pi}}}_\alpha + m_\alpha n_\alpha \mathbf{u}_\alpha \mathbf{u}_\alpha, \tag{2.39}$$

where $\underline{\underline{\mathbf{p}}}_\alpha = m_\alpha \int \mathbf{w}\mathbf{w} d\mathbf{v} = p_\alpha \underline{\underline{\mathbf{I}}} + \underline{\underline{\boldsymbol{\pi}}}_\alpha$ is the intrinsic pressure tensor. Here, $\underline{\underline{\mathbf{I}}}$ is the identity matrix, $p_\alpha = n_\alpha k T_\alpha$ is the isotropic static pressure, and $\underline{\underline{\boldsymbol{\pi}}}_\alpha$ is the anisotropic contribution to $\underline{\underline{\mathbf{p}}}_\alpha$ (also called the stress tensor or viscosity tensor). For an isotropic plasma at rest therefore, $\underline{\underline{\mathbf{p}}}_{\alpha,tot}$ has only diagonal components equal to $p_\alpha = n_\alpha k T_\alpha$. Furthermore, we can recast the total energy flux (2.37),

$$\mathbf{q}_{\alpha,tot} = \mathbf{q}_\alpha + \left(\frac{5}{2} p_\alpha + \frac{1}{2} n_\alpha m_\alpha u_\alpha^2 \right) \mathbf{u}_\alpha + \underline{\underline{\boldsymbol{\pi}}}_\alpha \cdot \mathbf{u}_\alpha, \tag{2.40}$$

where $\mathbf{q}_\alpha = \langle \frac{1}{2} m_\alpha n_\alpha w^2 \mathbf{w} \rangle$ is the conductive heat flux.

Moments of the distribution function as described form the basis of fluid models of plasma transport, which are distinct from a kinetic treatment by modelling the evolution of macroscopic plasma parameters like density and flow velocity. Clearly, some information is lost in averaging over velocity space in this way, which will be discussed further in Section 2.8. Nonetheless, it remains useful to make regular reference to these macroscopic plasma descriptions due to the clear intuitive meaning of concepts like temperature and heat flow.

2.5 Transport equations

Analogously to taking moments of the distribution function directly, we can take moments of the entire kinetic equation (2.20) to arrive at evolution equations for macroscopic quantities of

interest, i,e,

$$\int \phi \frac{\partial f_\alpha(t,\mathbf{r},\mathbf{v})}{\partial t} d\mathbf{v} + \int \phi \mathbf{v} \cdot \nabla f_\alpha(t,\mathbf{r},\mathbf{v}) d\mathbf{v} + \int \phi \mathbf{a} \cdot \nabla_{\mathbf{v}} f_\alpha(t,\mathbf{r},\mathbf{v}) d\mathbf{v} = \sum_\beta \int \phi C_{\alpha,\beta}(f_\alpha, f_\beta) d\mathbf{v}.$$

The resultant equations have reduced dimensionality (having no dependence on $\mathbf{v}$), and describe the transport of quantities which typically have some counterpart in human intuition. If we do this for $\phi = 1$,$m_\alpha \mathbf{v}$ and $\frac{1}{2} m_\alpha v^2$, we arrive at a set of conservation equations for mass, momentum and energy,

$$\frac{\partial n_\alpha}{\partial t} + \nabla \cdot (n_\alpha \mathbf{u}_\alpha) = S_\alpha, \tag{2.41a}$$

$$\frac{\partial}{\partial t}(m_\alpha n_\alpha \mathbf{u}_\alpha) + \nabla \cdot \underline{\underline{\mathbf{p}}}_{\alpha,tot} + Z_\alpha e n_\alpha (\mathbf{E} + \mathbf{u}_\alpha \times \mathbf{B}) = \mathbf{R}_\alpha, \tag{2.41b}$$

$$\frac{\partial W_\alpha}{\partial t} + \nabla \cdot \mathbf{q}_{\alpha,tot} + Z_\alpha e n_\alpha \mathbf{E} \cdot \mathbf{u}_\alpha = Q_\alpha, \tag{2.41c}$$

where S_α, $\mathbf{R}_\alpha$ and Q_α are the sources of particles, momentum and energy due to collisions with all species. The charge on each species is written $Z_\alpha e$ here to avoid confusion with the energy flux ($\mathbf{q}_{\alpha,tot}$).

It's worth noting that if we add the equations from all species in a plasma, assuming no net currents, the Lorentz force contributions cancel. The plasma transport equations then have the following general form,

$$\frac{\partial X}{\partial t} + \nabla \cdot \mathbf{\Gamma}_X = S_X,$$

where X is some conserved quantity, $\mathbf{\Gamma}_X$ is the flux of X and S_X is the source of X due to collisions (or may be externally imposed). As such, the conservation of each quantity X depends on a quantity $\mathbf{\Gamma}_X$ which is a moment involving a higher power of $\mathbf{v}$. Only three equations are listed in (2.41), but a precise description would require an infinite hierarchy of transport equations. For them to be useful, we therefore need to provide a closure at some point; a closure involving the energy flux in the energy equation (2.41c) will be discussed shortly. It is common to truncate at (2.41c) because the resultant set of equations is adequate in many circumstances, and higher-order moments lose their simplicity and explanatory power because

there are no simple analogues in human experience.

These transport equations (2.41) are very general in form, and not particularly useful at this stage: they are unbounded because we do not have an expression for $\mathbf{q}_{\alpha,tot}$ or $\underline{\underline{\boldsymbol{\pi}}}_\alpha$, and we have yet to define the source terms on the right hand sides. What's more, we are frequently interested in the evolution of quantities like temperature, related to the internal energy, rather than the total energy, as there is often a distinction to be drawn between the physics which is driven by the random motion of particles compared to their directed motion. We tackle this last issue by splitting up the particle velocity into intrinsic and bulk contributions again, $\mathbf{v} = \mathbf{w} + \mathbf{u}_\alpha$ with $\langle \mathbf{w} \rangle = 0$, as described in the previous section. Taking moments as before yields modified forms of the conservation equations in (2.41),

$$\frac{\partial n_\alpha}{\partial t} + \nabla \cdot (n_\alpha \mathbf{u}_\alpha) = S_\alpha, \tag{2.42a}$$

$$\frac{\partial}{\partial t}\left(m_\alpha n_\alpha \mathbf{u}_\alpha\right) + \nabla \cdot \left(m_\alpha n_\alpha \mathbf{u}_\alpha \mathbf{u}_\alpha\right) + \nabla p_\alpha + \nabla \cdot \underline{\underline{\boldsymbol{\pi}}}_\alpha + Z_\alpha e n_\alpha \left(\mathbf{E} + \mathbf{u}_\alpha \times \mathbf{B}\right) = \mathbf{R}_\alpha, \tag{2.42b}$$

$$\begin{aligned} \frac{\partial}{\partial t}\left(\frac{3}{2}p_\alpha + \frac{1}{2}m_\alpha n_\alpha u_\alpha^2\right) + \nabla \cdot \left[\mathbf{q}_\alpha + \left(\frac{5}{2}p_\alpha + \frac{1}{2}m_\alpha n_\alpha u_\alpha^2\right)\mathbf{u}_\alpha + \underline{\underline{\boldsymbol{\pi}}}_\alpha \cdot \mathbf{u}_\alpha\right] \\ = Z_\alpha e n_\alpha \mathbf{E} \cdot \mathbf{u}_\alpha + Q_\alpha, \end{aligned} \tag{2.42c}$$

where the total pressure and total energy flux have been rewritten using (2.39) and (2.40). The evolution equation for n_α has not changed but has been included again for completion. As written, these equations are still in the form of conserved quantities. With some manipulation, we can reformulate them as evolution equations for the density, flow velocity and temperature,

$$\frac{\partial n_\alpha}{\partial t} = -\nabla \cdot (n_\alpha \mathbf{u}_\alpha) + S_\alpha, \tag{2.43a}$$

$$\frac{\partial \mathbf{u}_\alpha}{\partial t} = -\mathbf{u}_\alpha \cdot \nabla \mathbf{u}_\alpha - \frac{S_\alpha}{n_\alpha}\mathbf{u}_\alpha - \frac{1}{m_\alpha n_\alpha}(\nabla p_\alpha + \nabla \cdot \underline{\underline{\boldsymbol{\pi}}}_\alpha) + \frac{Z_\alpha e}{m_\alpha}(\mathbf{E} + \mathbf{u}_\alpha \times \mathbf{B}) + \frac{\mathbf{R}_\alpha}{m_\alpha n_\alpha}, \tag{2.43b}$$

$$\begin{aligned} \frac{\partial k T_\alpha}{\partial t} = &- \mathbf{u}_\alpha \cdot \nabla (k T_\alpha) \\ &+ \frac{2}{3}\left[-k T_\alpha \nabla \cdot \mathbf{u}_\alpha - \underline{\underline{\boldsymbol{\pi}}}_\alpha : \nabla \mathbf{u} - \frac{1}{n_\alpha}\nabla \cdot \mathbf{q}_\alpha \right. \\ &\left. - \frac{S_\alpha}{n_\alpha}\left(\frac{3}{2}k T_\alpha - \frac{1}{2}m_\alpha u_\alpha^2\right) - \frac{\mathbf{u}_\alpha \cdot \mathbf{R}_\alpha}{n_\alpha} + \frac{Q_\alpha}{n_\alpha}\right]. \end{aligned} \tag{2.43c}$$

The two sets of equations in (2.42) and (2.43) will hereon be referred to as the conservative and intrinsic transport equations respectively. To make these equations solvable we must now define the unknowns, which are the source terms S_α, $\mathbf{R}_\alpha$ and Q_α, as well as $\mathbf{q}_\alpha$ and $\underline{\underline{\boldsymbol{\pi}}}_\alpha$. Some assumption on the shape of the distribution must be made, which allows unknowns to be written in terms of other moments for which we have evolution equations. Braginskii [48] provided the seminal example for a two-component plasma, where the plasma is treated as being close to Maxwellian,

$$f_\alpha = f_\alpha^0 + f_\alpha^1, \tag{2.44}$$

where f_α^0 is a drifting Maxwellian,

$$f_\alpha^0 = n_\alpha \left(\frac{m_\alpha}{2\pi k T_\alpha}\right)^{-3/2} \exp\left(-\frac{m_\alpha}{2kT_\alpha}(\mathbf{v}-\mathbf{u}_\alpha)^2\right) \tag{2.45}$$

and $f_\alpha^1 \ll f_\alpha^0$. We will not go through all of the Braginskii results here, but an important quantity with relevance to tokamak edge plasmas is the conductive heat flux along the direction parallel to the magnetic field, which for electrons is

$$q_{e,\parallel} = 0.71 n_e k T_e u_{e,\parallel} - \kappa_e \nabla_\parallel k T_e, \tag{2.46}$$

where the Spitzer-Härm thermal conductivity [49] is

$$\kappa_e = 3.2 \frac{n_e k T_e \tau_e}{m_e},$$

which uses the electron collision time,

$$\tau_e = \frac{3\sqrt{m_e}\,(kT_e)^{3/2}\,(4\pi\epsilon_0)^2}{4\sqrt{2\pi} Z_i n_e \ln\Lambda e^4}.$$

Quantities like (2.46) will be referred to as transport coefficients. Some more recent refinements to the Braginskii transport coefficients and extensions to multi-component plasmas have been provided by Helander [50] and Zhdanov [51].

In developing a general plasma transport model, it is common at this point to derive a form

of Ohm's law, which relates the electric and magnetic fields to plasma fluid quantities by neglecting the electron inertia, $m_e \partial \mathbf{u}_e / \partial t = 0$. For the plasma transport model used in this thesis we instead use Ampère-Maxwell's law (2.11d) to calculate the electric field, since we are primarily interested in the direction parallel to the magnetic field and will be solving the kinetic equation for the electrons directly.

The assumption that distributions are close to Maxwellian (2.44), a requirement in developing a solvable set of transport equations along the lines of Braginskii, limits the validity of these models. Further details and the consequences of this will be discussed in Section 2.8.

2.6 Plasma atomic physics

For plasmas at sufficiently high temperatures, it is often adequate to assume they are fully ionized. For a hydrogen plasma for example, a temperature above a few eV means it will be nearly 100% ionized. In tokamak exhaust physics, it is desirable to reduce the plasma temperature close to the walls as much as possible, potentially to the point where a significant fraction of the particle content is made up of neutrals. There is also significant interest in adding gases which are not part of the fuel mixture (impurities) to the edge plasma for their favourable radiative properties. Both electrons and ions in plasmas will readily collide with any neutral particles present, undergoing a host of elastic and inelastic collisional processes. Spontaneous processes, typically involving photon emission, can also occur on timescales which compete with these collisional processes. These plasma-atomic interactions can be very important for the particle, momentum and energy balance in scrape-off layer plasmas, and so need to be modelled.

We start by outlining the most important fundamental atomic processes in exhaust physics. For an atomic or ionic particle X, with electric charge $+z$ in some initial atomic state μ and final state ν with potential energies ε_μ and ε_ν, colliding with a plasma electron (e) or fuel ion (i) these are

- electron-impact ionization,

$$X_\mu^z + e \to X_\nu^{z+1} + 2e, \tag{2.47a}$$

- three-body recombination,

$$X_\mu^{z+1} + 2e \to X_\nu^z + e, \tag{2.47b}$$

- electron-impact excitation,

$$X_\mu^z + e \to X_\nu^z + e \tag{2.47c}$$

  with $\varepsilon_\nu > \varepsilon_\mu$,

- electron-impact deexcitation,

$$X_\mu^z + e \to X_\nu^z + e \tag{2.47d}$$

  with $\varepsilon_\nu < \varepsilon_\mu$,

- resonant charge exchange,

$$X_\mu^z + i \to i + X_\nu^z \tag{2.47e}$$

  where the plasma ion and particle X have swapped an electron and $\nu = \mu$,

- radiative recombination,

$$X_\mu^{z+1} + e \to X_\nu^z + \gamma \tag{2.47f}$$

  with emission of a photon γ,

- radiative deexcitation,

$$X_\mu^z \to X_\nu^z + \gamma \tag{2.47g}$$

  with $\varepsilon_\nu < \varepsilon_\mu$.

Ionization and three-body recombination are inverse processes, so we can combine (2.47a) and (2.47b) as

$$X_\mu^z + e \rightleftharpoons X_\nu^{z+1} + 2e. \tag{2.48}$$

Similarly for excitation/deexcitation, we can combine (2.47c) and (2.47d),

$$X_\mu^z + e \rightleftharpoons X_\nu^z + e. \tag{2.49}$$

This list of processes is not exhaustive, but does cover those which are dominant in the plasma regimes encountered in tokamak edge plasmas. Importantly, we have not included photon-induced ionization and excitation processes, which would allow us to write the radiative reactions (2.47f) and (2.47g) as reversible too. This is based on an assumption that the mean free paths of photons in tokamak plasmas are long, i.e. they are optically thin, so all photons emitted in radiative processes exit the plasma. This is generally a valid approximation, and provides a very useful cooling mechanism for scrape-off layer plasmas because isotropically emitted photons will deposit their energy over a wider area than the energy deposited by plasma in direct contact with the walls. For larger devices planned for the future, operated at higher densities, this assumption may need to be revisited.

The electron-impact processes listed here are dominant in tokamak edge plasmas. Each of these collisional processes have an associated cross-section which is in general dependent on the relative velocities of the colliding particles and the scattering angle. For any collisional process between electrons and some species X with density n_X, we can compute the number of collisions per unit time by taking the first moment of the relevant collision operator, $S = \int C_{e,X} d\mathbf{v}$, which can be written

$$S = n_X n_e K \tag{2.50}$$

with the definition of the rate coefficient as

$$K = \frac{1}{n_e} \int f_e(\mathbf{v}) v \sigma(v) d\mathbf{v} = \frac{1}{n_e} \int f_e(\varepsilon) v(\varepsilon) \sigma(\epsilon) d\varepsilon \tag{2.51}$$

The fact that the relative velocity is dominated by the electron velocity has been used here, and σ is the total rather than differential cross-section. K has also been written here on the right hand side in terms of the electron energy ε. Note that the integral over the electron distribution in (2.51) highlights that some sensitivity to a departure from Maxwellian electrons may exist.

This will be explored in Chapter 6.

To understand the effect of plasma-atomic interactions on tokamak plasmas, it is in principle necessary to track the effect of collisions with all types of atomic species present, where atomic just means any particle which is not fully ionized. These collisions will directly modify the distribution, and will appear as source terms in the transport equations (2.42). There are several ways we can avoid this brute force approach.

In the absence of any radiative processes, transport or external sources, the atomic levels of a given species present in a plasma will come to local thermodynamic equilibrium (LTE) with the electrons. Within a given ionization stage (the set of states with the same charge $+z$), this is the point when the rate of each excitation process is balanced by its inverse. The atomic states are then described by the Boltzmann distribution, where we can relate the densities of two states j and k with potential energy ε_j and ε_k ($\varepsilon_k > \varepsilon_j$),

$$\frac{n_k}{n_j} = \frac{g_k}{g_j} e^{-(\varepsilon_j - \varepsilon_k)/kT_e}, \tag{2.52}$$

where g_j is the statistical weight of state j. Similarly, at LTE the ionization rate matches the three-body recombination rate, and the densities of adjacent ionization stages with charge $+z$ and $+(z+1)$ are described by the Saha equation,

$$\frac{n_{z+1} n_e}{n_z} = \frac{2}{\lambda^3} \frac{g_{z+1}}{g_z} e^{-\Delta\varepsilon_z/kT_e} \tag{2.53}$$

where $\Delta\varepsilon_z$ is the ionization energy for a particle with charge z. LTE implies Maxwellian electrons so the rate coefficients (2.51) become functions of T_e only. Under these conditions therefore, it is straightforward to compute the source terms from plasma-atomic interactions in the plasma transport equations.

In tokamak edge plasmas, radiative processes do occur on competitive timescales to the collisional ones, and this will push the atomic state distributions away from the Saha-Boltzmann distribution, modifying the source terms in the plasma equations. Collisional-radiative models (CRMs) aim to capture the balance between these processes by computing the evolution of

atomic state densities in the presence of plasma electrons. Given the complexity of the atomic structure of even simple elements however, along with the fact that the number of processes scales with the square of the number of distinct atomic states, this is quite a challenge. To make headway, Bates et al. [52] originally outlined a method of capturing the dynamics of both collisional and radiative processes without resorting to a brute force computation. The method here follows the more recent formalisms of Summers [53] and Greenland [54]. We first define the evolution of the number density of atomic particles in state k (which may specify the electric charge as well as the internal atomic state),

$$\frac{dn_k}{dt} = n_e \sum_j n_j K^k_{e,j} + \sum_j A^k_j n_j - n_k n_e \sum_j K^j_{e,k} - n_k \sum_j A^j_k + n_e \sum_j r^k_j n_j - n_e n_k \sum_j r^j_k + \Gamma^k, \tag{2.54}$$

where

- $K^k_{e,j}$ is the rate coefficient for the production of particles in state k due to collisions between electrons and particles in state j, i.e. from ionization, excitation and their inverse processes[1],
- A^k_j is the transition rate (Einstein coefficient) for radiative deexcitation from state j to state k,
- r^k_j is the radiative recombination rate from j to k,
- Γ^k is the external source of state k.

This equation lends itself to being rewritten in a matrix form, which describes the evolution of the vector of all atomic states $\mathbf{n}$, where the total number of states is N,

$$\frac{d\mathbf{n}}{dt} = \mathbf{M}\mathbf{n} + \mathbf{\Gamma}, \tag{2.55}$$

[1]Note that, for three-body recombination, it is common to formulate the particle source in a way that reflects n_e^2 dependence, $S^{3br} = n_e^2 n_i \alpha$, for some ion density n_i and three-body recombination coefficient α. Here, we would define $\alpha = n_e K^{3br} = \int f_e v \sigma d\mathbf{v}$.

where $\mathbf{M}$ is the $N \times N$ rate matrix containing information on the transition rate between all states and $\mathbf{\Gamma}$ is the source of particles from collisions between species whose densities are not being evolved (in SOL modelling for example, we may evolve the atomic state densities separately and treat the electron and fuel ion plasma background as fixed or solved independently). The elements of $\mathbf{M}$ are

$$M_{jk} = n_e K^j_{e,k} + A^j_k + n_e r^j_k \qquad k > j \tag{2.56}$$

$$M_{jk} = n_e K^j_{e,k} \qquad k < j \tag{2.57}$$

$$M_{jj} = -\sum_{k \neq j} M_{kj} \tag{2.58}$$

Computing $\mathbf{M}$ directly is undesirable as it contains N^2 elements. Instead, we can define a subset of states P with size N_P, which we evolve, and a subset Q with size N_Q, which we do not. This allows us to rewrite (2.55) as in [54],

$$\frac{d}{dt}\begin{bmatrix}\mathbf{n}_P \\ \mathbf{n}_Q\end{bmatrix} = \begin{bmatrix}\mathbf{M}_{PP} & \mathbf{M}_{PQ} \\ \mathbf{M}_{QP} & \mathbf{M}_{QQ}\end{bmatrix}\begin{bmatrix}\mathbf{n}_P \\ \mathbf{n}_Q\end{bmatrix} + \begin{bmatrix}\mathbf{\Gamma}_P \\ \mathbf{\Gamma}_Q\end{bmatrix} = \begin{bmatrix}\frac{d\mathbf{n}_P}{dt} \\ 0\end{bmatrix}. \tag{2.59}$$

where $\mathbf{M}_{PP}$ is the $N_P \times N_P$ rate matrix for transitions between P states, $\mathbf{M}_{PQ}$ is the $N_P \times N_Q$ rate matrix for transitions of P states involving Q state densities, and so on. Using this, we can derive an evolution equation for just the P states,

$$\frac{d\mathbf{n}_P}{dt} = \mathbf{M}_{\text{eff}}\mathbf{n}_P + \mathbf{\Gamma}_{\text{eff}}, \tag{2.60}$$

where

$$\mathbf{M}_{\text{eff}} = \mathbf{M}_{PP} - \mathbf{M}_{PQ}\mathbf{M}^{-1}_{QQ}\mathbf{M}_{QP} \tag{2.61}$$

is the effective rate matrix and

$$\mathbf{\Gamma}_{\text{eff}} = -\mathbf{M}_{PQ}\mathbf{M}^{-1}_{QQ}\mathbf{\Gamma}_Q + \mathbf{\Gamma}_P \tag{2.62}$$

is the effective source. To compute the time evolution of $\mathbf{n}_P$, we now have only an $N_P \times N_P$

matrix to compute, which is hopefully much smaller than $\mathbf{M}$. For neutral hydrogen for example, which is frequently present close to the walls in tokamaks, it is usually sufficient to model the ground state only [52] such that $N_P = 1$ and $\mathbf{M}_{\text{eff}}$ contains the 'effective' ionization and recombination coefficients. These effective rate coefficients capture the complex nature of ionization and recombination, which can involve many intermediate steps. If we put a Maxwellian for the electron distribution into the definition of the rate coefficient (2.51), then $\mathbf{M}_{\text{eff}}$ and $\mathbf{\Gamma}_{\text{eff}}$ are functions of the electron temperature and density only, and can be precomputed. Much scrape-off layer modelling uses techniques along similar lines to compute the source terms in the transport equations (2.42) or (2.43) [53, 55–58].

We should note that this division into two separate subsets, P and Q, is based upon the assumption that the Q states evolve on timescales fast relative to plasma fluctuations, and therefore they can be treated as time-independent. A typical choice for the P states is the ground state of atomic ions, plus potentially some 'metastable' states. This is normally adequate, but more care may need to be taken for CRMs involving molecules [54].

2.7 Scrape-off layer models

So far, plasma transport has been discussed in the most general terms. Here we will now outline some specifics of scrape-off layer plasma modelling.

2.7.1 Outline of the scrape-off layer

In a tokamak, the magnetic field lines looping around the torus typically ergodically map out surfaces of constant magnetic flux. These toroidally nested surfaces are considered closed because, in the absence of collisions or drifts, plasma particles would stick to field lines on those surfaces and confinement would be perfect. Taking a cross-sectional slice through the torus, see Figure 2.2, the intersection of any solid surface (which we will call a limiter) with this magnetic geometry as described will result in the creation of a 'last closed flux surface' (LCFS). Any

position radially outward of the LCFS will sit on an open flux surface, where the field lines will terminate (after some toroidal distance) on the limiter. This is a limiter SOL.

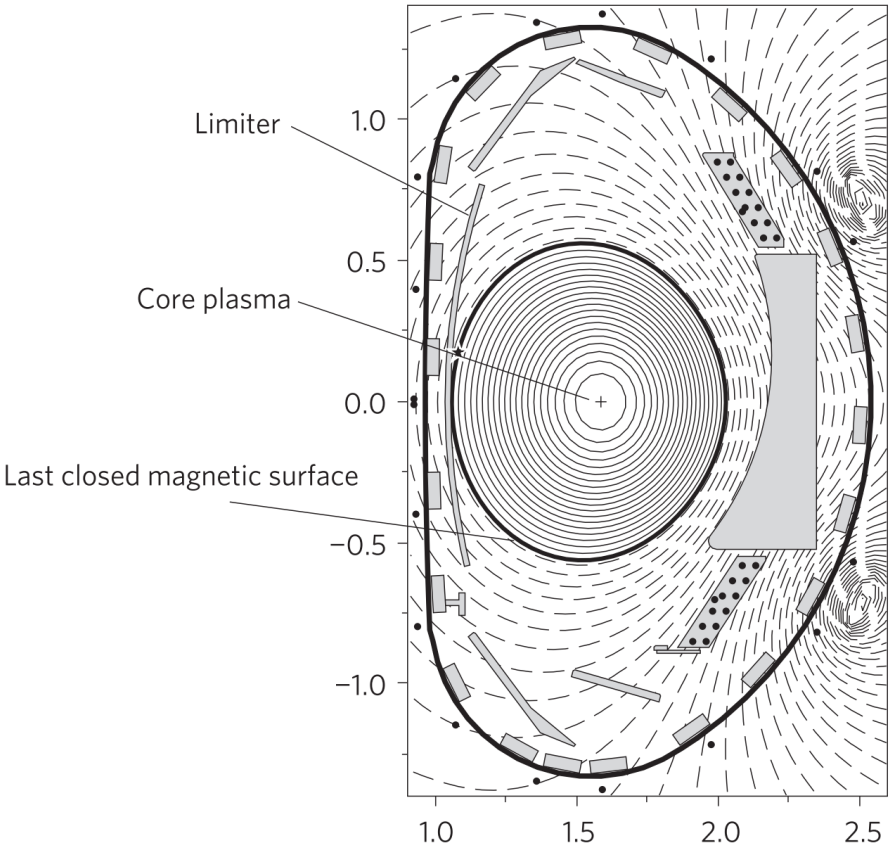

Figure 2.2: Schematic of a limiter SOL, showing a cross-section on the poloidal plane through a tokamak. The toroidal direction is into the page here. The scrape-off layer is the region radially outward of the last closed magnetic surface. Figure taken from [59].

For a strong magnetic field, plasma particles will orbit tightly around the field lines. This means that, while transport is uninhibited in the parallel direction, transport of any quantity in the perpendicular direction can only happen via drifts or collisions. While small, the effect of drifts and collisions is not negligible, meaning confinement to the closed flux surfaces is imperfect and the SOL is not merely a geometric designation and does in fact contain plasma. Calculation of the effective cross-field velocities from first principles is difficult, but experimental observations suggest values of the order $u_\perp \sim 1\text{m/s}$. This is in contrast to the parallel flow velocities, which reach the plasma sound speed close to the walls,

$$c_s = \sqrt{\frac{k(T_e + T_i)}{m_i}}, \tag{2.63}$$

which for a typical deuterium plasma in a tokamak gives $u_{\parallel} \sim c_s \sim 10^4$m/s. The large ratios in parallel to perpendicular fluxes that result from this highlights that the scrape-off layer is typically a thin, elongated region of plasma. Along with the diffusive nature of the cross-field transport, it is common and useful to model SOL plasmas in 1D, either in the parallel direction or projected onto a poloidal plane.

A key length scale in the SOL is the connection length, L, which is the parallel distance between solid surfaces. In Figure 2.2, this would be the total length of a field line (dashed) starting at one side of the limiter and culminating at the other. Because a cross-section in the poloidal plane is shown, this length may be much longer than the poloidal distance of this field line, depending on the ratio of the toroidal to poloidal components of the magnetic field.

An important aspect of SOL plasmas is the formation of the sheath in front of the walls, something which is common to all regions of plasma-surface interaction. Due to the high mobility of electrons compared to heavier ions, they will initially reach a surface first, setting up a net negative electric charge there. The ions will accelerate towards the wall under the influence of this potential, creating a region of net positive charge just in front. There is therefore a small region where quasineutrality is violated, over which there is a large drop in electric potential. Debye shielding ensures this potential drop does not extend far into the plasma, and the sheath region is typically a few Debye lengths thick [24]. It can be shown [24] that there is a condition imposed on the plasma by the presence of the sheath, which is that the ion flow velocity in the parallel direction is accelerated to at least the sound speed at the sheath entrance,

$$u_i \geq c_s, \tag{2.64}$$

which is known as the Bohm criterion. Ambipolar flux, where the ion particle flux is equal to that of the electrons and so there is no net plasma current to the walls, can be achieved with some cut-off in the forward-going part of the electron distribution function at the sheath entrance, so that only electrons with sufficient velocity reach the walls while all others are reflected back by the potential drop. This is shown in Figure 2.3. This is responsible for introducing strong anisotropy in the electron distribution and will be discussed further in this

thesis. The sheath results in a loss of energy from the SOL plasma, partly from the particle flux, but also partly from the preferential loss of high-energy particles in the case of electrons. We can define a sheath heat flux coefficient, γ, which helps quantify the energy flux across the sheath for a given species,

$$q_{sh} = \gamma k T \Gamma_{sh}, \tag{2.65}$$

where Γ_{sh} is the sheath particle flux, $\Gamma_{sh} \geq n_{sh} c_s$ from the Bohm criterion (for a density at the sheath of n_{sh}). For the electrons, assuming a Maxwellian distribution at the sheath entrance which is truncated at some velocity determined by the sheath potential drop gives

$$\gamma_e = 2 - 0.5 \ln \left(2\pi \left(1 + T_{i,sh}/T_{e,sh}\right) m_e/m_i\right) \tag{2.66}$$

Assuming a drifting Maxwellian for the ions gives $\gamma_i = 2.5$ (not including the contribution from the kinetic energy of the lost ions), although experiments suggest $\gamma_i \simeq 1.5$ is more appropriate [24].

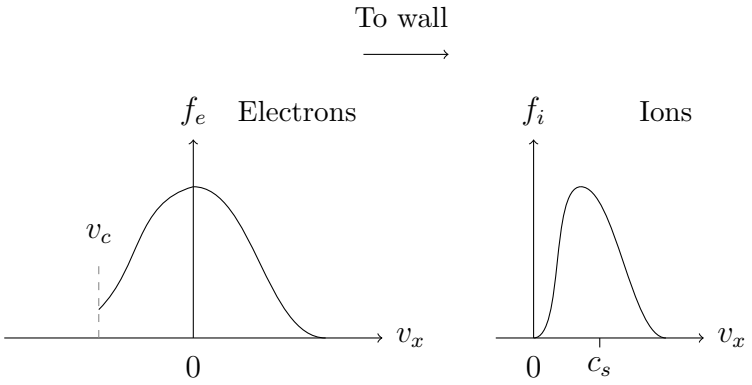

Figure 2.3: Characteristic electron and ion distributions at the entrance to the sheath. The electrons are close to Maxwellian, with a cut-off in the rearward-travelling part at v_c. The ions are approximately a drifting Maxwellian at the sound speed, c_s.

The plasma particles reaching the walls via the sheath tend to stick around long enough to undergo surface recombination (a distinct process from the volume recombination, (2.47b) and (2.47f), discussed in the previous section). The neutral particles are released back into the plasma, where they can be ionized again after travelling some distance. This process, known as recycling, provides the ingredients for steady-state flows to form in the SOL: there is a plasma sink at the sheath, and a source of plasma from ionized neutrals further away from the wall.

A key area of interest in SOL plasmas is the transport of impurity species, which can enter either via physical sputtering of wall materials (typically carbon or tungsten), or by deliberate injection in an attempt to cool the edge plasma. Plasma transport is in general a strong function of the electric charge Z of a given species, especially so for the radiative losses driven by Bremsstrahlung and inelastic collisions, and so a sufficiently accurate treatment of the atomic physics (which determines Z) alongside the transport physics is necessary. There is typically a delicate balance to be struck with SOL impurities: they are very effective at cooling the edge plasma, but can significantly degrade the energy confinement if they reach the core.

Another important ingredient in understanding SOL plasmas are transient events such as edge-localised modes (ELMs), which result in time-dependent sources of particles and energy entering the scrape-off layer. A tokamak operating in high confinement mode will have a radial pressure profile which features a region of increased pressure gradient close to the transition from the core to the edge, called an edge transport barrier or pedestal (see Figure 2.4). This transport barrier turns out to be somewhat unstable, and tends to periodically collapse and reform. During this collapse, some fraction of the core particle and energy content is released into the plasma over a short space of time, increasing fluxes into the SOL. There is significant interest in accessing ELM-free operating regimes in tokamaks, but it is also of interest how the SOL responds to this temporary increase in the inward particle and energy flux.

A final aspect of SOL physics to consider is filamentary transport, where filaments are elongated plasma structures seen in almost all tokamak devices. Similar to ELMs, filaments can be viewed as perturbations to upstream quantities resulting in a time-dependent sources of particles and energy into the SOL. However, their origin is different, arising instead from plasma turbulence, and filaments may originate in the divertor region as well as from the core. Filaments play a role in distributing power and particles across the plasma-facing components, and may also be important in accessing detachment [60].

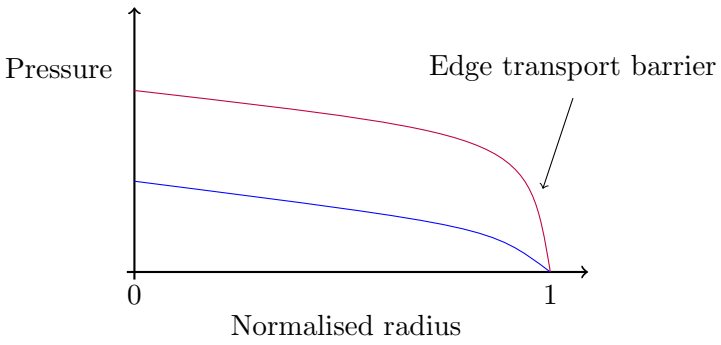

Figure 2.4: Typical radial profile of plasma pressure in a tokamak with (red) and without (blue) an edge transport barrier, where the radial coordinate is normalised to the minor radius of the tokamak. The edge transport barrier can release particles and energy into the SOL during periodic collapse and reformation.

2.7.2 Two-point model

A highly useful analytical tool for SOL plasmas is the two-point model (2PM) [24]. We will pick out two important locations in the SOL: upstream (u), which is some location far from the walls in the direction parallel to the magnetic field, and the target (t), which is at the wall or the sheath entrance. See Figure 2.5 for a simple diagram of the straightened-out SOL used in building the 2PM. Tokamak operators have some limited control over what happens upstream, so the aim is to understand how conditions there relate to conditions at the walls.

If we assume that all ionization happens in a thin region in front of the target, and that the plasma is stationary everywhere else, the parallel flow speed rapidly accelerates to the sound speed in the ionization region. We may also make a further simplifying assumption in taking the total (static plus dynamic) pressure as a constant along the flux tube.

At the upstream location therefore, assuming equal electron and ion temperatures, $p_u = 2n_u k T_u$. At the target we find $p_t = 2n_t k T_t + n_t m_i u_t^2$. Taking the equality of the Bohm criterion in (2.64), we can relate these pressures through

$$n_u T_u = 2 n_t T_t. \tag{2.67}$$

Since there is no flow velocity in the bulk of the SOL in this model, parallell heat flow $q_\parallel$ is conductive only. Power enters via cross-field transport from the core into the SOL, where

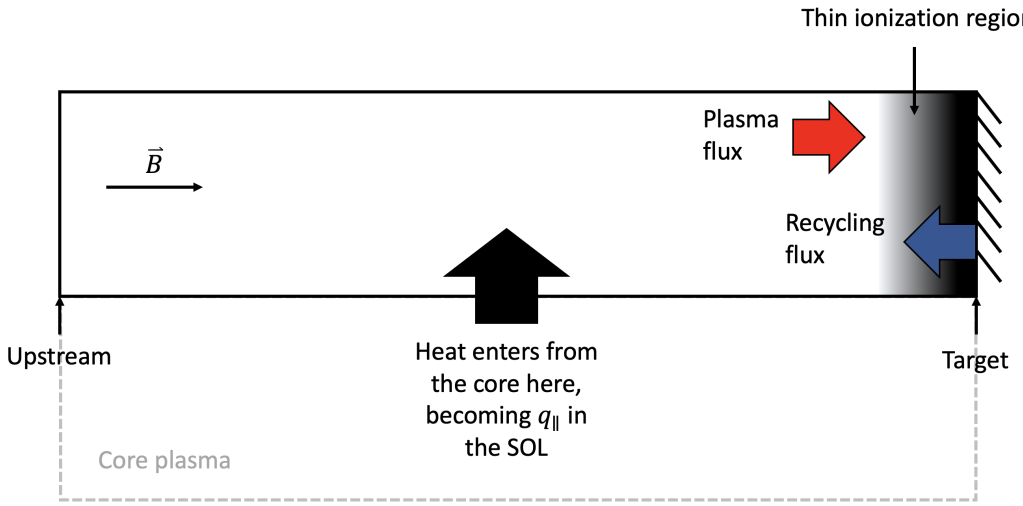

Figure 2.5: Simple diagram of the SOL, from which we can relate conditions at the target to those upstream using the two-point model. It is common to assume $q_\parallel$ enters entirely at the upstream location, as this does not make a significant difference to the model predictions [24].

parallel transport then takes over. Taking the classical Braginskii heat flow (2.46), we can show by assuming any heat entering the SOL leaves at the target that

$$T_u^{7/2} = T_t^{7/2} + \frac{7}{2}\frac{q_\parallel L}{\kappa_e}, \tag{2.68}$$

where $\nabla_\parallel q_\parallel = 0$ and so is constant along the domain. The length of the domain we are considering is given by L, and the heat conductivity is dominated by the electrons, $\kappa_e \gg \kappa_i$.

Finally, we can constrain $q_\parallel$ at the target by making some assumptions on the electron and ion distributions there, giving

$$q_\parallel = \gamma n_t T_t c_s, \tag{2.69}$$

where γ is the sheath heat transmission coefficient, $\gamma \sim 7$ [24], including contributions from both electrons and ions.

The 2PM is therefore given by equations (2.67 - 2.69), from which some important consequences drop out. $q_\parallel$ and n_u are the closest things to control knobs in this model, so we can find solutions for the other three unknowns with this set of equations. Fairly modest temperature drops along the SOL yield situations where $T_t^{7/2} \ll T_u^{7/2}$, simplifying (2.68) to

$$T_u^{7/2} \simeq \frac{7}{2}\frac{q_\parallel L}{\kappa_e},$$

which shows that the upstream temperature changes very slowly with all parameters. Combining this result with (2.67) and (2.69) yields

$$T_t \propto \frac{q_{\parallel}^{10/7}}{L^{4/7} n_u^2},$$

where it can be seen that increasing upstream density is a viable way of reducing target temperatures ($T_t \propto n_u^{-2}$). This is a useful result for achieving more benign target conditions, and increasing n_u also facilitates qualitatively different SOL regimes as will be discussed next.

2.7.3 Divertors and detachment

The limiter SOL shown in Figure 2.2 is not a particularly desirable tokamak configuration because of the close proximity of the solid surfaces with the core plasma. Heavy ions hitting the walls at the plasma sound speed can cause physical sputtering of the wall material, which can leach into the core and reduce confinement performance. There is a motivation therefore to find some way of dragging the region of plasma-surface interaction away from the core, which leads to the divertor configuration of a tokamak. See Figure 2.6. By inducing a current in coils radially outward of the core plasma, a figure-of-eight magnetic field is created when viewed in the poloidal plane. The centre of the eight is a magnetic null in the poloidal direction, called the X-point, and a flux surface passing through the X-point is the separatrix. The scrape-off layer is now defined as the region beyond the separatrix. The targets are positioned to intersect the field lines such that there is some radial separation between them and the core. The key advantage of the divertor configuration is to ensure that the region of plasma-surface interaction is kept away from the core, which means this region can be exploited to remove as much momentum and power from the plasma as possible, facilitating relatively docile target conditions without degrading core confinement.

It is common to characterise the operating regime of a tokamak scrape-off layer in terms of the temperature drop along the parallel length, which is directly related to the collisionality of the plasma. If we define a SOL collisionality parameter as the ratio of the connection length to the

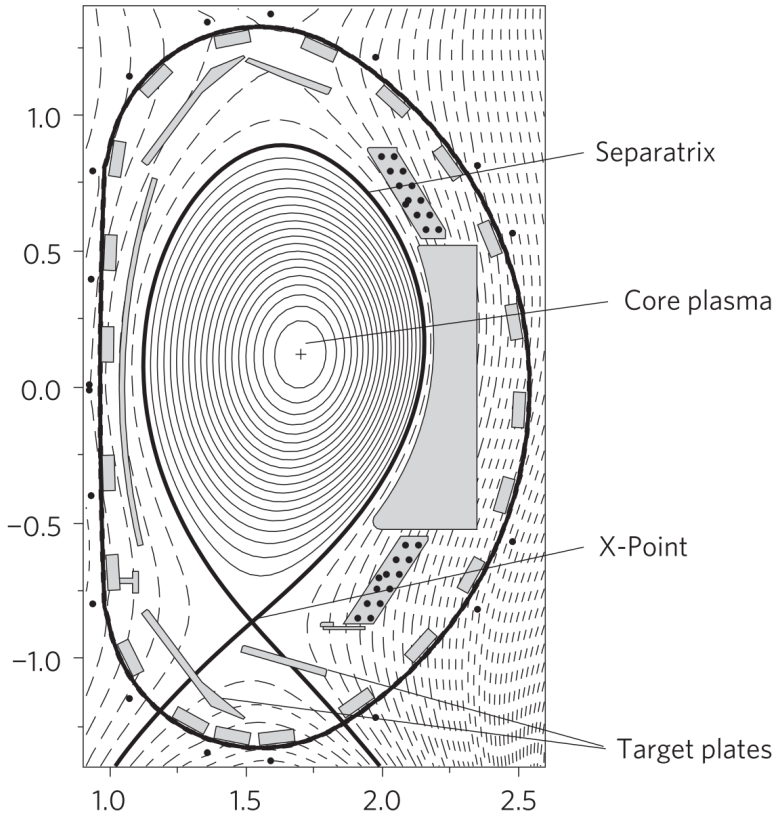

Figure 2.6: Schematic of a divertor SOL; the scrape-off layer is the region outside the separatrix. The axes units are metres. Figure taken from [59].

self-collision mean free path of particles upstream,

$$\nu^* = \frac{L}{\lambda_u} \simeq 10^{-16} \frac{L n_u}{T_u^2}, \tag{2.70}$$

with n_u in m^{-3} and T_u in eV, we can use the two-point model along with an assumption that $T_t^{7/2} \ll T_u^{7/2}$ to show that the ratio of upstream to target temperatures is

$$\frac{T_u}{T_t} \propto (\nu^*)^2.$$

For low collisionality we have an approximately isothermal SOL, $T_u \simeq T_t$, and the temperature and density profiles at equilibrium are primarily determined by the amount of energy leaving via the sheath. In this regime, high thermal conduction means a small temperature gradient is sufficient to transport the energy entering the SOL upstream towards the targets. This regime is therefore called 'sheath-limited'. For increased collisionality, thermal conduction plays an increasingly important role in determining the plasma profiles and the temperature drop is

large, leading to a 'conduction-limited' regime.

Divertors facilitate access to a third distinctive regime at higher collisionalities, 'detachment', where significant volumetric losses in the particle, momentum and/or energy content of the plasma help to partially extinguish the plasma in front of the targets. Detachment is characterised experimentally by a reduction in the particle flux to the surfaces as plasma density is increased, as shown in Figure 2.7, known as flux rollover. During detachment, typically $T_t < 2\text{eV}$, and a protective neutral cloud forms in front of the walls.

A high-collisionality divertor SOL can still be understood in simple analytical terms with a modified form of the two point model [24], see Figure 2.8. We start by defining a momentum loss factor, which is half the ratio of the pressure at the target to the pressure upstream, $f_{\text{mom}} = p_t/2p_u$. This arises due to frictional forces between the plasma and neutrals in front of the targets, and modifies (2.67) to become

$$f_{\text{mom}} n_u T_u = 2 n_t T_t. \tag{2.71}$$

In deriving the second equation of the two-point model (2.68) we have assumed that conductive heat flow dominates, but in reality some amount of convection wil occur, reducing temperature gradients. We can therefore define a conduction factor, f_{cond}, and use $f_{\text{cond}} q_\parallel$ for the heat flow within the SOL. This modifies (2.68) to become

$$T_u^{7/2} = T_t^{7/2} + \frac{7}{2} \frac{f_{\text{cond}} q_\parallel L}{\kappa_e}, \tag{2.72}$$

Finally, we capture the net effect of volumetric power losses within the scrape-off layer with the power loss factor, f_{pow}, such that the energy lost to the sheath is $q_{sh} = (1 - f_{\text{pow}}) q_\parallel$ so that (2.69) becomes

$$(1 - f_{\text{pow}}) q_\parallel = \gamma n_t T_t c_s. \tag{2.73}$$

With the modified 2PM (2.71 - 2.73), all of the complex transport physics is wrapped up in the values of f_{mom}, f_{cond} and f_{pow}, enabling straightforward analysis of experimental observations, for example the values which predict rollover in a given tokamak.

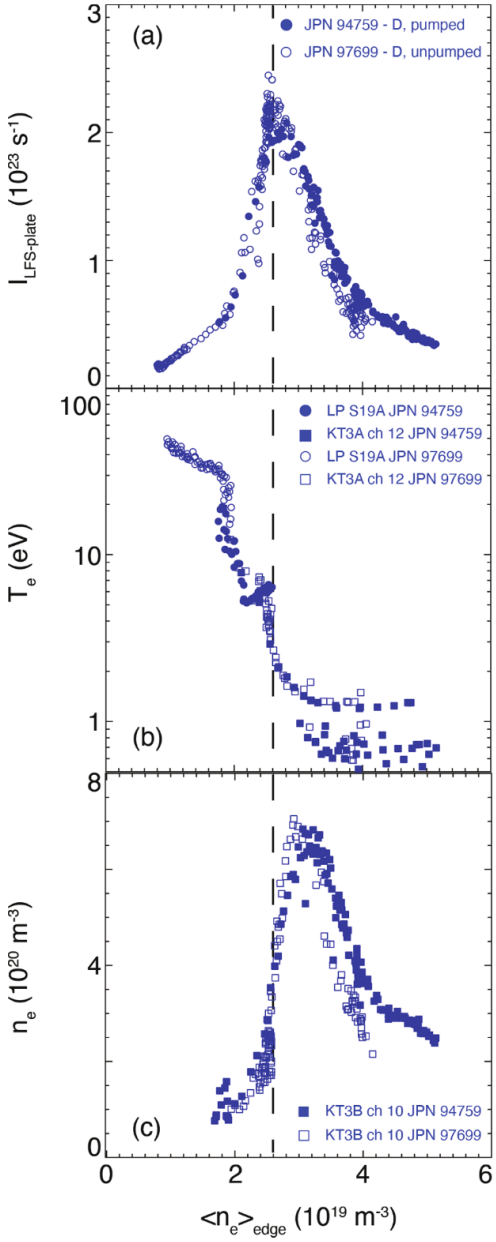

Figure 2.7: Experimental observation of rollover during experiments on the JET tokamak, indicating the onset of detachment, where the target ion flux (top) reduces at increasing plasma density. Figure reproduced from [61].

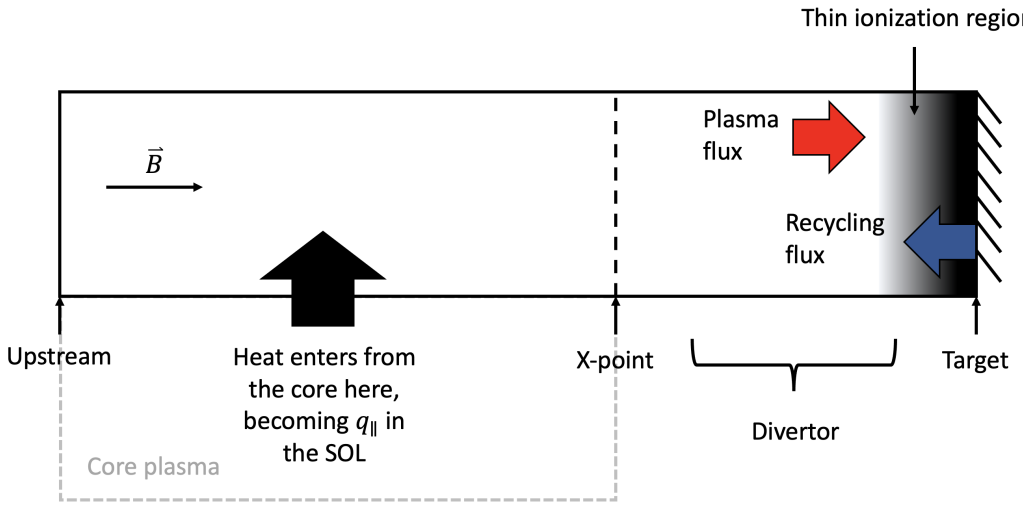

Figure 2.8: Simple diagram of the divertor SOL. Once again it is common to assume $q_{\parallel}$ enters entirely at the upstream location.

One further benefit of divertor configurations is that the magnetic geometry can be shaped in the divertor region with field coils to achieve expansion of the magnetic flux lines along the parallel direction. This flux tube expansion is being actively researched on tokamaks such as MAST-U, where it is expected to help reduce particle and heat fluxes towards the targets. This technique has also been shown to reduce the threshold for detachment with respect to control parameters such as the upstream density or the heat flux into the SOL, by an amount proportional to the degree of flux tube expansion [62].

2.8 Kinetic vs. fluid SOL transport models

The fact that fluid models lose information contained in the kinetic equation has been discussed in general terms so far, but we will now outline this more concretely. The issue is most clearly demonstrated in tokamak edge plasmas by the electron energy flux, where the component in the direction parallel to the magnetic field is

$$q_{\parallel} = \int \left(\frac{1}{2} m_e v^2 v_{\parallel}\right) f_e(\mathbf{v}) d\mathbf{v}. \tag{2.74}$$

If we plot the integrand of $q_{\parallel}$ as a function of the velocity magnitude, Figure 2.9, we can see that the dominant contribution to the energy flux comes from particles at around 2-3v_{th}, with the

thermal velocity defined in terms of the temperature for electrons as $v_{th} = \sqrt{2kT_e/m_e}$. Particles with velocity in this range are often referred to as heat carrying electrons (HCEs) [63]. The velocity-dependent collisional frequency of plasma electrons is [42]

$$\nu_e = \left(\frac{e^2}{4\pi\varepsilon_0 m_e}\right)^2 \frac{4\pi Z^2 n_i \ln\Lambda}{v^3} \propto v^{-3},$$

which means their collision mean free path is $\lambda_e = v/\nu_e \propto v^4$. The HCEs therefore travel on the order of ~ 30 times farther than the thermal bulk before depositing their energy. Note that these estimates are lower than the predictions in [63], where a different definition of v_{th} is used resulting in higher predicted ratios of the HCE to thermal bulk λ_e.

The consequence of this is that, in the presence of a steep temperature gradient, the HCEs can deposit their energy far beyond the region of changing temperature. The energy transport is then said to be non-local, because the local plasma state may depend on conditions which are spatially distant. Furthermore, there is a depletion of HCEs within the region of the temperature gradient because they have escaped, leading to suppression of the local energy flux there. The parameter which predicts this phenomenon is the Knudsen number k_N (specifically the heat transport Knudsen number), which is the ratio of the mean free path to a length scale of interest, which in this case is the distance which characterises the temperature gradient, $k_N = \lambda_e/L_{\nabla T_e}$. For local transport theory to be valid, $k_N \ll 1$ is required. The presence of HCEs mean that a k_N which is small but approaching unity can still lead to significant non-local transport.

This issue of non-local transport is a manifestation of the more general closure problem, where the hierarchy of moment equations in a fluid model must be truncated at some point, which is typically achieved by formulating the closing moment in terms of lower-order moments. A similar problem to the heat flux in Braginskii-like fluid equations also occurs for the viscosity term. Generally, these fluid equations are valid in the high collisionality limit, when the distribution function is close to Maxwellian. We will use the term 'non-local' here to be synonymous with situations where there is significant departure from Maxwellian distributions.

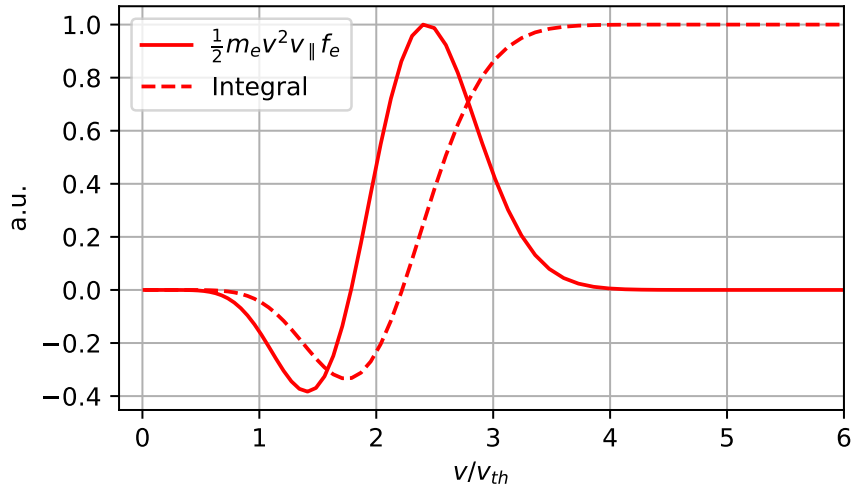

Figure 2.9: A plot of the energy flux density (2.74) as a function of velocity magnitude for the case where f_e is close to Maxwellian, normalised to the local thermal velocity. The dominant contribution is from electrons with $v/v_{th} \simeq 2-3$.

A very basic corrective treatment for non-local energy flux employs the use of a flux limiter. The classical Braginskii conductive heat flow (2.46) is unbounded when ∇T is large. For an entirely collisionless, Maxwellian plasma the energy flux reaches a maximum at the free-streaming one-way energy flux [64],

$$q_e^{FS} = \int_0^\infty dv_\parallel \int_{-\infty}^\infty dv_\perp \left(\frac{1}{2} m_e v^2 v_\parallel\right) f_e(\mathbf{v}) \simeq n_e k T_e v_{th}.$$

This provides a recipe for limiting the classical heat flux to some fraction of q_e^{FS},

$$q_e = \frac{q_e^{SH}}{1 + |q_e^{SH}/\alpha q_e^{FS}|}, \tag{2.75}$$

where q_e^{SH} is the Spitzer-Härm heat flux and α is the 'flux limiter', a tunable parameter. This procedure can capture the effect of heat flux suppression in low collisionality plasmas, but does not capture the transport of heat-carrying electrons directly, and there is no first-principles basis for choosing α. More sophisticated models exist, which aim to capture non-local heat flow without resorting to a fully kinetic treatment, and these will be discussed in the next section.

Another important process which may be affected by non-local transport in SOL plasmas is

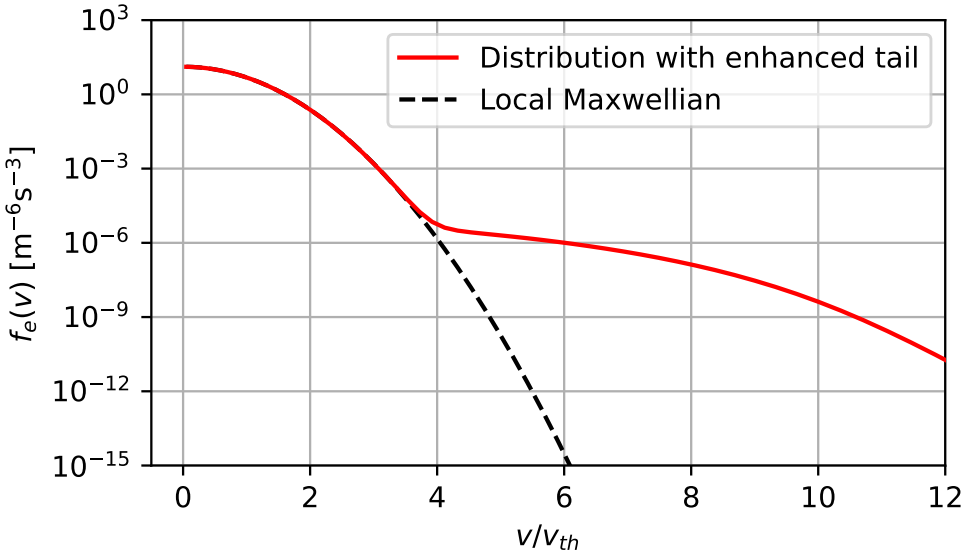

Figure 2.10: An example electron distribution (the isotropic part), taken from a kinetic SOL simulation with the SOL-KiT code, with an enhanced 'tail' of fast electrons due to non-local transport occurring in a steep temperature gradient. Inelastic processes with high threshold energies will sample the tail, and will encounter more electrons than in an equivalent Maxwellian at the local density and temperature.

plasma-atomic reactions. The assumption of Maxwellian electrons is ubiquitous in modelling these processes, as this ensures the rate matrices in the atomic state density evolution equation, (2.55) or (2.60), are functions of the electron temperature and density only (see Section 2.6). However, the non-local heat transport phenomenon outlined above can lead to an accumulation of fast electrons at the bottom of a steep temperature gradient. Inelastic collision processes which sample this region of the electron distribution may therefore show significant departures from Maxwellian-averaged rates, see Figure 2.10.

Tokamak scrape-off layers feature large parallel temperature gradients, dropping $\sim$ 100eV or more over tens of metres with no transport-inhibiting magnetic field as in other directions within a tokamak. For an upstream temperature $T_u = 250$eV, upstream density $n_u = 3 \times 10^{19}\text{m}^{-3}$ and connection length $L = 100$m (as envisaged in future devices, see Figure 1.9), the thermal electrons upstream have $k_N \sim 0.2$, but the HCEs have $k_N \sim 6$. It may be expected then that the tokamak SOL is sufficiently collisionless that non-local transport will be important, but realistic operating conditions also demand the plasma is cool close to the target and therefore highly collisional. Further complicating factors are the presence of the sheath, which adds

anisotropy to the electron distribution, and inelastic collisions which will preferentially sample parts of the distribution over others. The competition between these various processes is a central theme of this thesis, where we would like to understand the extent to which a kinetic treatment of electron transport is necessary, and how predictions may differ with a classical model.

2.9 Literature review

It's worthwhile now to present an overview of the research from recent years with relevance to the questions posed in this thesis. The research presented covers a wide range of adjacent disciplines, and the aim is to provide context in light of the research aims which will be investigated in later chapters. It is divided into sections broadly based on modelling approach, and chronologically therein.

2.9.1 SOL kinetic modelling

An important code for the study of SOL kinetics was developed in the 1990s by Batischev et al., called ALLA [65–68]. In one spatial dimension (parallel to the magnetic field) and two velocity dimensions (v and $\mu = v_\parallel/v$), kinetic equations were solved for the electrons, ions and neutral atoms. Fokker-Planck operators (2.32) for collisions between charged species are included, along with Boltzmann collisions (2.25) for electron-neutral inelastic collisions and ion-neutral charge exchange collisions. A simplified BGK collision operator [69] for neutral-neutral collisions is used,

$$C_{nn} = (f_n^M - f_n)/\tau_{nn},$$

where τ_{nn} is the neutral-neutral collision time and f_n^M is a drifting Maxwellian neutral distribution at the local density, flow velocity and temperature. Simulations of a 10m long scrape-off layer with line-averaged density $\langle n \rangle_l = 6 \times 10^{19}\mathrm{m}^{-3}$ were carried out with ALLA, in both steady-state and transient regimes, where in the latter an ELM-like event was simulated with a

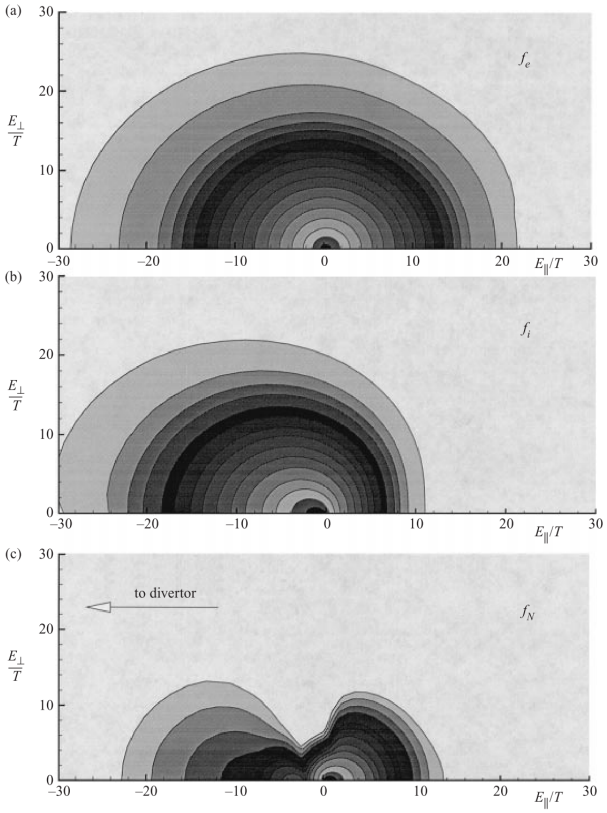

(a) Snapshot of the electron, ion and neutral distributions during a transient regime studied with the ALLA code. Anisotropies are seen in all three, particularly in the neutrals where the shape is attributed to charge exchange collisions.

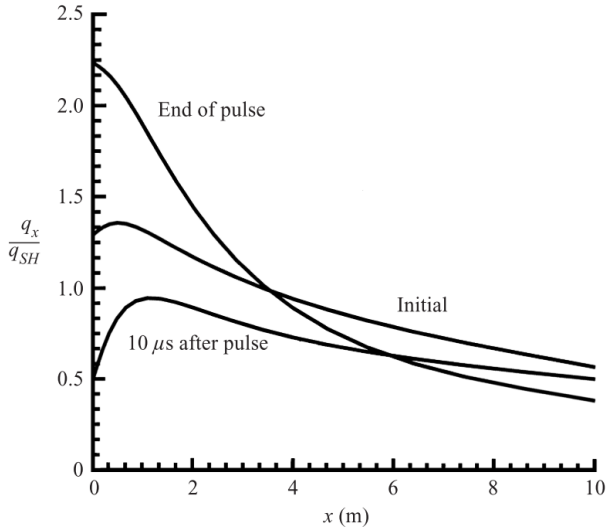

(b) Ratio of the kinetically-calculated electron heat flux to the Spitzer-Härm prediction at three different times during a simulated ELM with ALLA. The x-axis is the spatial coordinate, with the target at $x = 0$.

Figure 2.11: Results from time-dependent simulations with ALLA. Both figures reproduced from [68].

temporary increase in upstream heat flux from the core. During the ELM simulations, strong anisotropies were observed in the distributions of all species (Figure 2.11a) as well as departures from the Spitzer-Härm electron heat flux prediction (Figure 2.11b). ALLA set a surprisingly high benchmark for model fidelity in kinetic studies of the scrape-off layer for the time, which in some senses has not been exceeded in the intervening years. One drawback of ALLA is that a limited plasma regime was explored, making extrapolation to reactor-relevant devices (or even some present-day tokamaks) difficult. In addition, the lack of a benchmark fluid model to compare to has also made it hard to ascertain the magnitude of the effect a kinetic treatment has on important SOL parameters such as target heat fluxes.

A large body of work has resulted from the 1D particle-in-cell (PIC) code BIT1, developed by Tskhakaya et al. [70]. In the PIC method, a large number ($\sim 10^{10}$) of macroparticles are

tracked, moving according to the equations of motion in the presence of electric and magnetic fields and with a finite chance of undergoing a collisional process, alongside the self-consistent updating of the fields by solving Maxwell's equations. In this way, a solution to the kinetic equation is approximated statistically.

BIT1 has been used to show significant differences in conditions at the sheath when treated kinetically, compared to classical treatments [71, 72], where in the latter reference a detached, recombining SOL was simulated. The effect of impurities have been simulated in [73, 74], where carbon and tungsten ions have been included in the model and the focus has been on investigating the effect of erosion of tungsten from the target plates. The flux of tungsten ions into the SOL plasma was found to be low in these studies, with the main ion friction and potential drop across the sheath being responsible for significant redeposition of sputtered tungsten back onto the target plates. Non-local parallel heat transport has been observed with BIT1 [75, 76]. In [37], BIT1 was used to show that Langmuir probe measurements may significantly over- or underestimate T_e due to non-Maxwellian electrons in stationary and transient SOL regimes. ELMs have also been simulated [75], where a fit has been provided for the time-dependent response of the sheath heat flux coefficients. In [77, 78], further studies of ELMs have been carried out, where BIT1 was coupled to SOLPS-ITER for an ELM simulation with kinetic corrections to the sheath boundary conditions.

In summary, BIT1 is an extremely powerful tool allowing fully kinetic studies of SOL plasmas in 1D across a wide range of collisionalities, in time-dependent regimes and at equilibrium. Like all PIC codes however, statistical noise can be an issue. This was found in the studies with tungsten impurities, where the small numbers of highly-ionized tungsten ions made reliable estimates of tungsten leakage into the core (where very small fractions can strongly affect confinement) impossible. Furthermore, BIT1 is very computationally demanding, requiring $\sim 10^5 - 10^6$ CPU hours for each simulation [72], which makes broad parameter scans unfeasible.

A recent code developed to study SOL transport kinetically is KIPP [79]. KIPP is a continuum code solving a similar model to ALLA: the kinetic equation is solved in two velocity dimensions, $v_\parallel$ and $v_\perp$, along the parallel spatial direction. It was originally developed for electrons only,

but has since been extended to solve for the ions kinetically too [80]. In [63] and [3], it is shown that in typical SOL scenarios the heat carrying electrons are collisionless, and parallel heat flux suppression in the electrons was observed along with deviations in the sheath heat flux coefficient. In [81], Chankin et al. performed a quasi-2D kinetic electron study with KIPP by using profiles from EDGE2D (a fluid code for studying edge plasmas in the JET tokamak) at several radial locations as fixed backgrounds for KIPP runs, where the macroscopic profiles were kept constant in KIPP with particle and power sources. Once again, parallel heat flux suppression was observed along with heat flux enhancement close to the walls, although this latter effect is dominated by the convective contribution (see Figure 2.12). In [80], similar effects were observed when the ions were treated kinetically. Strong kinetic enhancement of the ion thermal conduction close to the targets was observed (by a factor of ~ 100), but this was not enough to match the electron contribution. An important numerical study with KIPP was performed by Zhao et al. [82], where an inelastic Boltzmann collision operator for electrons was implemented and used to study the effect of treating excitation and ionization of deuterium. It was found that there are only small kinetic effects on a) the effective ionization rates due to non-Maxwellian electrons, and b) the kinetic effect of electron cooling from inelastic collisions. It should be noted these conclusions apply to atomic processes involving deuterium, and may not necessarily be taken to hold for reactions with other impurity species.

The central work of this thesis is building upon the work carried out by Mijin et al. using the code SOL-KiT [4]. SOL-KiT is a self-contained code (i.e. no coupling is required) solving the kinetic equation for electrons along with a fluid model for the ions and neutral hydrogenic atoms, see Section 3.1 for a brief description of the code. The electrons can also be solved with a self-consistent fluid model allowing for direct comparison with the kinetic treatment, something which has been missing from most kinetic SOL studies to date. Similarly to behaviour observed in other kinetic codes, suppression upstream and enhancement close to the target of the parallel heat flux has been seen at equilibrium [83], but this has been shown to produce steeper temperature gradients at moderate collisionalities and a change in the onset of rollover (a proxy for detachment) during a scan of input power, Figure 2.13. During an ELM-like burst of energy into the SOL, it was shown in [84] how heat flux at the target rises quicker in the

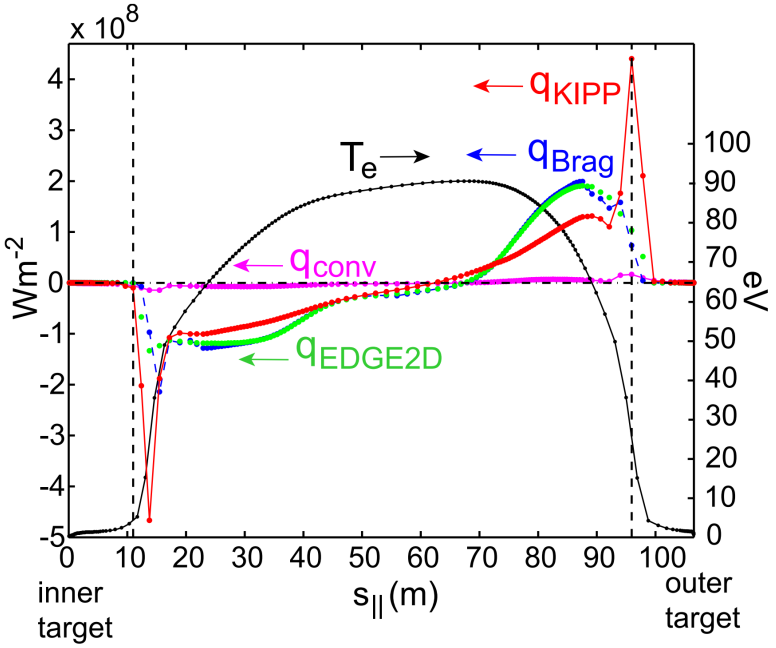

Figure 2.12: Spatial profile of the energy flux in a KIPP simulation couled to EDGE2D. Differences can be seen in the conductive contributions calculted kinetically with KIPP (red) and the Braginskii prediction (blue). Figure reproduced from [81].

kinetic model due to fast electron transport from upstream. Here, significant enhancements to the sheath heat flux transmission coefficient (and sheath potential drop) were seen as well as moderate increases in the deuterium ionization rate.

2.9.2 SOL fluid modelling

Fluid SOL models are much more computationally tractable than kinetic models, making them more amenable to including more realistic physics in the models, making precise experimental predictions, or running a large number of simulations if required (for example to carry out parameter scans). Much of the fluid modelling of the SOL in recent years has been carried out with 2D plasma transport codes such as SOLPS-ITER [34] and UEDGE [85]. These codes solve a 2D form of the plasma transport equations presented in Section 2.5 with closures from Braginskii [48] or Zhdanov [51, 86], coupled to a fluid or kinetic model for the neutral particles. In SOLPS-ITER, transport along the direction parallel to the magnetic field is solved using the fluid equations, sometimes with simple kinetic corrections in the form of flux limiters, while transport in the perpendicular direction uses diffusion-advection models

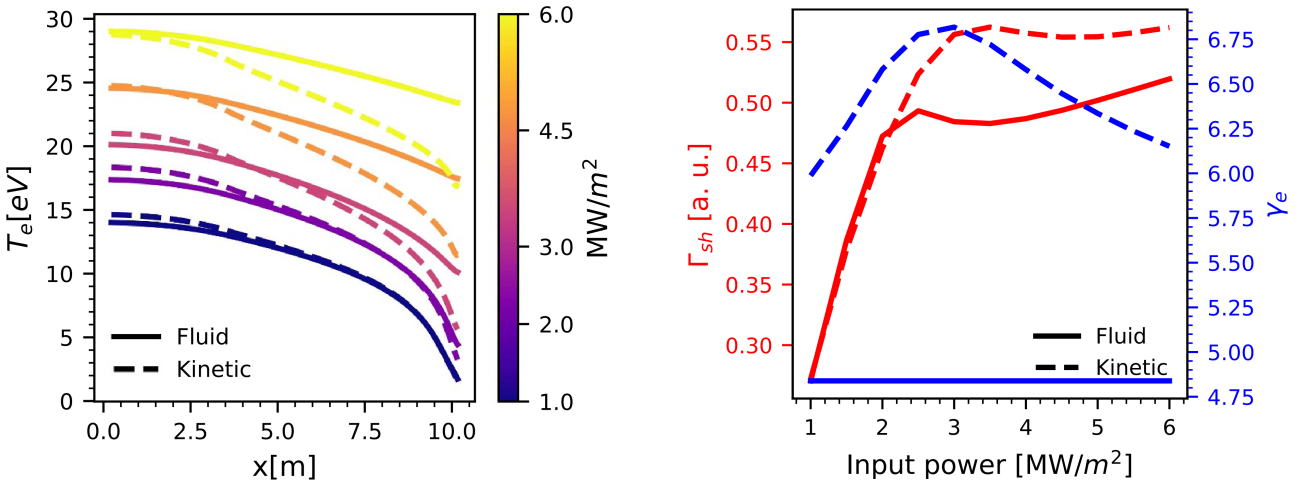

(a) (b)

Figure 2.13: (a): Electron temperature profiles in fluid and kinetic simulations, showing steeper temperature gradients due to heat flux suppression. (b): Flux rollover occurs earlier (i.e. at higher input power) when electrons are treated kinetically with SOL-KiT. Figures reproduced from [83].

with transport coefficients adjusted to match data from experiments. It is then possible to explore the sensitivity of plasma profiles and wall conditions to SOL 'inputs' such as the power from the core, the separatrix density, etc. This approach is very useful for understanding experimental observations, and is used for designing wall components in future devices, but has limited predictive capabilities. Codes exist which aim to solve for the cross-field transport self-consistently [87, 88], but an ongoing challenge is the simultaneous and accurate solution of the plasma and neutral dynamics.

In light of the complex and multi-faceted processes governing SOL dynamics, it is very useful sometimes to study a one-dimensional system with reduced model complexity. This approach offers much more straightforward analysis and affords first-principles explanations of key behaviour. Examples are SOLF1D [89], SD1D [90] and DIV1D [91], and studies have been carried out with a 1D version of SOLPS-ITER. With SD1D, which is based on the BOUT++ framework [88], Dudson et al. explored the processes contributing to detachment in density scans [90], see Figure 2.14. It was found that both momentum and power losses are required to reach detachment, and that recombination as a particle sink plays only a small role at the onset of detachment, but is increasingly important as detachment deepens. The SD1D model has been found recently to overestimate the hydrogen ionisation rate at high plasma densities [92],

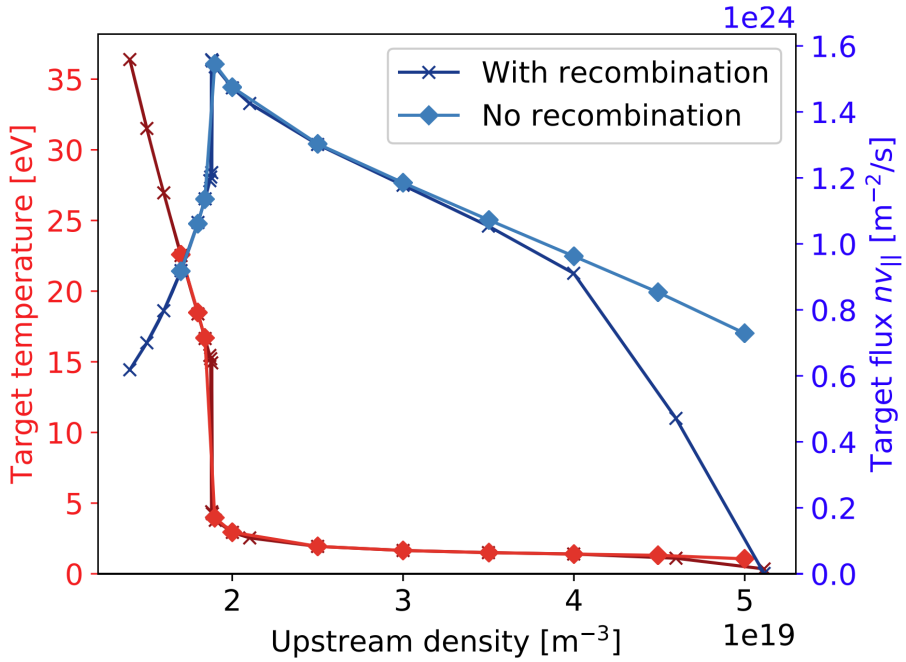

Figure 2.14: Target temperatures (red) and particle flux (blue) in density scans with SD1D. Here, the code is run with and without recombination, where it can be seen that differences only occur long after rollover. Figure reproduced from [90].

which changes rollover behaviour and is discussed in Chapter 5. Furthermore, the assumption of equal ion and electron temperatures in SD1D limits the validity of the energy transport in low collisionality regimes.

2.9.3 Reduced kinetic modelling

The results of kinetic modelling of SOL plasmas have highlighted the relevance of kinetic treatments of parallel transport. If the most significant differences in predictions made by kinetic models can be incorporated into a fluid model at low additional computational cost, then the typical trade-off between accuracy and model completeness may be avoided. A common approach is to use a flux limiter on the heat flux, but Fundamenski [64] showed that this simple approach is inadequate for predictive modelling due to the wide range of values it can take in different SOL plasma regimes as well as having time-dependence. The central issue of the complexity of kinetic models remains, however, so there is a clear motivation to develop more sophisticated models which aim to capture the important facets of non-local transport without resorting to a fully kinetic treatment.

Reduced kinetic models in this context are typically concerned with providing a more sophisticated calculation of the parallel heat flux within a fluid transport model. A prominent example is the model of Schurtz, Nicolaï and Busquet (SNB) [93]. Here, the deviation of the isotropic part of the electron distribution from Maxwellian, δf_0, is calculated using a simplified form of the kinetic equation and used to calculate the deviation from local (Braginskii) heat flow. If simplified collision operators are used such as BGK [69] or AWBS [94], then the calculation of δf_0 is local in velocity space and the additional computational cost is low. The SNB model has been used frequently in ICF applications [95–98], where key features of non-local transport are captured (both heat flux suppression and enhancement), but has also been shown to provide good quantitative agreement with a fully kinetic treatment in a SOL plasma context with a steep temperature drop [97]. The SNB model is derived by assuming time-derivatives in velocity space are zero, which means it is not clear that transient SOL regimes (where non-local transport may be particularly relevant [37, 83, 84]) will be captured accurately. Furthermore, a self-consistent treatment of non-local parallel transport with SNB alongside an appropriate sheath boundary condition has not yet been explored.

Another reduced kinetic model is that of Ji, Held and Sovinec [99], with modifications proposed by Omotani et al. [100]. Similarly to the SNB model, the perturbation in the electron distribution function from a local Maxwellian is calculated using a simplified, time-independent form of the VFP equation. This is then used to calculate the local parallel heat flux. In [97], it was found that the Ji-Held-Sovinec model showed good agreement with kinetic predictions of the heat flux in the SOL regimes studied. Agreement was worse than in the SNB model however, see Figure 2.15, and only suppression of the heat flux is captured and not enhancement. However, it was suggested that the range of applicability for different collisionalities may be larger with Ji-Held-Sovinec than SNB. Numerical issues with the Ji-Held-Sovinec have been reported simulating detached SOL conditions in [101].

In [101], Wigram et al. implemented the Ji-Held-Sovinec non-local transport model into the 1D fluid code SD1D, which was used to explore an ITER-like scrape-off layer problem. Doing so with a fully kinetic kinetic model would be computationally challenging due to the large domain length and significant change in plasma conditions from upstream to the targets. Here, signif-

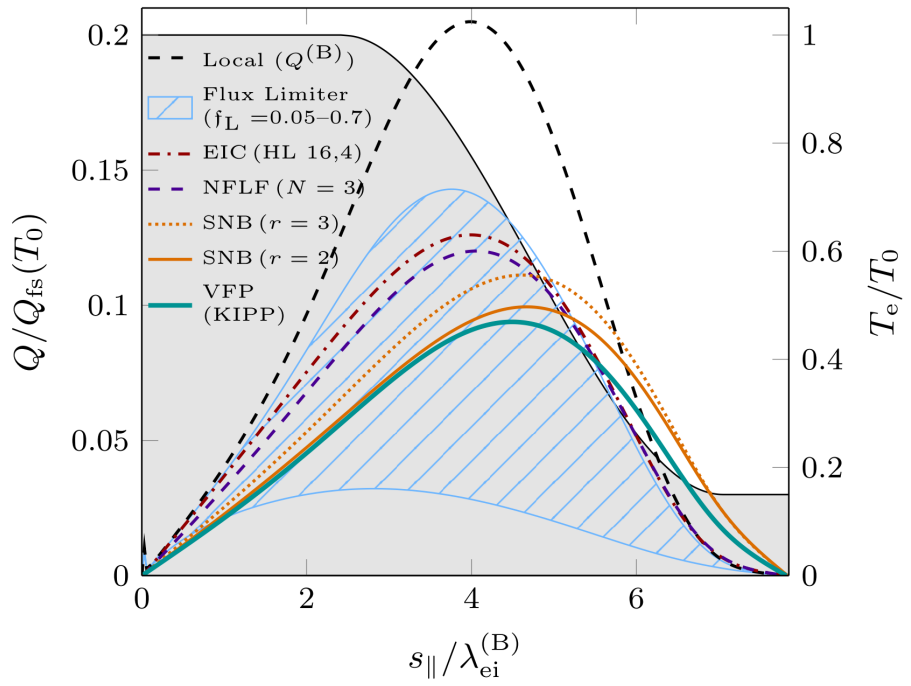

Figure 2.15: A comparison of different parallel heat flux models studied in [97]. The temperature drop is shown in shaded grey (right axis). The ratio of the heat flux prediction to the free-streaming value is shown on the left axis for KIPP (cyan); SNB with two variations of model parameters (orange, solid and dashed); the Ji-Held-Sovinec model (dot-dashed red, labelled 'EIC'); flux limited values for a range of limiters (light blue); and the local Braginksii value (black dashed).

icant non-local effects in the form of modified plasma profiles (see Figure 2.16) are predicted in future devices such as ITER and DEMO, where the SOL collisionality parameter ν^* is expected to be smaller than in current devices. It was also found that, by increasing the fractional abundance of a background radiating impurity species to stimulate detachment, the non-local transport model predicts detachment at higher impurity seeding than a flux-limited model. Neither the impurity radiation or the sheath boundary conditions were treated self-consistently with the non-local heat flux in this study.

Other reduced kinetic models exist (for example that of del Sorbo et al. [102, 103], and Manheimer et al. [104]) which have yet to be applied to a study of SOL plasmas. There is generally good agreement in the parallel heat flux using the models discussed here with kinetic predictions, with a much-reduced computational cost, but there is some uncertainty as to whether they are applicable to transient regimes because there is typically an underlying assumption that time-derivatives are zero in velocity space. However, it should be said that such models

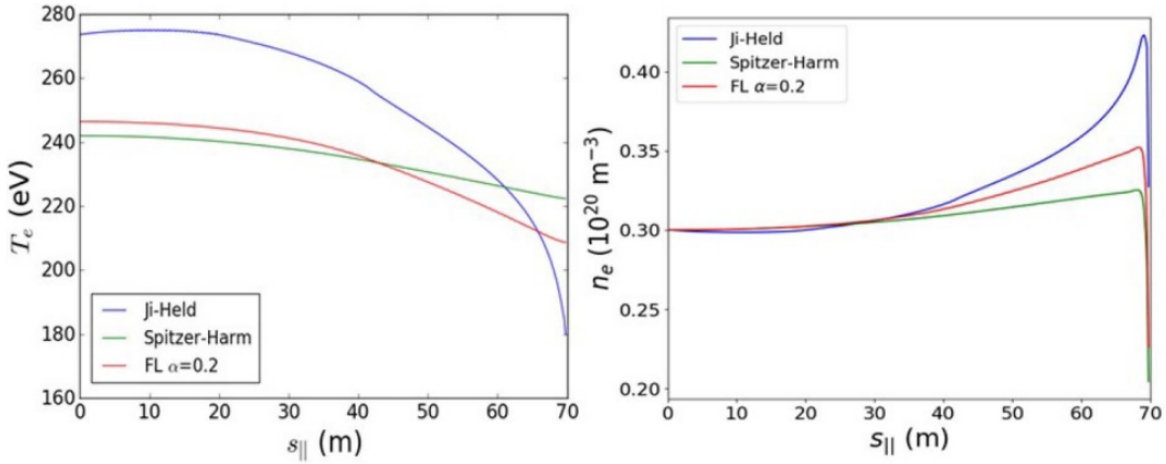

Figure 2.16: Temperature (left) and density (right) profiles in simulations of an ITER-like SOL using the SD1D code [101]. Profiles are shown for three parallel heat flux models: Braginksii/Spitzer-Härm, Ji-Held-Sovinec, and flux-limited with $\alpha = 0.2$.

can accurately resolve time-dependence in some cases [105]. A final point is that self-consistent treatments of the heat-flux using reduced kinetic models with other important aspects of SOL physics, for example the sheath boundary, are rare.

2.9.4 Simple SOL models

Due to the complexity of fluid SOL models, even relatively simple ones such as the 1D fluid model in SD1D [90], there remains signficiant interest in reduced, semi-analytic models which may offer simple yet powerful approaches to predicting the necessary operating conditions for future tokamaks.

An important example is the model by Lenygel [106] which aims to predict detachment onset for a given concentration of radiating impurity species, c_α. The Lengyel model is similar to the two-point model (Section 2.7.2) in that similar assumptions are made and the aim is to relate conditions at the target (t) to those upstream (u), but the effect of a radiating impurity species is incorporated into the calculation of the parallel heat flux. This leads to a modified expression for the parallel heat flux along the SOL, which becomes a function of the concentration of a given impurity species. In [107], Moulton et al. compared Lengyel model predictions for detachment onset with SOLPS-ITER simulations for an ITER baseline scenario, where the impurity concentration required for flux rollover was typically overpredicted by a factor of ~ 4,

but the qualitative predictions for scalings between $n_{e,u}$, $q_{\parallel,u}$ and c_α were in good agreement. Another example is the detachment location sensitivity (DLS) model of Lipschultz et al. [62], where an inverse relationship has been shown to exist between the degree of flux tube expansion (i.e. the ratio of the total magnetic field at the X-point to that at the target) and detachment onset.

Reduced models such as these typically make predictions which are functions of parameters which are sensitive to non-local transport effects such as the parallel heat flux, the sheath heat transmission coeficient and the rate coefficients of plasma-impurity reactions. Because of this, they offer a potential test of the sensitivity of qualitative SOL behaviour (such as detachment onset) to kinetic effects like heat flux suppression.

2.9.5 Conclusions

Here we have summarised some important recent research into SOL plasmas with relevance to the questions posed in this thesis. It can be seen that it is by now well-established that suppression of the heat flux compared to classical predictions is a common feature of SOL plasmas, and that this can lead to steeper temperature gradients and modified density profiles in moderate to low collisionality regimes. Furthermore, simple flux limiters applied to Spitzer-Härm heat flow are not appropriate for predictive modelling because the degree of flux suppression varies spatially and temporally, and is highly dependent on plasma profiles across the whole SOL domain.

It is less clear how significant these changes to the parallel heat flux will be for future tokamaks such as ITER and DEMO. These devices will almost certainly need to operate in detached mode, meaning target conditions will necessarily be highly collisional and so non-local transport may not be significant. This raises the question of whether kinetic effects may modify the onset of detachment, either in terms of the amount of impurity seeding required or the plasma density at the speparatrix. The work by Wigram et al. in [101] suggests kinetic effects may delay detachment onset, but the treatment of impurity radiation there was not self-consistent with the parallel heat flux. Some of these questions will be explored in detail in Chapter 5, where

kinetic simulations will be compared to fluid predictions in a range of plasma regimes, from attached to detached. Furthermore, in Chapter 6 the question of kinetic effects in the presence of impurities will begin to be investigated.

Few studies of non-local transport have been attempted in the context of a fully-featured SOL model which includes accurate ion and neutral physics as well as realistic geometry. Vasileska et al. [78] used the BIT1 code to compute kinetic boundary conditions in a study of ELMs with SOLPS-ITER, but this study did not simultaneously compute the parallel heat flux kinetically. In Chapter 3, a model for the ions and neutral particles in the context of a kinetic treatment of the electrons will be developed. This model has been applied to the physics investigations in later chapters.

Much kinetic modelling carried out to date has sought to identify the presence and magnitude of kinetic effects in scrape-off layer plasma regimes. However, there has not yet been a systematic attempt to quantify the strength of these kinetic effects with respect to SOL control parameters. This is clearly a challenge to do in any sufficiently realistic model given the multitude of uncertainties in other aspects of SOL physics, but it is currently an open question whether or not fluid models of parallel transport in the tokamak edge are appropriate for devices such as ITER, DEMO and SPARC. In Chapter 5, this will be addressed directly by attempting to develop a set of simple scaling laws which predict the magnitude of expected kinetic effects in a given SOL scenario, based on kinetic simulations across a broad range of conditions.

A key focus of much of the modelling work discussed here has been on kinetic effects in the parallel heat flux, particularly for electrons, and to a lesser extent the conditions at the sheath boundary. There has been less attention paid to non-local transport in other areas relevant to parallel transport such as the role of electron-ion equipartition and electron-impurity reaction rates, which will be explored here in Chapters 4 and 6.

We have not paid much attention here to ion kinetics, apart from mentioning the study performed by Chankin et al. [80] which looked at kinetic effects in the parallel ion transport. While we may not expect parallel thermal conduction of the ions to play as significant a role in plasma transport as for the electrons, there is clearly some interest in understanding the veloc-

ity distribution of ions incidient on the targets, which may for example alter physical sputtering rates. Ion kinetics may also be important in turbulent transport in the core and into the edge. Furthermore, it has recently been suggested that parallel heat flux suppression in the ions may significantly increase upstream ion temperatures in reactor-relevant tokamak conditions [108]. These considerations are beyond the scope of the work presented here, where there are many questions still to be answered in the area of electron kinetics.

Finally, it should also be noted that the treatment of SOL geometry in this thesis will be rather simplified despite it playing an important role in edge plasma transport, as evidenced by the studies cited in this section which feature a sophisticated geometrical treatment of the edge plasma. The discussion from hereon will be limited to transport in the parallel direction. This is motivated in part by computational considerations, where there is a price to be paid for solving the kinetic equation, and in part by an attempt to explore the fundamental physics at play, where the model chosen should be the minimum viable one such that conclusions are relevant, but analysis does not become too convoluted. One important geometric effect, flux tube expansion, has been considered and an approach to modelling it kinetically will be presented (without implementation) in Appendix C.

Chapter 3

Numerical modelling

The bulk of the work carried out in this thesis has made use of the kinetic electron code SOL-KiT, originally written by Mijin [4]. To carry out the studies which will be discussed in later chapters, I have developed and implemented several upgrades to SOL-KiT, with the aim of introducing additional physics not included in the original model and reducing the computational cost of running the code. These two avenues for improvement have been motivated by a desire to explore the effect of electron kinetics in more realistic SOL regimes, and to carry out parameter scans where we can identify the relevance of a kinetic treatment to current and future tokamak experiments. A third direction of the numerical modelling work carried out is in the treatment of non-Maxwellian reaction rates for SOL impurities. To assess the importance of kinetic effects in plasma-impurity reaction rates, and as a precursor to a self-consistent treatment of impurities in a code such as SOL-KiT, a separate collisional-radiative model (CRM) has been developed to investigate the atomic population kinetics of various tokamak-relevant impurities against background plasma profiles from SOL-KiT.

In this chapter, the original SOL-KiT model from [4] will be outlined first. Following this, three improvements to SOL-KiT will be presented: adding an ion temperature equation; adding a fluid neutral model; and bundling electron-neutral collision operators. Finally, a CRM for exploring the effect of non-Maxwellian reaction rates in SOL impurities will be presented. Benchmarking results for all newly-developed code will also be provided. As such, Section 3.1

is a review of previously published work carried out by Mijin [4], while Sections 3.2 onwards are a description of original work.

3.1 SOL-KiT

This section describes the original version of SOL-KiT, written by Mijin. All studies with SOL-KiT presented in later chapters used the upgraded version of SOL-KiT which are described in Sections 3.2, 3.3 and 3.4.

SOL-KiT is a 1D code, where the spatial coordinate x is oriented parallel to the magnetic field; see Figure 3.1 for a diagram of the SOL-KiT geometry. A hydrogenic plasma is modelled, consisting of electrons, singly-charged ions and neutral atoms (where the number density of excited states, specified by principal quantum number, are individually tracked). For the electrons, we can choose to simulate them by solving the kinetic equation or a set of equivalent, Braginskii-like fluid equations which are moments of the kinetic model. The ions are treated as a fluid, and a simple diffusive transport model is used for the neutrals. A collisional-radiative model is included for the evolution of the neutral atomic states and computing plasma-neutral source terms.

For the following discussion, unless specified otherwise the variable f with no subscript refers to the distribution function of the electrons. This section is largely adapted from [4,109], but is provided here to serve as a reference for the improvements to SOL-KiT which will be presented after. Only the key aspects of the SOL-KiT model are presented here; further details are provided in Appendix A. The development work on SOL-KiT has been incremental, meaning some aspects of the model which are presented early in this chapter will later be redefined. For physics investigations which are presented in later chapters it will be made clear which version of the code has been used.

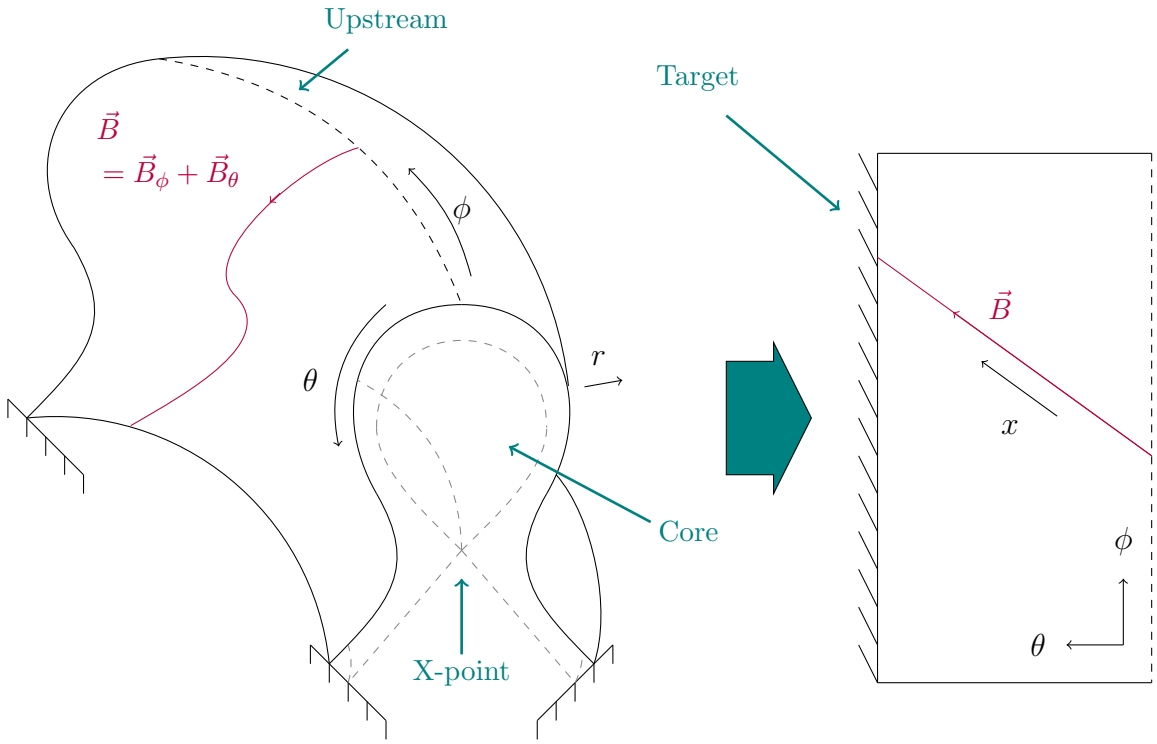

Figure 3.1: Diagram of SOL-KiT geometry. A flux surface in the scrape-off layer is shown on the left, where a single magnetic field line is drawn from a point upstream to the target (red). The radial, r, toroidal, ϕ, and poloidal, θ, directions are also shown. In SOL-KiT, this surface is 'flattened out' (right), and a single flux tube is modelled along the spatial coordinate x oriented parallel to $\vec{B}$, assuming toroidal symmetry and reflective symmetry around the upstream location, as well as uniform field strength.

3.1.1 Kinetic electron model

When the electrons are modelled kinetically, the electron velocity distribution function $f(t, x, \boldsymbol{v})$ is evolved according to the 1D form of the kinetic equation (2.20),

$$\frac{\partial f(t,x,\mathbf{v})}{\partial t} + v_x \frac{\partial f(t,x,\mathbf{v})}{\partial x} - \frac{e}{m_e} E \frac{\partial f(t,x,\mathbf{v})}{\partial v_x} = \sum_\alpha C_{e,\alpha}, \tag{3.1}$$

where $\mathbf{v}$ is the velocity space coordinate and $C_{e,\alpha}$ is the collision operator for collisions between electrons and species α (electrons, ions or neutral atoms). The spatial domain is along the x-axis, see Figure 3.1. For collisions between charged particles (electron-electron and electron-ion), the Fokker-Planck collision operator is implemented. For collisions between electrons and neutral atoms, the Boltzmann collision integral is used.

Similar to codes such as KALOS [110], IMPACT [111] and OSHUN [112], a spherical harmonic

expansion of f is employed as a physically meaningful method of dimensionality reduction, as discussed briefly in Section 2.2, based on the formalism of Shkarofsky et al. [42]. The cartesian velocity coordinates (v_x, v_y, v_z) are transformed to spherical coordinates (v, θ, φ). Spherical harmonics allow us to write a function in this coordinate system as a product of Legendre polynomials, $P_l^m(\cos\theta)$, and the complex phase, $e^{im\varphi}$. The distribution function becomes

$$f(v,\theta,\varphi) = \sum_{l=0}^{\infty} \sum_{m=-l}^{l} f_l^m(v) P_l^{|m|}(\cos\theta) e^{im\varphi}.$$

Macroscopic transport quantities become natural functions of different harmonics of f in this formalism. For a scalar function in v, its moment uses the $l = 0$ harmonic,

$$\int \phi f(\mathbf{v}) d\mathbf{v} = 4\pi \int_0^{\infty} \phi f_0^0(v) v^2 dv.$$

If $\boldsymbol{a}$ is a vector function of v, its moment uses the $l = 1$ harmonic,

$$\int \mathbf{a} f(\boldsymbol{v}) d\boldsymbol{v} = \frac{4\pi}{3} \int_0^{\infty} |\mathbf{a}| \begin{bmatrix} f_1^0 \\ 2Re(f_1^1) \\ -2Im(f_1^1) \end{bmatrix} v^2 dv,$$

and so on for higher-order tensor quantities.

Since the model is 1D in space and azimuthal symmetry about the x-axis is assumed in velocity space (as well as uniform magnetic field strength along x), magnetic field effects are ignored. This means the m indices are always zero and the decomposition reduces to one in Legendre polynomials only, $f(v,\theta) = \sum_l f_l(v) P_l(\cos\theta)$. The m superscript is hereby dropped.

As in the case of transport quantities, we can similarly decompose each term in the kinetic equation (3.1), resulting in a series of evolution equations for $f_l(t, x, v)$ up to some l_{max} for the highest resolved harmonic. Details are provided in Appendix A.1. The result is that the kinetic equation becomes

$$\frac{\partial f_l}{\partial t} = A_l + E_l + C_l \tag{3.2}$$

where A_l, E_l and C_l are the decomposed forms of the spatial advection, electric field and collision terms respectively. The spatial advection term is

$$A_l = -\frac{l}{2l-1} v \frac{\partial f_{l-1}}{\partial x} - \frac{l+1}{2l+3} v \frac{\partial f_{l+1}}{\partial x}. \tag{3.3}$$

The velocity space advection due to the electric field is

$$E_l = \frac{e}{m} E \left[\frac{l}{2l-1} G_{l-1} + \frac{l+1}{2l+3} H_{l+1} \right], \tag{3.4}$$

where

$$G_l(v) = v^l \frac{\partial v^{-l} f_l}{\partial v},$$
$$H_l(v) = \frac{1}{v^{l+1}} \frac{\partial v^{l+1} f_l}{\partial v}.$$

The collision terms, C_l, are somewhat more involved and so presented in A.2. Contributions to C_l come from electron-electron and electron-ion Coulomb collisions, where the Fokker-Planck operator (2.32) is decomposed in Legendre polynomials, and electron-neutral collisions with a decomposition of the Boltzmann collision operator (2.25). Included electron-neutral processes are elastic collisions, excitation, de-excitation, ionization and three-body recombination. There is also a heating operator, included to simulate energy entering the SOL from the core.

The electric field is calculated using Ampère-Maxwell's law, containing only the displacement current,

$$\frac{\partial E}{\partial t} = -\frac{1}{\varepsilon_0}(j_e + j_i), \tag{3.5}$$

where $j_e = -e\frac{4\pi}{3}\int_0^\infty v^3 f_1(v) dv$ is the electron current density and $j_i = e n_i u_i$ is the ion current density (where n_i is the ion density and u_i the ion flow velocity).

The model for the background ions and neutrals in kinetic mode is presented alongside the fluid electron model in the next section.

3.1.2 Fluid model

The fluid model for electrons is obtained by taking mass, momentum and energy moments of the 1D kinetic equation, either in its traditional form (3.1) or in the Legendre form (3.2), and then reformulating as evolution equations for the density, flow velocity and temperature. What results is a 1D form of the intrinsic transport equations presented in Chapter 2, equation (2.43), where isotropy is assumed so that $\underline{\underline{\boldsymbol{\pi}}}_e = 0$. We thus have equations for the electron density n_e,

$$\frac{\partial n_e}{\partial t} + \frac{\partial \left(n_e u_e\right)}{\partial x} = S_e, \tag{3.6}$$

flow velocity u_e,

$$\frac{\partial u_e}{\partial t} = -u_e \frac{\partial u_e}{\partial x} - \frac{e}{m_e} E - \frac{S_e}{n_e} u_e - \frac{1}{m_e n_e} \frac{\partial \left(n_e k T_e\right)}{\partial x} + \frac{R_e}{m_e n_e} \tag{3.7}$$

and temperature T_e,

$$\frac{\partial k T_e}{\partial t} = -u_e \frac{\partial k T_e}{\partial x} + \frac{2}{3}\left[-k T_e \frac{\partial u_e}{\partial x} - \frac{1}{n_e}\frac{\partial q_e}{\partial x} - \frac{S_e}{n_e}\left(\frac{3}{2} k T_e - \frac{m_e u_e^2}{2}\right) - \frac{u_e R_e}{m_e n_e} + \frac{Q_e}{n_e}\right]. \tag{3.8}$$

The parallel electric field is given by E. S_e, R_e and Q_e are sources of particles, momentum and energy, where there may be contributions from electron-ion collisions, electron-neutral collisions and external sources. Source term notation in this section will use subscripts for the species to which they apply, and superscripts for the process involved. No subscript means a quantity may be applied to equations for more than one species, sometimes with a change of sign.

The particle source term is

$$S_e = S^{ion} - S^{rec} + S_e^{ext}, \tag{3.9}$$

where S^{ion} is the particle source resulting from ionization and S^{rec} from recombination, and S_e^{ext} is any external particle source. The friction term contains contributions from electron-ion friction and from electron-neutral collisions,

$$R_e = R_e^{ei} + R_e^{en},$$

where the Braginskii form of R_e^{ei} is used [48],

$$R_e^{ei} = -R_i^{ei} = -\frac{m_e n_e}{\tau_e} 0.51 \left(u_e - u_i\right) - 0.71 n_e \frac{\partial \left(kT_e\right)}{\partial x}, \tag{3.10}$$

where u_i is the ion flow velocity and τ_e is the Braginskii electron collision time (2.5). The energy source Q_e is determined by electron-neutral collisions and external heating,

$$Q_e = Q_e^{en} + Q_e^{ext}, \tag{3.11}$$

where Q_e^{ext} is used to simulate energy input from the core. For an input heat flux q_{in} distributed uniformly over length L_h, $Q_e^{ext} = H(L_h - x) q_{in}/L_h$ where H is the step function, which is equivalent to the kinetic heating operator (A.17). No electron-ion energy transfer is included in this original version of SOL-KiT because the ions are assumed to be either cold or equal to the electron temperature. This assumption is relaxed in Section 3.2.

S_e^{en}, R_e^{en} and Q_e^{en} are computed by taking the appropriate moments of the Boltzmann collision operators

$$S_e^{en} = 4\pi \int_0^\infty dv v^2 \left(C_0^{el} + C_0^{ex} + C_0^{ion} + C_0^{3br}\right) \tag{3.12a}$$

$$R_e^{en} = \frac{4\pi}{3} \int_0^\infty dv \left(m_e v\right) v^2 \left(C_1^{el} + C_1^{ex} + C_1^{ion} + C_1^{3br}\right) \tag{3.12b}$$

$$Q_e^{en} = 4\pi \int_0^\infty dv \left(\frac{1}{2} m_e v^2\right) v^2 \left(C_0^{el} + C_0^{ex} + C_0^{ion} + C_0^{3br}\right) \tag{3.12c}$$

for operators from elastic, excitation, ionization and three-body recombination (see Appendix A.2 for definitions). A Maxwellian electron distribution is used in this fluid electron model,

$$\begin{aligned} f_0(v) &= n_e \left(\tfrac{m_e}{2\pi k T_e}\right)^{3/2} e^{\frac{-m_e v^2}{2kT_e}}, \\ f_1(v) &= -u_e \tfrac{\partial f_0}{\partial v}, \\ f_{l\geq 2}(v) &= 0. \end{aligned}$$

In this way, numerical equivalence with the kinetic model is ensured for the source terms, with differences arising solely from differences in the distribution function.

Closure of the fluid equations is achieved with the Braginskii expression for heat flow (2.46), presented again here,

$$q_e = 0.71 n_e k T_e u_e - \kappa_e \frac{\partial k T_e}{\partial x},$$

using the Spitzer-Härm value for heat conductivity, κ_e [49].

For the ions, only the flow velocity, u_i, is directly evolved. Quasi-neutrality is enforced, so the ion density is calculated with $n_i = n_e$. Ions are assumed to either be cold, or equal in temperature to the electrons, $T_i = T_e$. The ion flow velocity is evolved using a similar equation to (3.7) featuring the ion mass, m_i,

$$\frac{\partial u_i}{\partial t} = -u_i \frac{\partial u_i}{\partial x} + \frac{Ze}{m_i} E - \frac{S_i}{n_i} u_i - \frac{1}{m_i n_i} \frac{\partial \left(n_i k T_i\right)}{\partial x} + \frac{R_i}{m_i n_i}. \tag{3.13}$$

Particle sources S_i are the same for both species, $S_i = S_e$. The friction term, R_i, has contributions from electron-ion friction and ion-neutral friction via charge exchange collisions,

$$R_i = R_i^{ei} + R_i^{cx}. \tag{3.14}$$

For electron-ion friction, R_i^{ei}, in kinetic mode the momentum moment of the e-i collision operator is calculated, while in fluid mode the Braginskii expression is used (3.10), where momentum conservation is enforced with $R_i^{ei} = -R_e^{ei}$. The charge exchange friction between ions and neutrals is

$$R_i^{cx} = S^{cx} m_i (u_n - u_i), \tag{3.15}$$

where S^{cx} is the charge exchange rate per unit volume and u_n is the neutral flow velocity. A simplified form is considered, where neutrals are treated as a cold, stationary target, so that $u_n = 0$ and $S^{cx} = n_i |u_i| \sum_b n_b \sigma_{cx,b}$, where the density of a given neutral atomic state is n_b and the charge exchange cross-section is $\sigma_{cx,b}$. These are summed over all tracked atomic states[1],

[1]Note that the variable b here is used as both an index on the neutral atomic state and the principal quantum number of that state.

and the cross-sections are low-energy values of those given in Janev [113],

$$\sigma_{cx,1} = 3 \times 10^{-19}\ \mathrm{m}^2, \quad \sigma_{cx,2} = 2^4 \times 10^{-19}\ \mathrm{m}^2$$
$$\sigma_{cx,3} = 3^4 \times 7 \times 10^{-20}\ \mathrm{m}^2, \quad \sigma_{cx,b\geq 4} = b^4 \times 6 \times 10^{-20}\ \mathrm{m}^2.$$

Atomic neutrals are treated with a diffusive model, where the density of each excited state b evolves according to

$$\frac{\partial n_b}{\partial t} = \frac{\partial}{\partial x}\left(D_b \frac{\partial n_b}{\partial x}\right) + S_b, \tag{3.16}$$

where $b \in \{1, b_{max}\}$, $b = 1$ being the ground state. For a given state b, the particle source term S_b is similar in form to the right-hand side of the generic equation for the evolution of atomic state densities in plasmas presented in Chapter 2, equation (2.54),

$$\begin{aligned} S_b = &\sum_{b'<b} \left[K^{ex}_{b'\to b} n_e n_{b'} n_b - K^{deex}_{b\to b'} n_e n_b - A_{b\to b'}\right] \\ &+ \sum_{b'>b} \left[K^{deex}_{b'\to b} n_e n_{b'} - K^{ex}_{b\to b'} n_e n_b + A_{b'\to b} n_{b'}\right] \\ &- K^{ion}_b n_e n_b + K^{3br}_b n_e n_i + \beta_b n_e n_i. \end{aligned} \tag{3.17}$$

The rate coefficients for transitions due to excitation (ex), deexcitation ($deex$), ionisation (ion) and three-body recombination ($3br$) are given by K, which is defined

$$K = \frac{4\pi}{n_e} \int_0^\infty (\sigma(v)v) f_0(v) v^2 dv \tag{3.18}$$

for a process with cross-section σ. Radiative de-excitation coefficients are given by A and radiative recombination coefficients by β. For all terms, a subscript $b \to b'$ refers to a transition from initial state b to final state b'. From S_b, the particle source for the plasma species is then $S_e = -\sum_b S_b$, where only the ionization and recombination processes do not cancel so we can write $S_e = S^{ion} - S^{rec}$. The 1D diffusion coefficient D_b is

$$D_b = \frac{v_{th,n}}{2\left[(n_i + n_1)\,\sigma_{el,b} + \sigma_{cx,b} n_i\right]}, \tag{3.19}$$

where $\sigma_{el,b}$ is the cross-section for elastic electron-neutral collisions, where the Bohr radius is

used, n_1 is the ground state neutral density and $v_{th,n}$ is the thermal velocity of the neutrals, $v_{th,n} = \sqrt{2kT_n/m_i}$. The neutrals are assumed isothermal at $T_n = 3$ eV.

3.1.3 Boundary conditions

The upstream boundary is reflective, with all spatial gradients set to zero. At the target the plasma particles crossing the sheath boundary are lost and recycled as neutral particles, where the flow velocities are set equal to the sound speed according to the Bohm criterion, $u_e = u_i = c_s$, where $c_s = \sqrt{2kT_e/m_i}$. For a target plasma particle flux $\Gamma_t = n_t c_s$, neutral recycling is given by $\Gamma_{rec} = -F_{rec}\Gamma_t$, where F_{rec} is the recycling coefficient (a number between 0 and 1). The target density, n_t, is extrapolated from the last two spatial grid cells. There are no diffusive neutral fluxes at the boundary, such that $D_b \frac{\partial n_b}{\partial x} = 0$ in equation (3.16) for $b > 1$. For $b = 1$, recycling into the ground state is imposed by setting $D_1 \frac{\partial n_1}{\partial x} = \Gamma_{rec}$ at the boundary.

In fluid mode, the boundary condition on the electron heat flux is $q_t = \gamma_e n_t k T_t$, where

$$\gamma_e = 2 - 0.5 \ln \left(2\pi \left(1 + T_{i,t}/T_{e,t}\right) m_e/m_i\right) \tag{3.20}$$

is the sheath energy flux coefficient.

A zero-gradient boundary condition is used for the target temperature, T_t. The target density, n_t, is calculated using an extrapolation from previous spatial cells.

In kinetic mode, the velocity and energy flux boundary conditions are calculated self-consistently by applying a cut-off to the backwards-travelling part of the electron distribution at the sheath edge. The position of this cut-off can be calculated numerically given knowledge of the ion flux, where ambipolarity is assumed so that ion and electron fluxes across the sheath are equal.

3.2 Adding an ion temperature equation to SOL-KiT

Parts of this section are adapted from an article by the author published in the European Physical Journal Plus [39].

In a hydrogenic plasma, the ratio of the thermal conductivity for electrons and ions in the direction parallel to the magnetic field is $\kappa_e/\kappa_i \sim \sqrt{m_i/m_e} \sim 60$. Heat conduction is therefore dominated by the electrons, which provides a justification for models which treat the plasma with a single temperature with heat conduction at κ_e, for example the two-point model [24] and SD1D [90]. However, when thermal equilibration between the electrons and ions is not complete, as in the hot, low collisionality upstream regions of divertor tokamaks, this less-efficient ion heat conduction means we expect them to reach higher temperatures in the SOL than the electrons, assuming equal input power via cross-field transport from the core. We might expect this to play a role in determining plasma behaviour in the SOL and the eventual escape mechanism for energy that makes its way into the SOL. For example, physical sputtering yields are determined primarily by the amount of heat flux carried to the solid surfaces by the ions, while the amount of energy radiated away via inelastic collisions with neutral particles depends more on the properties of the electrons. There is therefore an interplay between thermal equilibration and parallel transport, with each affecting the other, which should be included in a sophisticated treatment of SOL plasmas.

Ion-electron energy transfer is an intrinsically velocity-dependent phenomenon in a similar way to the spatial transport of heat (see Section 2.8), where fast particles are able to transfer more energy but do so less frequently. Since there is also evidence of kinetic effects in other aspects of SOL plasma behaviour, it is natural to investigate whether a fluid model is adequate to describe this ion-electron energy exchange. In order to do this, a fluid ion temperature equation has been implemented in SOL-KiT along with a collision operator in the electron kinetic equation for f_0 (and equivalent for the fluid electron model). The model will be outlined, and then some tests to benchmark the implementation will be discussed. A study carried out with this version of SOL-KiT is presented in Chapter 4.

3.2.1 Model

A fluid equation for the ion temperature T_i can be derived in a very similar way to the T_e equation used in SOL-KiT (3.8), where we start with the kinetic equation for the ions (2.20) and take the mass, momentum and energy moments, splitting velocity into a flow component and random component, which gives a set of transport equations for conserved quantities like (2.42). In the 1D geometry of SOL-KiT, the energy equation is

$$\frac{\partial}{\partial t}\left(\frac{3}{2}p_i + \frac{1}{2}m_i n_i u_i^2\right) + \frac{\partial}{\partial x}\left(q_i + \left(\frac{5}{2}p_i + \frac{1}{2}m_i n_i u_i^2\right)u_i\right) = Zen_i E u_i + Q_i, \tag{3.21}$$

where we have assumed pressure isotropy, $\underline{\underline{\boldsymbol{\pi}}}_i = 0$, as in the electron fluid model. Here, $p_i = n_i k T_i$ is the ion pressure in terms of density, n_i, and temperature, T_i, q_i is the ion conductive heat flux and Q_i is the ion energy source. Straightforward manipulation of this equation, see A.3, allows us to arrive at an evolution equation for T_i,

$$\frac{\partial kT_i}{\partial t} = -u_i\frac{\partial kT_i}{\partial x} + \frac{2}{3}\left[-kT_i\frac{\partial u_i}{\partial x} - \frac{1}{n_i}\frac{\partial q_i}{\partial x} - \frac{S_i}{n_i}\left(\frac{3}{2}kT_i - \frac{1}{2}m_i u_i^2\right) - \frac{u_i}{n_i}R_i + \frac{Q_i}{n_i}\right]. \tag{3.22}$$

This equation has been implemented in SOL-KiT, see A.4 for details on the numerics. The friction term R_i and particle source S_i are the same as that used in the fluid model described in the previous section, equations (3.9) and (3.14). The Braginskii form of the ion heat flow is used with Spitzer-Härm conductivity [48, 49],

$$q_i = -\kappa_i\frac{\partial(kT_i)}{\partial x},$$

where $\kappa_i = 3.906 n_i k T_i \tau_i / m_i$, the ion collision time is

$$\tau_i = \frac{3\sqrt{m_i}(kT_i)^{\frac{3}{2}}(4\pi\epsilon_0)^2}{4\sqrt{\pi}Z^4 n_i \ln\Lambda e^4},$$

and $\ln\Lambda$ is the electron-ion Coulomb logarithm.

New source terms

The ion energy source,

$$Q_i = Q_i^{ext} + Q_i^{cx} + Q_i^s + Q_i^{ei}, \tag{3.23}$$

arises from external heating (simulating input power to the SOL from the core plasma), Q_i^{ext}, charge exchange collisions with neutrals, Q_i^{cx}, particle sources, Q_i^s, and from collisions with electrons, Q_i^{ei}. For a given heat flux q_{in} entering over a heating length L_h, $Q_i^{ext} = H(L_h - x)q_{in}/L_h$, where H is the step function. For Q_i^{cx}, only the contribution from the transfer of kinetic energy is included and not internal energy. This is to avoid an excessively large energy sink from charge exchange for situations where $T_i > T_n$, which was seen to arise in testing due to the fact that the neutral temperature is not evolved in this form of the model. Thus,

$$Q_i^{cx} = \frac{1}{2} m_i (u_n^2 - u_i^2) S^{cx}, \tag{3.24}$$

where u_n is the neutral flow velocity and S^{cx} is charge exchange rate per unit volume. As described in the previous section, the neutrals are treated as a cold, stationary target so $u_n = 0$ and $S^{cx} = n_i |u_i| \sum_b n_b \sigma_{cx,b}$. For Q_i^s, we include the effect of changing particle identity from ionization and recombination, where heavy particles retain their energy during such processes. This term is therefore

$$Q_i^s = S^{ion} \left(\frac{3}{2} k T_n + \frac{1}{2} m_n u_n^2 \right) - S^{rec} \left(\frac{3}{2} k T_i + \frac{1}{2} m_i u_i^2 \right) \tag{3.25}$$

for a net ionization source S^{ion} and recombination source S^{rec}, where $u_n = 0$ and the neutral temperature is $T_n = 3$ eV. The neutral mass is $m_n = m_i$ here. The electron-ion energy exchange, Q_i^{ei}, is discussed shortly.

For conservation of energy in this model, now that the ion energy is evolved independently, we must add an additional contribution R_i^s to the ion momentum source, R_i, which appears in (3.13) and (3.22), due to the exchange of particles during ionization and recombination and

the associated transfer of momentum. This is analogous to the Q_i^s term above. Thus we have

$$R_i = R_i^{ei} + R_i^{cx} + R_i^s, \tag{3.26}$$

with

$$R_i^s = S^{ion} m_n u_n - S^{rec} m_i u_i \tag{3.27}$$

and R_i^{cx} and R_i^{ei} unchanged from (3.15) and (3.10) respectively.

The electron-ion energy exchange is treated differently for fluid or kinetic electrons. For fluid electrons, a standard form [47] is used,

$$Q_i^{ei} = -Q_e^{ei} = -\frac{3m_e}{m_i}\frac{n_e k}{\tau_e}(T_i - T_e), \tag{3.28}$$

where the electron collision time is

$$\tau_e = \frac{3\sqrt{m_e}(kT_e)^{3/2}(4\pi\epsilon_0)^2}{4\sqrt{2\pi}Zn_e \ln\Lambda e^4}.$$

A positive value of Q_e^{ei} here corresponds to energy moving from the ions to the electrons.

When electrons are considered kinetically, the energy moment is taken of the collision operator for electron-ion collisions, C^{ei}, such that

$$Q_i^{ei} = -\int d\boldsymbol{v}\frac{1}{2}m_e v^2 C^{ei} = -4\pi \int dv \frac{1}{2}m_e v^4 C_0^{FP}, \tag{3.29}$$

where the Fokker-Planck collision operator for $l = 0$ is used, C_0^{FP}, since Q_e^{ei} is a scalar quantity (noting the second equality represents the transition from the usual formulation of the collision operator to the decomposition in spherical harmonics). C^{ei} is a function of both f and F, the ion distribution function. As described by Shkarofsky et al. in [42], we can obtain a form of this collision operator by starting from the Rosenbluth potential form of the Fokker-Planck collision operator for electron-ion collisions (2.32). By expanding this in spherical harmonics,

it can be shown that the $l = 0$ Fokker-Planck operator for electron-ion collisions becomes

$$\frac{1}{\Gamma_{ei}} C_0^{FP} = \frac{1}{3v^2} \frac{\partial}{\partial v} \left[\frac{3}{\mu_r} f_0 I_0 \left(F_0\right) + v \left(I_2 \left(F_0\right) + J_{-1} \left(F_0\right)\right) \frac{\partial f_0}{\partial v} \right], \tag{3.30}$$

where the integrals I_i and J_i are defined as

$$I_i \left(F_0\right) = \frac{4\pi}{v^i} \int_0^v F_0(u) u^{i+2} du, \quad J_i \left(F_0\right) = \frac{4\pi}{v^i} \int_v^\infty F_0(u) u^{i+2} du.$$

Next, we assume Maxwellian ions and we arrive at a form of the collision operator which is just a function of the electron distribution, f_0, and T_i,

$$C_{ei}^0 = \frac{1}{v^2} \frac{\partial}{\partial v} \left[\frac{\Gamma_{ei} I_0 m_e}{m_i} (f_0 + \frac{kT_i}{m_e v} \frac{\partial f_0}{\partial v}) \right], \tag{3.31}$$

where I_0 for Maxwellian F_0 has reduced to

$$I_0 = n_i \left(\mathrm{erf}\left(y\right) - y \, \mathrm{erf}'\left(y\right)\right),$$

where erf is the standard error function,

$$\mathrm{erf}(y) = \frac{2}{\sqrt{\pi}} \int_0^y e^{-t^2} dt$$

and erf$'$ is its derivative,

$$\mathrm{erf}'(y) = \frac{d}{dy} \mathrm{erf}(y) = \frac{2}{\sqrt{\pi}} e^{-y^2},$$

with y defined as the ratio of v to the ion thermal velocity, $y = v/v_{th,i} = v/\sqrt{2kT_i/m_i}$.

We can first note that I_0 tends to n_i for large y, and y is indeed large because the electron velocity is typically much larger than the ion thermal velocity. If we insert a Maxwellian for f_0 into (3.31), let $I_0 = n_i$ and recall the definition of Γ_{ei} (2.30), then the fluid expression for Q_i^{ei} (3.28) is recovered. If we do not assume $I_0 = n_i$, then a corrective factor appears which multiplies (3.31) by $(1 + m_e T_i / m_i T_e)^{-3/2}$, which is close to unity for all but extremely high T_i/T_e ratios.

In fluid mode, conservation of energy is achieved by adding Q_e^{ei}, equation (3.28), to the total energy source term Q_e in the electron temperature equation for fluid electrons. In kinetic mode, equation (3.31) is added to the right hand side of the electron kinetic equation (3.2), and the energy moment is taken to compute Q_i^{ei} in (3.23).

It should be pointed out that Q_i^{ei} as defined here, using the total rather than intrinsic velocity,

$$Q_i^{ei} = \int \frac{1}{2} m_i v^2 C_i^{ei} e d\mathbf{v} = \int \frac{1}{2} m_i |\mathbf{w} + \mathbf{u}_i|^2 C_i^{ei} d\mathbf{v},$$

is missing a contribution from Joule heating, so to match the Braginskii form we should have

$$Q_i^{ei} = -\frac{3 m_e n_e k}{m_i \tau}(T_i - T_e) + u_i R_i^{ei},$$

which would cancel with the $u_i R_i^{ei}$ term in the T_i equation (3.22), and result in the usual $(u_i - u_e) R_e^{ei}$ contribution in the T_e equation (3.8). However, to match this in the kinetic equation we would need to translate the collision operator (3.31), which for flowing ions can be considered as applicable in the centre of mass frame, back to the lab frame. The correction is expected to be small, in part because u_i is small relative to the electron thermal velocity in SOL plasmas, and also because no net currents can enter or leave the plasma in the SOL-KiT model so $u_i - u_e$ is also small. Therefore, we do not employ this correction and leave Q_i^{ei} as defined in (3.28) in fluid mode to ensure consistency with the kinetic treatment. However, an approach to performing this translation on collision operators has been considered and is outlined in Section 3.3.3.

Boundary conditions

At both upstream and sheath boundaries, zero gradient is assumed on T_i. There is a boundary condition imposed on the total (convective plus conductive) energy flux crossing the sheath,

$$q_{i,sh}^{tot} = \gamma_i n_t k T_{i,t} c_s + \frac{1}{2} m_i n_i u_i^2 c_s \tag{3.32}$$

where $\gamma_i = 2.5$ is the ion sheath heat flux coefficient, $T_{i,t}$ is the target ion temperature and n_t is the target density. The values of n_i and u_i in the second term are evaluated at the last evolved grid location. The sound speed at the target is now defined as $c_s = \sqrt{k(T_{e,t} + T_{i,t})/m_i}$, which modifies the electron boundary condition in fluid mode (see Section 3.1.3).

In order to implement this boundary condition in practice, because T_i is evolved rather than the ion energy density, in (3.22) q_i is set to zero at the boundary and $u_i = c_s$ is used for the convection term, $u_i \frac{\partial k T_i}{\partial x}$. The equations for n_i and u_i (where $u_i = c_s$ is also imposed at the boundary) supply the remaining total energy flux.

The value of γ_i implemented here is obtained with a simple treatment of the sheath boundary condition for ambipolar flow, where the ion distribution is set to a Maxwellian drifting at the sound speed at the sheath edge [24]. Physically, this value corresponds to the sheath having no net cooling effect on the ions, unlike the electrons, meaning energy is lost to the boundary solely through convection. Experiments suggest $\gamma_i \sim 1.5$ may be more appropriate [24], but the simple treatment is employed here.

3.2.2 Benchmarking

Electron-ion thermal equilibration

To test both the new collision operator for f_0 (3.31) and the Q^{ei} term in the fluid model (3.28), we observe the thermal equilibration between electrons and ions in a 0D system without neutrals. The initial temperatures are $T_e = 50$ eV, $T_i = 10$ eV and the density is constant at $n_e = 3 \times 10^{19}$ m^{-3}. Both fluid and kinetic electrons were simulated. In kinetic mode, the velocity grid consisted of 80 cells, with grid widths ranging from $\Delta v = 0.05 v_{th,0}$ to $0.35 v_{th,0}$ and total length $12.2 v_{th,0}$, where $v_{th,0}$ is the electron thermal velocity of a reference plasma at $T_e = 10$ eV. The timestep was the same in both fluid and kinetic simulations, $\Delta t = t_0$, where t_0 is the electron collision time of a reference plasma at 10 eV.

At this moderate collisionality, electron-electron collisions ensure f_0 stays close to Maxwellian

in kinetic mode, so that the temperature evolution should be the same in both simulations. In kinetic mode, by taking the energy moment of the collision operator (3.31) the temperatures should evolve according to

$$\frac{\partial T_e}{\partial t} = -\frac{\partial T_i}{\partial t} = -\frac{8 n_i \Gamma_{ei}}{3\sqrt{\pi}} \frac{m_e}{m_i} \frac{T_e - T_i}{\left(2kT_i/m_i + 2k_B T_e/m_e\right)^{3/2}},$$

which differs from the fluid expression by a factor $(1 + m_e T_i/m_i T_e)^{-3/2} \simeq 1$. This equation can be written [42]

$$\frac{\partial \xi}{\partial t'_{ei}} = -\frac{\xi}{(1+\xi)^{3/2}},$$

where

$$\xi = \frac{n_i(T_e - T_i)}{(n_i + n_e)T},$$

T being the temperature of the plasma as a whole, and

$$t'_{ei} = \frac{8\Gamma_{ei}(n_e + n_i)}{3\sqrt{\pi}} \frac{m_e}{m_i} \left(\frac{m_e}{2kT}\right)^{3/2} t.$$

The analytical solution to this, for a given initial ξ_0, is

$$\begin{aligned} t'_{ei} =& \frac{2}{3}\left[(1+\xi_0)^{3/2} - (1+\xi)^{3/2}\right] + 2\left[(1+\xi_0)^{1/2} - (1+\xi)^{1/2}\right] \\ &+ \ln\left[\frac{(1+\xi_0)^{1/2} - 1}{(1+\xi_0)^{1/2} + 1}\right] - \ln\left[\frac{(1+\xi)^{1/2} - 1}{(1+\xi)^{1/2} + 1}\right]. \end{aligned} \tag{3.33}$$

The time evolution of T_e and T_i is shown in Figure 3.2a for both kinetic and fluid electrons, where there is good agreement in the electron and ion profiles. Total plasma energy is conserved, to within 10^{-11} % in fluid mode and 10^{-4} % in kinetic mode. The deviation of the temperature difference from the analytical solution in (3.33), $\delta(T_e - T_i) = (T_e - T_i)^{SOL-KiT} - (T_e - T_i)^{analytical}$, is shown in Figure 3.2b. The error peaks at 0.1 eV in kinetic mode and 0.06 eV in fluid mode. In kinetic mode, the ions equilibrate slightly higher than the electrons; $T_e - T_i = -0.06$ eV at the last timestep. The reason for this is that some energy is lost numerically from the electrons in calculating the energy moment of the collision operator, even when $T_i = T_e$, due to finite grid effects.

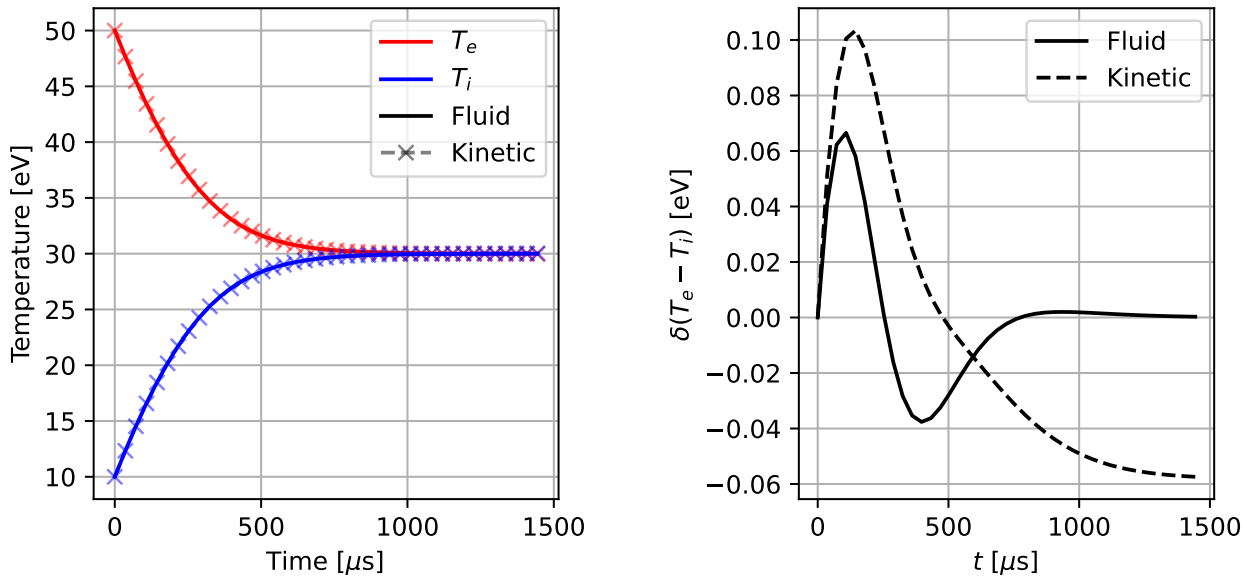

(a) (b)

Figure 3.2: (a): Thermal equilibration of ions and electrons over time for both fluid and kinetic electrons.

Energy balance

To test the energy conservation in the ions, a fully-featured SOL model for a deuterium plasma has been simulated. Ionization and recombination were both included, but only ground state neutrals were tracked. The electrons are fluid, and all other physics described in Sections 3.1.2 and 3.2.1 is included. Temperature and density profiles were initialised to the 2PM values,

$$T(x)\left(T_u^{7/2} + \tfrac{x}{L}\left(T_u^{7/2} - T_d^{7/2}\right)\right)^{2/7}$$
$$n(x) = n_u T_u / T(x)$$

where the temperature and densities were initially equal for the electrons and ions, $n_u = 7.8 \times 10^{18}$ m^{-3} and $T_u = 20$ eV. The simulation was then run until steady state conditions were reached. The length of the simulation domain was 6.7 m and $q_{in} = 1$MWm^{-2} of heating was delivered uniformly over the first 2.2 m, to both the ions and electrons (giving a total heating of 2 MWm^{-2}). 64 cell centres were used for the spatial grid, with cell widths ranging from 26.6cm upstream to 2.7cm at the target.

The temperature and density profiles are shown in Figure 3.3. We can see that the ion tem-

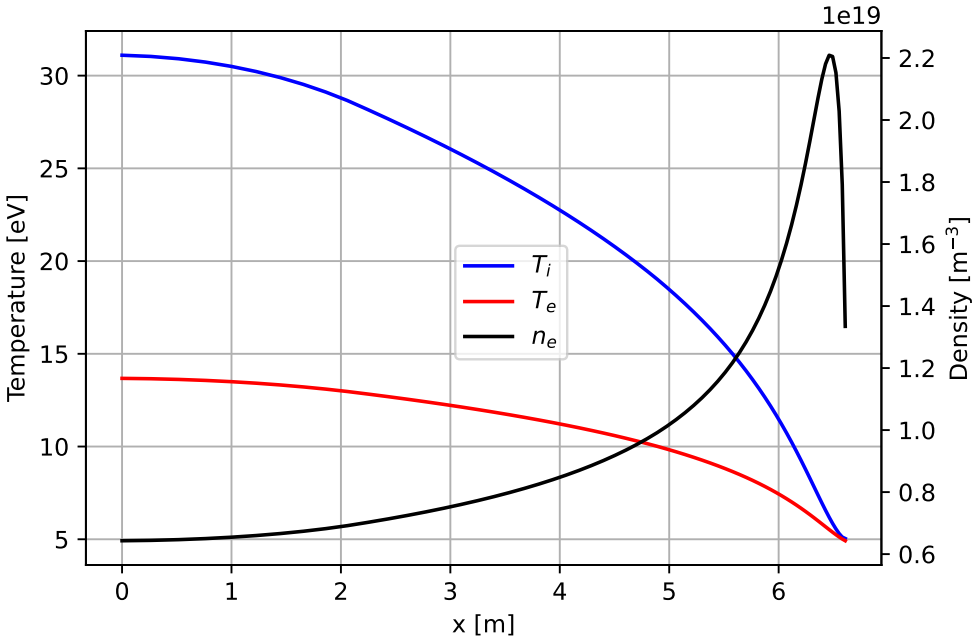

Figure 3.3: Profiles of T_i, T_e and n_e in the simulation described in this section. $x = 0$ is the upstream location, and the target is at $x = 6.7$ m.

perature equilibrates at around twice the electron temperature upstream, but they are nearly thermally equilibrated at the target.

To check for energy conservation, we rearrange the ion energy equation (3.21),

$$\begin{aligned}\frac{\partial W_i}{\partial t} =& \frac{\partial}{\partial t}\left(\frac{3}{2}p_i + \frac{1}{2}m_i n_i u_i^2\right) \\ =& -\frac{\partial}{\partial x}\left(q_i + \left(\frac{5}{2}p_i + \frac{1}{2}m_i n_i u_i^2\right)u_i\right) + e n_i E u_i + Q_i,\end{aligned}$$

where $\frac{\partial W_i}{\partial t} = 0$ at equilibrium. If we integrate this equation along the spatial domain, using the definition of $q_{i,sh}^{tot}$ at the boundary (3.32) and splitting Q_i into its constituent parts (3.23), we should find

$$q_{in} = q_{i,sh}^{tot} - q_i^E - q_i^s - q_i^{ei} - q_i^{cx}, \tag{3.34}$$

where $q_i^E = \int_L e n_i E u_i dx$, $q_i^s = \int_L Q_i^s dx$, $q_i^{ei} = \int_L Q_i^{ei} dx$ and $q_i^{cx} = \int_L Q_i^{cx} dx$. The result is shown in terms of energy flows into and out of the ions in Figure 3.4. There is a small discrepancy in the energy balance here, which has been shown by adding an additional contribution Δq, which is the difference between the left and right hand sides of (3.34). Here, Δq represents an

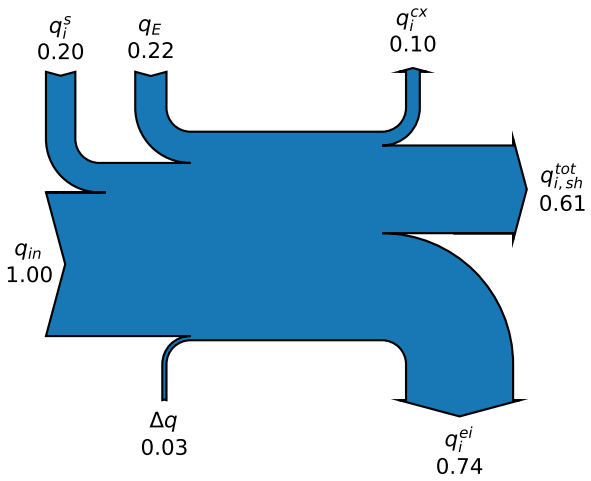

Figure 3.4: Energy flow diagram for the ions. All quantities are in units of MWm^{-3}. The additional quantity Δq is the numerical discrepancy between all energy entering and leaving the system.

additional heating source in the code, since an analysis of the code outputs cannot account for all energy leaving the system.

To understand where the source of this discrepancy lies, we can look at the conservation of intrinsic and kinetic energy separately. Rewriting (3.22) yields a pressure equation,

$$\frac{\partial}{\partial t}\left(\frac{3}{2}p_i\right) = -\frac{\partial}{\partial x}\left(q_i + \frac{5}{2}p_i u_i\right) + u_i\frac{\partial p_i}{\partial x} + \frac{1}{2}m_i u_i^2 S_i - u_i R_i + Q_i \tag{3.35}$$

which we can subtract from (3.21) to get an equation for the kinetic energy,

$$\frac{\partial}{\partial t}\left(\frac{1}{2}m_i n_i u_i^2\right) = -\frac{\partial}{\partial x}\left(\frac{1}{2}m_i n_i u_i^3\right) - u_i\frac{\partial p_i}{\partial x} + e n_i E u_i - \frac{1}{2}m_i u_i^2 S_i + u_i R_i. \tag{3.36}$$

Once again, at equilibrium the left hand sides of these equations are zero and the terms on the right should sum to zero. The spatial profiles of each of these terms is shown in Figure 3.5, where the x-axis is the distance from the sheath boundary and is shown on a log scale in order to highlight detail at the end of the domain. It is clear that the discrepancy is entirely localised to the last few cells.

By varying the grid from 32 cells to 256, we can see in Figure 3.6 how the discrepancy in the energy balance changes. The quantities $\Delta q^{kinetic}$ and $\Delta q^{intrinsic}$ are computed in the same

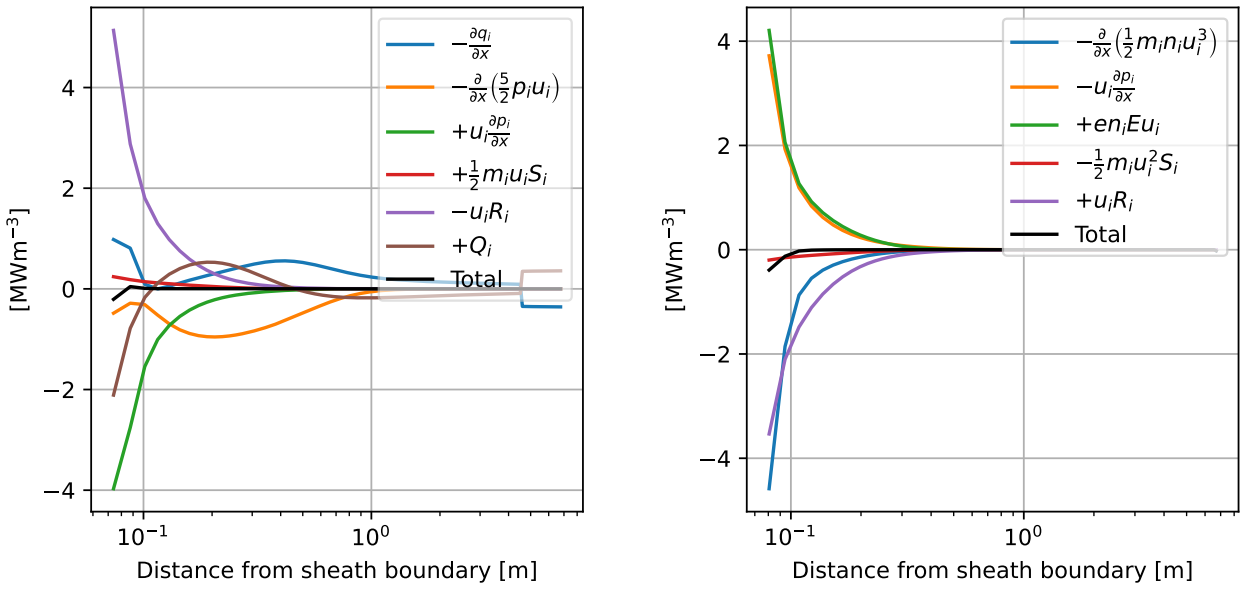

(a) Ion intrinsic energy balance. Spatial profiles of each term in (3.35) are shown.

(b) Ion kinetic energy balance. Each term in (3.36) is shown.

Figure 3.5: Profiles of the terms contributing to the ion intrinsic and kinetic energy balance. Totals are shown in black.

way as for the total energy equation, where $\Delta q = \Delta q^{kinetic} + \Delta q^{intrinsic}$. These are shown as functions of the grid width in the last cell, Δx_N. It can also be seen (dashed lines) how using upwinding in the ion momentum equation adds significant discrepancies in the energy balance.

Figure 3.6 shows that total error in the energy conservation can be kept under $\sim 1\%$ providing sufficient grid resolution is used and upwinding is not used in the ion velocity equation. The remaining discrepancies are likely due to finite grid error, as well as the fact that the equations solved in SOL-KiT are not in conservative form. While they are analytically equivalent, when discretised the equivalence is not exact between the equation for W_i (3.21) and the equations for n_i (3.6), u_i (3.13) and T_i (3.22), and so conservation properties are not necessarily ensured. This is particularly the case in regions with large spatial gradients in plasma parameters, as is found close to the target in 1D SOL simulations.

It should be noted that this discrepancy is found to be smaller in the electron energy balance in SOL-KiT [84]. This is because their total energy is dominated by intrinsic rather than kinetic energy, where it can be seen the latter is a larger contribution to Δq in the ions in Figure 3.6.

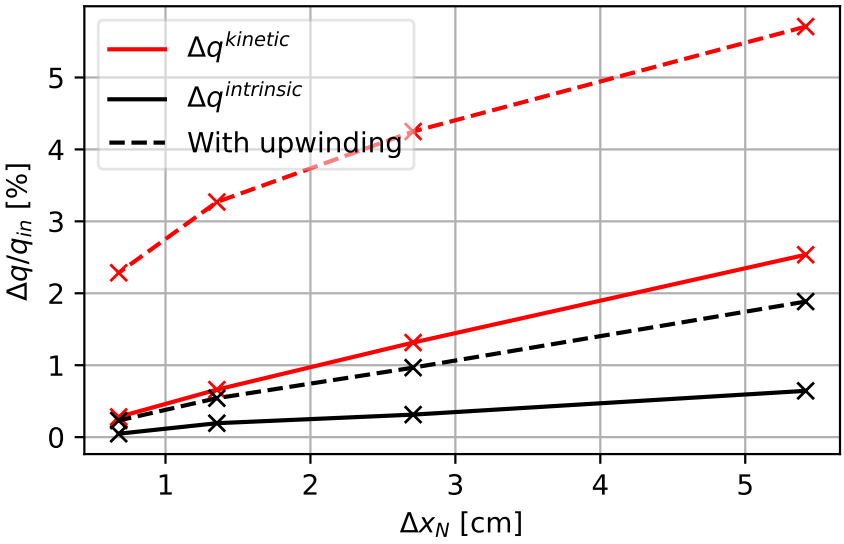

Figure 3.6: Intrinsic and kinetic contributions to Δq as a function of the grid width in the last cell, Δx_N.

3.3 Fluid neutral model

Neutral particles play a key role in the physics of tokamak edge plasmas. In even the most basic SOL models, such as the two-point model, the presence of a source of neutral particles at the walls is a necessary ingredient to making predictions of plasma conditions at the targets. Refinements to the two-point model recognise that the presence of this neutral gas in front of the targets, through which the plasma is flowing, will result in momentum and power losses from the plasma, due to both elastic and inelastic collisional processes.

The diffusive, isothermal neutral model in SOL-KiT aims to capture the dominant aspects of plasma-neutral physics in the SOL. As such, several important collisional and radiative processes are included self-consistently with the plasma model, both kinetically and in fluid mode. However, this model does not account properly for the momentum transfer due to plasma-neutral friction, as it assumes cold, stationary neutrals and the lost plasma momentum leaves the system. A proper treatment of this process will significantly change the neutral profile and therefore the plasma dynamics. The same can also be said for the exchange of energy with the neutrals, which is important for predicting the power balance in the SOL. The loss of momentum and power in plasma-neutral interactions has been shown to play an

important role in detachment onset [90], so treating both accurately is necessary if we wish to study detachment kinetically with SOL-KiT. More generally, the importance of the neutral dynamics in SOL plasmas means a more sophisticated model is required if we want to explore electron kinetics in more reactor-relevant regimes.

Common approaches to neutral modelling in the scrape-off layer adopt a particle-based approach, such as the Monte Carlo neutral codes EIRENE [57] and DEGAS 2 [114]. These are used because typical SOL neutral gases can be highly rarefied and so a fluid model will not necessarily accurately capture their dynamics [115], and because the magnetic field-aligned coordinates used in fluid plasma codes is not appropriate for neutral particles. However, Monte Carlo codes can be computationally demanding, as a large number of particles are needed to be modelled to get accurate statistics. As we are primarily concerned with physics investigations of electron kinetics in SOL-KiT, which is already a computationally expensive task, a fluid neutral model has been developed here. Furthermore, a fluid neutral model sits straightforwardly within the framework of the other fluid equations in SOL-KiT, reducing the development effort and numerical complexity of the code. In this section, we will describe the fluid neutral model which has been implemented in SOL-KiT, with additional equations for the neutral momentum and temperature, followed by a description of some benchmarking tests.

3.3.1 Model

Fluid equations for a monatomic neutral gas can be derived in a similar way to the general fluid plasma equations in equation (2.42), with the key difference that the Lorentz force term does not appear in the kinetic equation for a neutral particle species. If we do this, we arrive at a set of equations involving the neutral density n_n, flow velocity $\mathbf{u_n}$ and temperature T_n,

$$\frac{\partial n_n}{\partial t} + \nabla \cdot (n_n \mathbf{u}_n) = S_n, \tag{3.37a}$$

$$\frac{\partial}{\partial t}(n_n m_n \mathbf{u}_n) + \nabla \cdot (n_n m_n \mathbf{u}_n \mathbf{u}_n) + \nabla p_n + \nabla \cdot \underline{\underline{\boldsymbol{\pi}}}_n = \mathbf{R}_n, \tag{3.37b}$$

$$\tfrac{\partial}{\partial t}\left(\tfrac{3}{2}p_n + \tfrac{1}{2}n_n m_n u_n^2\right) + \nabla \cdot \left[\mathbf{q}_n + \left(\tfrac{5}{2}p_n + \tfrac{1}{2}n_n m_n u_n^2\right)\mathbf{u}_n + \underline{\underline{\boldsymbol{\pi}}}_n \cdot \mathbf{u}_n\right] = Q_n, \tag{3.37c}$$

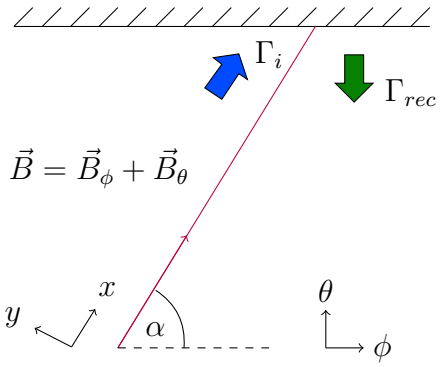

Figure 3.7: Geometry of the quasi-2D treatment of neutral transport described here. An ion flux incident on the walls, Γ_i, returns as a recycled neutral flux, Γ_{rec}, which will not be confined to the magnetic field in the same way.

where S_n, $\mathbf{R}_n$ and Q_n are particle, momentum and energy sources, $p_n = n_n k T_n$ is the isotropic neutral pressure, m_n is the neutral particle mass ($m_n \simeq m_i$ for hydrogenic neutrals), and $\mathbf{q}_n$ is the conductive heat flux.

We could at this point adopt the same approach used when deriving the plasma fluid equations, where we apply these generalised 3D equations to the particular case of 1D SOL modelling, and solve along the direction parallel to the magnetic field lines. However, neutral transport is not confined by the magnetic field in the same way, and transport across field lines cannot be so easily neglected.

So, to capture the neutral dynamics correctly, we should try to account for this cross-field transport in our 1D model. Adopting the same geometry as in the right of the SOL-KiT geometry diagram, Figure 3.1, in Figure 3.7 it is shown how the field lines are pitched at some angle α with respect to the direction parallel to the wall on a 2D flux surface in the SOL, where $\alpha = \tan^{-1}(B_\theta/B_\phi)$ for a magnetic field with poloidal and toroidal component magnitudes B_θ and B_ϕ respectively. The incident plasma ion flux, Γ_i, travels along this direction, but the flux of recycled neutral particles, Γ_{rec}, will not be bound to the field lines in the same way. The x and y axes in Figure 3.7 are defined as parallel and perpendicular to the magnetic field lines respectively. The $x - y$ plane is therefore rotated an angle α with respect to the ϕ, θ axes.

Consider a location in the $x - y$ plane at $r = (0, \Delta y)$; see the red dot in Figure 3.8. We define a new set of axes, x' and y', which are shifted in the toroidal direction such that the

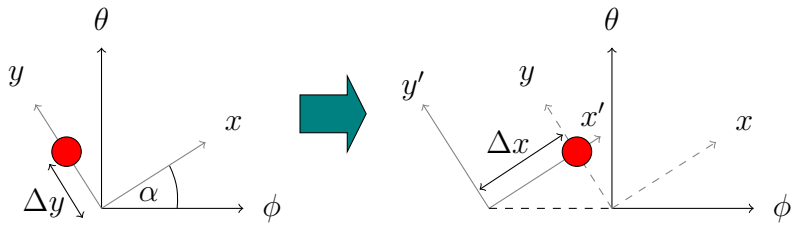

Figure 3.8: Transformation enabling perpendicular transport to be captured as an effective parrallel transport, under the assumption of toroidal symmetry. On the left, the red dot has a y-coordinate but the x-coordinate is zero. On the right, the location of the red dot in the $x' - y'$ plane can be described by an x'-coordinate only.

coordinate in this plane is $r' = (\Delta x, 0)$. Because we assume toroidal symmetry in this model, these coordinates are equivalent. We can therefore eliminate the y coordinate by projecting transport in the perpendicular direction onto the x-axis. For a distance Δy, the resulting $\Delta x = \Delta y / \tan\alpha$.

In the manner described above, we can capture perpendicular transport as an effective parallel transport in a 1D model. Taking the limit of small Δy, we can relate gradients in the parallel and perpendicular directions,

$$\frac{\partial}{\partial y} = \frac{1}{\tan\alpha}\frac{\partial}{\partial x}, \tag{3.38}$$

and therefore, for a velocity $\mathbf{u} = u_\parallel \hat{\mathbf{x}} + u_\perp \hat{\mathbf{y}}$, we can arrive at an effective velocity in the parallel direction,

$$u_{eff} = u_\parallel + \frac{u_\perp}{\tan\alpha}. \tag{3.39}$$

We can now use these two relations, (3.38) and (3.39), along with (3.37), to form a quasi-2D fluid model for the neutral particles (see Appendix B.1 for a full derivation), which features an equation for both the parallel and perpendicular neutral velocities $u_{n\parallel}$ and $u_{n\perp}$,

$$\frac{\partial n_b}{\partial t} = -\frac{\partial (n_b u_{n,eff})}{\partial x} + S_b, \tag{3.40a}$$

$$\frac{\partial u_{n\parallel}}{\partial t} = -u_{n,eff}\frac{\partial u_{n\parallel}}{\partial x} - \frac{1}{m_n n_n}\frac{\partial p_n}{\partial x} - \frac{S_n}{n_n}u_{n\parallel} + \frac{1}{m_n n_n}R_{n\parallel}, \tag{3.40b}$$

$$\frac{\partial u_{n\perp}}{\partial t} = -u_{n,eff}\frac{\partial u_{n\perp}}{\partial x} - \frac{1}{m_n n_n \tan\alpha}\frac{\partial p_n}{\partial x} - \frac{S_n}{n_n}u_{n\perp} + \frac{1}{m_n n_n}R_{n\perp}, \tag{3.40c}$$

$$\frac{\partial kT_n}{\partial t} = -u_{n,eff}\frac{\partial kT_n}{\partial x} + \frac{2}{3}\left[\frac{Q_n}{n_n} - kT_n\frac{\partial u_{n,eff}}{\partial x} - \frac{S_n}{n_n}\left(\frac{3}{2}kT_n - \frac{1}{2}m_n u_{n\parallel}^2\right) - \frac{1}{n_n}\left(1 + \frac{1}{\tan^2\alpha}\right)\frac{\partial q_n}{\partial x} - \frac{u_{n\parallel}R_{n\parallel}}{n_n}\right], \tag{3.40d}$$

where $R_{n\parallel}$ and $R_{n\perp}$ are the momentum source terms in the parallel and perpendicular directions. For the neutral heat flow q_n, we use the expression from Helander et al. [50],

$$q_n = -2.4\left(\frac{n_n T_n}{m_n \nu_{cx}}\right)\frac{\partial T_n}{\partial x}, \tag{3.41}$$

where ν_{cx} is the charge-exchange collision frequency. Note the subscript b on the density and source term in the mass continuity equation (3.40a), which comes from the fact that SOL-KiT solves for the density of each excited state of neutral hydrogen individually, with source terms made up of particle exchange both between neutrals and plasma (ionization and recombination) but also between atomic states (excitation and de-excitation). It would be computationally costly to solve individual velocity and temperature equations for each atomic state, and most probably unnecessary due to the strong coupling between each state via excitation and de-excitation. Therefore, $u_{n\parallel}$, $u_{n\perp}$ and T_n are solved for the entire neutral species using $n_n = \sum_b n_b$ and $S_n = \sum_b S_b$.

It should be noted that there is some similarity in this treatment of cross-field neutral transport in the scrape-off layer with that used in the SD1D code [90], where the parallel neutral transport is enhanced by a diffusive term. Such a model can be obtained by dropping the inertial terms in the $u_{n\perp}$ equation (3.40c); the perpendicular neutral dynamics is then determined by the balance between pressure gradients and friction, $R_{n\perp} = \frac{1}{\tan\alpha}\frac{\partial p_n}{\partial x}$. The neutrals experience a stationary plasma in the perpendicular direction, so $R_{n\perp} \propto u_{n\perp}$. This yields a modified form of (3.40a),

$$\frac{\partial n_b}{\partial t} = -\frac{\partial (n_b u_{n\parallel})}{\partial x} - \frac{1}{\tan^2\alpha}\frac{\partial}{\partial x}\left(D\frac{\partial p_n}{\partial x}\right) + S_b, \tag{3.42}$$

which looks like a typical mass continuity equation for flows in the parallel direction with an additional diffusive term arising from perpendicular transport, with a diffusion coefficient D enhanced by a geometric factor $1/\tan^2\alpha$. This enhanced diffusive factor is equivalent to the factor $\left(\frac{B_\phi}{B_\theta}\right)^2$ reported in [90].

While this neutral model captures the effect of cross-field neutral transport, it is not conservative in momentum or energy when the entire plasma-neutral system is considered, because of the assumption of no perpendicular plasma transport. This means that neutral frictional losses in the perpendicular direction are not transferred to the plasma, and similarly kinetic energy in the perpendicular direction is lost during particle exchange (e.g. ionisation). We could in principle carry out a similar quasi-2D transport treatment for the plasma here as well, but parallel transport is dominant for the plasma species and perpendicular transport depends on unknown transport coefficients.

A final point to mention is that there is of course a third, radial dimension to neutral SOL transport, which has not yet been considered here. A crude method of capturing this additional neutral transport is with a redistribution of the neutral recycling flux, similarly to the method used in DIV1D [91] and SD1D [90]. This has been implemented in SOL-KiT, but is not used in the physics investigations presented later in this thesis. For a redistribution coefficient R_d, a fraction $1-R_d$ of the recycling flux enters at the target, while the remainder is inserted uniformly as a volumetric particle source across the divertor leg, below the X-point. The redistributed neutrals are inserted with zero momentum at a temperature equation to the Franck-Condon dissociation energy, $T_{FC} = 3$ eV.

3.3.2 Source terms

This neutral model entails some new and updated source terms in the SOL-KiT model which need (re)defining.

The redistributed neutrals are added to the ground state, such that there is an additional contribution to S_b for the $b = 1$ equation,

$$S_1 = ... + \Gamma_{redist}/L_{redist} \tag{3.43}$$

where Γ_{redist} is the particle flux of the redistributed neutrals, defined in the section describing the boundary conditions (3.3.4), since it is a function of what is occurring at the target. The

redistribution length is $L_{redist} = L - L_{heating}$, i.e. particles are redistributed uniformly across the divertor leg, beyond the X-point.

The contributions to R_n are from charge exchange collisions between ions and neutrals, R_n^{cx}, and particle sources, R_n^s, so

$$R_{n\parallel} = R_{n\parallel}^{cx} + R_{n\parallel}^{s} \tag{3.44}$$

and

$$R_{n\perp} = R_{n\perp}^{cx} + R_{n\perp}^{s}. \tag{3.45}$$

We neglect the contribution from electron-neutral friction as it is smaller than the friction between heavy particles by $\sim m_e/m_i$. Also, there is no contribution to R_n from neutral redistribution because they are inserted with zero momentum. The energy source term is

$$Q_n = Q_n^{cx} + Q_n^{s}, \tag{3.46}$$

where Q_n^{cx} is the energy transfer in charge exchange collisions with ions and Q_n^s is the contribution from particle sources.

We will now outline the specific form of these terms, starting with charge exchange. The simple model used in SOL-KiT thus far should be extended to account for the finite momentum and temperature of both the ions and neutrals. Here, we use a simplified version of the forms developed by Pauls [116] and Meier [117], where the momentum transfer is derived from the Boltzmann operator for ion-neutral charge exchange collisions. The result is

$$R_{n\parallel}^{cx} = m_i(u_i - u_{n\parallel})S^{cx}, \tag{3.47a}$$

$$R_{n\perp}^{cx} = -m_i u_{n\perp} S^{cx}, \tag{3.47b}$$

where $S^{cx} = \sum_b \sigma_{cx,b}(v_{cx}) n_i n_b v_{cx}$, which is the charge exchange rate per unit volume. The summation is over all neutral excited states tracked, where the charge exchange cross-section for hydrogen used (from Janev [113]) varies with principal quantum number and is a function of the relative velocity of colliding particles. For this, we use a simple form of the characteristic

collision velocity from [117],

$$v_{cx} = \sqrt{\frac{8k}{\pi m_i}(T_i + T_n)}.$$

For the energy transfer, we have

$$Q_n^{cx} = \left(\frac{1}{2}m_i(u_i^2 - u_{n\parallel}^2) + \frac{3}{2}\left(kT_i - kT_n\right)\right) S^{cx}, \tag{3.48}$$

where again a simplified form of the expression from [117] is used.

The terms involving particle sources have a contribution from ionization, where the particle source is S^{ion}, and recombination, with particle source S^{rec}. The friction terms are

$$R_{n\parallel}^s = m_i u_{n\parallel} S^{ion} + m_i u_i S^{rec}, \tag{3.49a}$$

$$R_{n\perp}^s = -m_i u_{n\perp} S^{ion}. \tag{3.49b}$$

For the energy source we have

$$Q_n^s = \left(\frac{1}{2}m_i u_{n\parallel}^2 + \frac{3}{2}kT_n\right) S^{ion} - \left(\frac{1}{2}m_i u_i^2 + \frac{3}{2}kT_i\right) S^{rec} + \frac{3}{2}kT_{FC}\frac{\Gamma_{redist}}{L_{redist}}. \tag{3.50}$$

Note that, as we are now aiming to self-consistently solve for the neutral pressure and momentum, to maintain conservation properties we must update some of the source terms in the ion velocity and temperature equations, described in Sections 3.1.2 and 3.2.1. We update the friction term, $R_i = R_i^{cx} + R_i^s + R_i^{ei}$ which appears in (3.13) and (3.22), with new forms of R_i^{cx} and R_i^s

$$\begin{aligned} R_i^{cx} &= -R_{n\parallel}^{cx}, \\ R_i^s &= -R_{n\parallel}^s \end{aligned} \tag{3.51}$$

using $R_{n\parallel}^{cx}$ from (3.47a) and $R_{n\parallel}^s$ from (3.49a). Similarly, the ion energy source term $Q_i = Q_i^{ext} + Q_i^{cx} + Q_i^s + Q_i^{ei}$, which appears in (3.22), has updated forms of Q_i^{cx} and Q_i^s,

$$\begin{aligned} Q_i^{cx} &= -Q_n^{cx}, \\ Q_i^s &= -Q_n^s \end{aligned} \tag{3.52}$$

using Q_n^{cx} from (3.48) and Q_i^s from (3.50).

In the energy source terms (3.48) and (3.50), we have used $u_{n\|}$ rather than $u_{n,eff}$ for the neutral kinetic energy. The reason for this is that the quasi-2D model described here effectively allows neutral parallel pressure gradients to do excess work on the neutrals via acting on $u_{n\perp}$ as well as $u_{n\|}$. Therefore, some care must be taken to avoid an excessive energy source being introduced in the system in situations where the pitch angle α is small and therefore $u_{n\perp}$ may be large.

3.3.3 Electron collision operators for moving scatterers

With the bulk motion of the neutrals now included in the model, we may ask how the collision operators in the electron kinetic equation will change. Here we outline an approach to accounting for non-stationary scatterers in Boltzmann collisions, although it will subsequently argued that the modification does not justify the additional computational expense.

We start with collisions between electrons and neutrals, where in the centre-of-mass frame the electron distribution is $f(\mathbf{v})$ and the neutral distribution is $F(\mathbf{V}) \simeq n_n\delta(\mathbf{V})$. Electron velocities, again measured in the centre-of-mass frame, before and after the collision are $\mathbf{v}'$ and $\mathbf{v}$, and the scattering angle is χ. The pre- and post-collision neutral velocities are $\mathbf{V}'$ and $\mathbf{V}$. The relationship between $\mathbf{v}'$ and $\mathbf{v}$ depends on the collision process being considered, which we will not specify at this point. The Boltzmann collision integral is therefore

$$\begin{aligned} C_{e,n}d\mathbf{v} &= \int d\Omega' \int d\mathbf{V}' \left(n_n\delta\left(\mathbf{V}'\right) f\left(\mathbf{v}'\right) v'_{rel}\sigma\left(v'_{rel},\chi\right) d\mathbf{v}'\right) \\ &\quad - \int d\Omega \int d\mathbf{V} \left(n_n\delta(\mathbf{V}) f(\mathbf{v}) v_{rel}\sigma\left(v_{rel},\chi\right) d\mathbf{v}\right) \\ &= n_n \left(\int d\Omega' f(\mathbf{v}') v'\sigma(v',\chi) d\mathbf{v}' \right. \\ &\quad \left. - \int d\Omega f(\mathbf{v}) v\sigma(v,\chi) d\mathbf{v} \right), \end{aligned} \tag{3.53}$$

where we have used the fact that $v_{rel} = |\mathbf{V}-\mathbf{v}| \simeq v$ and $d\Omega$ is the solid angle element, integrated over all scattering angles.

The above equation can be decomposed into spherical harmonics to yield the collision operators

implemented in SOL-KiT (Appendix A.2). However, for neutrals which are not stationary the centre-of-mass frame is moving at some velocity $\mathbf{v}_c$ with respect to the lab frame. The electron velocity in the lab frame is therefore

$$\mathbf{v}_l = \mathbf{v} + \mathbf{v}_c \simeq \mathbf{v} + \mathbf{V},$$

where we assume $\mathbf{v}_c$ is dominated by the neutral velocity. To transform (3.53) back to the lab frame, we can Taylor expand $f(\mathbf{v}_l)$,

$$f(\mathbf{v}_l) = f(\mathbf{v} + \mathbf{V}) = f(\mathbf{v}) + \mathbf{V} \cdot \frac{\partial f}{\partial \mathbf{v}} + ...$$

If we truncate this expansion after two terms, then (3.53) becomes

$$\begin{aligned} C_{e,n} d\mathbf{v} =& n_n \left(\int d\Omega' \tilde{f}(\mathbf{v}') v' \sigma(v', \chi) d\mathbf{v}' \right. \\ & \left. - \int d\Omega \tilde{f}(\mathbf{v}) v \sigma(v, \chi) d\mathbf{v} \right), \end{aligned} \tag{3.54}$$

where for a neutral flow velocity $\mathbf{u}_n$,

$$\tilde{f}(\mathbf{v}) = f(\mathbf{v}) + \mathbf{u}_n \cdot \frac{\partial f}{\partial \mathbf{v}}, \tag{3.55}$$

i.e. the operator has the same form as previously, but acts on a shifted version of the electron distribution.

To proceed with the spherical harmonic expansion of this operator, we must expand $\tilde{f}(\mathbf{v})$. We first simplify the analysis by adopting the SOL-KiT assumption of azimuthal symmetry of the distribution function about the x-axis, meaning $\frac{\partial f}{\partial v_y} = \frac{\partial f}{\partial v_z} = 0$ and (3.55) becomes

$$\tilde{f}(\mathbf{v}) = f(\mathbf{v}) + u_n \frac{\partial f(\mathbf{v})}{\partial v_x}.$$

where $\mathbf{u}_n$ is assumed to lie solely along the x-axis. Rewriting this in (azimuthally-symmetric)

spherical coordinates $\mathbf{v} = (v, \theta)$, with θ being the angle from the x-axis, gives

$$\tilde{f} = f + u_n \left(\cos\theta \frac{\partial f}{\partial v} - \frac{\sin\theta}{v} \frac{\partial f}{\partial \theta} \right).$$

The second term here is equivalent in form to the electric field advection term in the 1D kinetic equation (3.1), and can be expanded in the same way using Legendre polynomial recurrence relations, as described in A.1. The result is that

$$\tilde{f}(\mathbf{v}) = \sum_l \tilde{f}_l(v) P_l(\cos\theta) \tag{3.56}$$

with

$$\tilde{f}_l = f_l(v) + u_n \left(\frac{l}{2l+1} G_{l-1} + \frac{l+1}{2l+3} H_{l+1} \right), \tag{3.57}$$

where G_l and H_l are unchanged from before,

$$G_l(v) = v^l \frac{\partial v^{-l} f_l}{\partial v},$$
$$H_l(v) = \frac{1}{v^{l+1}} \frac{\partial v^{l+1} f_l}{\partial v}.$$

Proceeding from this point, the spherical harmonic form of the collision operators for elastic and inelastic processes can be developed in the same way as before (see A.2), but with f_l replaced with $\tilde{f}_l$. For an expansion up to $l = 1$, a similar result is shown in [42].

The procedure outlined here would allow for total momentum conservation in the plasma-neutral model in SOL-KiT, as well as provide the capability to accurately capture the effect of electron-neutral collisions on the electric field. However, the inelastic collisions already represent a computational bottleneck in the code, and the coupling of adjacent harmonics in (3.57) represents a trebling of the number of operations required to evaluate each operator. It is natural therefore to ask whether such a refinement is worth it.

Firstly, the neutral velocity will be small compared to the electron thermal velocity in 1D SOL simulations, being at most approximately equal to the plasma sound speed. This means the correction to f_l, proportional to u_n, will be small. Furthermore, the momentum transfer in

electron-neutral collisions is smaller than between ion-neutral collisions by a ratio $m_e/m_n \simeq m_e/m_i$. Therefore, both the dynamics of the neutrals and the effect of electron friction on the electric field will be dominated by ion-neutral collisions. For these reasons, the correction to electron-neutral collision operators described here is not implemented in SOL-KiT, and the effect of electron-neutral momentum transfer is neglected from the neutral momentum equation.

3.3.4 Boundary conditions

Boundary conditions for a fluid neutral model in the presence of a wall are intrinsically more complex than for the plasma species. This is because there is a surface interaction, some amount of reflection, and a source of recycled ions at the boundary. A simple version is presented here, which has minimal free parameters and which assumes 100% reflection of the neutrals incident on the target, with some loss of energy. A more detailed boundary condition has been implemented, which includes the effect of less than 100% neutral reflection at the target and from which this simpler approach is derived, and this is presented in B.2.

To crudely capture some of the basic physics of cross-field neutral transport, we make use of a redistribution of the recycling flux. This is parameterised by a redistribution coefficient, R_d, where $R_d = 0$ means all recycling occurs at the target. For $R_d > 0$, the recycled ions which do not re-enter at the target are inserted as a volumetric particle source along the portion of the domain beyond the X-point, L_{redist}. Assuming 100% recycling of the ions incident on the target into neutral atoms, which have a particle flux $\Gamma_{i,t}$, the neutral particle flux at the target is then

$$\Gamma_{n,t} = -(1 - R_d)\Gamma_{i,t}, \tag{3.58}$$

and so the redistributed flux is $\Gamma_{redist} = -R_d\Gamma_{i,t}$.

The flow velocity at the target is

$$u_{n,t} = \frac{\Gamma_{n,t}}{n_{n,t}}. \tag{3.59}$$

We can find $n_{n,t}$ by assuming the neutral distribution at the wall is made up of two components: a Maxwellian at the neutral density just in front of the wall, n_n, and a distribution of recycled

neutrals emitted away from the wall at the Franck-Condon dissociation energy, $T_{FC} = 3$ eV. The flow velocity of this recycling distribution is $u_{rec} = -2v_{th}^{FC}(1-R_d)/3$, where $v_{th}^{FC} = \sqrt{2kT_{FC}/m_i}$, and so it has a density $n_{rec} = 3\Gamma_{i,t}/2v_{th}^{FC}$. The target neutral density is then

$$n_{n,t} = n_n + \frac{3\Gamma_{i,t}}{2v_{th}^{FC}}. \tag{3.60}$$

If both $u_{n\parallel}$ and $u_{n\perp}$ are evolved, this boundary condition on the flow velocity is applied to $u_{n,eff}$. The value of $u_{n\parallel}$ at the boundary is then free $\left(\frac{\partial u_{n\parallel}}{\partial x} = 0\right)$ and $u_{n\perp}$ is constrained by $u_{n,eff} = u_{n\parallel} + u_{n\perp}/\tan\alpha$.

The net energy flux of neutrals across the boundary is

$$q_{n,t} = \gamma_n kT_n n_n c_s - (1 - R_d)kT_{FC}\Gamma_{i,t}, \tag{3.61}$$

where $c_s = \sqrt{kT_n/m_i}$ is the neutral sound speed just in front of the wall and $\gamma_n = 0.25$ is a neutral wall heat transmission coefficient. This value assumes that neutrals incident on the wall are reflected back with, on average, 75% of their original energy, which is a reasonable estimate for deuterium neutrals incident on a Tungsten wall at small incidence angle from the TRIM database (`http://www.eirene.de/html/surface_data.html`). We can see that $q_{n,t}$ may be positive or negative depending on the neutral temperature at the wall and the recycling flux.

3.3.5 Benchmarking

Charge exchange friction

To test the updated form of charge exchange friction (3.47a), we perform a 0D simulation where the temperatures of all species are initialised to $T_e = T_i = T_n = 5$ eV, with flow velocities $u_i = -u_{n\parallel} = c_s = \sqrt{k(T_i + T_e)/m_i}$, where only the parallel neutral velocity is evolved. All neutrals are in the ground state, and the densities are equal at $n_i = n_n = 10^{19}$ m^{-3}. To isolate the effect of the friction term, we turn off electron-ion friction and the electric field, and do not evolve the temperature equations. We also do not include ionisation or recombination. The

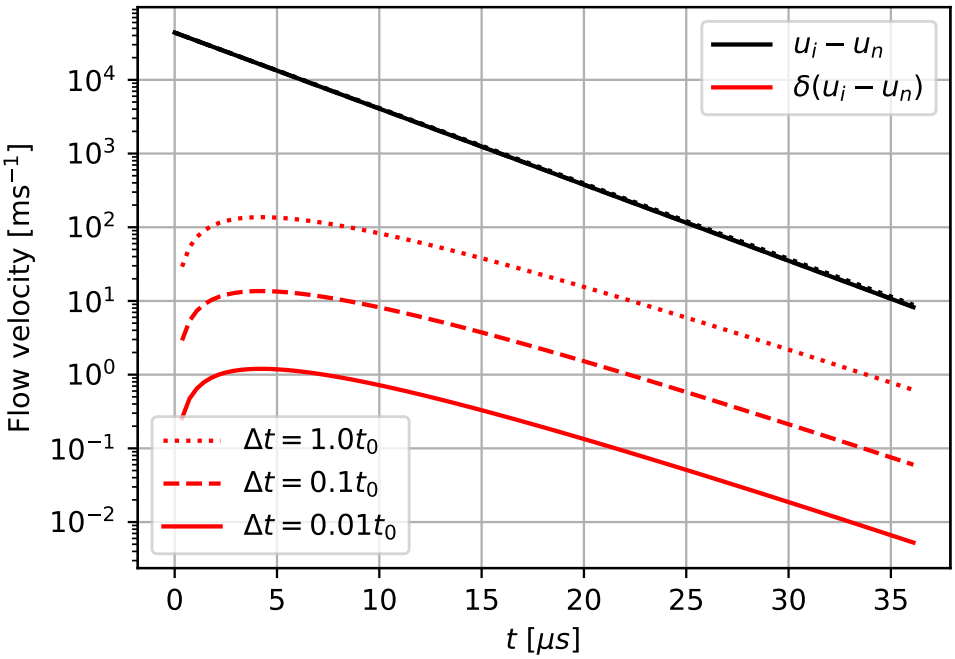

Figure 3.9: Equilibration of ion and neutral flow velocities over time due to charge exchange friction (3.47a). In red the deviation from the analytical solution is shown for three different integrating timesteps.

charge exchange rate and densities are then time-independent, and the analytical solution is

$$\frac{\partial \Delta u}{\partial t} = \Delta u(t_0) \exp(-2S^{cx}\Delta u/n_i)$$

where $\Delta u = u_i - u_n$ and $\Delta u(t_0)$ is the initial value of Δu. The simulation was run for 36 μs with different timesteps, from $\Delta t = 0.01t_0$ to $\Delta t = t_0$, where t_0 is the electron collision time of a reference plasma at 10 eV.

In Figure 3.9, we show the value of $\Delta u = u_i - u_n$ over time along with the deviation from the analytical solution, $\delta(u_i - u_n) = \Delta u^{SOL-KiT} - \Delta u^{analytical}$, for the different timesteps used. We can see that agreement is good, with a maximum error of a few percent at large values of t, when Δu is smallest. Total momentum is conserved to within $10^{-10}\%$ of the initial ion momentum in all simulations.

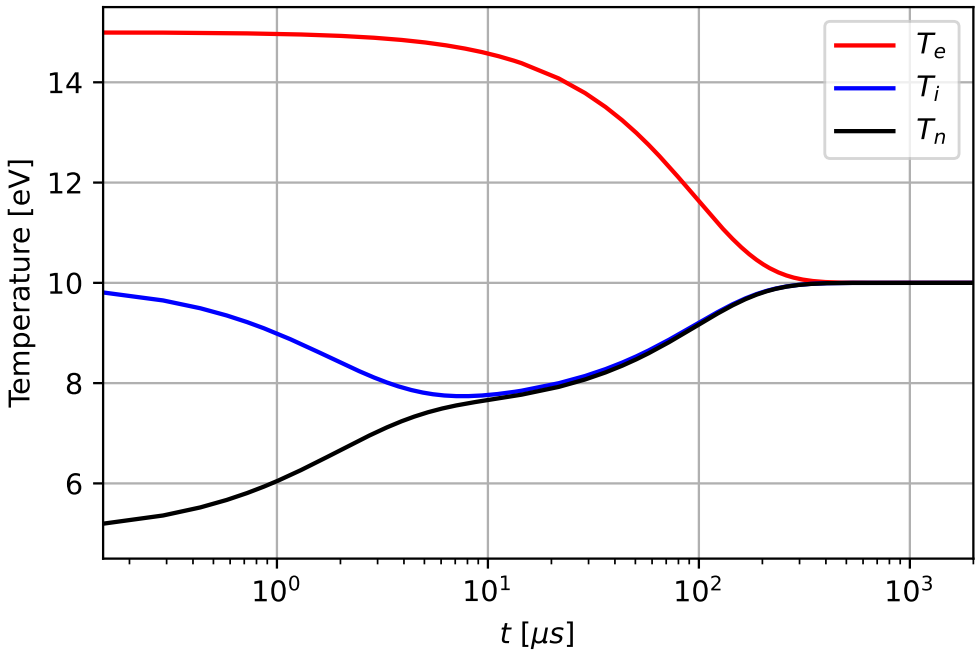

Figure 3.10: Thermal equilibration of electrons, ions and neutral species in SOL-KiT.

Thermal equilibration

In Figure 3.10, we show the thermal equilibration of a 0D simulation where we evolve the (fluid) electron, ion and neutral temperatures from initial values of 15, 10 and 5 eV respectively. There are no flows, the densities are equal at $n_e = n_i = n_n = 10^{19}$ m^{-3}, and only ground state neutrals are evolved.

For these conditions, the charge exchange collision time is $\tau_{cx} \sim 3$ μs, while the ion-electron collision time is $\tau_{ie} \sim 250$ μs, so the observed relaxation rates are as expected. The total plasma plus neutral energy density is conserved in this simulation to within numerical tolerance.

Energy and momentum balance

As in integrated test, we can check that momentum and energy are conserved in the total plasma plus neutral system, focussing on the ions and neutrals as new additions to the model. A 6.7m long SOL was simulated with 256 grid cells, with grid widths ranging from 67.7 cm upstream to 0.7cm at the target. The fluid model for the electrons, ions and neutrals was modelled,

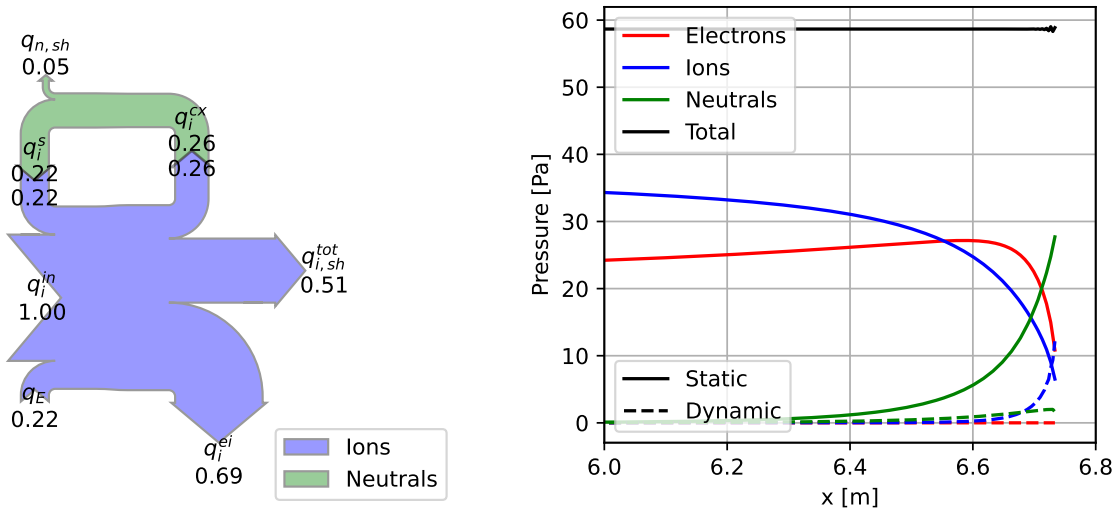

(a) (b)

Figure 3.11: (a): Energy flow diagram for the ion-neutral system in a realistic SOL simulation. All quantities are in MWm^{-2}. (b): Static and dynamic pressure profiles close to the target for electrons, ions and neutrals. Total pressure is shown in black, where a flat spatial profile indicates no numerical momentum sources are present.

assuming no neutral cross-field transport. Only ground state neutrals were included. An input power of $q_{in} = q_i^{in} q_e^{in} = 1\ \mathrm{MWm}^{-2}$ is injected upstream into both the ions and electrons.

In Figure 3.11a, we see the energy flow diagram for the ion-neutral system. It can be seen that total energy is conserved, to within 1.5% of q_{in}. Each energy channel is calculated in the same way as described for the ions in Section 3.2.2, by line-integrating all sources and taking the sheath values for energy transport quantities. The net energy flux across the boundary for the neutrals is the sum of the conductive loss and the input from recycled neutrals at 3 eV, $q_{n,sh}^{tot} = +0.05\ \mathrm{MWm}^{-2}$ here. $q_n^s = -q_i^s$ is the line-integrated energy source from particle sources (ionization and recombination).

In Figure 3.11b, we see the spatial profiles of static and dynamic pressure for each species, along with the total for the plasma-neutral system. There are no external momentum sources in this problem, so the momentum equations for each species should ensure the total pressure is constant throughout the domain. Small grid-scale errors can be seen close to the target, where pressure gradients are strongest. The maximum error is 0.6% of the total pressure.

Cross-field transport

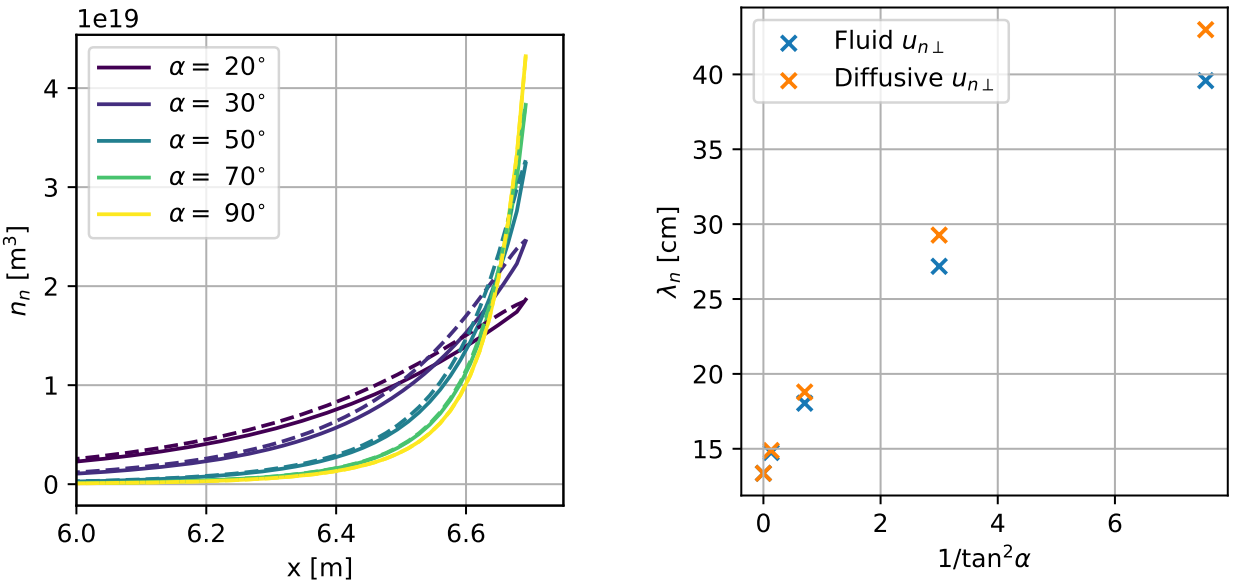

(a) (b)

Figure 3.12: (a): Neutral density profiles close to the wall for different values of the pitch angle α. Solid lines are for the fluid $u_{n\perp}$ model, dashed for the diffusive $u_{n\perp}$ model. (b): Neutral penetration distance, λ_n, as a function of the parameter $1/\tan^2\alpha$.

To verify that the quasi-2D neutral model does lead to enhanced transport upstream, a scan in pitch angle α has been carried out on a simple SOL problem. With 1 MWm^{-2} going into both the ions and the electrons (2 MWm^{-2} total), we solve the electron, ion and neutral fluid models simultaneously. 128 grid cells were used, with grid widths ranging from 13.4 cm upstream to 1.35 cm at the target. For $u_{n\perp}$, both the fluid momentum equation (3.40c) and the diffusive model (3.42) have been tested. Only ground state neutrals were evolved.

In Figure 3.12a, we see the neutral density profiles close to the target, where it can be seen that decreasing the pitch angle from 90° ($\vec{B}$ normal to the wall) to 20° results in a broader neutral cloud. Results for the fluid and diffusive calculations of $u_{n\perp}$ are similar. This can be represented by defining a neutral penetration distance, λ_n, as the distance from the wall over which the neutral density falls to $1/e$ of its value at the target. For the diffusive calculation of $u_{n\perp}$, the factor $1/\tan^2\alpha$ appears in front of the diffusion coefficient, so we would expect λ_n to scale with this parameter; this is shown in Figure 3.12b. The relationship is not linear in part because the neutrals are penetrating further into the hot upstream plasma at lower pitch

angles and so are ionized more readily.

In practice, it has been found that the fluid calculation of $u_{n\perp}$ presents some numerical challenges, where grid-scale oscillations occasionally appear and become unstable. A possible explanation for this is that $u_{n,eff}$ can become unphysically supersonic for small values of α. In these scenarios, a stable solution can be achieved by adding a viscosity term to the parallel neutral momentum equation, which has the form

$$\frac{\partial u_{n\parallel}}{\partial t} = ... - \frac{1}{n_n m_i}(\nabla \cdot \underline{\underline{\boldsymbol{\pi}}}_n)_\parallel = ... + \frac{\partial}{\partial x}\left(\eta_n \frac{\partial u_{n\parallel}}{\partial x}\right), \tag{3.62}$$

where the neutral viscosity arising from charge exchange collisions can be derived via Chapman-Enskog's method [50], $\eta_n = \frac{n_n k T_n}{n_i \sigma_{cx} v_{cx}}$. The corresponding viscous heating term is

$$\frac{\partial k T_n}{\partial t} = ... - \frac{2}{3n_n}(\underline{\underline{\boldsymbol{\pi}}}_n : \nabla \mathbf{u}_n)_\parallel = ... + \frac{2}{3n_n}\eta_n \left(\frac{\partial u_{n\parallel}}{\partial x}\right)^2. \tag{3.63}$$

3.4 Bundled atomic states in SOL-KiT

SOL-KiT models a number N_n of excited neutral states individually, each with a particle source term with contributions from numerous collisional and radiative processes. Calculating these source terms, which means computing the associated electron-neutral collision operators and associated moments, is computationally expensive. In the case of excitation/de-excitation collisions, we have to evaluate $\mathcal{O}(N_n^2)$ collision operators. Given that $N_n \gtrsim 20$ is required to accurately capture experimentally observed reaction rates, the number of collision operators required to be evaluated is $\gtrsim 400$, and so this represents a significant bottleneck in SOL-KiT run times. Therefore, we want to find a way of capturing realistic reaction rates without evaluating the full set of collision operators, by bundling excited states together. We can then solve a reduced number of equations and source terms for the bundle densities.

In developing an approach to bundled atomic states, we are aiming to improve the computational performance of the code without deviating significantly from the predictions made by

the full calculation. In particular, the method should yield similar source terms and impact on the electron distribution as the non-bundled approach.

The primary challenge of bundling is to separate the neutral state dependence in the collision operators from the velocity dependence, so that a single operator can be computed to approximate the effects of collisions across all states within a bundle. Similarly, we wish to extract individual neutral state dependence from all fluid source terms.

The motivation for bundling is twofold. Firstly, an order of magnitude improvement in compute times would facilitate SOL-KiT studies over a larger parameter space, for example in regimes relevant to a range of different tokamak devices. Given the general difficulty of scaling insights into SOL behaviour to future devices, this is hugely useful. Secondly, developing a bundling approach is necessary in order to render simulations of impurity transport with SOL-KiT tractable, due to the significantly more complex atomic physics of elements with high atomic number. As such, the technique outlined here, developed with hydrogenic neutrals in mind, may be seen as a prototype for handling other, more challenging plasma-neutral interactions.

In this section we will outline an approach to bundling collision operators. The method enables bundling of collision operators of the same type, primarily with the aim of reducing the number of excitation and de-excitation operators which are evaluated by the code. A more general but more abstract approach, where the effect of all collisional and radiative processes on the electron distribution are treated with a single 'effective' collision operator, is discussed briefly in Chapter 7. The model described in this section has been implemented in SOL-KiT for hydrogenic neutral atoms, and some benchmark results will be presented.

3.4.1 States and bundles

Atomic states are given subscript j, while bundles are labelled with subscript β. If N_n states are tracked, we group these into a smaller number N_β of bundles.

If we are to avoid solving for the full atomic state distribution of a given atomic species, we

must start with some knowledge of the internal distribution of neutrals within each bundle. We may make some assumption at this point, for example Boltzmann-distributed states, but we will avoid doing so prematurely. For a given neutral state j, which sits within bundle β, we will write the density

$$\frac{n_j}{n_\beta} = \mathcal{N}_\beta^j(...) \tag{3.64}$$

where $\mathcal{N}$ is some function which returns the relative density of state j, which may be specific to each bundle. The ellipses indicate that $\mathcal{N}_\beta^j$ may be a function of other parameters, for example the electron temperature as in the case of Boltzmann-distributed atomic states. The density of the bundle β is $n_\beta = \sum_{j\in\beta} n_j$, such that $\sum_{j\in\beta} \mathcal{N}_\beta^j = 1$.

3.4.2 Bundling of particle and energy sources

Bundling is more straightforward for particle and energy sources than for the collision operators themselves, so this is presented here first for clarity.

We start by considering an electron collisional process such as ionization or excitation. We adopt the same notation as in Section 2.6, where the rate coefficient for the production of particles in state k due to collisions between electrons and particles in state j is written $K_{e,j}^k$. The particle and energy sources from collisions between electrons and atomic states within a given bundle β are therefore

$$S_{e,\beta}^k = -\sum_{j\in\beta} K_{e,j}^k n_j,$$

and

$$Q_{e,\beta}^k = -\sum_{j\in\beta} K_{e,j}^k n_j \varepsilon_j^k,$$

where the minus sign indicates these are loss terms for particles in state j; inverse processes (three-body recombination and de-excitation) would be positive sources for j particles. The reaction rate is defined by taking the σv moment of f_0,

$$K_{e,\beta}^k = 4\pi \int dv v^3 f_0(v) \sigma_{e,j}^k(v),$$

$\sigma^k_{e,j}$ is the cross-section for collisions between electrons and particles in state j to produce particles in state k, and ε^k_j is the transition energy of this process.

We can bundle these terms straightforwardly by employing bundle-averaged quantities, denoted here by $\langle \ldots \rangle$. For the particle source, this is

$$S^k_{e,\beta} = -n_\beta \langle K \rangle^k_{e,\beta} = -n_\beta 4\pi \int dv v^3 f_0(v) \langle \sigma \rangle^k_{e,\beta}, \tag{3.65}$$

where the bundle-averaged cross-section is

$$\langle \sigma \rangle^k_{e,\beta} = \frac{1}{n_\beta} \sum_{j \in \beta} \sigma^k_{e,j} n_j = \sum_{j \in \beta} \sigma^k_{e,j} \mathcal{N}^j_\beta(...). \tag{3.66}$$

The bundled expression for the energy source term is

$$Q^k_{e,\beta} = -n_\beta 4\pi \int dv v^3 f_0(v) \langle \sigma\varepsilon \rangle^k_{e,\beta}, \tag{3.67}$$

where

$$\langle \sigma\varepsilon \rangle^k_{e,\beta} = \frac{1}{n_\beta} \sum_{j \in \beta} \sigma^k_{e,j} \varepsilon^k_j n_j = \sum_{j \in \beta} \sigma^k_{e,j} \varepsilon^k_j \mathcal{N}^j_\beta(...). \tag{3.68}$$

Friction terms cannot be treated with this approach because the momentum moments of collision operators do not reduce to the same simple form in which state and velocity dependence naturally separate. Note also that, while it may appear more straightforward to find some bundle-averaged transition energy $\langle \varepsilon \rangle^k_{e,\beta}$ to calculate $Q^k_{e,\beta}$, this depends on the relative rates for each process within the bundle, which depends on the electron distribution. As it turns out, this is required for evaluating the collision operators anyway (see next section), which also allows us to evaluate terms involving $l > 0$ moments of the collision operators.

3.4.3 Bundling of collision operators

The Boltzmann collision operator for inelastic collisions between electrons and an atomic species, as implemented in SOL-KiT (see A.2 for more details), is

$$(C_l)^k_{e,j} = -n_j v \left\{ \sigma^{tot}(v) f_l(v) - f_l(\alpha v)\alpha^2 \left(\sigma^{tot}(\alpha v) - \sigma^{(l)}(\alpha v) \right) \right\}, \tag{3.69}$$

where f_l is the electron distribution for the l^{th} harmonic and $\alpha = v'/v$, where the post-collision velocity is $v' = v(1 + 2\varepsilon^k_j/m_e v^2)^{1/2}$. We have dropped the subscript and superscript on $\sigma^k_{e,j}$ here to avoid the notation becoming overly cumbersome. The integral cross-section is defined $\sigma^{tot} = \int d\Omega \sigma(\chi, v)$, and $\sigma^{(l)} = \int d\Omega \left(1 - P_l(\cos\chi)\right) \sigma(\chi, v)$.

Bundling this collision operator is more challenging due to the evaluation of f_l and σ at αv, which makes extraction of the atomic state dependence less trivial because α is a function of the transition energy, ε^k_j. The two quantities needed to bundle (3.69) are the bundle-averaged cross-section, $\langle\sigma\rangle^k_{e,\beta}$, and the bundle-averaged transition energy, $\langle\varepsilon\rangle^k_{e,\beta}$.

$\langle\sigma\rangle^k_{e,\beta}$ is given by equation (3.66), while for $\langle\varepsilon\rangle^k_{e,\beta}$ we can use the fact that there exists a transition energy for which $Q^k_{e,\beta} = S^k_{e,\beta}\langle\varepsilon\rangle^k_{e,\beta}$. Rearranging and making use of equation (3.68) gives

$$\langle\varepsilon\rangle^k_{e,\beta} = \frac{Q^k_{e,\beta}}{S^k_{e,\beta}} = \frac{\int dv v^3 f_0(v) \langle\sigma\varepsilon\rangle^k_{e,\beta}}{\int dv v^3 f_0(v) \langle\sigma\rangle^k_{e,\beta}}. \tag{3.70}$$

These two quantities can be used to evaluate a single collision operator for each collisional process, identical in form to the original collision operator, which will yield the same energy and particle sources as the non-bundled approach, assuming the neutral distribution is the same. For excitation/de-excitation between bundles, we must sum over the states in the final bundle β', to get

$$\langle\sigma\rangle^{\beta'}_{e,\beta} = \sum_{k\in\beta'} \langle\sigma\rangle^k_{e,\beta}, \tag{3.71}$$

and

$$\langle\varepsilon\rangle^{\beta'}_{e,\beta} = \frac{Q^{\beta'}_{e,\beta}}{S^{\beta'}_{e,\beta}} = \frac{\sum_{k\in\beta'} Q^k_{e,\beta}}{\sum_{k\in\beta'} S^k_{e,\beta}}. \tag{3.72}$$

At this point, we have not yet provided a method for reducing the computational load of evaluating the collision operators because we still have to sum over all initial and final states to find the bundle-averaged quantities. This is achieved by pre-computing the values of $\langle\sigma\rangle$ and $\langle\varepsilon\rangle$ for each process and for each bundle, where we make some assumption on $\mathcal{N}$ and f_0. This is discussed in Section 3.4.6.

3.4.4 Effect of inelastic collisions within bundles

An important step is to capture the effect of inelastic collisions within bundles: if we were to reduce the full set of collision operators to a smaller set involving bundle-averaged transitions between bundles, using the method outlined in the previous section, the particle source from excitation and de-excitation collisions would cancel and we cannot estimate $\langle\varepsilon\rangle^{\beta'}_{e,\beta}$ for $\beta = \beta'$. To handle this, we can recognise that the steady-state behaviour is for radiative de-excitation to push the neutrals out of thermal equilibrium with the electrons, and energy must be taken from the electrons via the excitation collisions to maintain this state. This means

$$Q^{\beta}_{e,\beta} = Q^{rad-deex}_{\beta}, \tag{3.73}$$

where $Q^{rad-deex}_{\beta}$ is the loss of atomic energy of the neutrals due to radiative de-excitation,

$$Q^{rad-deex}_{\beta} = -n_\beta \sum_{j>k} A^k_j \varepsilon^k_j \mathcal{N}^j_\beta(...),$$

for $j, k \in \beta$, and where A^k_j is the spontaneous emission rate from j to k. We then evaluate $\langle\sigma\rangle^{\beta}_{e,\beta}$ and $S^{\beta}_{e,\beta}$ using excitation collisions only,

$$\langle\sigma\rangle^{\beta}_{e,\beta} = \sum_{j<k} \sigma^k_{e,j} \mathcal{N}^j_\beta(...) \tag{3.74}$$

and

$$S^{\beta}_{e,\beta} = -n_\beta 4\pi \int dv v^3 f_0(v) \langle\sigma\rangle^{\beta}_{e,\beta}, \tag{3.75}$$

which we can then use to calculate $\langle\varepsilon\rangle^{\beta}_{e,\beta} = Q^{rad-deex}_{\beta}/S^{\beta}_{e,\beta}$, similarly to (3.72).

3.4.5 Other processes

The general approach outlined here for electron collisional processes can be applied to the other atomic processes treated in SOL-KiT which do not involve electrons, namely charge exchange, radiative de-excitation (between bundles) and radiative recombination.

For radiative de-excitation, we only need a bundled particle source. This is

$$S_{\beta}^{\beta'} = -n_{\beta} \sum_{k \in \beta'} \sum_{j \in \beta} A_j^k \mathcal{N}_{\beta}^j(...) \tag{3.76}$$

for $k < j$.

For radiative recombination, we have

$$S_{rad-rec}^{\beta} = \sum_{j \in \beta} n_e n_i \alpha^j(T_e), \tag{3.77}$$

where α^j is the rate coefficient for radiative recombination into state j, which is a function of the electron temperature.

Finally, for charge exchange we just need to compute the particle source S^{cx}, which then enters the friction and energy sources as described in the section on the fluid neutral model source terms, 3.3.2. The result is

$$S^{cx} = \sum_{\beta} n_{\beta} \sum_{j \in \beta} \sigma_{cx,j}(v_{cx}) n_i v_{cx} \mathcal{N}_{\beta}^j(...), \tag{3.78}$$

where the first sum is over all bundles.

3.4.6 Implementation

We can now discuss the implementation of this approach to bundling of atomic hydrogen in SOL-KiT. Each state represents atoms with a given principal quantum number, from the ground state up to N_n, where the state index j also refers to the principal quantum number.

For simplicity, we assume the neutrals are Boltzmann-distributed within each bundle, which allows us to relate the densities of state j and some other state with lower energy j_c (which will be specified shortly),

$$\frac{n_j}{n_{j_c}} = \frac{g_j}{g_{j_c}} e^{-\varepsilon^j_{j_c}/kT_e},$$

where g_j is the statistical weight of state j, which for hydrogen is $g_j = 2j^2$. The transition energies for hydrogen are $\varepsilon^j_{j_c} = \varepsilon_j - \varepsilon_{j_c} = -13.6\left(\frac{1}{j^2} - \frac{1}{j_c{}^2}\right)$ eV. If j_c is the lowest-energy state within the bundle β, then we can use the fact that $\sum_{j\in\beta} \mathcal{N}^j_\beta(...) = 1$ to define

$$\mathcal{N}^j_\beta(...) = \mathcal{N}^j_\beta(T_e) = \frac{g_j e^{-\varepsilon^j_{j_c}/kT_e}}{\sum_{j\in\beta} g_j e^{-\varepsilon^j_{j_c}/kT_e}}, \tag{3.79}$$

where the relative density of a state within a bundle is now a function of the electron temperature as well as the state index.

We may now decide how to divide up the modelled atomic states into bundles. The use of Boltzmann-distributed neutrals within bundles suggests that a logical approach is with a closure, where lower states are modelled in full and all states equal to or greater than j_c are placed into a single bundle. This captures the fact that atomic states with high principal quantum number are expected to be more collisionally coupled to the electrons than lower states, and hence the Boltzmann-distribution is a more accurate description. The number of collision operators which need to be evaluated is then proportional to $\sim j_c^2$.

For the calculation of $\langle\varepsilon\rangle^{\beta'}_{e,\beta}$ (3.72) we need to estimate f_0. Since most inelastic processes for hydrogen atoms have transition energies well below 10 eV, which is approximately at or lower than the expected electron temperature close to the walls in scrape-off layer plasmas, these collisions will be sampling a highly collisional part of the electron distribution. We may therefore assume f_0 is Maxwellian at T_e and some reference density. This density will cancel (see (3.70)) and so $\langle\varepsilon\rangle^{\beta'}_{e,\beta}$ is also only a function of the electron temperature.

For a number N_β bundles, for each electron collisional process (ionization, three-body recombination, excitation and de-excitation) we pre-compute the values of $\langle\sigma\rangle^{\beta'}_{e,\beta}$ and $\langle\varepsilon\rangle^{\beta'}_{e,\beta}$ for a range of electron temperatures. We use 50 values of T_e, from 0.1 to 250 eV, on a geometrically-

spaced grid. A linear interpolation is then used at runtime to get the required local values at each spatial grid cell. For the other processes considered (radiative recombination, radiative de-excitation and charge exchange), we do the same for the particle sources.

The conservative implementation of inelastic collisions in SOL-KiT requires pre-computing a set of grid weights, W_{nm}, which determine the contribution of the emission in velocity space from a cell m to an absorption in cell n (see [4] for details). These weights are a function of the transition energy, $W_{nm} = W_{nm}(\varepsilon)$, and so for a given set of collisional atomic processes which are to be modelled it is possible to compute the full set of weights required at initialisation for each unique value of ε. However, in the approach to bundling outlined here, the bundle-averaged transition energy for each process is now a function of the electron temperature and therefore evolves in time and varies spatially. To resolve this, we pre-compute a set of weights on a mirrored geometric grid from $\varepsilon = 10^{-4}$ eV to ± 13.6 eV. At runtime, we then find the nearest value on this transition energy grid, which we label $\hat{\varepsilon}$, to the local value of $\langle\varepsilon\rangle_{e,\beta}^{\beta'}$, given by (3.72), and use those grid weights. It is then necessary to scale the reaction rate accordingly, which we do by multiplying the cross-section by $\langle\varepsilon\rangle_{e,\beta}^{\beta'}/\hat{\varepsilon}$.

3.4.7 Benchmarking

The aim of this benchmarking section is to answer two questions of the bundling method outlined above. Firstly, is it accurate? And secondly, is it fast?

Detailed balance

To test the source terms and electron collision operators, we confirm that detailed balance can be achieved for the bundled neutral states. In a 0D system, we initialise a fully ionized plasma to $T_e = 3$ eV and $n_e = 2.0 \times 10^{19}$ m^{-3}. The neutral state/bundle densities are evolved until equilibrium is reached for $j_c = 2$, where all states greater than or equal to j_c are bundled together. The maximum principal quantum number of the modelled states was $N_n = 30$. Electrons were treated kinetically, and all collisional processes involving electrons (ionization,

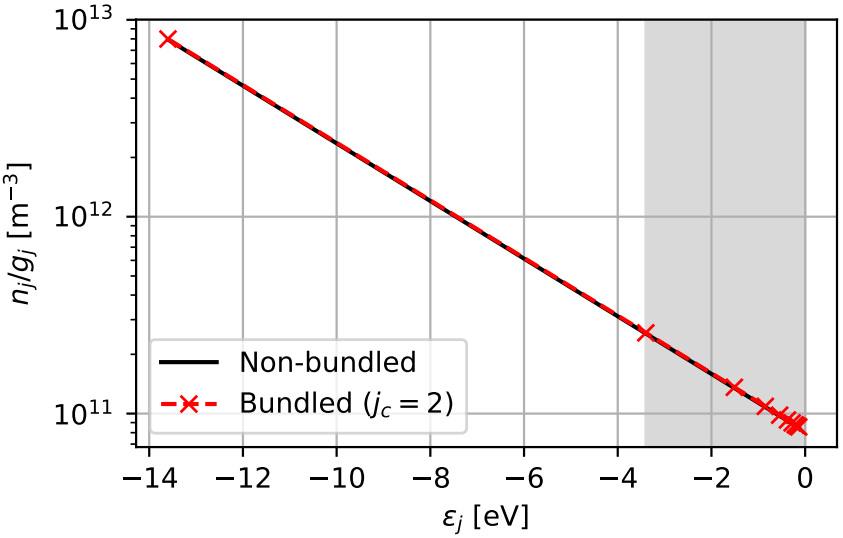

Figure 3.13: Atomic state densities of neutral hydrogen, normalised to the statistical weight g_j. The case of bundled neutrals from $j_c = 2$ up to $j = 30$ is shown in red, and compared with a simulation without bundling. The x-axis is the ionization energy of each state, where the shaded grey region highlights the bundled part of the distribution.

three-body recombination, excitation and de-excitation) were turned on.

Given that all neutrals above the cut-off are assumed to be Boltzmann-distributed, and radiative processes were not included in this test, we should achieve a Saha-Boltzmann distribution. This means all neutral states (both above and below j_c) will be Boltzmann-distributed, and for any value of j_c the electron density is expected to be

$$\frac{n_e^2}{n_{tot} - n_e} = \frac{2}{\lambda^3} \frac{e^{-I/kT_e}}{\sum_j g_j e^{-(I-\varepsilon_j)/kT_e}}, \tag{3.80}$$

where $n_{tot} = n_e + \sum_j n_j$, λ is the electron de Broglie wavelength, $\lambda = \sqrt{\frac{h^2}{2\pi m_e kT_e}}$, h being Planck's constant, $I = 13.6$ eV is the ionization energy for hydrogen and ε_j is the energy of state j, $\varepsilon_j = I/j^2$. For bundled atomic states, we can recover the individual densities from n_β (which is what is actually evolved), using the definition of $\mathcal{N}_\beta^j(T_e)$ from (3.79).

The atomic state distribution is shown in Figure 3.13, and compared to the case without bundling. The bundled part of the distribution is shaded grey. There is good agreement in the densities of states both above and below j_c, with a maximum relative error of 0.8 %.

The expected ionization degree, $X = n_e/n_{tot}$, can be calculated from (3.80). The relative error between this and the ionization degree observed in the simulation with bundling is 1.4×10^{-6} %. The source of this error is the linear interpolation of bundled-averaged quantities ($\langle\sigma\rangle$, $\langle\varepsilon\rangle$, etc) for the local value of T_e. If we double the number of precomputed values for these quantities, this error in ionization degree reduces by around an order of magnitude. For reference, the error in ionization degree for the case without bundling is 1.3×10^{-8} %.

Similar performance was seen in fluid mode, where a number of different values of j_c were tested and no dependence of the error in the ionization degree on j_c was observed.

Integrated test

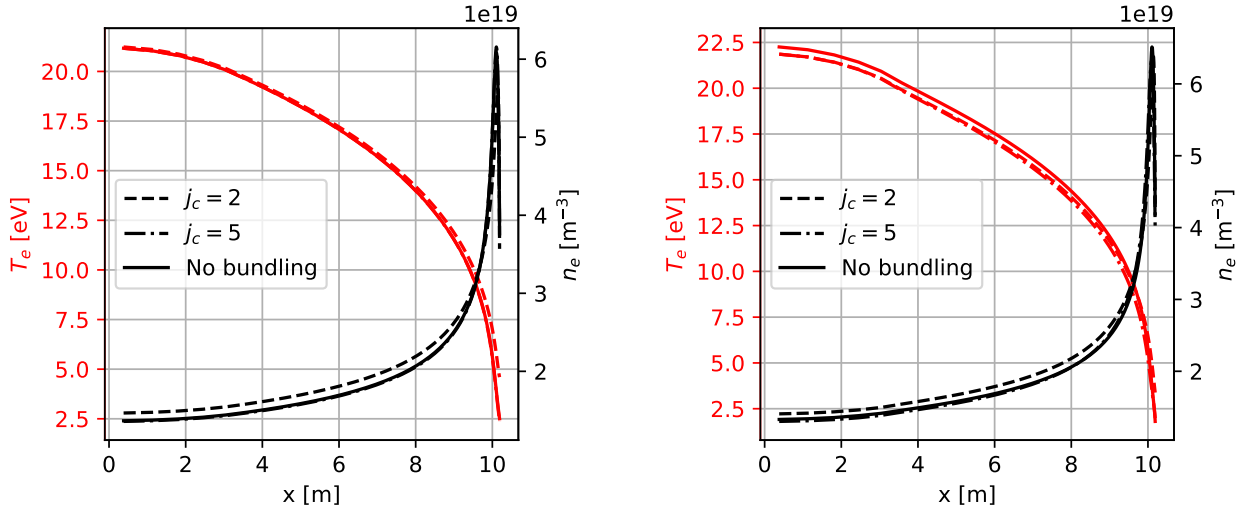

(a) Fluid electrons

(b) Kinetic electrons

Figure 3.14: Electron temperature (red) and density (black) profiles for simulations with bundling for $j_c = 2$, $j_c = 5$, and without bundling.

We now compare the effect of bundling in an integrated SOL test. For both fluid and kinetic electrons, we model a 10.19 m scrape-off layer with 64 spatial grid cells, spaced logarithmically with grid widths ranging from 0.76 m upstream to 0.50 cm at the target. No ion temperature equation was evolved, and the diffusive neutral model was used. The input power to the electrons was $q_{in} = 4$ MWm^{-2}. The velocity grid consisted of 80 cells, with grid widths ranging from $\Delta v = 0.05 v_{th,0}$ to $0.35 v_{th,0}$ and total length $12.2 v_{th,0}$, where $v_{th,0}$ is the electron thermal velocity of a reference plasma at $T_e = 10$ eV. In kinetic mode, the highest resolved harmonic was

$l_{max} = 1$. The line-averaged density was 2×10^{19} m^{-3}. All electron-neutral inelastic collisional processes were turned on. 30 neutral states were included in the model; with no bundling, all 30 states are evolved directly. The temperature and density were initialised to 2PM profiles, and allowed to evolve until equilibrium was reached.

	$T_{e,t}$ [eV]	
	Fluid	Kinetic
$j_c = 2$	4.60	3.38
$j_c = 5$	2.37	1.98
No bundling	2.50	1.81

Table 3.1: Target temperatures for simulations with and without bundling, with both fluid and kinetic electrons.

Temperature and density profiles for $j_c = 2$ and $j_c = 5$ are shown in Figure 3.14, and compared to simulations without bundling. The target electron temperatures are shown in Table 3.1. Agreement is good for $j_c = 5$, although the differences are larger in kinetic mode. This is expected due to the assumption of Maxwellian f_0 in pre-computing the bundle-averaged quantities, meaning kinetic effects in electron-neutral collisions may be underestimated.

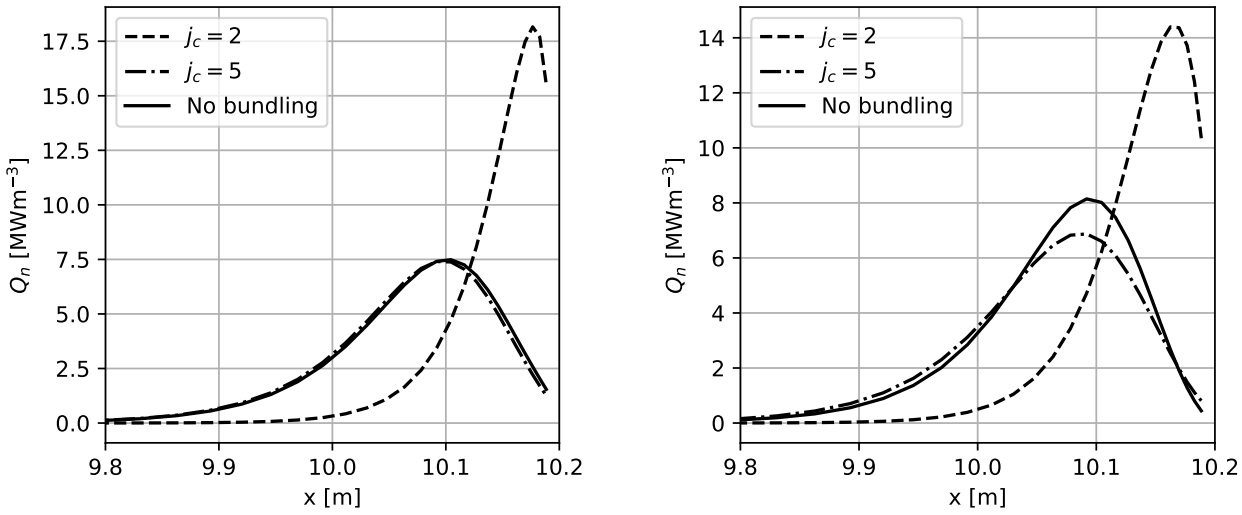

(a) Fluid electrons

(b) Kinetic electrons

Figure 3.15: Spatial profiles of the electron energy given to neutrals, Q_n, close to the target.

In Figure 3.15, we show spatial profiles of the net electron energy loss to neutrals Q_n, defined as the sum of the energy moment of all electron-neutral collision operators minus the neutral radiated energy. It is clear that, despite reasonable agreement in the T_e and n_e profiles for

bundling with $j_c = 2$, this is inadequate for capturing the total energy loss due to electron-neutral collisions and a higher value of j_c is necessary.

Computational speed-up

To estimate the computational savings from this bundling method, we initialise a scrape-off layer simulation to two-point model profiles for the density and temperature, with $n_u = 1.5 \times 10^{19}$ m^{-3}, $T_u = 18$ eV and $T_t = 5$ eV. Both fluid and kinetic electron models are compared, the ion temperature is not evolved and the neutrals are diffusive. In kinetic mode, the maximum harmonic evolved was $l_{max} = 1$. All atomic processes are turned on. 30 neutral states were included. There are 64 spatial grid cells, and 80 velocity grid cells. We run SOL-KiT for 100 timesteps for a simulation time of 0.77 μs, varying j_c and comparing the run time to the non-bundled approach. All simulations were run with 4 parallel processes on an Intel i9 CPU.

j_c	Fluid run time	Kinetic run time
No bundling	5:23	35:54
15	0:14	5:38
10	0:08	4:36
8	0:07	3:53
5	0:04	3:08
2	0:03	3:03

Table 3.2: Computational run time (minutes:seconds) for fluid and kinetic SOL simulations with different values of the cut-off state index, j_c, using the bundling method outlined in the text.

The results are shown in Table 3.2. We can see that even a relatively high cut-off of $j_c = 15$ provides significant speed improvements, and that the advantages plateau around $j_c = 5$. Speed-ups are greater in fluid mode, highlighting the contribution of other terms in the kinetic equation to the total run time.

The large drop from the no bundling cases to $j_c = 15$ arises due to the fact that cross-sections for inverse processes, de-excitation and three-body recombination, are functions of T_e. With bundling on, they are pre-computed at different values of T_e and the local value is linearly interpolated at each timestep. Without bundling, these cross-sections are re-computed using

analytical formulae at each spatial cell for each timestep, which proves to be a more costly procedure.

Combined with the integrated test results in the previous section, a value of $j_c = 5$ provides a good balance between speed and accuracy, so this has been used for the simulations which use bundling in Chapters 5 and 6.

3.5 Collisional radiative model for SOL impurities

The final piece of development work which will be discussed in this chapter is a relatively simple collisional radiative model which has been developed to investigate the effect of non-Maxwellian electron distributions on reaction rates for SOL impurities. The motivation here lies in the fact that electron distributions with strongly enhanced high-energy tails, as are often seen in kinetic simulations of SOL plasmas, may lead to significantly different reaction rates for inelastic collisions with impurity species. These impurity species may come from physical sputtering, in which case we would consider species such as carbon, tungsten or beryllium, or they may be injected deliberately in order to cool the edge region by radiating away plasma energy, in which case some typical species considered are nitrogen, neon and argon. For the latter category of impurities, the impurity concentration is an important control parameter for tokamak operators, and it is strongly linked with the overall device performance. The balancing act of impurity seeding involves cooling the edge plasma sufficiently to ensure target heat loads are low, but not so much that impurities can reach the core plasm. If they do reach the core, they can become highly ionized and radiate away significant energy, degrading the energy confinement of the tokamak. Both the cooling effect of impurities and their transport is largely determined by atomic physics, in particular excitation and ionisation rates, and so modelling these processes accurately is important for future tokamak design and operation.

The starting point for such an investigation is to first determine whether a kinetic treatment is worth doing. The assumption of Maxwellian-averaged reaction rates is ubiquitous in SOL atomic physics databases, in large part because it makes the problem tractable. The number of

atomic states required for an accurate treatment of typical SOL impurities is in the thousands, so a self-consistent treatment, where the electron distribution is solved alongside the atomic population kinetics, is much more computationally expensive. To relax the assumption of Maxwellian electrons will require the development of techniques to overcome this problem (see discussion in Chapter 7), but first we will investigate how predictions of impurity atomic physics differ between Maxwellian and non-Maxwellian electrons assuming they are a fixed background, i.e. whether there is a kinetic effect worth exploring further. To this end, a method of solving the system of atomic state density equations for SOL-relevant impurities has been developed, called SIKE (Scrape-off layer Impurities with Kinetic Electrons), and is described in this section.

The full code and atomic data for SIKE is available on Github, `https://github.com/ImperialCollegeLondon/SIKE`. It is written in Python, and makes use of the petsc4py module which provides access to the PETSc suite of matrix solver routines [118].

3.5.1 SIKE model

The model used in SIKE very closely follows that described in Section 2.6, with the relevant parts repeated here in condensed form.

For a given impurity species, we solve the density evolution equations for each tracked atomic level, assuming no transport or external sources/sinks. For an atomic state k, with a given ionization level and electronic configuration, the density evolves according to

$$\frac{dn_k}{dt} = n_e \sum_j n_j K^k_{e,j} + \sum_j A^k_j n_j - n_k n_e \sum_j K^j_{e,k} - n_k \sum_j A^j_k + n_e \sum_j r^k_j n_j - n_e n_k \sum_j r^j_k, \quad (3.81)$$

where $K^k_{e,j}$ is the rate coefficient for the production of particles in some state k due to collisions with electrons and particles in state j (ionization, three-body recombination, excitation and de-excitation), A^k_j is the radiative transition rate from state j to k (which includes spontaneous de-excitation and auto-ionization), r^k_j is the radiative recombination rate from j to k, and n_e is the electron density. The collisional rates are calculated by integrating over the isotropic part

of the electron distribution, f_0,

$$K^k_{e,j} = \frac{4\pi}{n_e}\int_0^\infty v^2(v\sigma^k_{e,j}(v))f_0(v)dv. \tag{3.82}$$

As such, the inputs to the code are either a set of f_0 distributions, defined on a given spatial and velocity grid, or spatial profiles of electron temperature and density, in which case Maxwellian electrons are assumed. If distribution functions are provided, the equations are solved for both the provided values of f_0 and Maxwellians at the same temperature and density.

The system of equations defined by (3.81) for all k is written in matrix form,

$$\frac{d\mathbf{n}}{dt} = \mathbf{M}\mathbf{n}, \tag{3.83}$$

where $\mathbf{n}$ is the vector containing all n_k, and the rate matrix $\mathbf{M}$ is filled according to

$$M_{jk} = n_e K^j_{e,k} + A^j_k + n_e r^j_k, \qquad k > j \tag{3.84}$$

$$M_{jk} = n_e K^j_{e,k}, \qquad k < j \tag{3.85}$$

$$M_{jj} = -\sum_{k\neq j} M_{kj}. \tag{3.86}$$

We may solve for equilibrium state densities by either evolving (3.83) using implicit time integration, or by solving the matrix equation directly for $\frac{d\mathbf{n}}{dt} = 0$. In the latter approach, an additional equation specifying the total impurity density is be added to (3.83),

$$n^{tot}_{imp} = \sum_k n_k, \tag{3.87}$$

which simply adds a row of ones to $\mathbf{M}$, and means we can solve via

$$\mathbf{n} = \mathbf{M}^{-1}\mathbf{A}, \tag{3.88}$$

where

$$\mathbf{A} = \begin{bmatrix} \frac{d\mathbf{n}}{dt} \\ n_{imp}^{tot} \end{bmatrix} = \begin{bmatrix} 0 \\ n_{imp}^{tot} \end{bmatrix}. \tag{3.89}$$

This is equivalent to finding the null space of $\mathbf{M}$, and then applying the constraint given by (3.87).

It is useful to compute the effective particle source terms, for example for recombination from one ionization stage of the impurity species to another, which is a complex function of multi-step collisional and radiative processes involving many atomic levels. We compute these in the manner described in Section 2.6. Dividing the impurity atomic states into P states and Q states, where the time derivatives of Q states are zero, allows us to re-write (3.83),

$$\frac{d}{dt}\begin{bmatrix} \mathbf{n}_P \\ \mathbf{n}_Q \end{bmatrix} = \begin{bmatrix} \mathbf{M}_{PP} & \mathbf{M}_{PQ} \\ \mathbf{M}_{QP} & \mathbf{M}_{QQ} \end{bmatrix} \begin{bmatrix} \mathbf{n}_P \\ \mathbf{n}_Q \end{bmatrix} = \begin{bmatrix} \frac{d\mathbf{n}_P}{dt} \\ 0 \end{bmatrix} \tag{3.90}$$

and so

$$\frac{d\mathbf{n}_P}{dt} = \mathbf{M}_{\text{eff}}\mathbf{n}_P, \tag{3.91}$$

where

$$\mathbf{M}_{\text{eff}} = \mathbf{M}_{PP} - \mathbf{M}_{PQ}\mathbf{M}_{QQ}^{-1}\mathbf{M}_{QP}. \tag{3.92}$$

We may choose arbitrarily which states belong in the P subset. A useful choice is the ground states of each ionization stage of the impurity species, in which case the lower off-diagonal elements of $\mathbf{M}_{\text{eff}}$ are the effective ionization coefficients, and the upper off-diagonal elements are the effective recombination coefficients. It should be noted that, if we evolve (3.91) in time, we will arrive at the same equilibrium as solving the larger set of equations in (3.83), where the densities of the Q states can be extracted via

$$\mathbf{n}_Q = -\mathbf{M}_{QQ}^{-1}\mathbf{M}_{QP}\mathbf{n}_P. \tag{3.93}$$

Another useful output is the electron energy loss due to inelastic collisions with the impurity species, where we are typically interested in the contribution from each ionization stage sepa-

rately. At equilibrium, the energy to drive radiative emission comes from electron collisional processes, so we can compute the electron energy loss from all z-ionized levels (given by the subset Z) with

$$Q_z = \sum_{k' \in Z} \sum_{k \in Z} A_k^{k'} n_k \varepsilon_k^{k'} + \sum_{j \in Z'} \sum_{k \in Z} n_e r_k^j n_k \varepsilon_k^j \tag{3.94}$$

where we have a sum over all radiative de-excitation transitions within Z and all radiative recombination transitions from Z to Z', where Z' is the set of all $(z-1)$-ionized levels.

3.5.2 Atomic data

Comprehensive sets of atomic data for SOL-relevant impurity species are not readily available. Experimentally-verified data exists, for example on the NIFS database(`https://dbshino.nifs.ac.jp/`), but these datasets typically cover a limited subset of atomic levels and transitions. For this reason, the atomic data used in SIKE has been generated using the Flexible Atomic Code (FAC) [119]. This approach sacrifices some accuracy, for example the energy levels are typically only accurate to within 1-2 eV, but does ensure that the dataset used is fully self-consistent. This is important, as missing transitions can result in significantly different or even unphysical equilibrium density distributions, for example in the case of 'orphaned' levels which can be populated but not de-populated (or vice versa).

For each impurity species considered, atomic data is generated with FAC for

- energy levels,
- radiative de-excitation rates,
- auto-ionization rates (spontaneous emission of an electron from a highly-excited atomic state),
- radiative recombination cross-sections,
- electron-impact ionization cross-sections, from which we can obtain three-body recombination cross-sections via detailed balance,

- electron-impact excitation cross-sections, from which we can obtain de-excitation cross-sections via detailed balance.

Energy levels for an ion with a given number of electrons are computed in FAC by diagonalizing the relativistic Hamiltonian, and collisional cross-sections are treated in the distorted wave approximation. Further details on the theory and numerics of FAC can be found in [119].

The cross-section data is generated on an energy grid made of 16 points spaced geometrically from $\epsilon' = 3.6 \times 10^{-3}$ eV to 500 eV, where ϵ' is the post-collision electron energy. We assume cross-sections fall to zero at $\epsilon' = 0$. For $\epsilon' > 500$ eV, or for ϵ' greater than 200 times the transition energy in the case of excitation, we use the high-energy asymptotic fits provided by FAC. This is a polynomial fit for ionization and radiative recombination, and the Bethe formula is used for excitation. With this, we can specify the cross-section data on an arbitrary energy grid on which an electron distribution is defined, for example from SOL-KiT, by appropriate translation to the pre-collision energies and linear interpolation.

Species	Levels	Transitions
Helium	217	20658
Lithium	496	61949
Beryllium	1069	151529
Boron	1278	180461
Carbon	1479	200485
Nitrogen	1775	230721
Oxygen	2069	261085
Neon	2553	310975

Table 3.3: The number of levels and transitions in the FAC-generated atomic data for different impurity species.

Atomic data has been computed with FAC for all ionization stages of helium, lithium, beryllium, boron, carbon, nitrogen, oxygen and neon. Atomic levels are resolved in n (principal quantum number), l (orbital angular momentum quantum number) and j (total angular momentum quantum number). The total number of levels and transitions for which data has been computed is listed in Table 3.3. Datasets have also been generated which are aggregated in j-levels, assuming an even distribution of states with a given value of n and l, which allows for a more efficient computation if required by reducing the number of levels and transitions by

approximately a factor of 5.

Cross-sections for inverse processes are calculated using the principal of detailed balance. For an inelastic process with transition energy ε, the pre- and post-collision velocities are related via

$$\frac{1}{2}m_e v'^2 = \frac{1}{2}m_e v^2 + \varepsilon.$$

Therefore, for a given excitation cross-section $\sigma_{e,j}^{j'}$ for transitions from state j to j', the de-excitation cross-section is

$$\sigma_{e,j'}^{j}(v') = \frac{g_j}{g_{j'}}\frac{v^2}{v'^2}\sigma_{e,j}^{j'}(v), \tag{3.95}$$

where g_j is the statistical weight of state j. Similarly, three-body recombination cross-sections are calculated from a given ionization cross-section $\sigma_{e,j}^{j'}$,

$$\sigma_{e,j'}^{j}(v') = \frac{1}{2}n_e\lambda^3\frac{g_j}{g_{j'}}\frac{v^2}{v'^2}\sigma_{e,j}^{j'}(v), \tag{3.96}$$

where $\lambda = \sqrt{\frac{h^2}{2\pi m_e k T_e}}$ is the de Broglie wavelength of an electron at T_e.

3.5.3 Numerics

Inputs to the code (either f_0 and a velocity grid, or T_e and n_e profiles) and expected in standard units. That is, [$\mathrm{m^{-6}s^{-3}}$] for f_0, [$\mathrm{ms^{-1}}$] for velocity grids, [eV] for T_e and [$\mathrm{m^{-3}}$] for n_e. Within the code, all quantities are normalised. Temperature and density are normalised to T_0 and n_0, which are taken to be the mean quantities of the input values of T_e and n_e (calculated from moments of the distribution if f_0 is provided as input). We then normalise velocities to $v_{th,0}$, which is the thermal velocity of electrons at T_0, and times to τ_0, which is the Braginskii collision time of electrons at T_0. Cross-sections are normalised to $\sigma_0 = 8.797 \times 10^{-21}\mathrm{m^{-2}}$, which is the cross-section of a circle with the Bohr radius. Normalised quantities, denoted with a tilde, are

therefore

$$\tilde{T}_e = T_e/T_0, \quad \tilde{t} = t/\tau_0,$$
$$\tilde{n}_e = n_e/n_0, \quad \tilde{f}_0 = v_{th,0}^3 f_0/n_0,$$
$$\tilde{\varepsilon} = \varepsilon/T_0, \quad \tilde{\sigma} = \sigma/\sigma_0.$$

Rate coefficients (3.82) are calculated with midpoint numerical integration. For a velocity grid with cell-centred values v_j, a given rate coefficient is therefore

$$K = \frac{4\pi}{n_e} \sum_j v_j^3 \sigma(v_j) f_0(v_j) \Delta v_j. \tag{3.97}$$

The inverse process cross-sections, (3.95) and (3.96), are calculated for values of $v_j' = \sqrt{v_j^2 + 2\varepsilon/m_e}$ for a process with transition energy ε. These cross-sections are then linearly interpolated to the velocity grid v_j to calculate the appropriate rate coefficients. While this is not a fully conservative approach, this is not considered to be an issue since the electron distribution is not evolved.

The rate matrix $\mathbf{M}$ is constructed as a PETSc sparse matrix, or optionally as a collection of spatially local 2D numpy arrays. The global matrix approach is not strictly necessary, since the rate matrix for each spatial cell is completely independent and also typically quite dense, meaning a series of dense local matrices (i.e. one for each spatial cell) does suffice. However, this choice has been made to enable the addition of an impurity transport model to the code at a future date, which will link adjacent local rate matrices. PETSc matrix inversion routines can be used to solve for the state densities. Several matrix pre-conditioners and Krylov subspace methods have been tested; the most reliable combination was found to be the block Jacobi pre-conditioner and the bi-conjugate gradient solver. Alternatives may be specified at input.

A direct solve of the density evolution equation (3.88) has been found to occasionally be numerically unstable, sometimes producing negative densities. This is understood to be due to the significant scale separation in the elements of $\mathbf{M}$, which results in a matrix with a high

condition number relative to the numerical tolerance of the code. For this reason, an alternative approach has been implemented which is slower but more stable, where the density evolution equation (3.83) is evolved in time. For this we use backwards Euler time integration, where the array of densities at timestep $i+1$ is calculated using

$$\mathbf{n}^{i+1} = (\mathbf{I} - \Delta t \mathbf{M})^{-1} \mathbf{n}^{i},$$

where Δt is the timestep, $\mathbf{I}$ is the identity matrix and $\mathbf{M}$ is independent of time since the electron quantities are not evolved. This step is performed repeatedly until

$$\frac{d\mathbf{n}}{dt} \simeq \frac{\mathbf{n}^{i+1} - \mathbf{n}^{i}}{\Delta t}$$

falls below a threshold value, specified at input. This allows us to get close to a solution without the numerical problems introduced by attempting to compute the exact solution.

3.5.4 Benchmarking

Saha-Boltzmann distribution test

In the absence of any radiative processes, the atomic state distribution at equilibrium for each ionization stage should follow a Boltzmann distribution, i.e.

$$\frac{n_j}{n_0} = \frac{g_j}{g_0} e^{-\varepsilon_0^j / kT_e},$$

where 0 indicates the ground state of the given ionization stage. In Figure 3.16a, we compare the state density distribution for Li^+ at equilibrium, obtained with SIKE with radiative processes turned off, with the Boltzmann distribution at $T_e = 2$ eV. The densities are shown normalised to the statistical weight, where the total impurity density was initialised to 10^{20} m^{-3}, and the energy of each level is displayed relative to the bare ion, which has $\varepsilon = 0$ eV. The maximum error in the SIKE prediction is $10^3 m^{-3}$ for the state with $\varepsilon = -138.2$ eV, which is $\sim 10^{-15}$ in normalised density units, i.e. close to the machine precision.

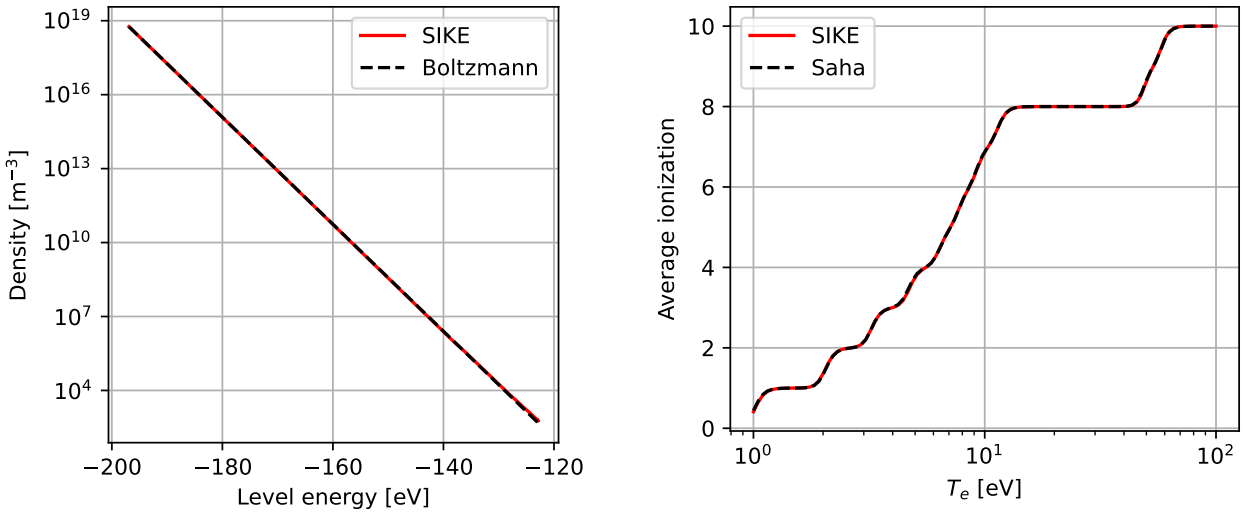

(a) (b)

Figure 3.16: (a): Atomic state density distribution from SIKE for Li^+ at $T_e = 2$ eV, without radiative processes, compared to the Boltzmann distribution. (b): Average ionization from SIKE for Ne at a range of T_e, compared to the Saha ionization equilibrium.

Similarly, the distribution of ionization stages should follow the Saha ionization equilibrium in the absence of radiative recombination,

$$\frac{n_{z+1} n_e}{n_z} = \frac{2}{\lambda^3} \frac{g_{z+1}}{g_z} e^{-\varepsilon^z_{z+1}/kT_e},$$

where λ is the electron de Broglie wavelength, and z refers to a given ionization stage. In Figure 3.16b, the average ionization resulting from the Saha equilibrium prediction is compared to SIKE for Ne at a range of electron temperatures, where only ionization between ground states is considered. The maximum error in the average ionization prediction is 0.05 at $T_e = 4.6$ eV.

Comparison with ADAS

A commonly used database for impurity reaction rates is ADAS `https://open.adas.ac.uk/`, which provides ionization stage-resolved coefficients for quantities such as ionization rates and radiative energy loss for a range of SOL-relevant impurity species. ADAS rates assume Maxwellian electrons, so we would expect some level of agreement with SIKE outputs under the same assumptions. It should be made clear, however, that SIKE's purpose is not to make

precise quantitative predictions, but rather it is to capture the differences between a kinetic and fluid treatment of plasma-impurity reactions. The aim of this comparison with ADAS is to ensure that predictions from SIKE are in approximately the right ballpark.

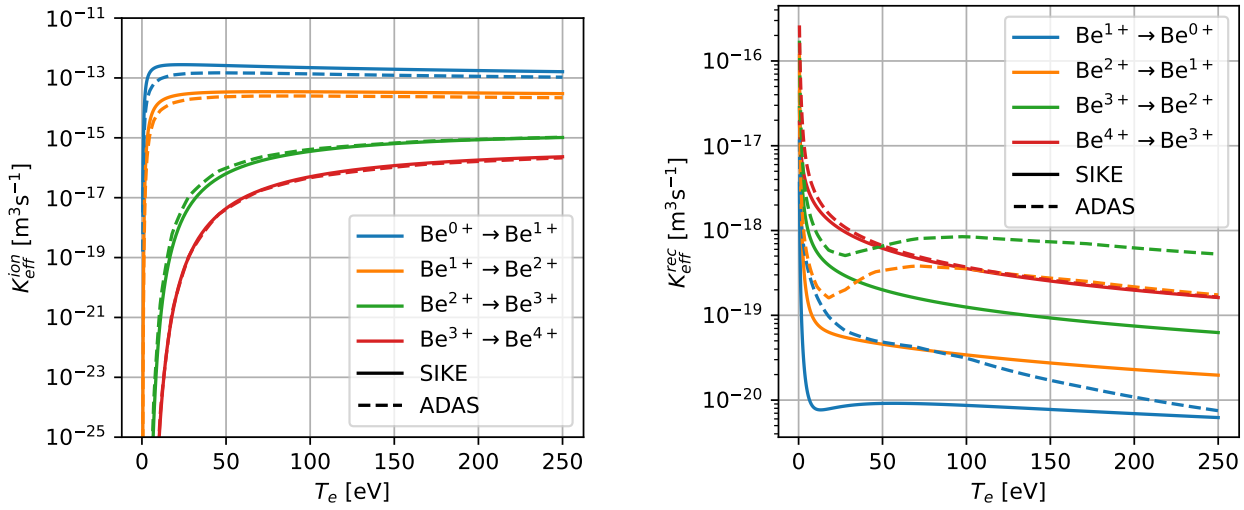

(a) (b)

Figure 3.17: Effective ionization (a) and recombination (b) rate coefficients for each ionization stage of beryllium, as calculated with SIKE and compared to ADAS for a range of electron temperatures.

In Figure 3.17, we compare for beryllium the effective ionization and recombination coefficients from SIKE, K_{eff}^{ion} and K_{eff}^{rec}, assuming only the ground states are evolved in time, with those from ADAS at a range of T_e, from 0.5 to 250 eV, for $n_e = 10^{20}$ m^{-3}. These are defined via $\mathbf{M}_{eff}$; see Section 3.5.1. Agreement is generally good for the ionization coefficients, being within around a factor of 2 at all temperatures. There are larger discrepancies in the recombination coefficients, up to an order of magnitude at some temperatures. The source of these differences is most likely to be from differences in the energy levels. These are not published with ADAS, but comparing the FAC predictions to those on the NIST database [120] highlights differences of up to a few eV for some low-energy levels of Beryllium. The ionization coefficients are arguably more important to the impurity and main plasma dynamics than recombination coefficients, since the latter only become significant at very low electron temperatures.

In Figure 3.18, we compare the radiative energy loss curves (3.94), or 'cooling curves', for each ionization stage of Beryllium as a function of T_e. Again we see reasonably good agreement,

within around a factor of 3 across all temperatures.

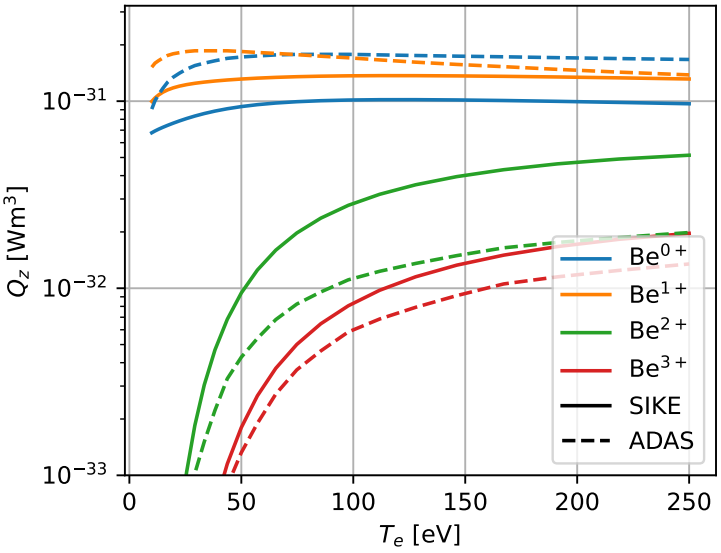

Figure 3.18: Cooling curves for Beryllium as a function of T_e, with SIKE results compared to ADAS.

As a further test of SIKE calculations, the average ionization at equilibrium, $\bar{z}$, has been calculated three ways:

1. using the FAC atomic data, directly calculating the rate equations for all states,
2. using values of K_{eff}^{ion} and K_{eff}^{rec} from ADAS (specifically the the SCD and ACD files from `https://open.adas.ac.uk/adf11`),
3. a dataset of curated collisional cross-sections for Carbon published by Suno and Kato [121].

The Suno & Kato dataset does not include radiative processes or level energies, so spontaneous emission rates and atomic level energies are obtained from the NIST database [120] and radiative recombination rates are obtained from ADAS (specifically the ADF08 files from `https://open.adas.ac.uk/adf08`, which are true rates and not effective rates). On a temperature profile from $T_e = 0.5$ eV to 100 eV, $n_e = 10^{20}$ m^{-3}, these three methods of calculating $\bar{z}$ are shown in Figure 3.19. We can see that, firstly, agreement between the FAC and ADAS data is reasonable, suggesting that the differences in effective recombination coefficients seen in Figure 3.17b are

not severely affecting the ionization balance. Secondly, the use of the Suno & Kato dataset, which is expected to be more accurate than the FAC dataset, improves agreement with ADAS. The implication here is that disagreements between SIKE and other tools may be resolved by modifying the atomic data, although this can be a detailed and time-consuming task.

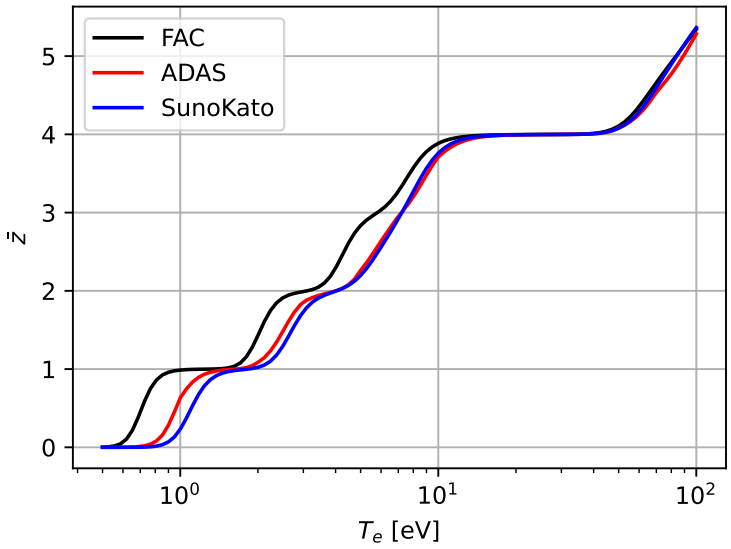

Figure 3.19: Comparison of the average ionization, $\bar{z}$, for Carbon, calculated using atomic data from FAC, ADAS and published by Suno & Kato [121].

Chapter 4

Investigation of kinetic effects in ion-electron energy transfer

This chapter is based on the article by D. Power, S. Mijin, F. Militello, and R. J. Kingham., *Ion-electron energy transfer in kinetic and fluid modelling of the tokamak scrape-off layer*, The European Physical Journal Plus, 136(11):1-13, 2021. The work described in this chapter has been carried out in collaboration with the co-authors of this paper, but I am the lead author and carried out all SOL-KiT simulations and analysis presented. Parts of this paper are reproduced here under CCA4.0 license, copyright of the authors.

Abstract

Using the 1D kinetic electron code SOL-KiT, simulations of the tokamak scrape-off layer were carried out to explore the presence of kinetic effects in energy transfer between the ions and electrons. During steady-state conditions, it was found that the ion-electron energy transfer is well-described by a fluid model, with only minimal differences seen when electrons are treated kinetically. During transient regimes (featuring a burst of energy into the scrape-off layer) we see evidence of enhanced energy exchange when calculated kinetically as compared to a fluid model. The kinetic correction represents an additional 8-38% ion-electron energy transfer across the domain, depending on the pre-transient plasma

collisionality. Compared to the total energy going into the plasma during the transient, the correction is less than 1%, so its impact on plasma profiles may be small. The effect is seen to increase in strength along the domain, peaking in front of the divertor target. The overall discrepancy (integrated along the domain) increases during the transient energy burst and disappears on a similar timescale. However, at the target the effect peaks later and takes several multiples of the transient duration to relax. This effect may be only partially explained by an additional population of cold electrons arising from neutral ionization.

4.1 Introduction

As discussed in Section 3.2, we expect the ions to generally reach higher temperatures in SOL plasmas if the total power going into both the ions and electrons via cross-field transport from the core is approximately equal. Therefore, we expect energy to flow to the electrons through elastic ion-electron collisions. This energy transfer may play a role in determining plasma behaviour in the SOL and the method through which energy escapes. Since kinetic effects are observed in other aspects of SOL behaviour, as shown in Section 2.9, an investigation will be presented here into whether a fluid model is appropriate for ion-electron energy exchange.

Here, results are presented of 1D simulations of the divertor SOL using the kinetic electron code SOL-KiT [4], which has been outlined in Chapter 3, and upgraded as described in Section 3.2. Simulations of equilibria and transients have been run for a divertor SOL in a medium-sized tokamak at a range of different collisionalities, described in section 4.2. The focus of this investigation is the transfer of energy between the electrons and ions, and it will be shown (section 4.3) that a kinetic treatment of the electrons results in modifications to the amount of energy transfer as compared to a fluid approximation under certain conditions. Potential causes and consequences of this effect will be discussed in Section 4.4. Also in Section 4.4, the outcomes of this work will be used to direct the investigations carried out in subsequent chapters.

4.2 Simulation setup

The original SOL-KiT model was extended to include a fluid ion temperature equation for this study, which was described in detail in Section 3.2. The version of SOL-KiT used in this study is the one which has been described there (further improvements discussed in Chapter 3 were added at a later date): a temperature equation is evolved for the ions, while the neutrals are treated as diffusive. The electrons are solved both kinetically and with a fluid model.

The spatial domain was 10.18m in length, where symmetry about the midplane is assumed so that this represents half of the connection length of the modelled SOL. External heating is applied over the first 3.51m, simulating input power to the SOL from the core. For both fluid and kinetic electrons, equilibrium conditions were obtained for four input powers, $q_{in} = 1.0\text{MWm}^{-2}$, 3.0MWm^{-2}, 4.5MWm^{-2} and 6.0MWm^{-2}. Equal amounts go into the electrons and ions, so that the total input power is $2q_{in}$. In the discussion that follows, runs are referred to by the q_{in} going to each species, not the total input. The plasma response to conductive transients was also simulated, where the input power was temporarily increased to $q_{in} = 45\text{MWm}^{-2}$ for a duration of 10μs, before returning to the original input power.

The spatial domain was divided into 64 cells, representing the region between the midplane and the sheath entrance. Spatial cells were spaced logarithmically, with higher resolution close to the target. Spatial grid widths ranged from 0.48m to 0.03m. In velocity space (for kinetic electron runs), a geometric grid of 80 cells was used up to a velocity of $\sim 12v_{th,0}$, where $v_{th,0}$ is the thermal velocity of electrons at a reference temperature of 10eV. The resolution was higher at low velocities, such that grid widths ranged from $0.05v_{th,0}$ to $0.35v_{th,0}$.

For kinetic runs, the kinetic equation was solved up to the harmonic $l_{max} = 3$. A constant line-averaged plasma plus neutral density of $\langle n \rangle = 10^{19}\text{m}^{-3}$ was maintained through 100% recycling of neutral deuterium atoms, where thirty excited states were modelled.

4.3 Results

It is informative to first present the equilibrium plasma profiles obtained for two input powers, $q_{in} = 1\text{MWm}^{-2}$ and 6MWm^{-2}, shown in Figure 4.1. Solid lines show results for fluid electrons, while dashed lines represent simulations with kinetic electrons. For the 1MWm^{-2} case we see a detached profile, however the 6MWm^{-2} case is not detached. The low power run shows minimal differences when the electrons are treated kinetically, while in the high power run (corresponding to lower collisionality) a steeper electron temperature gradient is seen (this effect is discussed in [83]). As expected, the ions tend to be hotter than the electrons, especially upstream, owing to their lower heat conductivity.

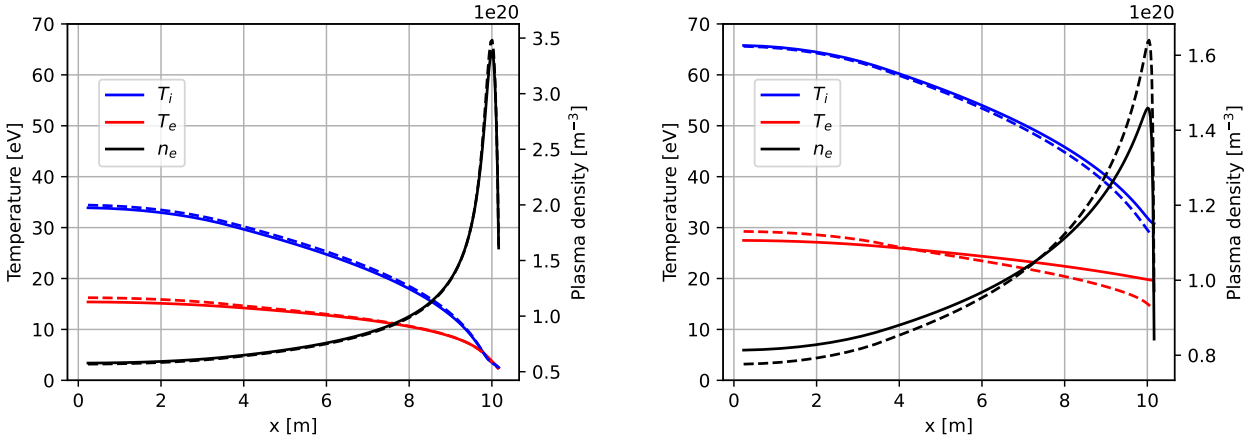

(a) Plasma conditions in equilibrium for an input power of 1MWm^{-2}.

(b) Plasma conditions in equilibrium for an input power of 6MWm^{-2}.

Figure 4.1: Plasma temperature and density profiles for a detached and non-detached case (1MWm^{-2} and 6MWm^{-2} input power respectively). Solid/dashed lines represent simulations with fluid/kinetic electrons. The boundary at $x = 0$ is the midplane, while $x \sim 10$m is the sheath entrance.

For the focus of this study, we now turn to the energy transfer between electrons and ions, $Q_e^{ei} = -Q_i^{ei}$. The notation will be simplified here compared to that used in Section 3.2, where we will write $Q_e^{ei} = Q_{ei}$ such that a positive Q_{ei} means energy is being transferred from the ions to the electrons. We limit the analysis to the kinetic runs, exploring differences in Q_{ei} caused by deviations of the electron distribution function from Maxwellian. In Figure 4.2, we compare

the heat exchange calculated using

$$Q_{ei}^{kin} = -\int d\mathbf{v} \frac{1}{2} m_e v^2 C^{ei},$$

for the f_0 obtained by SOL-KiT with an equivalent-temperature Maxwellian, Q_{ei}^{fl}. C^{ei} here is the electron-ion collision operator. For Maxwellian electrons, this calculation is equivalent to using the familiar Braginskii expression,

$$Q_{ei}^{fl} = \frac{3m_e}{m_i} \frac{n_e k}{\tau_e} (T_i - T_e).$$

Heat exchange across all runs peaks close to the target due to reduced temperatures and increased densities leading to higher collisionality there, outcompeting the reduced temperature differences (see Figure 4.1). For the lowest power run, the uptick at $x \simeq 10$m arises because the electrons and ions decouple slightly just in front of the sheath entrance, presumably due to differences in the sheath heat transmission coefficients. Small differences can be seen between a kinetic and fluid calculation of Q_{ei}, across all runs, particularly in the high power cases close to the target, but there is good overall agreement. In all cases, a kinetic treatment leads to a (small) suppression of energy transfer upstream, and enhanced energy transfer close to the target. Table 4.1 shows the total energy transfer in equilibrium integrated over the whole domain, i.e. $\langle Q_{ei} \rangle = \int Q_{ei} dx$. The differences are minimal, being less than 0.01MWm^{-2} in all cases, suggesting Q_{ei} is well-described by a fluid model here.

q_{in} [MWm^{-2}]	$\langle Q_{ei}^{fl} \rangle$ [MWm^{-2}]	$\langle Q_{ei}^{kin} \rangle$ [MWm^{-2}]
1.0	0.78	0.79
3.0	1.42	1.43
4.5	1.35	1.36
6.0	1.21	1.22

Table 4.1: Line-integrated ion-electron energy transfer using a kinetic or fluid model, for four different equilibrium conditions.

For the conductive transients studied, Figure 4.3 shows the difference in Q_{ei} when calculated kinetically or with the fluid model, $Q_{ei}^{kin} - Q_{ei}^{fl}$, for a spatial cell in the middle of the domain ($x \simeq 5$m) and close to the target ($x \simeq 10$m). The different runs are referred to here by the

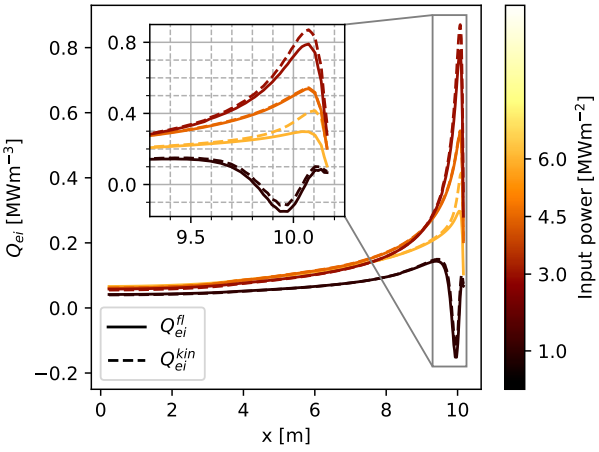

Figure 4.2: Ion-electron energy exchange for kinetic equilibria at four different input powers (positive values mean energy is going to the electrons), for the electron distribution obtained by SOL-KiT, Q_{ei}^{kin} (dashed), and for an equivalent-temperature Maxwellian, Q_{ei}^{fl} (solid).

value of q_{in} prior to the transient, which represents the background plasma conditions on which the transient was launched. All runs experience the same increase of q_{in} to 45MWm^{-2} for 10μs, before returning to the original input power.

In the middle of the domain (Figure 4.3a), we see enhanced energy transfer associated with the transient across all runs, before relaxing quickly to the pre-burst value (slight suppression) and a small secondary perturbation on an acoustic timescale at $t \simeq 100\mu$s. The peak occurs in all runs before the transient energy burst has finished, at around 4μs. For context, in order of increasing q_{in} the peaks in Figure 4.3a represent respectively 25%, 12%, 9% and 7% enhancement of Q_{ei}^{kin} compared to Q_{ei}^{fl}.

Close to the target (Figure 4.3b), we see peak differences in energy exchange an order of magnitude larger than that in the middle of the domain, and slower relaxation to the pre-transient level, occurring on a timescale of the order 40-100μs. The peak kinetic enhancement of Q_{ei} happens at different times for different background plasmas, occurring 10-30μs after the transient has ended. For the 4.5MWm^{-2} and 6MWm^{-2} runs, the peak represents 111% and 77% enhancement of Q_{ei}^{kin} compared to Q_{ei}^{fl}. For the 1MWm^{-2} and 3MWm^{-2} runs, the peak occurs at times when $Q_{ei}^{fl} = 0$, so a kinetic treatment of Q_{ei} captures energy transfer which is missed under a fluid treatment.

To assess the total magnitude of the effect seen here, we again integrate over the spatial domain

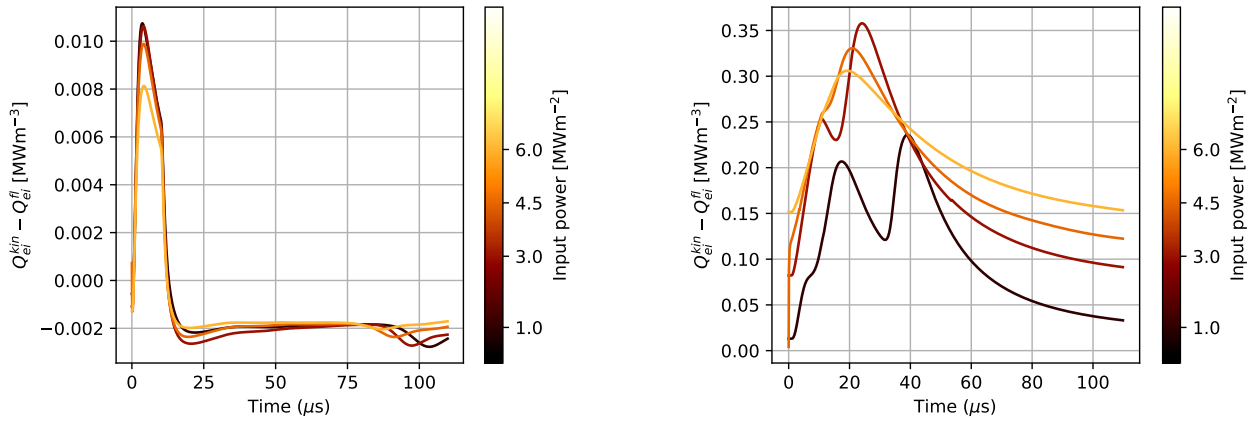

(a) $x = 5.16$m (b) $x = 10.16$m

Figure 4.3: Time evolution of the difference in Q_{ei} for kinetic (Q_{ei}^{kin}) and fluid (Q_{ei}^{fl}) electrons, for conductive transients launched on background equilibria obtained at four different input powers. The origin of the ripple effect occurring on an electron timescale in the lowest power run at the target (right) is unclear, but may be connected to an oscillating detachment front.

and take the difference for a kinetic and fluid treatment at each point in time, $\langle Q_{ei}^{kin} \rangle - \langle Q_{ei}^{fl} \rangle$. This is shown in Figure 4.4. We see that the peak kinetic enhancement of $\langle Q_{ei} \rangle$ is slightly stronger for low power runs (corresponding to higher collisionality before the transient), and that the duration of the effect is similar to that of the transient energy burst. This is despite the fact that the area of strongest enhancement, close to the target, takes longer to relax than elsewhere - this may be explained by the fact this particularly strong effect occurs over a relatively small region. Taking the first 10μs and subsequent 40μs (up to $t = 50\mu$s), Table 4.2 compares the time integrated total energy transfer from the ions to the electrons during the simulations, $W_{ei} = \int \langle Q_{ei} \rangle dt$. During the transient energy burst (first 10μs), a kinetic treatment predicts 38% more energy transfer than a fluid model for the 1MWm^{-2} background, with the effect reducing to 8% for the 6MWm^{-2} background. There are much smaller differences in the subsequent 40μs, peaking at 3% enhancement for the 1MWm^{-2} background, suggesting the effect is significant only during the burst phase of the transient.

	First 10μs		Subsequent 40μs	
q_{in} [MWm^{-2}]	W_{ei}^{fl} [Jm^{-2}]	W_{ei}^{kin} [Jm^{-2}]	W_{ei}^{fl} [Jm^{-2}]	W_{ei}^{kin} [Jm^{-2}]
1.0	2.43	3.35	35.70	36.82
3.0	9.09	10.04	52.34	53.52
4.5	9.31	10.11	41.28	42.25
6.0	8.82	9.50	35.28	36.27

Table 4.2: Total time-integrated ion-electron energy transfer using a kinetic or fluid model, comparing the first 10μs (duration of transient energy burst) with the following 40μs. For context, the total input energy to the plasma during the first 10μs is 900Jm^{-2}.

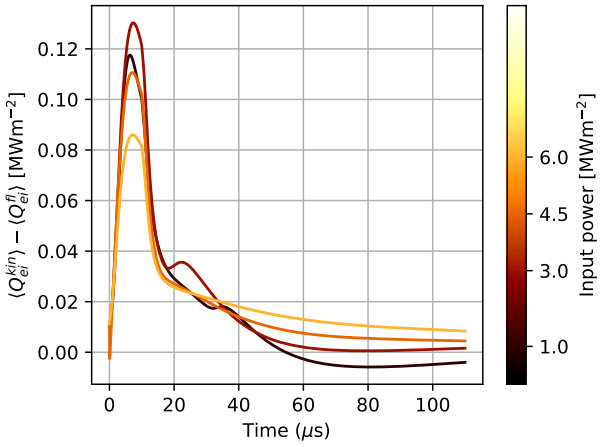

Figure 4.4: Evolution during a conductive transient of the difference in Q_{ei} when calculated with the SOL-KiT-obtained f_0 and a Maxwellian, integrated over the spatial domain.

4.4 Discussion and conclusions

We have seen that ion-electron energy transfer is described well by a fluid model in the steady-state SOL regimes studied here. Differences that do exist appear unlikely to affect plasma profiles and behaviour as they are small in magnitude and occur over a relatively small region. During transient regimes, however, a kinetic treatment of the electrons predicts additional heat exchange, particularly during the transient energy burst into the SOL. Before proceeding, it's worth noting that finite grid effects are unlikely to be contributing significantly to these effects. A subset of the runs analysed here were repeated on a velocity grid with quadrupled resolution (not presented here), and only negligible differences were seen.

We may investigate the cause of the observed effects by looking at the electron distribution in a region of kinetic enhancement of Q_{ei}, and its effect on the collision operator. In Figure 4.5,

these quantities are shown for a spatial cell close to the target ($x = 10.16m$) at a timestamp correlating with the peak of the enhancement in the 3MWm^{-2} transient run in Figure 4.3b ($t = 25\mu\text{s}$).

The obtained distribution in this region deviates strongly from a Maxwellian (Figure 4.5a), featuring an additional low-temperature electron population, depletion around the middle of the energy range and an enhanced high-energy tail. This deviation contributes to the enhancement of Q_{ei}, as can be seen in Figure 4.5b, where the integrand (dashed) of the energy moment of the collision operator, $Q_{ei} = \int \frac{1}{2} m v^2 C^0_{ei} d\mathbf{v}$, is plotted alongside the running integral (solid), as a function of electron energy. Shown are the curves for the SOL-KiT-obtained distribution and a Maxwellian, as well as that of a two-temperature Maxwellian (discussed shortly). A distinct low-energy feature can be seen, which is not present for the Maxwellian. Around the middle of the energy range, there is also some additional kinetic contribution to Q_{ei}. The high energy tail does not contribute to the kinetic enhancement of Q_{ei} here, as expected due to the low collisionality of fast electrons.

We might expect the additional cold electrons seen in the f_0 obtained by SOL-KiT, which produces the distinct low-energy contribution to Q_{ei} seen in Figure 4.5b, to originate from electrons involved in collisional ionization. While the exact form of this collisional operator implemented in SOL-KiT places the ejected electrons in the lowest velocity cell, and so the effect may be exaggerated, we would anyway expect electrons generated during the ionization process to be colder than the background population due to loss of the ionization energy. By fitting a two-temperature Maxwellian to the contribution to Q_{ei}, keeping overall density and temperature the same, good agreement is obtained with the low-energy feature in Figure 4.5b (inset) with $T_e^{cold} = 0.12\text{eV}$ and $n_e^{cold} = 3.7 \times 10^{15}\text{m}^{-3}$. This accounts for 0.13MWm^{-3} of the additional 0.34MWm^{-3} energy exchange seen here when treated kinetically. Putting a two-temperature Maxwellian into the collision operator yields $Q_{ei} = Q_{ei}^{cold} + Q_{ei}^{bulk}$, where Q_{ei}^{cold} and Q_{ei}^{bulk} take the form of Equation (3.28) with the appropriate temperature and density for the cold population and the bulk electron population respectively. It is feasible, but not done here, that a value for the temperature and density of the cold electron population based on considerations of the ionization rate may be obtained, which could be used to modify the value

of Q_{ei} used in fluid simulations.

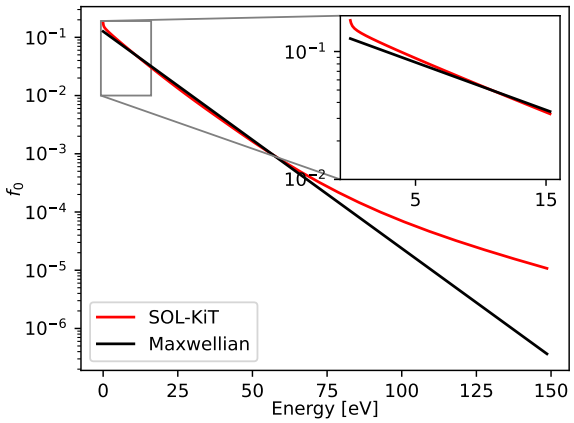

(a) f_0 obtained by SOL-KiT (red) and an equivalent-temperature Maxwellian (black). An enhanced low-temperature electron population can be seen in the SOL-KiT distribution (inset). The electron temperature at this point is 11.2eV.

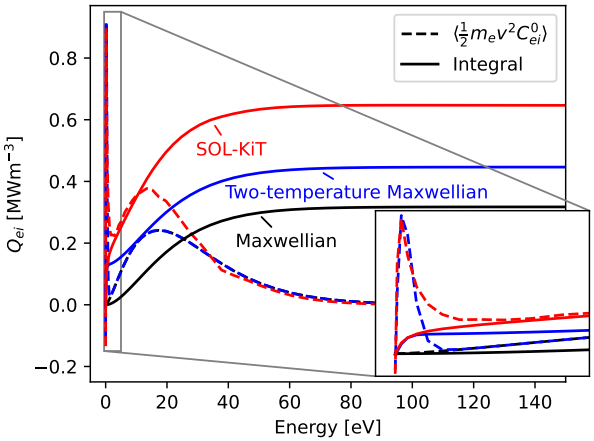

(b) The contribution to $Q_{ei} = \int \frac{1}{2} m v^2 C^0_{ei} d\mathbf{v}$ as a function of energy. The integrand (dashed) is shown alongside the running integral (solid). Results for the f_0 obtained by SOL-KiT (red) are shown alongside those for an equivalent Maxwellian (black) and a Maxwellian with an additional cold electron population (blue).

Figure 4.5: Electron distribution function and contribution to Q_{ei} at $x = 10.16$m, during a transient on a 3MWm^{-2} background at the peak Q_{ei} enhancement ($t \simeq 25\mu$s). The low-energy feature in the contribution to Q_{ei} (right, inset) is well-approximated by a two-temperature Maxwellian, but does not explain the entire discrepancy.

So, the addition of a population of cold electrons arising from ionization appears to explain around a third of the enhancement in energy exchange seen here when electrons are treated kinetically. There are several factors contributing to the distortion of f_0 from Maxwellian at this location, including the presence of the sheath as well as plasma-neutral interactions and sharp temperature gradients. A simple model accounting just for ionized electrons does not fully account for the kinetic enhancement in Q_{ei} seen, and the majority component of the effect may require a kinetic model to capture accurately. It should also be noted that this effect is seen in regions where minimal ionization is occurring, albeit less strongly, as seen in Figure 4.3a.

From the discussion here it is feasible then that transient regimes may lead to increased energy coupling between electrons and ions in the divertor SOL, which would manifest as hotter electron temperatures and colder ion temperatures at the target. This would in turn impact sputtering yields and target heat flux. On the other hand, kinetic corrections to Q_{ei} on the or-

der of $1\mathrm{Jm}^{-2}$, as seen in Table 4.2, contrast with a total input energy to the plasma of $900\mathrm{Jm}^{-2}$ during the 10μs transient. So while a kinetic effect is apparent, even strong enhancement of Q_{ei} may not significantly affect plasma behaviour. Further investigation would therefore be required to determine the extent to which plasma profiles are modified by this effect. Given the overall, line-integrated value of the kinetic enhancement in Q_{ei} appears to only be significant during the energy burst phase of the conductive transients modelled, any impact on plasma profiles would be dependent on the frequency and duration of the transient events. For example, type I edge-localised modes (ELMs) would drive this effect differently to type III ELMs. Some saturation of the effect is observed in Figure 4.4 before the energy burst has ended, raising the possibility that there is a ceiling to its magnitude, and that more energetic transients do not result in stronger kinetic enhancement of Q_{ei}. On the other hand, the effect appears to persist long after the energy burst at regions close to the target compared to elsewhere in the domain (Figure 4.5b), and the saturation behaviour is not observed, so that target temperatures may be affected even if the overall energy exchange between species is modified only slightly.

An important overall result of this study is that kinetic effects in ion-electron energy transfer appear likely to be less significant in determining SOL behaviour in the regimes studied than modifications to the parallel heat transport, which has been seen for example in [68, 81–83, 97, 101]. This suggests that further research efforts should be directed towards either an improved understanding of kinetic modifications to parallel heat transport, or other processes which are important in determining the SOL power balance, such as plasma-impurity interactions. Therefore, in Chapter 5, the former will be addressed, while in Chapter 6 the impact of kinetic effects in plasma-impurity reactions will be investigated.

This study is, to the author's knowledge, the first to directly compare fluid and kinetic calculations of electron-ion energy transfer in SOL plasmas. However, we may compare the results here to the study by Zhao et al. [82], and Adamek et al. [122]. In [82], the kinetic electron code KIPP is coupled to the SOLPS fluid code, and a density scan is performed for a 1D SOL with 25m connection length in equilibrium conditions. The ion-electron energy transfer channel is shown there to be dwarfed by the parallel heat flux and radiated power. In [122], the particle-in-cell code BIT1 is used to simulate an ELM in a 15m SOL flux tube. There, it is found that

energy transfer between the ions and electrons via Coulomb collisions during the ELM is small. While neither of these studies provides a comparison with an equivalent fluid model, they do both provide further evidence that Q_{ei} is not a likely source of kinetic effects in SOL plasmas.

On the other hand, in [123], Costea et al. suggest that, during kinetic simulations of a transient, hot upstream particle source, a decoupling of the hot electrons and hot ions may result in excess kinetic energy transfer between the two species via changes to the electric field. This effect would not be captured by a fluid model. For this reason, an interesting piece of future work would be to simulate an upstream particle source with SOL-KiT in a similar way to the energy source in this study, and directly quantify the effect of any differences of this nature by comparing with the fluid treatment.

Chapter 5

Scaling laws for electron kinetic effects in tokamak scrape-off layer plasmas

This chapter is based on an article by D. Power, S. Mijin, M. Wigram, F. Militello, and R. J. Kingham., *Scaling laws for electron kinetic effects in tokamak scrape-off layer plasmas*, which has been published in Nuclear Fusion (`https://doi.org/10.1088/1741-4326/acdca6`). Parts of this paper are reproduced here under CC BY 4.0 license, copyright of the authors. The work presented in this chapter has been carried out in collaboration with the co-authors, but I am the lead author, and I performed the SOL-KiT simulations and analysis which is presented.

Abstract

Tokamak edge (scrape-off layer) plasmas can exhibit non-local transport in the direction parallel to the magnetic field due to steep temperature gradients. This effect along with its consequences has been explored at equilibrium for a range of conditions, from sheath-limited to detached, using the 1D kinetic electron code SOL-KiT, where the electrons are treated kinetically and compared to a self-consistent fluid model. Line-averaged suppression of the kinetic heat flux (compared to Spitzer-Härm) of up to 50% is observed, contrasting with up to 98% enhancement of the sheath heat transmission coefficient, γ_e. Simple scaling laws in terms of basic SOL parameters for both effects are presented. By

implementing these scalings as corrections to the fluid model, we find good agreement with the kinetic model for target electron temperatures. It is found that the strongest kinetic effects in γ_e are observed at low-intermediate collisionalities, and tend to increase (keeping upstream collisionality fixed) at increasing upstream densities and temperatures. On the other hand, the heat flux suppression is found to increase monotonically as upstream collisionality decreases. The conditions simulated encompass collisionalities relevant to current and future tokamaks.

5.1 Introduction

As discussed previously in this thesis, transport in SOL plasmas is often treated with fluid models, where a Braginskii-like set of transport equations [48] may be solved. However, the presence of steep temperature gradients parallel to the magnetic field, as would be expected in reactor-class devices, means heat transport can become non-local . This can be quantified with the upstream collisionality parameter $\nu_u^* = L/\lambda_u$ [24], defined as the ratio of the parallel SOL length L and the upstream mean free path λ_u. Conditions where ν_u^* is small and temperature gradients are large may not be described accurately by a fluid model.

This effect has been explored in recent years [68,72,81–83,97,100,101,124], where it is now well-documented that kinetic suppression of the heat flux can result in steeper temperature gradients and lower target temperatures when compared to a fluid model. Somewhat less understood is the region of operating parameter space where such effects may become important, and the consequences for the overall energy balance at equilibrium (i.e. how energy going into the SOL makes its way out). Furthermore, it has been suggested by Coster et al. [125] that a population of fast electrons from upstream in the plasma close to the walls may facilitate divertor detachment at lower upstream densities. Overall, it is still unclear whether kinetic effects in parallel transport pose a significant uncertainty in modelling approaches for future devices.

Here we present kinetic and fluid simulations of a 1D SOL plasma model, across a wide range of

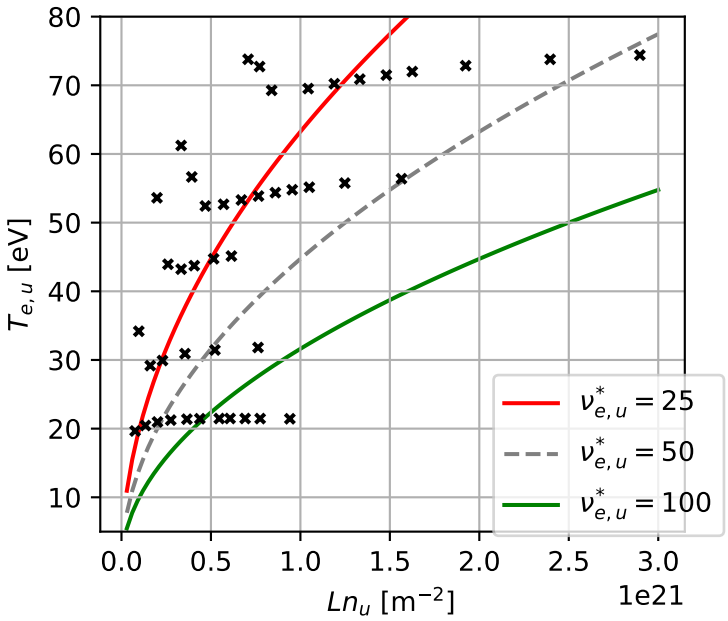

Figure 5.1: SOL-KiT simulations carried out for this study, where each black dot represents a simulation at a given q_{in} and $\langle n_0 \rangle$. The exact values of n_u and $T_{e,u}$ are taken from the kinetic simulations. For context, lines of constant collisionality are shown at $\nu^*_{e,u} = 25$, 50 and 100.

the relevant parameter space (input power, plasma density and connection length), in order to assess and understand kinetic deviations from fluid model predictions. The model description is omitted here as it has been described in detail in Chapter 3. In Section 5.2, there will be an explanation of the simulations that have been carried out. The results will then be summarised (Section 5.3), highlighting the areas in which kinetic effects are (and are not) seen. Following a discussion of the observed results (Section 5.4), scaling relationships in terms of basic SOL parameters will be presented for the main kinetic effects seen - enhancement to the sheath heat transmission coefficient and suppression of the parallel conductive electron heat flux - in Section 5.5. These will be used to reproduce electron temperature profiles from kinetic simulations in a (corrected) fluid model. A prediction is made for the strength of these kinetic effects in ITER.

5.2 Parameter scan simulations

For this study, the original version of SOL-KiT (described in Section 3.1) was upgraded to include an ion temperature equation, a fluid neutral model and bundling on the electron-neutral

collision operators. These improvements are described in Sections 3.2, 3.3 and 3.4 respectively.

Two SOL parameters which we have some degree of control over in tokamaks (and which determine SOL behaviour) are T_u and n_u, the plasma temperature and density measured at some upstream location. In these simulations, these are varied by changing the input power flux to the SOL from the core, q_{in}, and the initial line-averaged plasma density, $\langle n_0 \rangle = \frac{1}{L}\int_0^L n_e(t=0)dx$, where the plasma is fully ionised at initialisation. The total number of particles (plasma plus neutrals) stays constant in the simulations due to 100% recycling of the target particle flux. The input heat flux is distributed uniformly across the heating region, L_{heat}, as a volumetric energy source, Q_{in}, such that $q_{in} = \int_0^{L_{heat}} Q_{in}dx = L_{heat}Q_{in}$.

Of interest in this study is how conditions upstream determine the electron transport, and a useful measure of this is the electron upstream collisionality parameter $\nu^*_{e,u}$, defined as the ratio of the connection length L to the electron Coulomb mean free path upstream $\lambda_{ee,u}$ [24],

$$\nu^*_{e,u} = \frac{L}{\lambda_{ee,u}} \simeq 10^{-16}\frac{Ln_u}{T^2_{e,u}} \tag{5.1}$$

for $T_{e,u}$ in [eV] and n_u in [m^{-3}]. Note that this differs slightly from some forms of $\nu^* = L/\lambda_u$ employed in the literature (e.g. [101]), and $\nu^*_{e,u}$ here will typically be smaller than collisionality defined in terms of total plasma temperature because $T_{i,u} > T_{e,u}$ generally.

For a deuterium plasma, a number of density scans were performed at different input powers and connection lengths. Connection lengths ranged from $L = 11.93$m to 30.97m, input powers from $q_{in} = 4\mathrm{MWm}^{-2}$ to $128\mathrm{MWm}^{-2}$, and densities from $\langle n_0 \rangle = 1.0\times10^{19}\mathrm{m}^{-3}$ to $1.4\times10^{20}\mathrm{m}^{-3}$. With these input parameters, the simulations cover $\nu^*_{e,u}$ from 6.3 to 203.6. At the lowest collisionalities the plasma is sheath-limited, while detachment is reached at the highest values of $\nu^*_{e,u}$ (measured by rollover of the target particle flux).

q_{in} is distributed over approximately the first third of the domain and spread equally between the ions and electrons; 100% of plasma particles lost to the sheath are recycled as neutrals, and the pitch angle used in the neutral model was $\alpha = 15°$. Note that this pitch angle is somewhat larger than may be expected in some current and future tokamak experiments. It

was found originally that very small angles appeared to be related to some numerical difficulties reaching convergence in the least collisional simulations, so a larger angle was used to reduce the risk of the (long-running) kinetic simulations failing. 100 spatial cells were used, which were spaced logarithmically with higher resolution close to the target. For the simulations with the longest connection length, the spatial grid widths ranged from 2.28m upstream to 1.05mm at the target. In velocity space (for kinetic electron runs), a geometric grid of 80 cells was used up to a velocity of $\simeq 12v_{th,0}$,where $v_{th,0}$ is the thermal velocity of electrons at a reference temperature of 10eV. The resolution was higher at low velocities, such that grid widths ranged from $0.05v_{th,0}$ to $0.35v_{th,0}$. In the kinetic runs, the kinetic equation for electrons (3.2) was solved up to the spherical harmonic $l_{max} = 3$.

For the neutral bundling, a cut-off index of $j_c = 5$ was used, meaning the first four neutral atomic states are evolved in full, and all excited states with principal quantum number $n \geq 5$ are bundled together.

To reach equilibrium, determined by when the power and particle balance has converged, the kinetic simulations with SOL-KiT each take a few weeks running on 8 CPUs, while the fluid simulations typically take a day or less on 4 cores.

These simulations are situated on the $T_{e,u}$-Ln_u plane along with lines of constant $\nu^*_{e,u}$ in Figure 5.1. For reference, present-day tokamaks (JET, DIII-D, etc.) operate with $Ln_u \simeq 10^{20}-10^{21}\mathrm{m}^{-2}$ and $T_{e,u} \simeq 20 - 60$eV. Future devices like ITER and DEMO will operate with $Ln_u \sim 1 \times 10^{21} - 4 \times 10^{21}\mathrm{m}^{-2}$ and $T_{e,u} \sim 150 - 300$eV [126, 127]. Simulating such regimes kinetically is computationally demanding, but this study represents an attempt to explore kinetic effects in regimes beyond those attainable in existing devices. The simulations presented here fall short of reaching the highest values of $T_{e,u}$ expected in future tokamaks, but do encompass reactor-relevant values of Ln_u, detached conditions, and a broad range of upstream collisionalities.

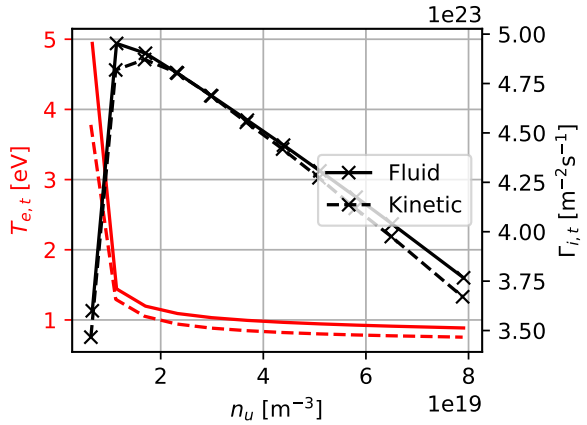

(a) $q_{in} = 4\text{MWm}^{-2}$, $L = 11.93\text{m}$.

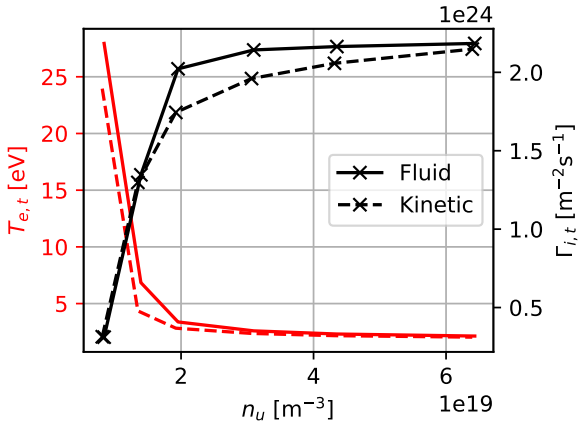

(b) $q_{in} = 16\text{MWm}^{-2}$, $L = 11.93\text{m}$.

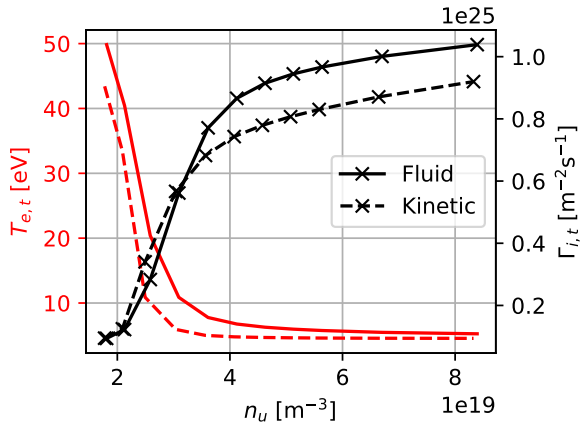

(c) $q_{in} = 80\text{MWm}^{-2}$, $L = 18.79\text{m}$.

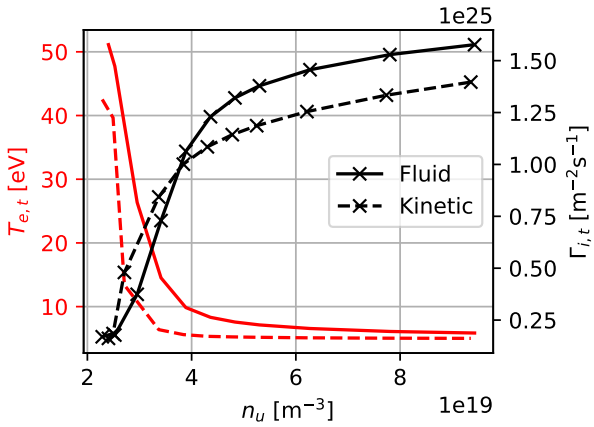

(d) $q_{in} = 128\text{MWm}^{-2}$, $L = 30.96\text{m}$.

Figure 5.2: Target electron temperatures, $T_{e,t}$, and ion fluxes, $\Gamma_{i,t}$, for four of the density scans at different input powers and connection lengths. Results with fluid and kinetic electrons are shown. The lowest input power runs exhibit detachment, indicated by rollover of $\Gamma_{i,t}$.

5.3 Results

We start by displaying in Figure 5.2 the target temperatures and particle fluxes of four of the density scans carried out. Rollover of the target flux, an indicator of detachment onset, is expected when particle, momentum and power losses are sufficient to reduce the target flux despite increasing plasma density. Only the lowest-power run reaches flux rollover here, while all other runs are partially or fully attached. The absence of rollover at high input powers is not unexpected given the lack of impurity radiation in the SOL-KiT model, which would provide additional power dissipation. It can be seen in Figure 5.2 that target temperatures are lower when the electrons are treated kinetically, with the biggest differences in both absolute and

relative terms occurring at low upstream densities. However, there are only small differences observed in the rollover behaviour in the one density scan which does reach detachment, 5.2a, where a kinetic treatment of the electrons does not change the position of detachment onset when varying n_u, i.e. the qualitative behaviour of $\Gamma_{i,t}$ is the same. There is a decrease in $\Gamma_{i,t}$ with kinetic electrons at high upstream densities, up to around 15%, while there is a slight increase at low densities.

The reduction in target temperatures in Figure 5.2 is a reflection of the suppression of the parallel conductive electron heat flux which is observed in kinetic simulations, as has been observed in other kinetic studies of parallel transport [32, 81, 84, 97]. This can be seen in Figure 5.3a, which shows temperature profiles for two simulations at low collisionality, along with differences in target electron temperatures across all simulations in Figure 5.4. Figure 5.3b shows the ratio of the kinetic to Spitzer-Härm heat flux calculated on the kinetic plasma profiles in 5.3a. This suppression of the heat flux relative to that predicted by a fluid treatment, where for a given heat conductivity κ the Spitzer-Härm heat flux is $q_{\parallel,e}^{SH} = -\kappa \nabla T$, arises due to fast electrons not depositing their energy locally due to their large mean free path relative to the temperature gradient length scale. This means that a steeper temperature gradient is required to achieve the same heat flux along the SOL, which is fixed by q_{in}. There is an uptick in T_e close to the wall in the least collisional simulations, which is seen in the hotter T_e profile in Figure 5.3a and as a spike in the heat flux ratio in Figure 5.3b.

In Figure 5.5 we can see the accumulation of fast electrons from upstream at the target, where an electron energy distribution from just in front of the sheath boundary is shown. There is a clear enhanced high-energy tail, while the thermal bulk is close to the local Maxwellian.

In Figure 5.6, the kinetic enhancement of the sheath heat transmission coefficient is shown, γ_e, shown as $\Delta\gamma_e = \gamma_e^{kinetic} - \gamma_e^{fluid}$. Maximum and minimum values of $\Delta\gamma_e$ seen here are 4.96 and 0.47. Differences in γ_e here arise because, in kinetic mode, γ_e is calculated self-consistently from the logical boundary condition on the electron distribution, whereas in fluid mode it is calculated from fluid quantities in the classical way (3.20). For reference, in fluid mode typically $\gamma_e \simeq 4.8$, and this varies slowly with SOL conditions. In Figure 5.6, there is a non-monotonic

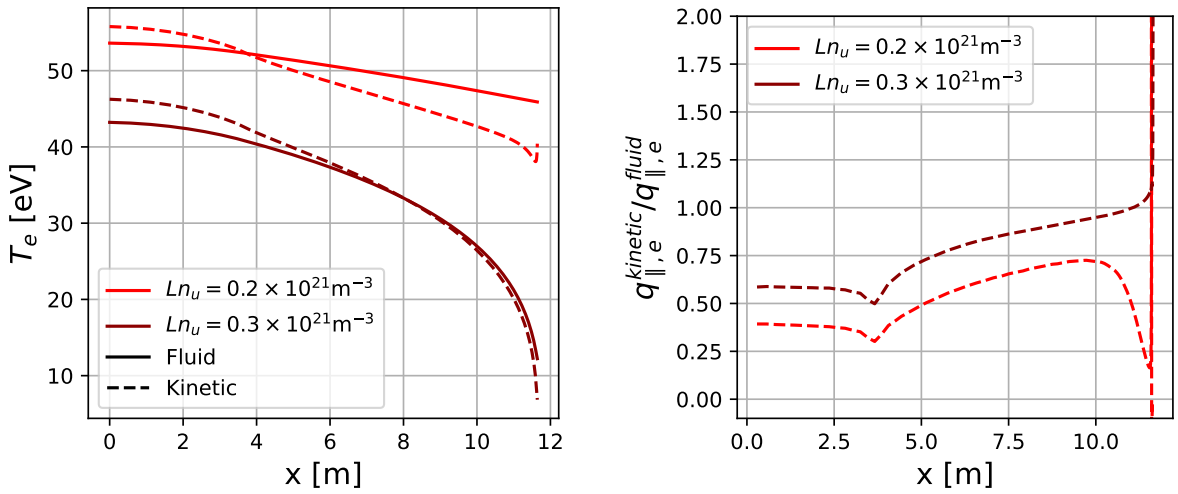

(a) Fluid and kinetic electron temperature profiles.

(b) Ratio of the kinetic to Spitzer-Härm conductive heat flux for the kinetic simulations in (a).

Figure 5.3: Kinetic heat flux suppression resulting in steeper temperature gradients and lower target temperatures for two low collisionality simulations ($q_{in} = 64\mathrm{MWm}^{-2}$, $L = 11.93\mathrm{m}$).

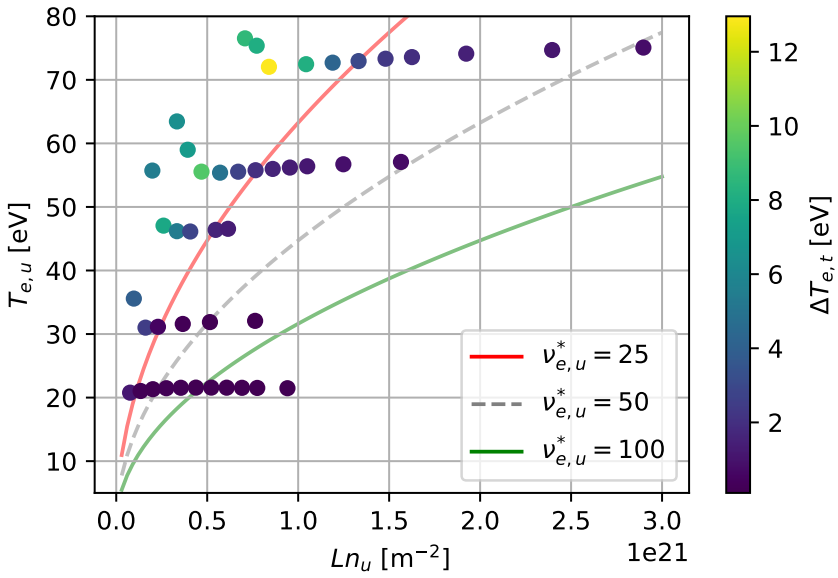

Figure 5.4: Difference in target temperatures for kinetic vs. fluid electrons across all simulations, $\Delta T_{e,t} = T_{e,t}^{fluid} - T_{e,t}^{kinetic}$.

behaviour in $\Delta\gamma_e$, where the classical value is approached at both high and low collisionalities. Similar behaviour was seen in a power scan in [84] and in a collisionality scan in [3]. The largest differences occur at low-intermediate collisionalities, but there is an additional increase in magnitude of this effect along lines of constant collisionality, moving towards larger $T_{e,u}$ and n_u. This can be seen by tracing along the red $\nu^*_{e,u} = 25$ line in Figure 5.6, where simulations at

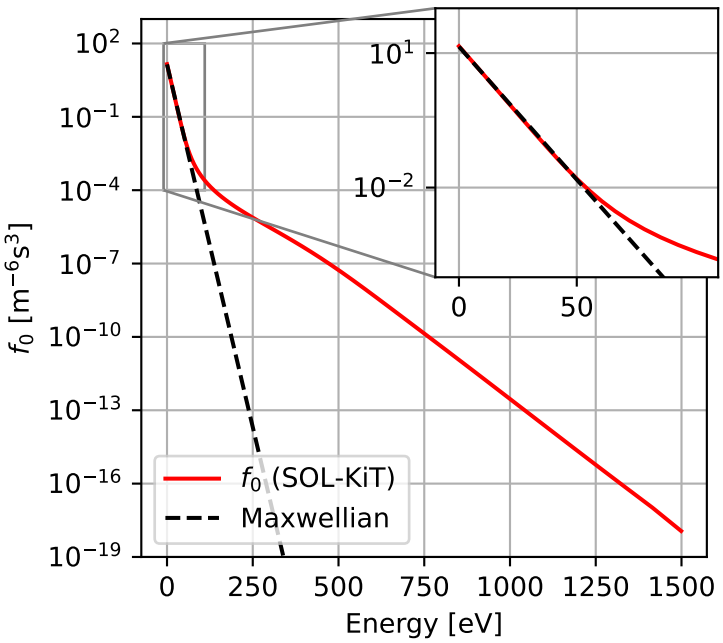

Figure 5.5: Electron energy distribution (isotropic part) close to the wall in a SOL-KiT simulation ($q_{in} = 64\text{MWm}^{-2}$, $L = 11.93m$, $\langle n_0 \rangle = 5 \times 10^{19}\text{m}^{-3}$). Dashed line is the local Maxwellian. A prominent high-energy tail and thermalised bulk can both be seen. $T_e = 7.3\text{eV}$, $n_e = 3.2 \times 10^{20}\text{m}^{-3}$.

higher $T_{e,u}$ have larger $\Delta\gamma_e$. Additionally, even at the highest collisionalities, where we would expect good agreement between fluid and kinetic predictions, there is a residual $\Delta\gamma_e \simeq 0.5$. It would therefore appear that convergence of γ_e to the fluid value is slow as a function of $\nu^*_{e,u}$.

Given the enhancement in γ_e for kinetic electrons, it is natural to investigate the heat lost to the sheath boundary, $q_{sh,e} = \gamma_e k T_{e,t} \Gamma_{i,t}$, where $T_{e,t}$ is the electron temperature at the target. This is shown in Figure 5.7, where the variation of $q_{sh,e}$ for kinetic and fluid simulations with n_u is plotted for simulations grouped by connection length and input power.. In contrast to the kinetic enhancement in γ_e, we see that $q_{sh,e}$ is generally in good agreement for kinetic and fluid simulations. This is perhaps not surprising, since $q_{sh,e}$ is to a large extent fixed by q_{in}, as well as the fact that kinetic enhancement in γ_e may be offset by the reduction in target temperatures (Figure 5.3a). However, this does show that the overall power balance in these simulations (for example, how much power is radiated away by electron-neutral collisions) is broadly unchanged despite modifications to the conductive transport as well as behaviour at the boundary.

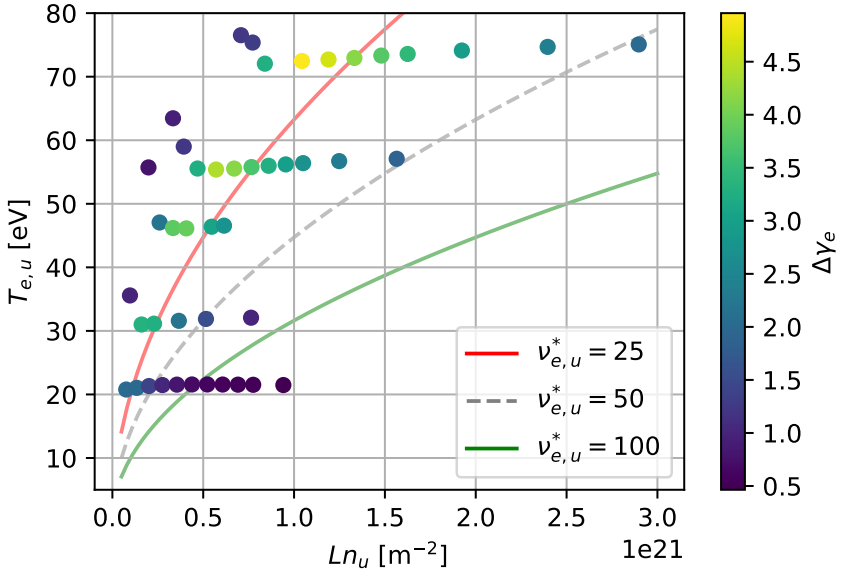

Figure 5.6: Enhancement to the electron sheath heat transmission coefficient, $\Delta\gamma_e = \gamma_e^{kinetic} - \gamma_e^{fluid}$, across all simulations.

Finally, it is worth commenting that the findings in [84] and [82], that electron-neutral reaction rates are well-approximated by Maxwellian-averaged rates, is replicated in this study. Differences in rate coefficients for deuterium ionisation and line radiation are negligible. Some differences in the total line-integrated particle source do exist in kinetic simulations (which takes into account ionisation and recombination as well as multi-step processes involving ex/de-excitation), but these are all under 10%, and are driven purely by differences in temperature profiles.

5.4 Discussion

The detachment behaviour observed in these simulations contrasts somewhat with the observation of flux rollover at $n_u \sim 2 \times 10^{19}$m^{-3} in the study by Dudson et al. in [90], which uses a similar simulation setup for the SD1D fluid code with $q_{in} = 50$ MWm^{-2} and $L = 30$m. With the model presented here, q_{in} must be reduced to below 25 MWm^{-2} to reach detachment at this connection length. A separate investigation has highlighted that an underestimation of the ionisation rate at high electron densities in SD1D may be the part of the reason for this

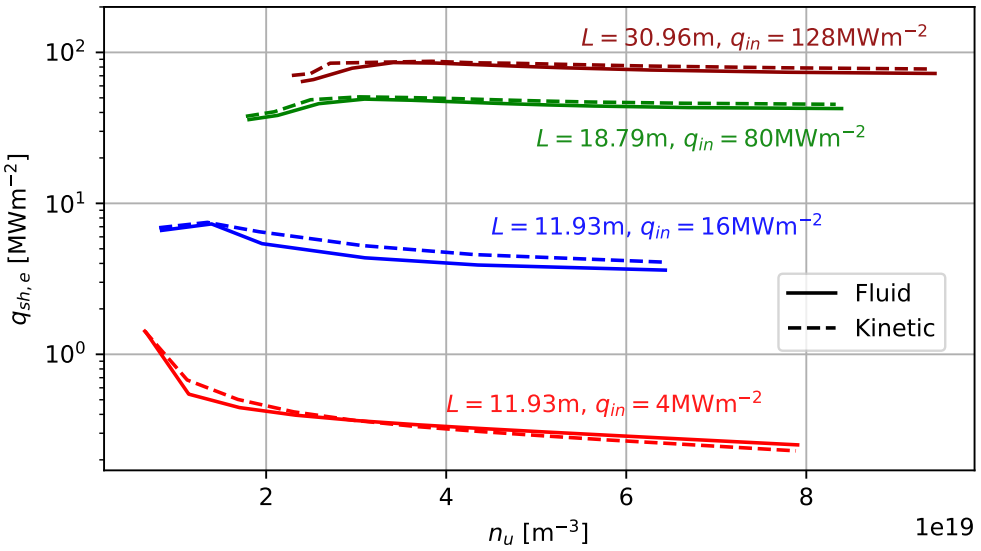

Figure 5.7: Sheath heat flux from electrons, $q_{sh,e}$, for kinetic and fluid simulations, grouped into density scans at different connection lengths and input powers.

difference [92], as well as the fact that SOL-KiT does not include impurity radiation or flux tube expansion.

The uptick in T_e close to the target in the least collisional simulations is seen in the hotter T_e profile in Figure 5.3a and in a spike in the heat flux ratio in Figure 5.3b, where $q_{\parallel,e}^{kinetic}$ can become negative in some simulations. This is the reason why the least collisional simulations do not have the largest differences in target temperatures (Figure 5.4) despite exhibiting higher flux suppression, where the uptick in T_e close to the wall to some extent cancels the increased temperature gradient. This feature comes primarily from the perpendicular electron temperature, which has been seen elsewhere [**?**, 128], where it is proposed to be related to an enhancement in the parallel flux of the perpendicular electron energy.

The results in Figure 5.2 suggest that a kinetic treatment of electron transport does not predict easier access to detachment. However, it should be said that only the most collisional density scan considered here actually reaches detachment, which is where kinetic effects are weakest, and it is possible that differences in detachment thresholds may exist in conditions with higher $T_{e,u}$.

The largely unchanged target flux behaviour in simulations with kinetic electrons, along with

broadly similar heat loads to the walls (Figure 5.7), is indicative of the fact that a kinetic electron treatment does not significantly change the particle, momentum or power balance at equilibrium in this 1D SOL model. This is despite strong heat flux suppression (Figure 5.3) and enhancement of the sheath heat transmission coefficient (Figure 5.6). This can be understood as resulting from the fact that heat transport is primarily determined by the input power q_{in}. While a modified temperature profile is needed in kinetic mode to achieve the same parallel heat flux in these simulations, this is compensated by an enhanced γ_e which gives a similar $q_{sh,e}$, leaving the power balance broadly unchanged. In addition, differences in the temperature profile are insufficient to significantly change the particle source from electron-neutral interactions.

This power balance behaviour would not necessarily continue to be the case in the presence of strong radiation sinks from impurities, where modified temperature profiles and reaction rates could lead to differences in overall energy transport. This is the subject of an ongoing study.

The unchanged power balance despite the presence of kinetic effects in parallel heat flux and γ_e suggests that any attempt to capture kinetic effects in a fluid framework would need to consider both phenomena. As such, approaches which treat only the modified heat flux [101] or the boundary condition [77] may not provide better predictive power than a purely fluid model.

The strong enhancements to γ_e are a result of the modified potential drop across the sheath when calculated kinetically. This depends on v_c, the cut-off velocity at which the electron distribution at the sheath is truncated. The value of v_c is set to ensure ambipolar particle flux, and is therefore somewhat sensitive to a strongly enhanced tail of the electron distribution, of the kind observed in Figure 5.5. This may therefore have consequences for measurements of the electron heat flux, which requires knowledge of γ_e, and the electron temperature, where electrons are assumed to be close to Maxwellian. In [37], Tskhakaya et al. observed large discrepancies in simulated Langmuir probe measurements of T_e due to the departure of the electrons from Maxwellian. Similarly to the study presented here, the largest discrepancies were seen at intermediate collisionalities.

It is worth noting that the most collisional kinetic simulations here exhibit a γ_e which is ~ 0.5

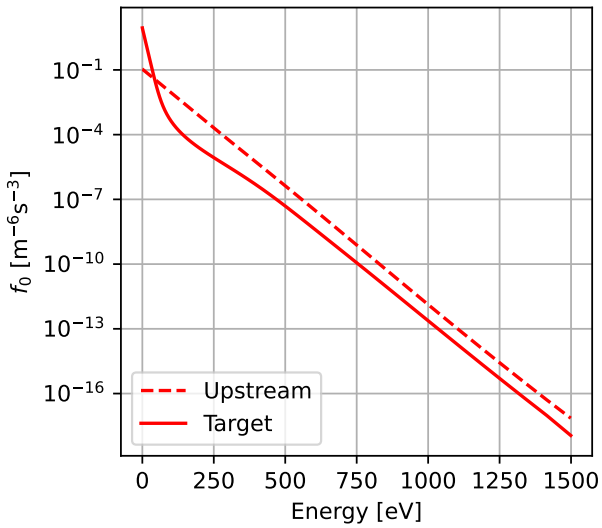

Figure 5.8: Electron energy distributions at two locations, upstream ($T_e = 39.9eV$) and close to the wall ($T_e = 8.0$eV). Electrons are close to Maxwellian upstream, and the fast tail survives to some extent further downstream. The gradient of the tail, related directly to the temperature on these axes, is the same in both cases.

higher than the classical value (3.20). Since the electron and ion momenta are treated separately and used to solve for the electric field in this model, this residual discrepancy is not from the pre-sheath acceleration of the ions. Instead, it is a result of the departure of the electrons from Maxwellian at the wall.

As discussed, and shown in [84] and [82], electron-impact ionisation rates of hydrogen are very well approximated by a Maxwellian distribution. This is unsurprising when considering the distribution shown in Figure 5.5, which is non-Maxwellian in the tail but very close to Maxwellian in the thermal bulk. Given the energy threshold of inelastic processes involving hydrogen are all at or lower than 13.6eV, the Maxwellian bulk electrons dominate the rates. This does suggest however that inelastic processes with threshold energies $\gtrsim$ 50eV (e.g. ionisation of high-Z impurities) may exhibit strong kinetic enhancement due to the presence of this enhanced tail. An ongoing study is currently investigating this.

The enhanced tail of the electron distribution seen close to the wall in these simulations is an imprint from upstream, as can be seen clearly in Figure 5.8, where the upstream distribution is plotted alongside that close to the target. Therefore, if we assume the tail of the distribution at the target has temperature $T_{e,t}^{tail} = T_{e,u}$, then two conditions existing simultaneously produce

a 'strongly enhanced' tail, which can lead to strong kinetic effects as discussed. These are $T_{e,u} \gg T_{e,t}$ and small $\nu^*_{e,u}$.

In this study, we see that the imprint can survive up to moderate values of $\nu^*_{e,u}$ and hence drive kinetic effects, for example in the peak enhancement to γ_e occurring at $\nu^*_{e,u} \simeq 20$ (Figure 5.6). It is the interplay of upstream collisionality and parallel temperature drops which determines the strength of this imprint. For tokamak edge plasmas with large $T_{e,u}$ as well as significant power dissipation via impurities, we might expect both of these conditions to be satisfied.

Contrary to the heat flux suppression, which appears to be a monotonic function of $\nu^*_{e,u}$, the enhancement to γ_e is more complex. It peaks at $\nu^*_{e,u} \simeq 20$, but also appears to increase for increasing $T_{e,u}$ at constant $\nu^*_{e,u}$. If this behaviour can be extrapolated to reactor-class devices then we may expect significant deviations from classical values of γ_e. This is discussed further in the next section.

5.5 Scaling relationships for observed kinetic effects

Any attempt at capturing kinetic effects at equilibrium in a fluid model of the scrape-off layer would appear to need to capture both modifications to the heat flux and enhancement to the sheath heat transmission coefficient. While models do exist for the former [93, 99, 102], they do not typically provide a self-consistent method for calculating modifications to the boundary behaviour. In [75], Tskhakaya et al. provide fits to the modifications to γ_e and parallel heat flux for the time-dependent response to a simulated edge-localised mode (ELM). Here, fits to the kinetic modifications to γ_e and $q_{\parallel,e}$ seen at equilibrium across a range of $T_{e,u}$ and n_u (and hence $\nu^*_{e,u}$) have been presented as functions of basic SOL parameters.

The approach taken in developing the relationships presented here has been to parameterise each simulation in terms of SOL quantities which are either control parameters or are easily obtainable from experiment or simulation. We can then quantify the two strongest kinetic effects observed in the kinetic simulations, which will be called kinetic factors. These are the

line-averaged heat flux suppression

$$f_{\kappa_e} = \frac{1}{L}\int q_{\parallel,e}^{kinetic}/q_{\parallel,e}^{SH}dx,$$

and the enhancement to γ_e,

$$\Delta\gamma_e = \gamma_e^{kinetic} - \gamma_e^{fluid}.$$

We have then used a least squares fit, allowing a set of fit parameters to vary, to find combinations of these SOL parameters which provide the best predictive power for the kinetic factors. In general, it has been found that there are several forms of the relationships between these kinetic factors and SOL parameters which provide a comparably good fit. In this case, it has been chosen to present fits which are functions of a small number of SOL parameters to avoid over-fitting the data and keep the approach simple, and which also have physically realistic asymptotic behaviour (for example, f_{κ_e} should be close to 1 at high collisionality).

The fits presented here are in terms of control/upstream SOL parameters only. If there is knowledge of the target conditions, for example in a SOL fluid code, relationships with very good predictive power have been found, in particular for $\Delta\gamma_e$. One example is provided below. However, it has been found that some of these do not extrapolate well to conditions where the upstream collisionality is low and power dissipation is large, for example due to impurity radiation. Conditions of this nature have not been simulated yet with SOL-KiT, although this is planned for future work.

The proposed relationship for the heat flux suppression is

$$f_{\kappa_e} = a\exp\big\{(b(\nu_{e,u}^*)^c)\big\} + d, \tag{5.2}$$

with

$$a = 0.696, \quad b = -8.059, \quad c = -1.074, \quad d = 0.260.$$

This is a function of $\nu_{e,u}^*$ only, which was found to be sufficient for an accurate prediction of f_{κ_e}. This is plotted against the simulation data in Figure 5.9, where the RMS error on the fit

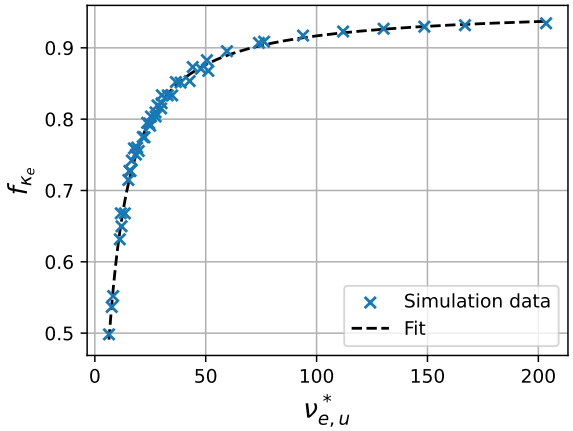

Figure 5.9: The variation of f_{κ_e} as a function of $\nu^*_{e,u}$ in simulations alongside the fit in equation (5.2).

is 0.01. There is clearly significant heat flux suppression at low upstream collisionalities. If this behaviour can be extrapolated beyond the region of $\nu^*_{e,u}$ explored here, this will lead to increased temperature gradients in sheath-limited regimes where the plasma would otherwise be expected to be nearly isothermal. This can be seen to some extent in the temperature profiles of the low collisionality runs in Figure 5.3a.

For the enhancement to the electron sheath heat transmission coefficient, we have

$$\Delta\gamma_e = \frac{a(q_{in})^b \exp\left(c\nu^*_{e,u}\right)}{1 + d\exp\left(e\nu^*_{e,u}\right)} + 0.5 \tag{5.3}$$

with

$$a = 9.93 \times 10^{-4}, \quad b = 0.186, \quad c = 0.514, \quad d = 2.62 \times 10^{-4}, e = 0.553.$$

This is shown in Figure 5.10 and compared to simulation data for several values of q_{in}. The RMS error on this fit across all simulation data is 0.18. It can be seen that this fit captures both the peak to $\Delta\gamma_e$ at $\nu^*_{e,u} \sim 20$ and that fact that the peak increases slowly with q_{in}. It also drops to 0.5 for $\nu^*_{e,u} \lesssim 7$, but there is some disagreement with the simulation data in this regime so precise values may be higher. This low collisionality behaviour is somewhat speculative, but it is reasonable to expect that $\Delta\nu^*_{e,u}$ will at any rate be small at low collisionalities. This is because temperature gradients, which appear to be a necessary condition for significant enhancement to γ_e, are likely to be smaller at very low collisionalities than for intermediate

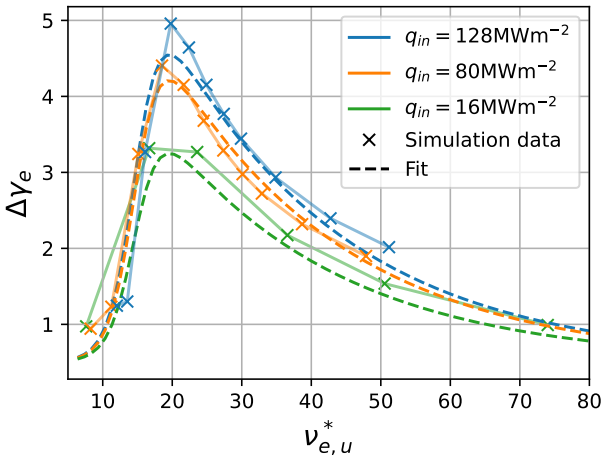

Figure 5.10: Fit to $\Delta\gamma_e$ from equation (5.3) as a function of $\nu^*_{e,u}$ for several values of q_{in}. Data from simulations with the same q_{in} is shown alongside.

$\nu^*_{e,u}$. This is, however, complicated somewhat by the increased heat flux suppression predicted at low collisionalities.

By including conditions at the target into the fits, and considering relationships of the form $\Delta\gamma_e = a_0 \prod_i X_i^{a_i}$, where a_i are fit parameters and X_i are SOL parameters, it was found that

$$\Delta\gamma_e = a \left(\frac{n_u}{10^{20}}\right)^b (T_{e,u})^c (T_{e,t})^d (q_{in})^e,$$

with $a = 3.768, b = -1.123, c = -1.603, d = -0.886, e = 1.556$ is a good fit to the data, with an error of 0.10. Fits in terms of fewer SOL parameters than this have also been found, but the error is comparable to that of the fit in (5.3). In addition, it was found that this fit predicts unphysically large values of $\Delta\gamma_e$ when upstream collisionality is small but temperature gradients are large. This was found to be a common issue with fits of this kind, where SOL conditions upstream and at the target are correlated and therefore there is a risk of over-fitting to the simulation data presented here. As such, it is recommended to use (5.3) in regimes not studied here, despite slightly worse agreement with the SOL-KiT data, because physically realistic limiting behaviour is ensured. It is also worth noting that no relationship of this kind was found to perform better for f_{κ_e} than (5.2).

The scalings presented here are straightforward to implement in a fluid model. Because of the spatial variation in heat flux suppression observed in these simulations (see Figure 5.3b),

implementing the line-averaged quantity f_{κ_e} as a prefactor to the Spitzer-Härm conductivity may not yield accurate temperature profiles, but should be adequate for predicting the overall power balance and target temperatures. These scalings may also be used in simple analytical SOL models such as the modified two-point model [129] or the Lengyel model for predicting detachment onset with radiating impurities [106].

To test these relationships, (5.2) and (5.3) have been implemented in the fluid version of SOL-KiT, using self-consistent values of $\nu^*_{e,u}$, to calculate the modifications to $\gamma_e = \gamma_e^{fluid} + \Delta\gamma_e$ and $q_{\parallel,e} = f_{\kappa_e} q^{SH}_{\parallel,e}$. In Figure 5.11a, the target temperatures in kinetic simulations are compared with those in fluid simulations, with and without the kinetic corrections. Temperature profiles for a particular simulation are shown in Figure 5.11b. Agreement with $T_{e,t}$ is good, with the RMS error reduced from 43.3% to 8.2% with the addition of the kinetic corrections. Temperature profiles show that agreement is improved at the upstream and target locations, but differences exist in the rest of the domain and the T_e uptick close to the wall is not captured. This is expected due to the line-averaging of f_{κ_e}.

If we assume these scalings can be applied for larger values of $T_{e,u}$ and Ln_u, then for the plasma profiles obtained with the ITER scenario modelled in [126] ('standard transport' case; profiles shown in Figure 5.12b), Figure 5.12a shows the expected values of kinetic factors as a function of radial distance at the outer midplane. Here, $q_{in} = 800\text{MWm}^{-2}$ at the separatrix has been assumed, with a radial decay width of $\lambda_q = 3\text{mm}$. The collisionality ranges from $\nu^*_{e,u} \sim 6 - 25$. We see values of $\Delta\gamma_e$ up to 2.59 at the peak, representing an enhancement of around 50% over the classical value, and over 50% heat flux suppression just beyond the separatrix. It would be straightforward to implement (5.2) and (5.3) in a code such as SOLPS-ITER to explore the significance of such effects.

As an additional test of how these scaling relationships behave in reactor relevant conditions, the scaling equations were implemented (by co-author M. Wigram) into a two-point model (2PM) [24] solver, with modifications to the thermal conduction and sheath heat transmission coefficient provided by equations (5.2) and (5.3). This is used to solve iteratively for target conditions, with and without the kinetic factors, in a range of SOL conditions similar to those

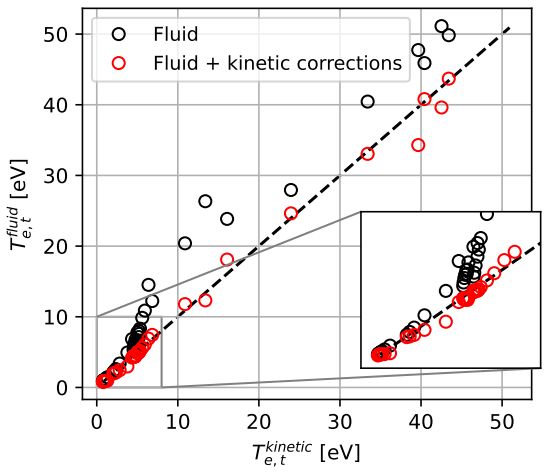

(a) Target electron temperatures in kinetic simulations (x-axis) compared with fluid / fluid with kinetic corrections.

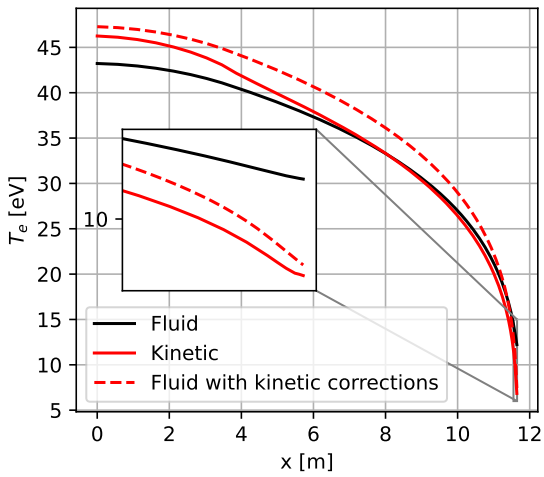

(b) Fluid, kinetic and fluid with kinetic corrections temperature profiles for a simulation with $q_{in} = 64\text{MWm}^{-2}$, $Ln_u = 0.3 \times 10^{21}\text{m}^{-2}$.

Figure 5.11: Adding kinetic corrections to SOL-KiT fluid mode using equations (5.3) and (5.2).

expected in the SPARC tokamak [33]. The range of $\nu^*_{e,u}$ covered was ∼0.2-100. Significantly steeper temperature gradients, with higher $T_{e,u}$ and lower $T_{e,t}$, were observed at low and intermediate collisionalities due to the added f_{κ_e} and $\Delta\gamma_e$ factors. This is part of a forthcoming study which is planned to be published elsewhere.

A caveat to the fits presented is that the plasma model in SOL-KiT does not currently include flux tube expansion (or other SOL geometry effects) or contributions from molecules or impurity species. The former will alter plasma behaviour, in particular with respect to detachment, and there may also be a kinetic effect due to the mirror force on the electrons. The latter will represent additional particle, momentum and energy sources/sinks. An ongoing project to redevelop SOL-KiT with a more flexible physics model, as well as improved computational efficiency and parallelisation, should make it possible to study kinetic effects in the presence of such additional physics.

5.6 Conclusion

Kinetic studies of electron transport in tokamak scrape-off layer plasmas across a range of input powers and densities have been presented, under steady-state conditions.

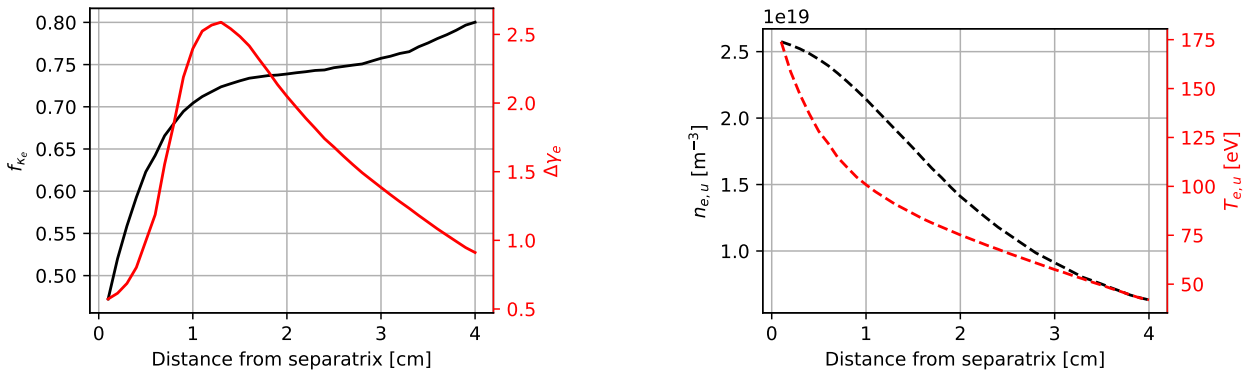

(a) (b)

Figure 5.12: Radial profiles at the outer midplane of (a) kinetic factors and (b) plasma density and electron temperature for the ITER scenario modelled in [126].

One of the primary aims of this study has been to validate the local approximation in fluid models, which are frequently employed to model SOL plasmas. We see that, for SOL equilibria, a kinetic treatment of the electrons does not change qualitative behaviour in terms of the particle flux to the target with this plasma model, as shown in Figure 5.2, despite changes to the electron temperature profiles and reductions in the target temperatures (Figure 5.3).

Typically, it has been assumed that the classical value of γ_e is valid at equilibrium, but here there are differences of up to 98%, as shown in Figure 5.6. A qualitative understanding of this enhancement in terms of an imprint of the fast electrons from upstream on the electron distribution at the target has been provided. The presence of this enhanced tail is predicted to have significant impacts on collision rates for inelastic processes with threshold energies $\gtrsim$ 50eV, for example the ionisation of plasma impurities. This is the subject of an ongoing study.

The enhancement of γ_e and reduction in $q_{\parallel,e}$ at equilibrium is shown to follow scalings based on basic SOL parameters, (5.2) & (5.3). The performance of these fits is shown in Figures 5.9 and 5.10. To test the ability of these corrections to capture kinetic effects in SOL simulations, it has been shown that implementing them in the fluid version of SOL-KiT does improve agreement with the fully kinetic T_e profiles. While there are caveats to the use of these scalings outside of SOL-KiT simulations, particularly in relation to the aspects of SOL physics not included in the model used here, it does suggest it is viable to capture kinetic effects at equilibrium in studies of future devices, either in fluid codes or reduced analytical models. Extrapolating to the ITER

tokamak for example does predict significant kinetic effects, suggesting at the very least that further study into non-local parallel transport in reactor-class tokamaks is warranted.

To the authors' knowledge, this is the first attempt at providing relatively simple scaling laws for kinetic effects in equilibrium SOL plasmas. The principle that kinetic effects are directly related to basic descriptors of SOL conditions is a potentially useful approach to analysing their significance.

The modifications to γ_e and $q_{\parallel,e}$ in conjunction with good agreement in power balance and target particle flux behaviour (discussed in Section 5.4 and shown in Figure 5.2), suggest that both effects contribute in a way which approximately cancels. As such, attempts to capture kinetic effects in fluid models should treat both phenomena simultaneously.

In this study, the changes to γ_e and $q_{\parallel,e}$ are in contrast to the behaviour at equilibrium found using the PIC code BIT1 in [130]. There, γ_e is found to be well-approximated by the classical value, and $q_{\parallel,e}$ is a non-monotonic function of collisionality, which is contradicted by (5.2). There are significant differences in the simulations carried out in [130], in particular that plasma-neutral interactions were neglected and that only attached regimes were studied. Furthermore, the differences in γ_e seen here are of a similar magnitude to those seen with the KIPP code in [81].

It should also be noted that this investigation has been done for equilibrium plasma conditions. For the sheath boundary condition in particular, much stronger kinetic effects may be present in transient regimes as shown in [83, 130], albeit for short durations relative to inter-ELM equilibria.

In this chapter, we have explored in detail how a kinetic treatment of the electrons changes parallel heat transport behaviour. The main drawback of the simulations presented here is that they do not include impurities, which are expected to be present to some degree in most future tokamak experiments, and which will will significantly alter the power balance in SOL plasmas. There is therefore a strong motivation to begin exploring how these phenomena might interact, and this will therefore be the focus of the next chapter.

Chapter 6

Kinetic effects in plasma-impurity reaction rates

Abstract

Plasma-impurity reaction rates are a crucial part of modelling impurity transport in tokamak scrape-off layer (SOL) plasmas. To avoid calculating the full set of rates for the large number of important processes involved, a set of effective rates are typically derived which assume Maxwellian electrons. Here, the validity of this approach is investigated by computing the full set of rate equations for a fixed plasma background from kinetic and fluid SOL simulations. Results are presented for lithium, beryllium, carbon, nitrogen and neon. In kinetic SOL simulations, the electron distribution is non-Maxwellian close to the wall and the plasma profiles are modified, and both effects are considered here. It is found that the former results in considerable enhancement to ionization and excitation rates for some impurity ions at low electron temperatures, up to many orders of magnitude. However, it is found that the modified profiles act to reverse the impact of this rate enhancement to some extent. The net effect, comparing a fully kinetic to a fully fluid treatment of reaction rates, is shown to result in changes to the average ionization of up to $+0.38$ for neon and -0.73 for nitrogen in the region close to the wall. Differences of order $\pm 50\%$ in the total radiated power are observed at low and moderate SOL collisionalities,

but this is seen in regimes where the magnitude of the radiated power is small for both treatments. Agreement is good for all quantities in the hotter upstream region.

6.1 Introduction

The work presented thus far in this thesis has focussed on the effects of modelling electron transport kinetically. An important missing piece of the physics in the simulations presented in Chapters 4 and 5 is the presence of impurities - elements present in the plasma which are not part of the fuel mixture. Impurities can significantly impact the plasma behaviour in both the edge and the core, and so their behaviour and interaction with the fuel plasma must be understood. Of particular interest is the plasma-impurity reaction rates, since this defines the radiative and transport properties of a given species present in a tokamak plasma.

The vast majority of tokamak devices currently under design or construction plan to utilise the radiative properties of an impurity species to achieve favourable conditions at the plasma-surface interface. A typical approach to modelling impurities in SOL plasmas is to take effective rate coefficients from a database such as ADAS (`https://open.adas.ac.uk/`), which assumes Maxwellian electrons, and use these as inputs to a transport model for the fuel and impurity plasma species (e.g. [58,131–133]). However, as seen in previous chapters, the electrons may be far from Maxwellian in SOL plasmas with moderate to low upstream collisionality and steep temperature gradients, which are the conditions envisaged in reactor-class devices. For the case of electron-impact reactions such as ionization and excitation, where there is a minimum energy which the incident electrons must possess for the reaction to occur, a modification to the number of particles in the tail of the distribution may significantly alter the rate at which the reaction proceeds. Furthermore, a kinetic treatment of the electron transport can lead to modified plasma profiles, which may be expected to also change the impurity physics.

To illustrate the effect of non-Maxwellian electron distributions, we may compare what happens to a SOL-relevant impurity species in the presence of Maxwellian electrons with a situation where the electron distribution contains a (small) fraction of hot particles. Using the SIKE

collisional radiative model, as described in Section 3.5, this is shown for neon in Figure 6.1. For the 'two-temperature' solution, we use an electron distribution which is the sum of a bulk Maxwellian at n_{cold}, T_{cold}, and a hot Maxwellian at $n_{hot} = 10^{-5} n_{cold}$, $T_{hot} = 100\text{eV}$[1]. For an electron density of $n_e = 10^{19}\text{m}^{-3}$, the temperature is varied from $T_e = 0.5$ to 25eV. The presence of a population of hot electrons clearly modifies the ionization balance, as can be seen in the density profiles for each ionization stage, Figure 6.1a, and the average ionization, Figure 6.1b.

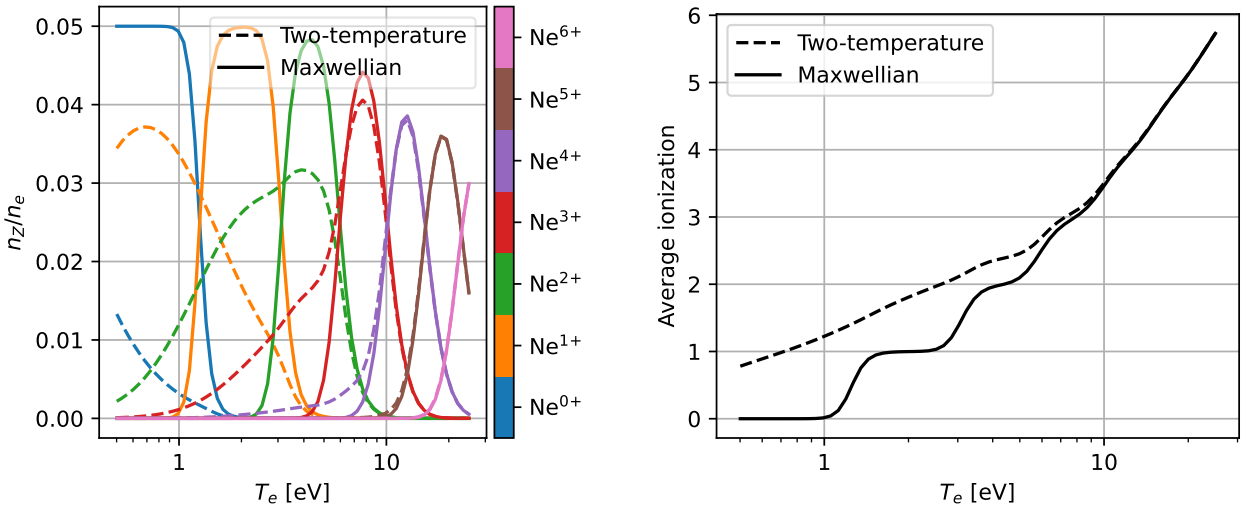

(a) Fractional density of each ionization stage.

(b) Average ionization.

Figure 6.1: Fractional density and average ionization of neon as a function of electron temperature. Results for Maxwellian electrons are shown in solid, dashed lines are results for a two-temperature distribution with 0.001% of electrons at $T_{hot} = 100\text{eV}$.

To investigate this, SIKE will be used to assess the validity of Maxwellian-averaged plasma-impurity reaction rates using electron distributions from equilibrium SOL-KiT simulations of a realistic scrape-off layer. We will also explore the differences in plasma-impurity physics between fluid and kinetic SOL-KiT simulations. The SIKE model will be very briefly restated along with important quantities describing the impurities (6.2), the simulation setup will be presented (6.3), followed by the results (6.4) and discussion (6.5).

[1]The density of this distribution is then $n_e = n_{hot} + n_{cold}$, and the temperature is $T_e = (n_{cold}T_{cold} + n_{hot}T_{hot})/n_e$.

6.2 SIKE model and derived atomic physics quantities

As was described in Section 3.5.1 (some of which is briefly restated here), for a given impurity species we solve the density evolution equations for each tracked atomic level, assuming no transport or external sources/sinks. For an atomic state k, with a given ionization level and electronic configuration, the density evolves according to

$$\frac{dn_k}{dt} = n_e \sum_j n_j K^k_{e,j} + \sum_j A^k_j n_j - n_k n_e \sum_j K^j_{e,k} - n_k \sum_j A^j_k + n_e \sum_j r^k_j n_j - n_e n_k \sum_j r^j_k, \quad (6.1)$$

where $K^k_{e,j}$ is the rate coefficient for the production of particles in state k due to collisions with electrons and particles in state j (ionization, three-body recombination, excitation and de-excitation), A^k_j is the radiative transition rate from state j to k (which includes spontaneous de-excitation and auto-ionization), r^k_j is the radiative recombination rate from j to k, and n_e is the electron density. The collisional rates are calculated by integrating over the isotropic part of the electron distribution, f_0,

$$K^k_{e,j} = \frac{4\pi}{n_e} \int_0^\infty v^2 (v \sigma^k_{e,j}(v)) f_0(v) dv. \quad (6.2)$$

The system of equations defined by (6.1) for all k is written in matrix form,

$$\frac{d\mathbf{n}}{dt} = \mathbf{M}\mathbf{n}, \quad (6.3)$$

where $\mathbf{n}$ is the vector containing all n_k, and the rate matrix $\mathbf{M}$ is filled according to

$$M_{jk} = n_e K^j_{e,k} + A^j_k + n_e r^j_k, \qquad k > j \quad (6.4)$$

$$M_{jk} = n_e K^j_{e,k}, \qquad k < j \quad (6.5)$$

$$M_{jj} = -\sum_{k \neq j} M_{kj}. \quad (6.6)$$

We solve for equilibrium state densities by evolving (6.3) using implicit time integration.

From 6.3, we can compute a set of effective ionization and recombination coefficients between

the ground states of each ionization stage. In Section 3.5.1, it is shown how to calculate this via an effective rate matrix. Alternatively, we can define it explicitly in terms of the elements of $\mathbf{M}$. The effective ionization coefficient is

$$K_{eff}^{ion,z} = K_{e,z}^{z^+} - \mathbf{K}_{e,i'}^{z^+}\mathbf{M}_{ii'}^{-1}\mathbf{M}_{iz}, \tag{6.7}$$

which describes ionization from a given ground state z to a ground state of a higher ionization stage z^+. Here, i and i' are indices of all non-ground states in the same ionization stage as z, and $\mathbf{K}_{e,i'}^{z^+}$ is the array of all possible ionization coefficients from states i' to z^+. Similarly, the effective recombination coefficients from a ground state z to that of a lower ionization stage z^- may be written

$$K_{eff}^{rec,z} = r_z^{z^-} - \mathbf{M}_{zi'}\mathbf{M}_{ii'}^{-1}\mathbf{r}_i^{z^-}, \tag{6.8}$$

where $\mathbf{r}_i^{z^-}$ is the array of all recombination coefficients from i to z^-.

It is often useful to compute the average ionization for the impurity species as a whole,

$$\bar{z} = \frac{\sum n_k z_k}{n_{z,tot}}, \tag{6.9}$$

where the summation is over all states, $n_{z,tot} = \sum n_k$ is the total impurity density, and z_k is the ionization of level k (i.e. the level has electric charge $+ez_k$).

Another useful output is the electron energy loss due to inelastic collisions with the impurity species, where we are typically interested in the contribution from each ionization stage separately. At equilibrium, the energy to drive radiative emission comes from electron collisional processes, so we can compute the electron energy loss from all z-ionized levels (denoted by the set Z) with

$$Q_z = \sum_{k,k' \in Z} A_k^{k'} n_k \varepsilon_k^{k'} = n_e \left(\sum_{k>k'} K_{e,k}^{k'} n_k \varepsilon_k^{k'} - \sum_{k<k'} K_{e,k}^{k'} n_k \varepsilon_k^{k'} \right), \tag{6.10}$$

where we have a sum over all radiative de-excitation transitions within Z. The second equality here represents the fact that, at equilibrium and without transport effects, the radiated energy is supplied by the cooling of the the electrons via collisional excitation and de-excitation.

Normalising to the electron and total impurity density gives a line emission coefficient,

$$L_z = \frac{Q_z}{n_e n_z} \tag{6.11}$$

It is also useful to aggregate both these quantities for all ionization stages, such that the total radiated power is

$$Q_{z,tot} = \sum_z Q_z, \tag{6.12}$$

which is simply summed over all ionization stages, and the average line emission per ion is

$$\bar{L}_z = \frac{\sum L_z n_z}{n_{z,tot}}, \tag{6.13}$$

where $n_z = \sum_{k \in Z} n_k$ is the density of particles of ionization stage z.

Note that there is an additional contribution to radiative losses from recombination, but this is small in the plasma conditions studied here and so is neglected in the analysis.

6.3 Setup

For a given plasma background, SIKE allows us to compute the impurity atomic state distribution. The plasma backgrounds used in this study come from equilibrium simulations with SOL-KiT, which is described in Section 3.1. The SOL-KiT simulations used are a subset of those presented in Chapter 5. The full details of these simulations are outlined in Section 5.2, with the key aspects repeated here.

These SOL-KiT simulations are for a scrape-off layer with connection length $L = 30.96$m, total input power $q_{in} = 128\text{MWm}^{-2}$. The line-averaged plasma plus neutral density, $\langle n \rangle$, was varied from $3 \times 10^{19}\text{m}^{-3}$ to $14 \times 10^{19}\text{m}^{-3}$, giving a range of upstream collisionality parameters, $\nu^*_{e,u} \simeq 10^{16} n_u / T^2_{e,u}$, from 12 to 51. The simulations were run for both kinetic and fluid electrons. In kinetic mode, the maximum resolved harmonic was $l_{max} = 3$. Figure 6.2 shows an example plasma profile and electron distribution for one of these simulations. Three distributions are

shown in Figure 6.2b: the distribution at a location close to the target from the kinetic run, an equivalent Maxwellian at the same local temperature and density, and a Maxwellian at the same location (but different temperature and density) from the fluid run. These three ways of treating the electrons will be used as the basis for the forthcoming analysis.

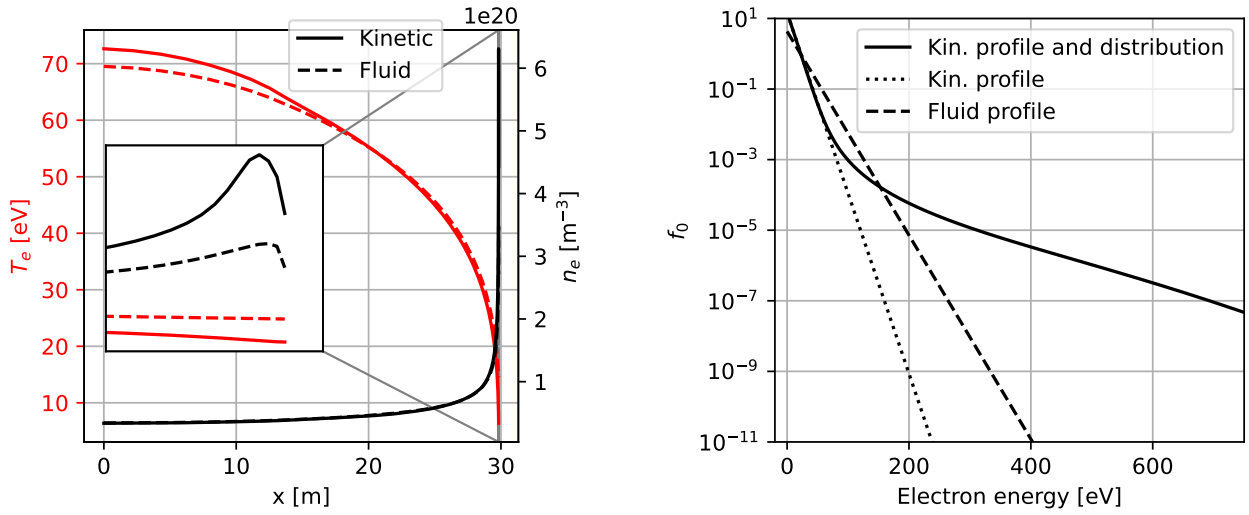

(a) (b)

Figure 6.2: (a): Example temperature and density profiles of a kinetic and fluid simulation used in this study, $\langle n \rangle = 4.7 \times 10^{19}\text{m}^{-3}$, $\nu^*_{e,u} = 19.8$. (b): Isotropic part of the electron distribution close to the target for this example simulation. Shown is the evolved distribution in the kinetic simulation ('Kin. profile and distribution'), a Maxwellian at the local temperature and density in the kinetic simulation ('Kin. profile'), and a Maxwellian at the temperature and density of the same location from the fluid run ('Fluid profile').

To compute the impurity atomic state densities, outputs from the SOL-KiT simulations were provided as input to SIKE. For the kinetic SOL-KiT simulations, these outputs were the electron distribution and velocity grid. The impurity state densities were then solved for both this electron distribution and Maxwellian electrons with the same T_e and n_e profiles. For SOL-KiT simulations with fluid electrons, the electron temperature and density profiles were provided as input to SIKE, and the distributions were assumed to be Maxwellian on the same velocity grid as the kinetic runs. The impurity species treated were lithium, beryllium, carbon, nitrogen and neon. The impurities were initialised to a Saha-Boltzmann distribution, and then evolved in time until convergence. The total impurity density was set to 1% of the local electron density in all runs.

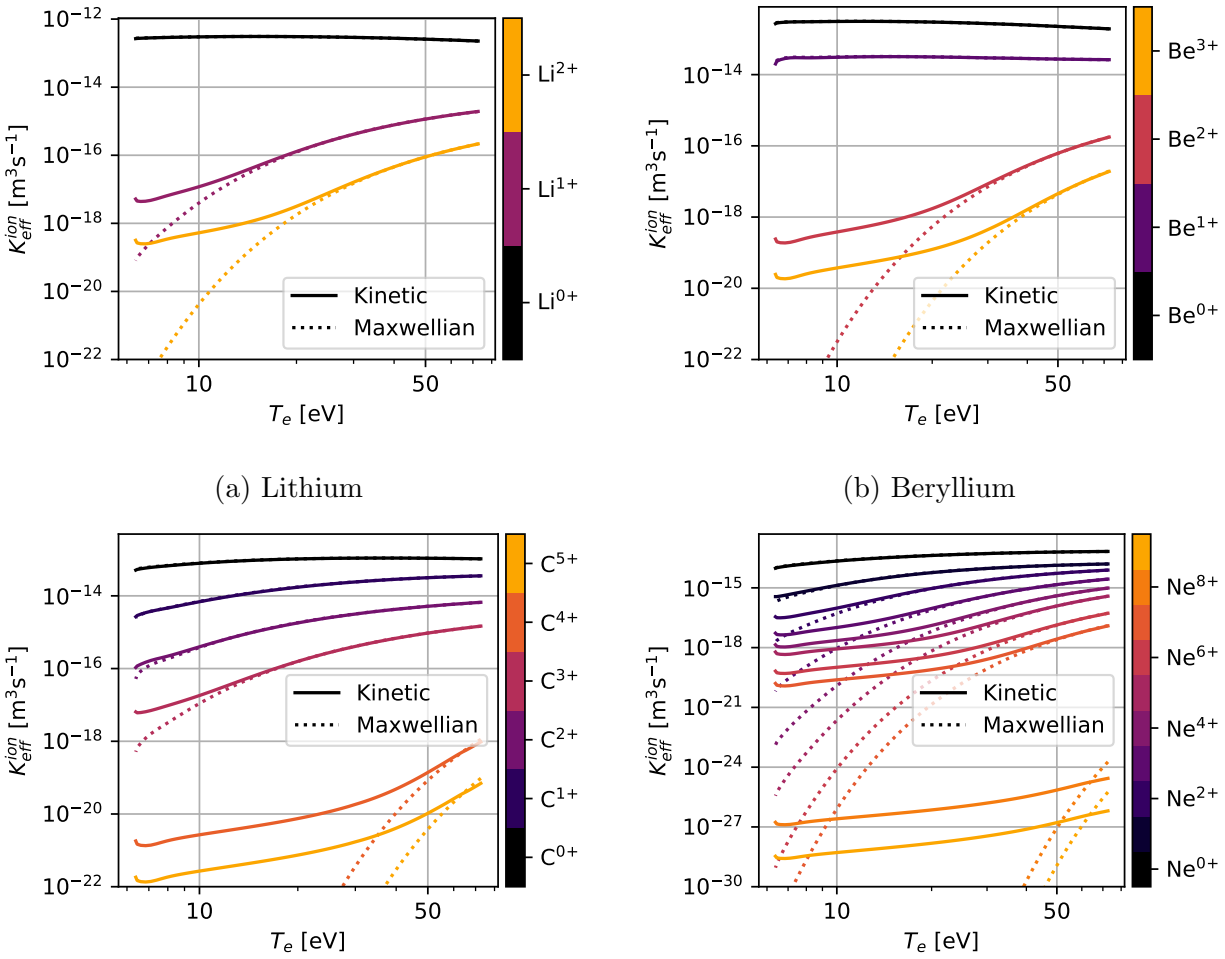

(a) Lithium

(b) Beryllium

(c) Carbon

(d) Neon

Figure 6.3: Effective ionization coefficients for lithium, beryllium, carbon and neon, where the plasma background is the kinetic run shown in Figure 6.2. Dashed lines are for the electron distribution from the SOL-KiT simulation, and solid lines are for Maxwellian electrons. The X^{Z+} labels refer to the particle before ionization, i.e. the process $X^{Z+} \rightarrow X^{(Z+1)+}$.

6.4 Results

The amount of relevant data generated in this study is quite large: five impurity species have been treated on 12 plasma backgrounds, with the electrons treated in three separate ways. It is informative to present some of this data in full, but to avoid the analysis becoming overly dense detailed results will in general be presented for only a subset of the modelled impurity species on a single plasma background (the one shown in Figure 6.2). Results for all impurity species across all plasma backgrounds will be presented for some aggregated quantities.

For all impurities across all plasma backgrounds, there are significant enhancements to the

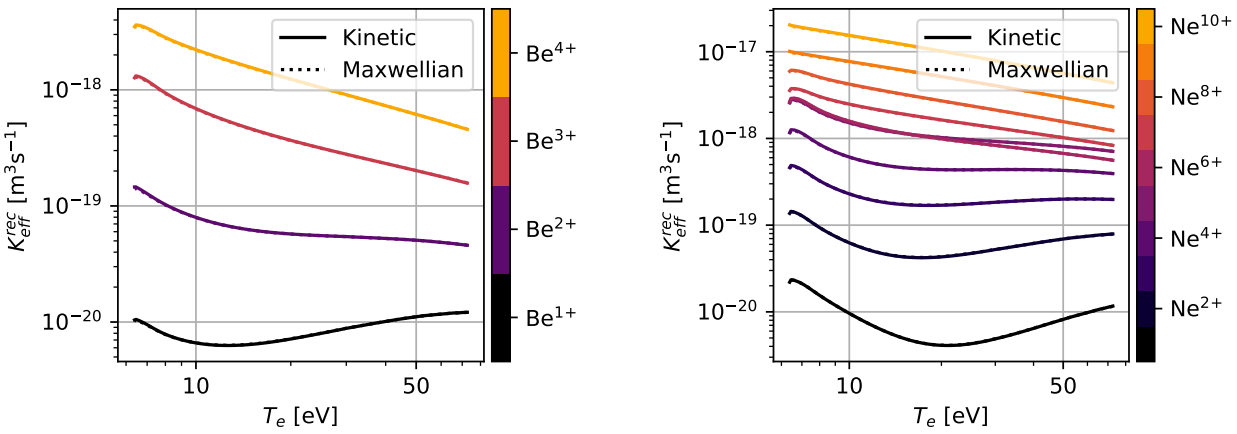

(a) Beryllium (b) Neon

Figure 6.4: Effective recombination coefficients for beryllium and neon, where the plasma background is the kinetic run shown in Figure 6.2. Dashed lines are for the electron distribution from the SOL-KiT simulation and solid lines are for Maxwellian electrons, but differences are minimal. The X^{Z+} labels refer to the particle before recombination, i.e. the process $X^{Z+} \rightarrow X^{(Z-1)+}$.

ionization rate coefficients, K_{eff}^{ion}, when solved for the simulated electron distributions and compared to Maxwellians. This is shown for lithium, beryllium, carbon and neon in Figure 6.3. The 'Maxwellian' calculation also uses the plasma profile from the kinetic run; we will discuss the effect of different plasma profiles between kinetic and fluid plasma simulations later in this section. From Figure 6.3, we see the kinetic enhancement to K_{eff}^{ion} is strongest for highly ionized impurity atoms at low temperatures, where the rate increases many orders of magnitude. This may be described as a flattening of the rates with respect to T_e, which is due to the presence of fast electrons from the hot upstream region in the cooler plasma close to the wall. Ionization rates of the neutral atom generally agree well for all impurity species. We do not necessarily expect a high proportion of highly ionized impurities to be present at low electron temperatures, so these changes may not be as drastic as it appears at first glance. This is discussed in more detail shortly.

It is interesting to note that there is a slight suppression of the ionization rate of Ne^{8+} and Ne^{9+} at the highest temperatures seen in Figure 6.3d. This results from the fact that the tail of the electron distribution is quite strongly depleted in the heating region in SOL-KiT simulations, an effect which correlates with the input power. It is possible that this is an artefact of the

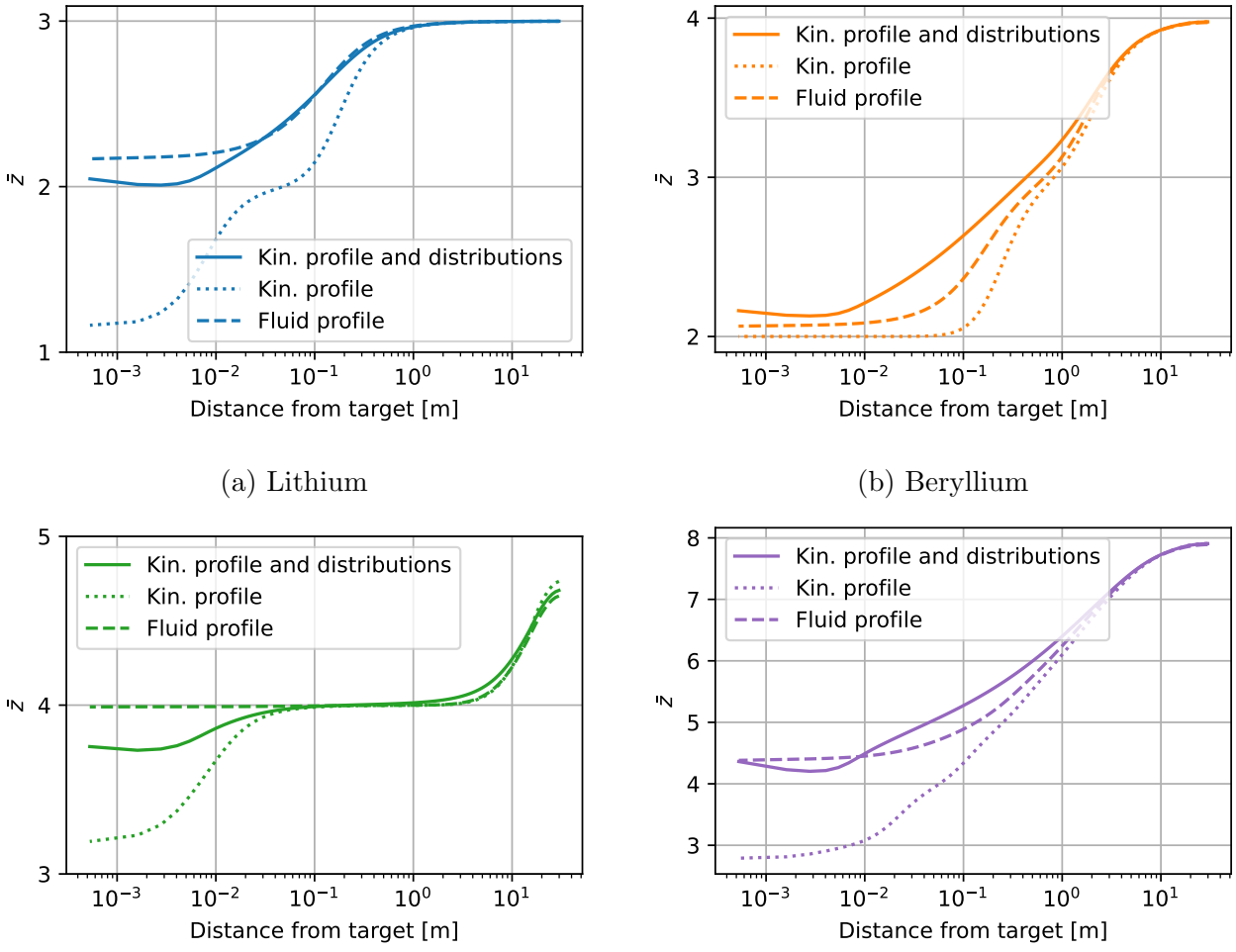

(a) Lithium

(b) Beryllium

(c) Carbon

(d) Neon

Figure 6.5: Average ionization for kinetic electrons, Maxwellian electrons on a kinetic plasma profile, and Maxwellian electrons on a fluid plasma profile.

heating operator implemented in SOL-KiT, but this would require further investigation.

In Figure 6.4, we compare the effective recombination rate coefficients, K_{eff}^{rec}, shown for beryllium and neon. We see very good agreement across all ionization stages at all temperatures, to within a few percent.

We can explore how these changes to the ionization coefficients, but not the recombination coefficients, affect the ionization balance of different impurity species. There are two kinetic effects to consider here: the departure of the electrons from Maxwellian, which we will call the distribution effect, and the modified temperature and density profiles in kinetic vs. fluid SOL-KiT simulations, which we will call the profile effect.

In Figure 6.5, we show the average ionization for several species, where we compare the results for kinetic electrons, Maxwellian electrons on the plasma profile from the kinetic SOL-KiT simulation, and Maxwellian electrons on the plasma profile from the fluid simulation. The x-axis here is now the spatial distance from the target instead of T_e because the fluid and kinetic SOL-KiT simulations cover different temperature ranges.

Differences in $\bar{z}$ peak close to the target. Differences between kinetic and Maxwellian electrons on the same profile are larger than between a fully kinetic and fully fluid treatment, suggesting that the distribution effect is cancelled out to some extent by the profile effect. This is perhaps intuitive, since the lower target temperatures in kinetic simulations also coincide with a population of hot electrons in the tail. For inelastic processes with some threshold energy, such as ionization, this enhanced tail will serve to increase reaction rates and close the gap with the Maxwellian-averaged rates at a higher temperature.

This effect is seen more clearly when we compare the difference in $\bar{z}$, as shown in Figure 6.6 for all impurity species. In Figure 6.6a, we plot the difference arising from the distribution effect as

$$\Delta\bar{z}^{d} = \bar{z}^{kin} - \bar{z}^{Max},$$

where $\bar{z}^{kin}$ is the average ionization for kinetic electrons from the kinetic SOL-KiT simulation and $\bar{z}^{Max}$ is that for Maxwellian electrons on the same plasma profile. In Figure 6.6b, we plot

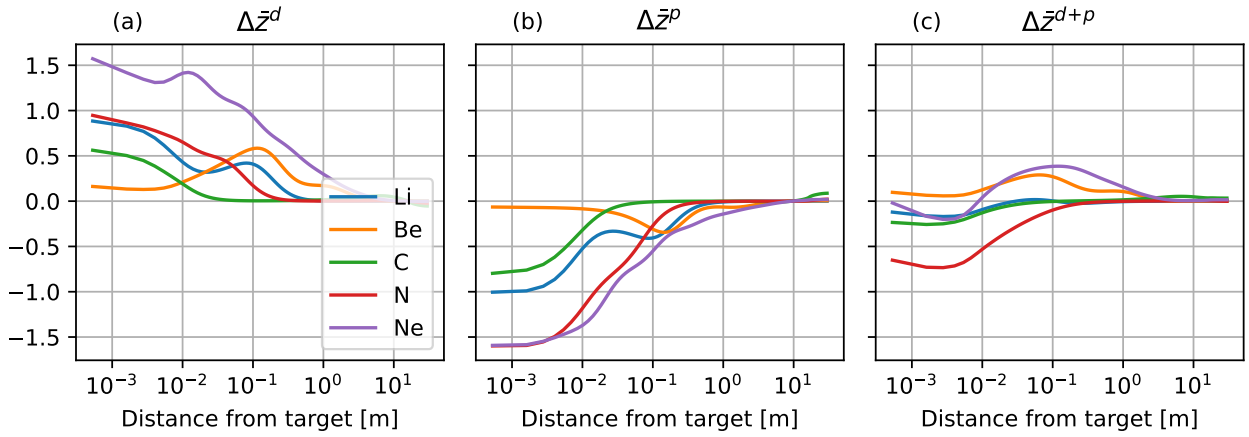

Figure 6.6: Difference in $\bar{z}$ for different treatments of the background electrons from a SOL-KiT simulation. (a): distribution effect, (b): profile effect, (c): profile + distribution effect (i.e. fully kinetic vs fully fluid treatment).

the difference arising from the profile effect,

$$\Delta\bar{z}^p = \bar{z}^{Max} - \bar{z}^{fl},$$

where $\bar{z}^{fl}$ is the average ionization for Maxwellian electrons on the fluid plasma profile. Finally, in Figure 6.6c, we show the difference arising from both effects,

$$\Delta\bar{z}^{d+p} = \bar{z}^{kin} - \bar{z}^{fl} = \Delta\bar{z}^d + \Delta\bar{z}^p.$$

We see that $\Delta\bar{z}^d$ is similar in magnitude but opposite in sign to $\Delta\bar{z}^p$ for all impurities, and that they partially cancel when considering the fully kinetic vs. fully fluid comparison, $\Delta\bar{z}^{d+p}$. There is good agreement between all three approaches in the hotter upstream region.

We may now turn our attention to the radiative losses predicted for impurities present in the plasma background which is being considered. In Figure 6.7, we see the excitation radiation per ion, L_z, for lithium, beryllium, carbon and neon. This is shown here for kinetic and Maxwellian electrons on the kinetic plasma profile from Figure 6.2. Similarly to the ionization rates, Figure 6.3, there are enhancements to the rate of energy loss due to excitation when the evolved electron distribution is used, particularly in the cold regions close to the target. These enhancements are almost exclusively found in the hydrogen-like (Li^{2+}, Be^{3+}, ...) and

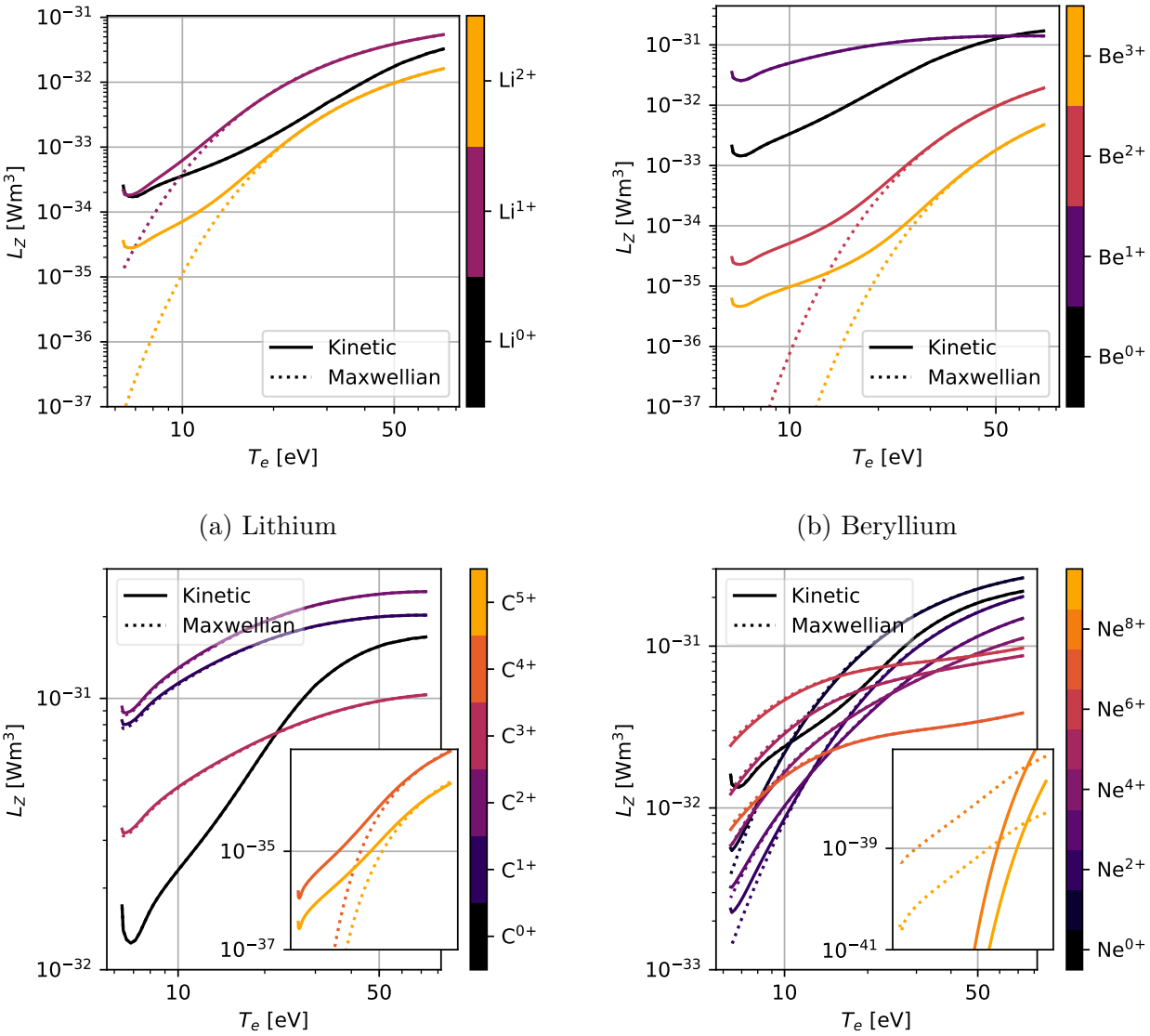

(a) Lithium

(b) Beryllium

(c) Carbon

(d) Neon

Figure 6.7: Cooling curves (excitation radiation per ion) for four impurity species for kinetic and Maxwellian electrons on a plasma profile from the kinetic SOL-KiT run in 6.2.

helium-like (Li^{1+}, Be^{2+}, ...) ions, and all other impurity ions show good agreement, at least to within a factor of two. This is most likely due to the fact that atomic energy level spacings are larger in these highly-ionized stages, meaning tail electrons are contributing more to the collisional excitation rates.

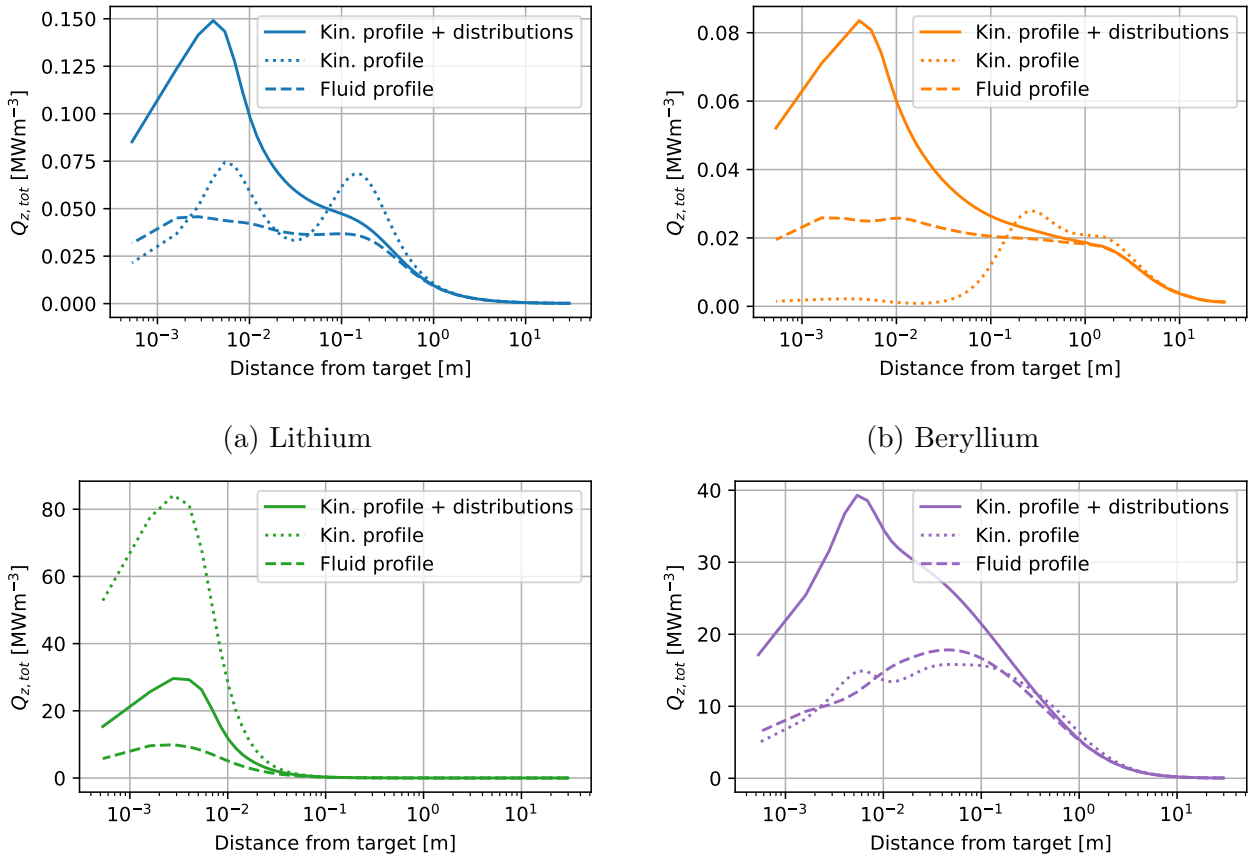

(a) Lithium

(b) Beryllium

(c) Carbon

(d) Neon

Figure 6.8: Spatial profiles of the impurity line radiation for the three different treatments of the electrons.

As in the case of the ionization rates, the cooling curves per ion do not tell the whole story, and we must look at the overall radiative loss rates. In Figure 6.8, the spatial profile of $Q_{z,tot}$ (defined in equation (6.12)) is plotted. In all cases, the fully kinetic calculation of $Q_{z,tot}$ ('kin. profile + distributions') peaks higher than the fluid treatment ('fluid profile') close to the target. Comparing just the effect of the electron distribution ('kin. profile + distributions' vs. 'kin. profile'), the sign and magnitude of the difference varies across impurity species. There are some differences in the characteristic shape of the radiation profiles, which will be discussed in the next section.

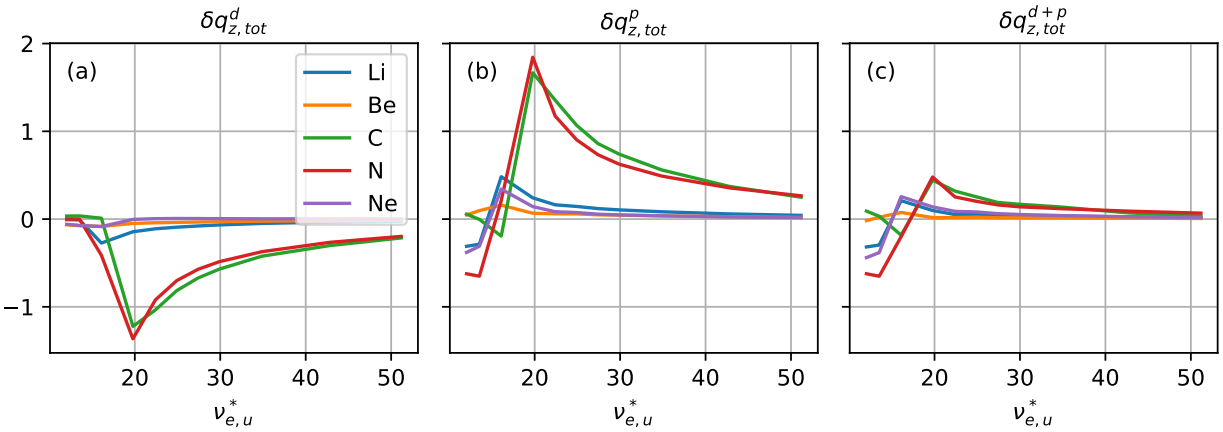

Figure 6.9: Relative differences in the total radiated power from impurities for different treatments of the background electrons from a SOL-KiT density scan. (a): distribution effect, (b): profile effect, (c): profile + distribution effect.

We will now consider the line-averaged radiative losses, $q_{z,tot} = \int_L Q_{z,tot} dx$, to gain an understanding of how these kinetic affects might change the power balance in a SOL plasma. Similarly to the results for the ionization balance, we will look at the contribution from the distribution effect and the profile effect separately. In Figure 6.9a, the distribution effect is considered,

$$\delta q^{d}_{z,tot} = (q^{kin}_{z,tot} - q^{Max}_{z,tot})/q^{fl}_{z,tot},$$

where $q^{kin}_{z,tot}$ is the total radiated power for the fully kinetic electrons, $q^{Max}_{z,tot}$ is for the Maxwellian electrons on the plasma profile from the kinetic SOL-KiT simulations, and this is normalised to $q^{fl}_{z,tot}$, which is for Maxwellian electrons on the fluid plasma profiles. In Figure 6.9b, the profile effect is considered,

$$\delta q^{p}_{z,tot} = (q^{Max}_{z,tot} - q^{fl}_{z,tot})/q^{fl}_{z,tot},$$

and in Figure 6.9c we compare the fully kinetic vs. fully fluid treatment,

$$\delta q^{d+p}_{z,tot} = (q^{kin}_{z,tot} - q^{fl}_{z,tot})/q^{fl}_{z,tot} = \delta q^{d}_{z,tot} + \delta q^{p}_{z,tot}.$$

To also understand how this behaviour varies with plasma conditions, this is plotted as a function of $\nu^{*}_{e,u}$ for the SOL-KiT density scan. Results are in Figure 6.9.

The distribution effect, Figure 6.9a, shows that Maxwellian-averaged rates on the same plasma

background generally lead to an over-prediction of the total radiated power from impurities. This is particularly the case for carbon and nitrogen at intermediate collisionalities, where the kinetic treatment results in $\delta q^d_{Z,tot} = -1.2$ at $\nu^*_{e,u} \simeq 20$. This is perhaps counter-intuitive, since we have seen in Figure 6.7 how kinetic electrons increase the energy rates from excitation. The reason for the reduction in $q_{z,tot}$ here is that different ions have different radiative properties, and changes in the ionization balance bring these to the fore. For carbon, the kinetic electrons increase the average ionization from ∼3 to ∼4, and C^{4+} is a much less efficient radiator (Figure 6.7c). Agreement for the other impurities is generally good, although some moderate differences are seen at low collisionalities.

The profile effect, Figure 6.9b, generally acts in the opposite direction to the distribution effect, but comparing the fully kinetic with the fully fluid treatment, Figure 6.9c, we see that the cancellation is not complete. For example, the suppression of radiated power for carbon and nitrogen from the distribution effect at $\nu^*_{e,u} \simeq 20$ has been turned into an approximately 45% enhancement in the radiated power compared to the fluid treatment. Differences remain in all impurity species at low collisionalities, and generally lead to a lower predicted value of $q_{z,tot}$ for the kinetic treatment, apart from in the case of carbon. There is convergence in the values of $q_{z,tot}$ predicted at high collisionalities for all impurity species, as expected.

6.5 Discussion

Calculations of the effective ionization rate coefficients show that assuming Maxwellian electrons can drastically underestimate the rates compared to a realistic electron distribution close to the target in SOL simulations, Figure 6.3. This is particularly the case for highly-ionized impurity ions at low electron temperatures, while the rates for neutral and near-neutral particles show good agreement at all temperatures. The reason for the rate increases is the accumulation of fast electrons close to the target in the SOL-KiT simulations considered, which is shown in Figure 6.2b as an enhanced tail of the electron energy distribution. For inelastic processes with high threshold energies, there are many times more electrons above the threshold than

for an equivalent Maxwellian distribution at the same temperature. However, since these enhancements occur at low T_e, where the average impurity ionization is low, the modifications to the ionization balance are moderate. Considering only the effect of the electron distribution, a kinetic treatment predicts higher average ionization by an amount which varies for the impurity species, but peaks at +1.6 in front of the target for neon (Figure 6.6a).

When the fully kinetic treatment of the ionization balance is compared with the fully fluid treatment, there is improved agreement, as seen in Figure 6.6c. This behaviour is caused by the fact that the enhanced rates due to the distribution effect are nullified to an extent by the profile effect, where fluid simulations predict higher T_e close to the targets. The net change is smaller in magnitude than either the distribution or profile effect considered alone, and is positive or negative depending on the impurity species and spatial location. It peaks close to the target at +0.38 for neon and -0.73 for nitrogen, Figure 6.6c.

Changes to the effective recombination rate coefficients, Figure 6.4, are negligible. This is unsurprising, given that the cross-sections for both radiative and three-body recombination are typically largest at low values of the incident electron energy, and these electrons are well-thermalised in the plasma regimes studied here.

The behaviour described above for the ionization balance also occurs to some extent in the radiative loss rates due to impurities. However, the situation is a little more complicated because there are three possible ways in which kinetic effects can occur,

(i) changes to the excitation radiation per ion,

(ii) changes to the ionization balance,

(iii) changes to the electron temperature profiles.

There are some significant differences in the excitation radiation rates per ion due to the non-Maxwellian electron distributions, Figure 6.7, but they are primarily confined to highly-ionized ions at low T_e, which suggests that (i) is small. Indeed, this has been confirmed to be the case for carbon, nitrogen and neon, where Maxwellian values of L_z can be used with kinetic

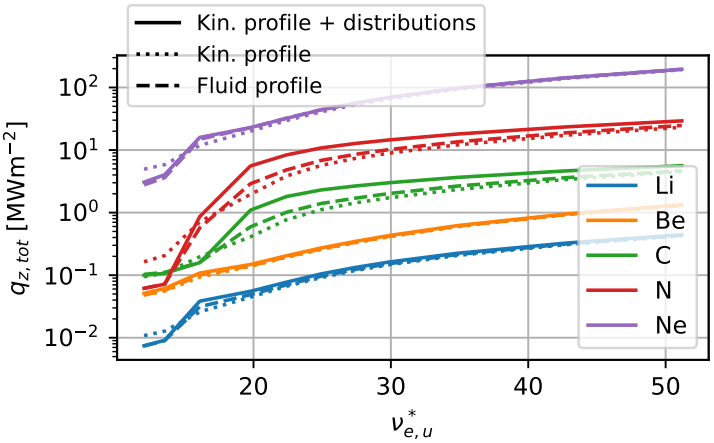

Figure 6.10: The magnitude of the total radiated power as a function of $\nu^*_{e,u}$ for each plasma background and each impurity species.

calculations of the ionization balance to recover the fully kinetic $Q_{z,tot}$ in Figure 6.8. However, this approach was found to be inadequate for lithium and beryllium.

The remaining contribution from the distribution effect, (ii), results from the fact that different ionization stages have different radiative properties, and this is entirely responsible for the changes seen in Figure 6.9a for carbon, nitrogen and neon. It should be pointed out that the reduction in radiated power seen in Figure 6.9a is to some extent a coincidence of the fact that the changes to the ionization balance result in an increase in density of impurity ions which are less efficient radiators, for example C^{4+}. Changes to the ionization balance can result in an increase in radiated power, as seen close to the target in the radiation profile for lithium in Figure 6.8a, but this depends on the relative radiative efficiency of the impurity ions being considered.

The contribution from (iii), which is the profile effect, is clearly significant as seen in Figure 6.9b, and generally acts in the opposite direction to the distribution effect without completely cancelling.

It is clearly a complex set of processes which lead to kinetic effects changing the radiation profiles and the total radiated power, which makes a prediction of the sign and magnitude of such kinetic effects challenging. Qualitatively, the changes observed can be explained by electrons close to the target acting as if they were Maxwellian at a higher temperature. However, since the cooling

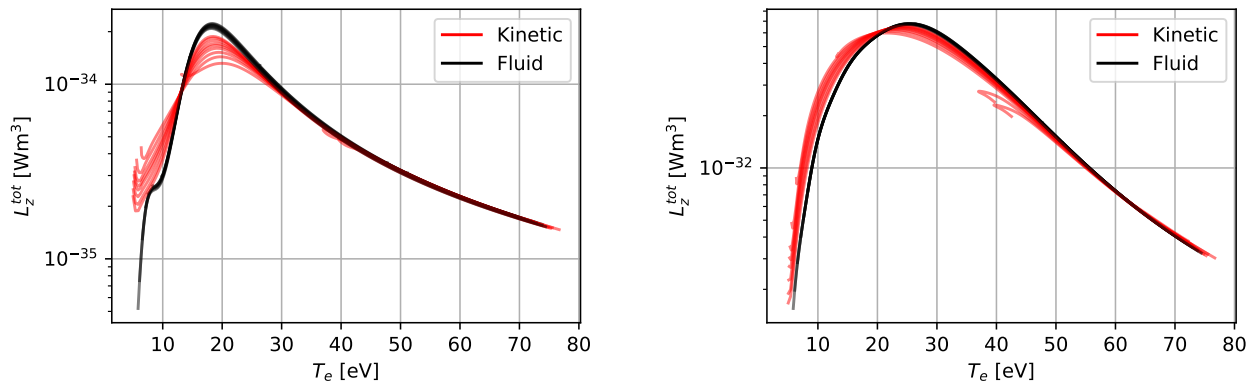

(a) Lithium (b) Neon

Figure 6.11: Average excitation radiation per ion, $\bar{L}_z$, plotted for all simulations for a kinetic and fluid treatment of the electrons.

effects of impurities can have sharp gradients with respect to T_e, both positive and negative, it is difficult to make a general prediction for the impact this will have.

It is worth noting that differences in radiated power, while significant for some impurities, are generally biggest in regions where the total radiated power is low. This can be seen in Figure 6.10, where $q_{z,tot}$ is plotted with $\nu^*_{e,u}$ for each impurity. The fact that absolute differences are significant at low collisionalities could plausibly change behaviour during impurity seeding, for example, which will be required to facilitate benign target conditions in such regimes where the upstream SOL is hot. A self-consistent treatment, where the corresponding impact of the impurities on the electrons is modelled, would be worthwhile to investigate this.

An additional kinetic effect observed in the impurity radiation results, seen to some extent in Figure 6.8, is in the spatial profile of the radiative peak, which is of diagnostic interest in tokamak experiments. In Figure 6.11, we show the total excitation radiation per ion, $\bar{L}_z$, for lithium and neon across all simulations on top of each other as a function of T_e. Black lines are the fully fluid treatments and red lines are fully kinetic. It is seen that, for a kinetic treatment, $\bar{L}_z$ is generally higher at lower temperatures and peaks at a different temperature. For lithium, the peak is at a higher temperature, while for neon it is lower. This suggests that a kinetic treatment of impurity radiation may do a better job of accurately predicting the position of the radiative front in a divertor tokamak.

A somewhat similar study to the one presented here is the one by Zhao et al. [82], where very good agreement was found between ADAS rates and a kinetic treatment of inelastic collision rates between electrons and neutral hydrogen. The kinetic electron code KIPP was used there, and the scrape-off layer conditions simulated were broadly similar to the ones considered here. This result has also been observed with SOL-KiT, as discussed in Chapter 5.

In [134] and [135], Garland et al. explore the effect of relativistic enhancements to electron-impact inelastic cross-sections. This is relevant to tokamaks, because runaway electrons with relativistic energies can be produced under certain conditions, and impurity injection (neon and argon are considered in [135]) is proposed as a method to control them. This is a distinct process from the one considered here, where differences in observed rates are due to modifications to the cross-sections as well as to the electron distribution. There, the distribution effect of this population of very fast electrons (representing a factor 10^{-3} of the bulk electrons) is shown to be small, but the effect of relativistic corrections to the cross-sections results in significant changes to the ionization balance and the radiated power. This does further highlight that Maxwellian-averaged (and typically non-relativistic) reaction rates should be approached with some caution in tokamak edge plasma modelling, and that particular care must be taken to treat inelastic collisions appropriately when the problem requires a kinetic treatment.

Similar tools to SIKE are AURORA [58] and ColRadPy [131]. While these are both more fully-featured atomic physics codes than SIKE, it is not straightforward to relax the assumption of Maxwellian electrons in either of them. An interesting piece of future work would be to incorporate the impurity transport model from AURORA into SIKE. This would enable studies of kinetic effects in plasma-impurity reactions under conditions where sources and transport are important, and this could in principle be coupled to kinetic simulations with a code such as SOL-KiT for a more self-consistent treatment.

6.6 Conclusions

We have seen how both non-Maxwellian electrons and kinetic differences in the plasma profiles in scrape-off layer simulations can result in different predictions for plasma-impurity reaction rates in several fusion-relevant impurity species. Comparing to Maxwellian rates, it has been shown that ionization rates and excitation energy loss rates can show considerable kinetic enhancement close to the target in these SOL plasma backgrounds for highly-ionized impurity ions, while recombination rates are well-approximated by Maxwellian electrons.

If we confine the analysis to just the effect of the departure of the SOL electrons from Maxwellian, the net result of these effects is to considerably increase the average ionization and change the line radiation profiles. However, when the different plasma profiles from kinetic vs. fluid treatments of the electron transport are also accounted for, the differences are to some extent cancelled out. The remaining differences in average ionization are small, typically within 15%. For the radiated power, significant relative differences remain in SOL conditions with low collisionality, but the total radiative losses are small in these regimes.

A common theme of the results presented here is that, where kinetic effects are apparent, they vary in sign and magnitude depending on the particular properties of the impurity species being considered, the local plasma conditions and the overall scrape-off layer regime. It is therefore challenging to make generic statements of the importance of kinetic effects at this stage.

The fact that kinetic effects are large when considering just differences in the electron distributions or the plasma profiles alone, but not together, mirrors one of the conclusions of the investigation in Chapter 5. There, it was observed that kinetic SOL simulations predict both conductive heat flux suppression and enhancement to the sheath heat transmission coefficient, and it was concluded that accounting for both of these effects would be necessary if aiming to capture kinetic effects in a fluid model. The situation is similar here: it would in principle be possible to capture the enhancement to the ionization and excitation rates observed in kinetic SOL simulations and incorporate these as modifications to Maxwellian-averaged rates from a database such as ADAS. However, if this is not done in conjunction with the modifications to

the plasma profiles due to kinetic effects in the electron transport, there is a risk that the results would be less accurate than an entirely fluid approach. The flip side of this is that the use of flux limiters or other reduced kinetic models such as SNB [93] or Ji-Held-Sovinec [99], which are commonly-used approaches to capturing kinetic modifications to the electron parallel heat flux, is akin to introducing a profile effect in the reaction rates but ignoring the distribution effect. Given that these broadly cancel in the results shown here, a reduced kinetic model which treats only the heat flux may therefore make agreement with a fully kinetic model worse.

Chapter 7

Conclusion

7.1 Summary of results

The performance of magnetic confinement fusion experiments is to a large extent determined by the physics occurring at the edge of the device. Particles and energy will make their way to the walls via the scrape-off layer, and the physics at play in this region is multi-faceted and involves processes acting on a wide array of spatial and temporal scales. Modelling these edge plasmas is therefore challenging, but there is a strong motivation to do so accurately.

Plasma transport in the direction parallel to the magnetic fields in the scrape-off layer dominates over other directions, and is an important factor in determining the heat loads to the walls. Classical, Braginskii-like transport theory is often used to make predictions or explain experimental results for SOL plasmas, but the steep temperature gradients which are typically present means transport can become non-local, and so a kinetic approach may be more appropriate. There is therefore a need to validate the classical approach to SOL transport modelling, and this has been a key motivation of the work presented here.

Having seen that a kinetic treatment highlights some differences with fluid model predictions, primarily for the electrons, in the work by Batishcheva et al. [68], Chankin et al. [81], Mijin et al. [83], among others, one of the primary aims has been to extend the analysis of non-local

transport in tokamak scrape-off layer plasmas to include more of the dominant physics at play in real devices in numerical simulations. This includes allowing for the distinct behaviour of the electron and ion energy transport in SOL plasmas, capturing the important role played by neutral transport, and including the effect of radiating impurities. The development work required to carry out kinetic studies of these behaviours has been described in detail in Chapter 3. This has included significant extensions to an existing code, SOL-KiT, and the development of a collisional radiative model for investigations of impurity atomic physics in SOL plasmas, SIKE. Another research aim has been to better understand the SOL regimes where kinetic effects are more apparent, and hence where fluid models may be less appropriate. This was a key motivation for the investigation presented in Chapter 5.

In Chapter 4, we saw that a fluid treatment of the energy transfer between the ions and electrons, Q_{ie}, is a good approximation at equilibrium in the medium-sized tokamak conditions studied. Some kinetic enhancements to this rate of energy exchange were observed during edge-localised mode (ELM)-like transient conditions, but the differences were small compared to the total energy going into the SOL during the transient, and parallel transport of the input power was the dominant mechanism. Subsequent investigations therefore focussed on other processes which are likely to be more important in determining the SOL power balance and/or exhibit strong kinetic effects: parallel transport and the presence of radiating impurities.

In Chapter 5, a large number of kinetic and fluid simulations were carried out with a more fully-featured SOL model. In density scans, it was found that a kinetic treatment does not predict changes in the onset of detachment, and there is generally good agreement in the particle fluxes at the target. It was also found that there was good agreement between kinetic and fluid predictions of the target heat fluxes, despite significant differences in the temperature profiles (driven by electron conductive heat flux suppression) and kinetic enhancements to the electron sheath heat transmission coefficient, γ_e. This suggests that there is some degree of cancelling which occurs between the modifications to the parallel heat transport and γ_e, resulting in minimal changes to the power balance. It was found that the heat flux suppression effect increases monotonically as the upstream collisionality parameter, $\nu^*_{e,u}$, is decreased. On the other hand, γ_e is classical at high and low collisionalities but is enhanced when calculated

kinetically at intermediate collisionalities, peaking at $\nu^*_{e,u} \sim 20$. Simple scaling laws for these two kinetic effects were presented, which may be applied to fluid modelling or 0D analyses of future experiments.

The final physics investigation carried out was into plasma-impurity reaction rates, presented in Chapter 6. Using a newly-developed collisional-radiative model, plasma profiles and electron distributions from kinetic and fluid SOL simulations were used as fixed plasma backgrounds and the resultant impurity ionization balance and radiative power losses were investigated. Two distinct kinetic effects were observed, one driven by the departure of the electrons from Maxwellian in kinetic simulations, and one driven by the different plasma profiles. Taken alone, each of these effects is significant. However, when taken together the kinetic effects are much weaker, although they do persist to some extent in conditions with small $\nu^*_{e,u}$.

7.2 Conclusions

7.2.1 Numerical development

A key challenge of kinetic plasma simulations, and one reason why fluid models remain popular, is that they are computationally expensive. The enhancements to the SOL-KiT code presented in Chapter 3, and in particular the atomic state bundling in Section 3.4, have enabled parameter scans of parallel electron kinetics in SOL simulations with realistic ion and neutral physics (Chapter 5). This has in turn facilitated the development of scaling laws for two important kinetic effects. Without the computational speed-up provided by bundling, this would not have been possible in a reasonable time-frame. Furthermore, the fact that this speed-up is achieved without significant loss of accuracy suggests that more fully-featured physics investigations using kinetic models may be possible in the future, in particular for problems where the bottleneck is of a similar nature, for example in simulating impurities.

The collisional radiative model developed in Section 3.5, SIKE, has facilitated an initial investigation into kinetic effects in plasma-impurity reaction rates in SOL plasmas. This code may

be applied to other research problems in the future, not necessarily limited to tokamak plasma regimes. The advantage of SIKE is that a full set of self-consistent, fine structure resolved atomic data from the Flexible Atomic Code (FAC) is included, and all that is required as input is a plasma profile. The form of the atomic data - json files which are human-readable and can easily be loaded as dictionaries in commonly-used programming languages - also facilitates straightforward modification or addition of new data. This means that other impurity species may be investigated, or the atomic data may be refined to provide greater agreement with experiment. Interesting improvements to SIKE would be to add an impurity transport model and/or sources and sinks of impurity particles. This would require minimal structural changes to the code since a global sparse PETSc matrix has already been implemented, and would enable studies of impurity physics in realistic tokamak regimes where impurity transport is important. A limitation of SIKE is that the plasma is assumed to be optically thin. Photon-induced reactions are included in the FAC data, so this assumption may be relaxed to extend the code's applicability to high-density SOL plasmas and non-tokamak applications, but this would require knowledge of the background radiation.

The extensions to SOL-KiT described in Chapter 3 have extended the range of problems which can be studied by the code. A remaining limitation of SOL-KiT is the lack of realistic geometric effects, one of the most significant of which is flux tube expansion. This is an active area of research, where novel divertor configurations have shown promise in facilitating detachment [62, 136, 137]. An interesting study would be to explore the interaction of kinetic effects in 1D SOL models with expanding field lines. Two upgrades to SOL-KiT would be required to do this: a modification to the spatial gradient terms to account for changing cross-sectional areas of the flux tube, which is straightforward, and a treatment of the magnetic mirror force in the electron kinetic equation, which is less so. A method of treating the mirror force in a Legendre decomposition of the electron kinetic equation is outlined in Appendix C.

7.2.2 Physics investigations

A key result of Chapter 5 is that detachment onset is not affected by a kinetic treatment of the electron parallel transport. This should, however, be placed in the context that only the density scan with the lowest input power actually reached detachment in that study. It is possible that, at very high input powers and in the presence of radiating impurities (i.e. reactor-relevant conditions), kinetic effects may be important in detachment onset. It is in these conditions where the scaling laws in Chapter 5 predict significant heat flux suppression, and kinetic modifications to the impurity radiation in Chapter 6 are largest. This highlights the need for a self-consistent study of kinetic electrons with impurities.

It is worth noting that the result in Chapter 5, with modified electron temperature profiles but largely unchanged heat fluxes compared to a fluid model, may have a further significance in altering the three-dimensional turbulence behaviour, as noted in [100]. Fully kinetic simulations in 3D are computationally challenging, but the scaling laws presented in Chapter 5 may offer a simple way to do a preliminary investigation of this effect.

While an obvious next step in the work on kinetic effects in plasma-impurity physics is to carry out a self-consistent study, a computationally tractable method of doing so must be developed first. One approach may be to use SIKE to assess the extent to which the fine structure resolved atomic data can be compressed or aggregated while still capturing the kinetic effects observed in Chapter 6. In addition, the atomic state bundling techniques developed in Section 3.4 may be used to further reduce the number of collision operators and impurity atomic states which need to be evolved. A logical enhancement of this technique would be to drop the assumption of Boltzmann-distributed states within bundles, and instead use SIKE to make estimates of atomic state distributions as functions of macroscopic plasma parameters.

An alternative approach to bundled atomic states is to develop collisional-radiative 'effective' cross-sections for inelastic processes, in a similar way to the effective ionization and recombination rates discussed in Section 2.6. This would involve weighting the rate matrix with the appropriate cross-sections to produce a single effective cross-section which accounts for the

cumulative effect of many processes, and would yield the same particle and energy sources for the same electron distribution. To evaluate effective Boltzmann collision operators with this approach, it would also be necessary to compute effective transition energies.

It is possible that an even simpler approach would be viable, such as the effective cooling operators implemented in KIPP [3]. Minimal detailed knowledge of the impurity atomic physics is required, and the net cooling effect due to radiation is applied to the electron distribution either uniformly in velocity space or preferentially to the tail. This would not capture kinetic effects in electron-impurity reactions directly, but would facilitate kinetic studies of the interaction of parallel transport with significant power dissipation. Moreover, while the focus here has been on plasma-impurity reaction rates, there are other questions posed by a kinetic treatment of SOL electrons. One example is a study of kinetic effects on the thermal forces, which may modify impurity transport properties.

The scaling laws for kinetic effects presented in Chapter 5 are novel, and provide the ability to capture kinetic modifications to parallel transport in fluid codes and simple analytical models. This is an improvement over traditional approaches which use flux limiters, as there is no reliance on a tunable parameter which can change depending on the plasma conditions [64]. Furthermore, the results in Chapter 5 suggest that a flux limiter alone, even if tuned correctly, may incorrectly capture the heat loads on the walls, which show good agreement with a fluid treatment because the heat flux suppression and enhancement to γ_e largely cancel. Similar behaviour has also been seen in the kinetic effects in impurities. A flux limiter applied to a fluid code would predict changes to impurity radiation profiles (via modified temperature profiles) which are not seen in a fully kinetic treatment due to modifications to the Maxwellian-averaged reaction rates. This is, therefore, a key result of this study, which suggests that the use of flux limiters on their own is inadequate at capturing kinetic effects in SOL plasmas. The same can be said for other reduced kinetic models such as SNB [93] or Ji-Held-Sovinec [99], which do not require fine-tuning in the same way as a flux limiter, but still only treat the parallel heat flux.

Appendix A

SOL-KiT further details

Some more details of the SOL-KiT model are provided here as a reference. All instances of f without subscript here refer to the distribution of the electrons.

A.1 Derivation of the Legendre decomposition of the kinetic equation

In one spatial dimension oriented along the x-axis, the kinetic equation is

$$\frac{\partial f(\mathbf{v})}{\partial t} + v_x \frac{\partial f}{\partial x} + a_x \frac{\partial f}{\partial v_x} = \sum_\alpha C_{e,\alpha}, \tag{A.1}$$

where $a_x = -\frac{e}{m_e} E$ is the acceleration due to the electric field. Writing this in spherical coordinates gives

$$\frac{\partial f(\mathbf{v})}{\partial t} + v \cos\theta \frac{\partial f}{\partial x} + a_x \left(\cos\theta \frac{\partial f}{\partial v} - \frac{\sin\theta}{v} \frac{\partial f}{\partial \theta} \right) = \sum_\alpha C_{e,\alpha}, \tag{A.2}$$

where θ is the angle between $\mathbf{v}$ and the x-axis.

If we let $\xi = \cos\theta$, this becomes

$$\frac{\partial f(\mathbf{v})}{\partial t} + v\xi \frac{\partial f}{\partial x} + a_x \left(\xi \frac{\partial f}{\partial v} - \frac{1-\xi^2}{v} \frac{\partial f}{\partial \xi} \right) = \sum_\alpha C_{e,\alpha}. \tag{A.3}$$

We may now apply the spherical harmonic expansion of $f(\mathbf{v})$, which reduces to an expansion in Legendre polynomials in one spatial dimension,

$$f(\mathbf{v}) = \sum_{l=0}^{\infty} f_l(v) P_l(\xi) \simeq \sum_{l=0}^{l_{max}} f_l(v) P_l(\xi), \tag{A.4}$$

where the second equality comes from truncating this expansion at some harmonic l_{max}. Substituting (A.4) into each term in (A.3), and making use of the Legendre polynomial recurrence relations,

$$\xi P_l = \frac{l+1}{2l+1} P_{l+1} + \frac{l}{2l+1} P_{l-1}, \tag{A.5a}$$

$$(\xi^2 - 1)\frac{dP_l}{d\xi} = \frac{l(l+1)}{2l+1}(P_{l+1} - P_{l-1}), \tag{A.5b}$$

yields the following form of the kinetic equation,

$$\begin{aligned} &\sum_{l=0} \left\{ \frac{\partial f_l}{\partial t} \right\} P_l + \sum_{l=0} \left\{ v\frac{\partial f_l}{\partial x} + a_x \left(\frac{\partial f_l}{\partial v} + \frac{f_l}{v}(l+1) \right) \right\} \frac{l}{2l+1} P_{l-1} \\ &+ \sum_{l=0} \left\{ v\frac{\partial f_l}{\partial x} + a_x \left(\frac{\partial f_l}{\partial v} - \frac{f_l}{v} l \right) \right\} \frac{l+1}{2l+1} P_{l+1} = \sum_{l=0} \left\{ \sum_{\alpha} C^l_{e,\alpha} \right\} P_l, \end{aligned} \tag{A.6}$$

where we have also decomposed the collision operators in Legendre polynomials, $C_{e,\alpha} = \sum C^l_{e,\alpha} P_l$, which is discussed in Section A.2.

We can now change the summation indices in (A.6) and exploit vanishing terms, which allows us to group terms involving the same Legendre polynomials. This gives

$$\begin{aligned} &\sum_{l=0} \left[\frac{\partial f_l}{\partial t} + \left\{ v\frac{\partial f_{l+1}}{\partial x} + a_x \left(\frac{\partial f_{l+1}}{\partial v} + \frac{f_{l+1}}{v}(l+2) \right) \right\} \frac{l+1}{2l+3} \right. \\ &\left. + \left\{ v\frac{\partial f_{l-1}}{\partial x} + a_x \left(\frac{\partial f_{l-1}}{\partial v} - \frac{f_{l-1}}{v}(l-1) \right) \right\} \frac{l}{2l-1} \right] P_l = \sum_{l=0} \left\{ \sum_{\alpha} C^l_{e,\alpha} \right\} P_l. \end{aligned} \tag{A.7}$$

This can be written as a set of equations for each coefficient $f_l(v)$, as outlined in Section 3.1.1,

$$\frac{\partial f_l}{\partial t} = A_l + E_l + C_l, \tag{A.8}$$

where

$$A_l = -\frac{l}{2l-1} v \frac{\partial f_{l-1}}{\partial x} - \frac{l+1}{2l+3} v \frac{\partial f_{l+1}}{\partial x},$$

is the spatial advection term,

$$E_l = -a_x E \left\{ \frac{l}{2l-1} G_{l-1} + \frac{l+1}{2l+3} H_{l+1} \right\}$$

is the velocity space advection due to the electric field, with

$$G_l(v) = v^l \frac{\partial v^{-l} f_l}{\partial v},$$
$$H_l(v) = \frac{1}{v^{l+1}} \frac{\partial v^{l+1} f_l}{\partial v},$$

and, finally, the collision terms are

$$C_l = \sum_\alpha C^l_{e,\alpha}.$$

A.2 Collision operators in the Legendre decomposition of the kinetic equation

A.2.1 Coulomb collision terms

For the electrons, SOL-KiT includes the effect of Coulomb collisions between charged species and both elastic and inelastic collisions with neutrals. The treatments are quite different, and we start with the Coulomb collisions.

Starting from the Fokker-Planck collision operator in terms of the Rosenbluth potentials (2.32) for species α, with distribution f, colliding with species β, with distribution F, it is decomposed in spherical harmonics following the procedure laid out by Shkarosfky et al. [42]. The distributions of both species are split into isotropic and anisotropic parts, $f = f_0 + f_a$ and $F = F_0 + F_a$, where we assume the anisotropic part is small so that the Fokker-Planck operator

can be linearised. For $l = 0$ this becomes

$$C_0^{FP} = \sum_\beta \Gamma_{\alpha,\beta} \frac{1}{3v^2} \frac{\partial}{\partial v} \left[\frac{3}{\mu} f_0 I_0 \left(F_0\right) + v \left(I_2 \left(F_0\right) + J_{-1} \left(F_0\right) \right) \frac{\partial f_0}{\partial v} \right], \tag{A.9}$$

while for $l \geq 1$, the result is [112]

$$\begin{aligned} C_{l\geq 1}^{FP} = \sum_\beta \Gamma_{\alpha,\beta} \Bigg\{ & \frac{4\pi}{\mu} [F_0 f_l + f_0 F_l] \\ & - \frac{(\mu-1)}{\mu v^2} \left(\frac{\partial f_0}{\partial v} \left[\frac{l+1}{2l+1} I_l \left(F_l\right) - \frac{l}{2l+1} J_{-1-l} \left(F_l\right) \right] + I_0 \left(F_0\right) \frac{\partial f_l}{\partial v} \right) \\ & + \frac{I_2 \left(F_0\right) + J_{-1} \left(F_0\right)}{3v} \frac{\partial^2 f_l}{\partial v^2} \\ & + \frac{-I_2 \left(F_0\right) + 2J_{-1} \left(F_0\right) + 3I_0 \left(F_0\right)}{3v^2} \frac{\partial f_l}{\partial v} \\ & - \frac{l(l+1)}{2} \frac{-I_2 \left(F_0\right) + 2J_{-1} \left(F_0\right) + 3I_0 \left(F_0\right)}{3v^3} f_l \\ & + \frac{1}{2v} \frac{\partial^2 f_0}{\partial v^2} \left[L_1 I_{l+2} \left(F_l\right) + L_1 J_{-1-l} \left(F_l\right) + L_2 I_l \left(F_l\right) + L_2 J_{1-l} \left(F_l\right) \right] \\ & + \frac{1}{v^2} \frac{\partial f_0}{\partial v} \left[L_3 I_{l+2} \left(F_l\right) + L_4 J_{-1-l} \left(F_l\right) + L_5 I_l \left(F_l\right) + L_6 J_{1-l} \left(F_l\right) \right] \Bigg\}, \end{aligned} \tag{A.10}$$

where $\mu = m_\beta / m_\alpha$, $\Gamma_{\alpha,\beta}$ is a collection of constants defined in (2.30), I_l and J_l are a set of integrals defined as

$$I_j(F_l) = \frac{4\pi}{v^j} \int_0^v F_l(u) u^{j+2} du, \quad J_j(F_l) = \frac{4\pi}{v^j} \int_v^\infty F_l(u) u^{j+2} du,$$

and the L coefficients are constants in terms of l,

$$\begin{aligned} L_1 &= \tfrac{(l+1)(l+2)}{(2l+1)(2l+3)}, \quad L_2 = -\tfrac{(l-1)l}{(2l+1)(2l-1)}, \quad L_3 = -\tfrac{(l+1)l/2+l+1}{(2l+1)(2l+3)} \\ L_4 &= \tfrac{-(l+1)l/2+l+2}{(2l+1)(2l+3)}, \quad L_5 = \tfrac{(l+1)l/2+l-1}{(2l+1)(2l-1)}, \quad L_6 = -\tfrac{(l+1)l/2-l}{(2l+1)(2l-1)}. \end{aligned}$$

For collisions between electrons, $\alpha = \beta = e$ and $\mu = 1$, equations (A.9) and (A.10) are implemented in full. For collisions with ions ($\alpha = e$, $\beta = i$), a Dirac delta is assumed for the ion distribution at their flow velocity, $F(\mathbf{v}) = n_i \delta(\mathbf{v} - \mathbf{u}_i)$, which in the Legendre expansion is

$$F_l = \frac{n_i (2l+1)}{4\pi} \delta(v - u_i).$$

This simplifies (A.10) as the I_j and J_j integrals reduce to step functions. The $l = 0$ term for electron-ion collisions (A.9), responsible for the transfer of energy between the two species, is not included because the ion temperature is not evolved (either assuming they are cold or at the same temperature as the electrons).

A.2.2 Boltzmann collision terms

Both elastic and inelastic collisions between electrons and neutrals are included in the SOL-KiT model. For the latter, we have contributions from excitation/de-excitation, ionization and three-body recombination. The decomposition of the Boltzmann collision operator (2.25) in Legendre polynomials again follows the formalism of Shkarofsky et al. [42].

Starting with elastic electron-neutral collisions, the neutral distribution is assumed to be a delta function at $\mathbf{v} = 0$. Although the mass ratio m_e/m_n is small, if we assume the electron velocity magnitude does not change in collisions, i.e. that $|\mathbf{v}_\alpha^i| = |\mathbf{v}_\alpha^f|$ in equation (2.25), the collision operator for $l = 0$ disappears. Instead, we assume the change in velocity is merely small and use a Taylor expansion, giving

$$C_0^{el} = \sum_b \frac{m_e}{m_n + m_e} \frac{1}{v^2} \frac{\partial}{\partial v} \left\{ n_b v^4 \left(\int d^2\Omega (1 - \cos\chi) \sigma_{el,b}(\chi, v) \right) \left(f_0 + \frac{kT_n}{m_e v} \frac{\partial f_0}{\partial v} \right) \right\}, \quad \text{(A.11)}$$

where the sum is over all neutral atomic states b, n_b is the density of neutrals in state b, T_n is the neutral temperature and $\sigma_{el,b}(\chi, v)$ is the differential cross-section for elastic collisions, which is a function of v and the scattering angle χ. For $l \geq 1$, we do employ the assumption of constant velocity magnitude and the collision operator is

$$C_{l\geq 1}^{el} = \sum_b -n_b v f_l \left\{ \int d^2\Omega (1 - P_l(\cos\chi)) \sigma_{el,b}(\chi, v) \right\}, \quad \text{(A.12)}$$

where P_l is the l^{th} Legendre polynomial.

For inelastic collisions the procedure of Makabe et al. [44] is used. We first treat inelastic collisions which conserve particle number (i.e. excitation and de-excitation). For a process

with energy loss ε, the pre- and post-collision velocities are related via

$$\frac{1}{2}m_e v'^2 = \frac{1}{2}m_e v^2 + \varepsilon.$$

We can then define $\alpha = v'/v = \sqrt{1 + \frac{2\varepsilon}{m_e v^2}}$, and the collision operator for any l becomes

$$C_l^{ex} = \sum_{b,b'} -n_b v \left\{ \sigma^{tot}_{b\to b'}(v) f_l(v) - f_l(\alpha v)\alpha^2 \left(\sigma^{tot}_{b\to b'}(\alpha v) - \sigma^{(l)}_{b\to b'}(\alpha v) \right) \right\} \tag{A.13}$$

where the sum is over transitions from all initial atomic states b to final states b', where for excitation $b < b'$, and for de-excitation $b > b'$. Also, $\sigma^{tot} = \int d^2\Omega \sigma(\chi, v)$ is the integral cross-section, $\sigma^{(l)} = \int d^2\Omega (1 - P_l(\cos\chi))\sigma(\chi, v)$ is the cross-section for a given harmonic l, and $\sigma_{b\to b'}$ refers to the cross-section for excitation or de-excitation from b to b'.

For ionization, a collisional process which does not conserve particles, it is in theory necessary to know how the post-collision energy and momentum is shared between the incident and ejected electrons. However, a simplification is employed where it is assumed the ejected electron is stationary, and the incident electron therefore has post-collision energy $\frac{1}{2}m_e v'^2 = \frac{1}{2}m_e v^2 + \varepsilon$, as was the case for excitation. The ionization collision operator is then the sum of a term identical in form to the excitation collision operator (A.13) and a term which places ionized electrons at $v = 0$,

$$\begin{aligned} C_l^{ion} = \sum_b \Bigg[& -n_b v \left\{ \sigma^{tot}_{ion,b}(v) f_l(v) - f_l(\alpha v)\alpha^2 \left(\sigma^{tot}_{ion,b}(\alpha v) - \sigma^{(l)}_{ion,b}(\alpha v) \right) \right\} \\ & + n_b n_e K_{ion,b} \frac{\delta(v)}{4\pi v^2} \delta_{l,0} \Bigg], \end{aligned} \tag{A.14}$$

where $\sigma_{ion,b}$ is the ionization cross-section of neutrals in state b, and $K_{ion,b}$ is the ionization rate coefficient, where

$$K = \frac{1}{n_e} 4\pi \int dv v^3 f_0(v) \sigma^{tot}(v).$$

Finally, for three-body recombination we have an operator with nearly identical form to (A.14),

$$C_l^{3br} = \sum_b \Big[-n_b v \left\{ \sigma_{3br,b}^{tot}(v) f_l(v) - f_l(\alpha v)\alpha^2 \left(\sigma_{3br,b}^{tot}(\alpha v) - \sigma_{3br,b}^{(l)}(\alpha v) \right) \right\} \\ -n_b n_e K_{3br,b} \frac{\delta(v)}{4\pi v^2} \delta_{l,0} \Big], \tag{A.15}$$

except the term responsible for the particle source has reversed sign and $\varepsilon < 0$.

One remaining aspect of these operators which needs specifying is the cross-sections used. For all processes, differential cross-sections have not been used in practice and instead integral cross-sections are used, leading to a set of simplifications discussed shortly. For elastic collisions, the Bohr radius is used. For excitation, cross-sections for hydrogenic atoms from Janev [113] are used. Deexcitation cross-sections are related via detailed balance,

$$\sigma_{b' \to b}^{tot}(v') = \frac{g_b}{g_{b'}} \frac{v^2}{v'^2} \sigma_{b \to b'}^{tot}(v)$$

for $b' > b$, where g_b is the statistical weight of state b. Similarly for ionization, cross-sections from Janev are used [113], and three-body recombination cross-sections come from detailed balance,

$$\sigma_{3br,b}^{tot}(v') = \frac{1}{2} n_e g_b \left(\frac{h^2}{2\pi m_e k T_e} \right)^{3/2} \frac{v^2}{v'^2} \sigma_{ion,b}^{tot}(v),$$

where h is Planck's constant.

For cross-sections with no scattering angle dependence, we get the simplified set of Boltzmann

collision operators,

$$
\begin{aligned}
C_0^{el} &= \sum_b \frac{m_e}{m_n + m_e}\frac{1}{v^2}\frac{\partial}{\partial v}\left\{n_b v^4 \sigma_{el,b}^{tot}(v)\left(f_0 + \frac{kT_n}{m_e v}\frac{\partial f_0}{\partial v}\right)\right\},\\
C_{l\geq 1}^{el} &= \sum_b -n_b v f_l \sigma_{el,b}^{tot}(v),\\
C_l^{ex} &= \sum_{b,b'} -n_b v\left\{\sigma_{b\to b'}^{tot}(v) f_l(v) - \delta_{l,0} f_l(\alpha v)\alpha^2 \sigma_{b\to b'}^{tot}(\alpha v)\right\}\\
C_l^{ion} &= \sum_b \left[-n_b v\left\{\sigma_{ion,b}^{tot}(v) f_l(v) - \delta_{l,0} f_l(\alpha v)\alpha^2 \sigma_{ion,b}^{tot}(\alpha v)\right\} + n_b n_e K_b^{ion}\frac{\delta(v)}{4\pi v^2}\delta_{l,0}\right],\\
C_l^{3br} &= \sum_b \left[-n_b v\left\{\sigma_{3br,b}^{tot}(v) f_l(v) - \delta_{l,0} f_l(\alpha v)\alpha^2 \sigma_{3br,b}^{tot}(\alpha v)\right\} - n_b n_e K_b^{3br}\frac{\delta(v)}{4\pi v^2}\delta_{l,0}\right],
\end{aligned}
\tag{A.16}
$$

Thus equations (A.9), (A.10) and (A.16) constitute all collisional contributions to the term C_l in the Legendre decomposition of the electron kinetic equation (3.2), as implemented in SOL-KiT.

A.2.3 Heating operator

An additional contribution to C_l is a spatially uniform heating operator, which enables simulation of input power from the core into the SOL. This has the form

$$
C_0^{heat} = \Theta\left(L_h - x\right) D(x,t)\frac{1}{3v^2}\frac{\partial}{\partial v}v^2\frac{\partial f_0}{\partial v}, \tag{A.17}
$$

where Θ is the step function, L_h is the length over which heating occurs and $D(x,t) = q_{in}(t)/m_e n_e(x,t)L_h$ for an input heat flux q_{in}. Defining Q_e^{ext} as the energy moment of the heating operator, $Q_e^{ext} = 4\pi\int(\frac{1}{2}m_e v^2)v^2 C_0^{heat}dv$, we see that $Q_e^{ext} = q_{in}/L_h$ as expected.

A.3 Ion temperature equation derivation

Starting from the generic plasma transport equations (2.42), we assume isotropic ion pressure. Therefore, in the direction parallel to the magnetic field (the x-axis) and for deuterium ions we

have

$$\frac{\partial n_i}{\partial t} + \frac{\partial}{\partial x}(n_i u_i) = S_i, \tag{A.18a}$$

$$\frac{\partial}{\partial t}\left(m_i n_i u_i\right) + \frac{\partial}{\partial x}(m_i n_i u_i^2) + \frac{\partial n_i k T_i}{\partial x} + e n_i E = R_i, \tag{A.18b}$$

$$\begin{aligned}\frac{\partial}{\partial t}\left(\frac{3}{2}n_i k T_i + \frac{1}{2}m_i n_i u_i^2\right) + \frac{\partial}{\partial x}\left(q_i + \left(\frac{5}{2}n_i k T_i + \frac{1}{2}m_i n_i u_i^2\right) u_i\right) \\ = e n_i E u_i + Q_i,\end{aligned} \tag{A.18c}$$

The ion momentum equation (A.18b) can be combined with (A.18a) to give

$$m_i n_i \frac{\partial u_i}{\partial t} + m_i n_i u_i \frac{\partial u_i}{\partial x} + m_i S_i u_i + \frac{\partial\left(n_i k T_i\right)}{\partial x} = n_i Z e E + R_i. \tag{A.19}$$

Similarly, the ion energy equation (A.18c) can be written

$$\begin{aligned}n_i\left(\frac{\partial}{\partial t} + u_i\frac{\partial}{\partial x} + S_i\right)\left(\frac{3}{2}k T_i + \frac{1}{2}m_i u_i^2\right) + \frac{\partial}{\partial x}(q_i + n_i k T_i u_i) \\ = e n_i E u_i + Q_i.\end{aligned} \tag{A.20}$$

We then subtract the u_i equation (A.19), multiplied by u_i, from (A.20) to give

$$\frac{3}{2}n_i\left(\frac{\partial k T_i}{\partial t} + u_i\frac{\partial k T_i}{\partial x}\right) + \frac{\partial q_i}{\partial x} + n_i k T_i \frac{\partial u_i}{\partial x} + \left(\frac{3}{2}k T_i - \frac{1}{2}m_i u_i^2\right) S_i = Q_i - u_i R_i. \tag{A.21}$$

Finally, this is rearranged to give an evolution equation for the ion temperature,

$$\frac{\partial k T_i}{\partial t} = -u_i\frac{\partial k T_i}{\partial x} + \frac{2}{3}\left[-k T_i\frac{\partial u_i}{\partial x} - \frac{1}{n_i}\frac{\partial q_i}{\partial x} - \frac{S_i}{n_i}\left(\frac{3}{2}k T_i - \frac{1}{2}m_i u_i^2\right) - \frac{u_i}{n_i}R_i + \frac{Q_i}{n_i}\right]. \tag{A.22}$$

A.4 Numerics

Here, a brief description of the SOL-KiT numerics is provided. For more details, see [4].

All evolved quantities are normalised with reference to a plasma with temperature T_0 (in eV) and density n_0 (in m^{-3}). Velocities are thus normalised to the electron thermal speed, $v_{th,0} = \sqrt{2eT_0/m_e}$. Time is normalised to the 90° electron-ion collision time, $t_0 = v_{th,0}^3/(\Gamma_{ei,0} n_0 \ln\Lambda_{ei,0}/Z)$.

Here, $\Gamma_{ei,0} = Z^2e^4/4\pi(m_e\epsilon_0)^2$ and $\ln\Lambda_{ei,0}$ is the electron-ion Coulomb logarithm at T_0 and n_0. Distances are normalised with $x_0 = v_{th,0}t_0$. All normalised quantities, denoted with a tilde, can therefore be defined,

$$\tilde{v} = \frac{v}{v_{th,0}}, \quad \tilde{t} = \frac{t}{t_0}, \quad \tilde{x} = \frac{x}{x_0}, \tilde{f}_l = \frac{f_l}{n_0 v_{th,0}^{-3}},$$
$$\tilde{E} = \frac{Eet_0}{m_e v_{th},0}, \quad \tilde{q} = \frac{q}{m_e n_0 v_{th,0}^3}, \quad \tilde{T} = \frac{T}{T_0},$$
$$\tilde{\varepsilon} = \frac{\varepsilon}{T_0}, \quad \tilde{\sigma} = \frac{\sigma}{\sigma_0}, \quad \tilde{n} = \frac{n}{n_0}, \quad \tilde{u} = \frac{u}{v_{th,0}}.$$

From hereon the tilde will be dropped.

The velocity grid is a cell-centred grid of N_v cells with increasing grid widths. The initial grid width is Δv_1, and the width multiplier c_v. Therefore, the grid is defined

$$v_1 = \frac{1}{2}\Delta v_1, \quad \Delta v_n = c_v \Delta v_{n-1}, \quad v_n = v_{n-1} + \frac{1}{2}(\Delta v_n + \Delta v_{n-1}).$$

The spatial grid consists of cell centres and cell faces. The total number of cell centers is N_c. Quantities such as T, n and f_0 are evolved on the cell centres, while quantities which relate to fluxes, such as u and f_1, are evolved on cell edges. A linear interpolation is then carried out to estimate the value of these quantities on non-evolved grid locations. Spatial grid widths, Δx^c, are defined for cell centres, decreasing exponentially from the upstream location (at $x = 0$) to the target. The two extremes are defined at input. The grid is thus

$$x_1 = 0, \quad x_k = x_{k-1} + \frac{1}{2}\Delta x_m^c,$$

where $m = k$ if k is odd (cell centres) or $m = k - 1$ if k is even (cell edges). A visual representation of the grid, including both boundaries, is shown in Figure A.1.

Implicit time integration is carried out using the backwards Euler method. For a variable vector F, containing all evolved variables at all grid locations, and a matrix M, which applies all terms in the SOL-KiT equations which evolve the quantities in F, the variable vector is evolved from timestep i to $i + 1$ with

$$F^{i+1} = (I - \Delta t M(F^{i^*}))^{-1} F^i,$$

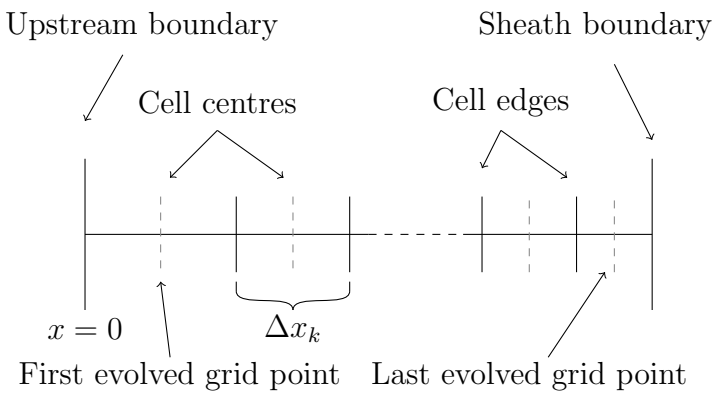

Figure A.1: Diagram of SOL-KiT spatial grid, showing cell centres and boundaries. The first and last evolved grid points are both cell centres, with boundary conditions applied on the upstream and sheath boundary cell edges.

where I is the identity matrix and M is evaluated at the lagged timestep i^*. This is solved iteratively by setting $i^* = i$ initially, then updating M and so on until convergence.

For all derivatives (in velocity and configuration space), finite differencing is used. Velocity derivatives are evaluated with central differencing, where for some function F evaluated at spatial location x_k and velocity location v_n,

$$\frac{\partial F}{\partial v}\left(x_k, v_n\right) = \frac{F\left(x_k, v_{n+1}\right) - F\left(x_k, v_{n-1}\right)}{v_{n+1} - v_{n-1}},$$

and

$$\frac{\partial^2 F}{\partial v^2}\left(x_k, v_n\right) = \frac{1}{\Delta v_n}\left(\frac{F\left(x_k, v_{n+1}\right) - F\left(x_k, v_n\right)}{v_{n+1} - v_n} - \frac{F\left(x_k, v_n\right) - F\left(x_k, v_{n-1}\right)}{v_n - v_{n-1}}\right).$$

An exception to this is in the velocity advection terms in the kinetic equation, where a conservative form is used instead,

$$\frac{\partial F}{\partial v}\left(x_k, v_n\right) = \frac{F\left(x_k, v_{n+1/2}\right) - F\left(x_k, v_{n-1/2}\right)}{\Delta v_n},$$

using linear interpolation to compute values at $v_{n\pm1/2}$. Spatial derivatives are treated with central differencing, except for when upwinding is used, in which case

$$\frac{\partial F}{\partial x}(x_k) = \frac{F(x_k) - F(x_{k-1})}{x_k - x_{k-1}}, \quad u(x_k) \geq 0,$$

$$\frac{\partial F}{\partial x}(x_k) = \frac{F(x_{k+1}) - F(x_k)}{x_{k+1} - x_k}, \quad u(x_k) < 0.$$

The diffusion terms are, in velocity space,

$$\frac{\partial}{\partial v}\left(A\frac{\partial F}{\partial v}\right)(x_k, v_n) = \frac{1}{\Delta v_n}\left[A\left(x_k, v_{n+1/2}\right)\frac{F\left(x_k, v_{n+1}\right) - F\left(x_k, v_n\right)}{v_{n+1} - v_n} - A\left(x_k, v_{n-1/2}\right)\frac{F\left(x_k, v_n\right) - F\left(x_k, v_{n-1}\right)}{v_n - v_{n-1}}\right],$$

and in configuration space,

$$\frac{\partial}{\partial x}\left(A\frac{\partial F}{\partial x}\right)(x_k) = \frac{1}{x_{k+2} - x_{k-2}}\left[A\left(x_{k+1}\right)\frac{F\left(x_{k+2}\right) - F\left(x_k\right)}{x_{k+2} - x_k} - A\left(x_{k-1}\right)\frac{F\left(x_k\right) - F\left(x_{k-2}\right)}{x_k - x_{k-2}}\right],$$

for some diffusion coefficient A.

Appendix B

Fluid neutral model details

B.1 Transport model derivation

We start from the neutral transport equations, assuming isotropic pressure,

$$\frac{\partial n_b}{\partial t} + \nabla \cdot (n_b \mathbf{u}_n) = S_b, \tag{B.1a}$$

$$\frac{\partial}{\partial t}\left(m_n n_n \mathbf{u}_n\right) + \nabla \cdot \left(m_n n_n \mathbf{u}_n \mathbf{u}_n\right) + \nabla p_n = \mathbf{R}_n, \tag{B.1b}$$

$$\frac{\partial}{\partial t}\left(\frac{3}{2}p_n + \frac{1}{2}m_n n_n u_n^2\right) + \nabla \cdot \left[\mathbf{q}_n + \left(\frac{5}{2}p_n + \frac{1}{2}m_n n_n u_n^2\right)\mathbf{u}_n\right] = Q_n, \tag{B.1c}$$

where for the mass continuity equation (B.1a) we treat each neutral excited state individually, and $n_n = \sum_b n_b$ and $S_n = \sum_b S_b$ are the total neutral density and particle source respectively.

As outlined in Section 3.3, we will consider a quasi-2D geometry, where gradients in the direction parallel to the magnetic field, x, can be related to those in the perpendicular direction, y, via

$$\frac{\partial}{\partial y} = \frac{1}{\tan\alpha}\frac{\partial}{\partial x}, \tag{B.2}$$

and therefore, for a velocity $\mathbf{u} = u_\parallel \hat{\mathbf{x}} + u_\perp \hat{\mathbf{y}}$, we can arrive at an effective velocity in the parallel

direction,

$$u_{eff} = u_{\parallel} + \frac{u_{\perp}}{\tan\alpha}. \tag{B.3}$$

Here, α is the pitch angle of the magnetic field, measured from the direction of normal incidence to the wall (see Figure 3.7).

Using (B.2) and (B.3),

$$\nabla \cdot (n_b \mathbf{u_n}) = \frac{\partial(n_b u_{n\parallel})}{\partial x} + \frac{\partial(n_b u_{n\perp})}{\partial y} = \frac{\partial(n_b u_{n,eff})}{\partial x}$$

and so (B.3) becomes

$$\frac{\partial n_b}{\partial t} = -\frac{\partial(n_b u_{n,eff})}{\partial x} + S_b. \tag{B.4}$$

For the momentum equation, we can separate into a parallel component,

$$\begin{aligned} \frac{\partial}{\partial t}\left(m_n n_n u_{n\parallel}\right) &= -\left(\frac{\partial}{\partial x}(m_n n_n u_{n\parallel}^2) + \frac{\partial}{\partial y}(m_n n_n u_{n\parallel} u_{n\perp})\right) - \frac{\partial p_n}{\partial x} + R_{n\parallel}, \\ &= -\frac{\partial}{\partial x}\left(m_n n_n u_{n\parallel} u_{n,eff} + p_n\right) + R_{n\parallel} \end{aligned} \tag{B.5}$$

and a perpendicular component,

$$\begin{aligned} \frac{\partial}{\partial t}\left(m_n n_n u_{n\perp}\right) &= -\left(\frac{\partial}{\partial x}(m_n n_n u_{n\parallel} u_{n\perp}) + \frac{\partial}{\partial y}(m_n n_n u_{n\perp}^2)\right) - \frac{\partial p_n}{\partial y} + R_{n\perp}, \\ &= -\frac{\partial}{\partial x}\left(m_n n_n u_{n\perp} u_{n,eff} + \frac{1}{\tan\alpha} p_n\right) + R_{n\perp} \end{aligned} \tag{B.6}$$

From these two equations, and using (B.4), we can obtain

$$n_n m_n \frac{\partial u_{n\parallel}}{\partial t} + n_n m_n u_{n,eff} \frac{\partial u_{n\parallel}}{\partial x} + \frac{\partial p_n}{\partial x} + m_n S_n u_{n\parallel} = R_{n\parallel}, \tag{B.7}$$

and

$$n_n m_n \frac{\partial u_{n\perp}}{\partial t} + n_n m_n u_{n,eff} \frac{\partial u_{n\perp}}{\partial x} + \frac{1}{\tan\alpha}\frac{\partial p_n}{\partial x} + m_n S_n u_{n\perp} = R_{n\perp}, \tag{B.8}$$

from which we can arrive at the form of the $u_{n\parallel}$ and $u_{n\perp}$ evolution equations implemented in SOL-KiT, (3.40b) and (3.40c), by dividing through by $m_n n_n$ and rearranging.

For the energy equation, we can use (B.2) and (B.3) to rewrite it as

$$\frac{\partial}{\partial t}\left(\frac{3}{2}n_n kT_n + \frac{1}{2}m_n n_n u_n^2\right) + \left(1 + \frac{1}{\tan^2\alpha}\right)\frac{\partial q_n}{\partial x} + \frac{\partial}{\partial x}\left(\left(\frac{5}{2}p_n + \frac{1}{2}m_n n_n u_n^2\right)u_{n,eff}\right) = Q_n, \tag{B.9}$$

where we have used the Helander form of the neutral heat flow [50],

$$\mathbf{q_n} = -2.4\frac{n_n kT_n}{m_n \nu_{cx}}\nabla kT_n$$

allowing us to write

$$\begin{aligned}\nabla\cdot\mathbf{q_n} &= \frac{\partial}{\partial x}\left(-2.4\frac{n_n kT_n}{m_n\nu_{cx}}\frac{\partial kT_n}{\partial x}\right) + \frac{\partial}{\partial y}\left(-2.4\frac{n_n kT_n}{m_n\nu_{cx}}\frac{\partial kT_n}{\partial y}\right)\\ &= \left(1+\frac{1}{\tan^2\alpha}\right)\frac{\partial q_n}{\partial x}\end{aligned}$$

with $q_n = -2.4\frac{n_n kT_n}{m_n\nu_{cx}}\frac{\partial kT_n}{\partial x}$. Now we use (B.1a) to rewrite (B.9),

$$n_n\left(\frac{\partial}{\partial t} + u_{n,eff}\frac{\partial}{\partial x} + S_n\right)\left(\frac{3}{2}kT_n + \frac{1}{2}m_n u_n^2\right) + \left(1+\frac{1}{\tan^2\alpha}\right)\frac{\partial q_n}{\partial x} + \frac{\partial}{\partial x}(n_n kT_n u_{n,eff}) = Q_n. \tag{B.10}$$

Finally, we take equation (B.10) − (equation (B.7) $\times u_{n\parallel}$ + equation (B.8) $\times u_{n\perp}$) to give

$$\frac{3}{2}n_n\left(\frac{\partial kT_n}{\partial t} + u_{n,eff}\frac{\partial kT}{\partial x}\right) + \left(1+\frac{1}{\tan^2\alpha}\right)\frac{\partial q_n}{\partial x} + n_n kT_n\frac{\partial u_{n,eff}}{\partial x} + S_n\left(\frac{3}{2}kT_n - \frac{1}{2}m_n u_n^2\right) = Q_n - u_{n\parallel}R_{n\parallel} - u_{n\perp}R_{n\perp}. \tag{B.11}$$

Straightforward rearrangement of this gives the form of the neutral temperature equation which has been implemented in SOL-KiT, equation (3.40d). As noted in Section 3.3, we choose to avoid introducing excessive neutral energy sources or sinks in this model with small values of the pitch angle α by only using the parallel components of the S_n and R_n terms in (B.11).

B.2 Boundary conditions

Boundary conditions for a fluid neutral model in the presence of a wall are intrinsically more complex than for the plasma species. This is because there is a surface interaction, some amount of reflection, and a source of recycled ions at the boundary. The approach taken here follows a similar outline to that of Horsten et al. [138, 139], applied to a 1D (or quasi-2D) simulation domain and with a simplified treatment of the surface physics.

We start by describing the neutral distribution at the boundary as consisting of three one-sided component distributions,

$$f_{n,t}(\mathbf{v}) = f_{inc}(\mathbf{v}) + f_{ref}(\mathbf{v}) + f_{rec}(\mathbf{v}), \tag{B.12}$$

where f_{inc} is the incident (forward-going) neutral distribution, f_{ref} is the reflection of f_{inc}, and f_{rec} is the distribution of recycled particles, which we take to be made up of Franck-Condon atoms. We assume all incident ions are released from the wall as molecules which quickly dissociate to become Franck-Condon atoms, i.e. there is no 'fast recycling' of ions.

We can now define the components of $f_{n,t}$ in more detail. We will take f_{inc} to be a half-Maxwellian at the same density and temperature of the neutrals in the last evolved location,

$$f_{inc}(\mathbf{v}) = H(v_x) n_n \left(\frac{m_i}{2\pi k T_n}\right)^{3/2} \exp\left(-\frac{m_i v^2}{2kT_n}\right), \tag{B.13}$$

where H is the Heaviside step function. The reflected distribution is the other half of the incident distribution, where reflected neutrals return with a fraction α_n of their incident energy and a fraction R_r of the incident particles are reflected,

$$f_{ref}(\mathbf{v}) = R_r H(-v_x) \frac{n_n}{\sqrt{\alpha_n}} \left(\frac{m_i}{2\pi k T_n \alpha_n}\right)^{3/2} \exp\left(-\frac{m_i v^2}{2kT_n\alpha_n}\right). \tag{B.14}$$

The recycled distribution consists of atoms emitted from the wall at $T_{FC} = 3$ eV, which is

written in spherical coordinates as

$$f_{rec}(\mathbf{v}) = (1 - R_d)H(\theta - \pi/2)n_{rec}\frac{\cos(\pi - \theta)}{\pi v^2}\delta(v - v_{th}^{FC}), \tag{B.15}$$

where we have made use of the cosine emission law, with the emission angle measured from the normal to the wall, and R_d is the fraction of recycled neutrals which are redistributed further upstream instead of being recycled at the target. The density of this distribution is n_{rec} (to be defined later), and $v_{th}^{FC} = \sqrt{2kT_{FC}/m_n}$. This is made up of recycled ions as well as non-reflected neutrals (which are absorbed and then re-emitted as Franck-Condon atoms).

With this, we can take the appropriate moments of $f_{n,t}$ to calculate the boundary conditions on the fluid neutral equations, where we need values of the particle flux, flow velocity and energy flux.

Particle flux

For the particle flux, $\Gamma_{n,t}$, we have

$$\begin{aligned}\Gamma_{n,t} &= \int v_x f_{n,t}(\mathbf{v})d\mathbf{v} \\ &= \underbrace{\int v_x f_{inc} d\mathbf{v}}_{\Gamma_{inc}} + \underbrace{\int v_x f_{ref} d\mathbf{v}}_{\Gamma_{ref}} + \underbrace{\int v_x f_{rec} d\mathbf{v}}_{\Gamma_{rec}},\end{aligned} \tag{B.16}$$

where each term evaluates to

$$\begin{aligned}\Gamma_{inc} &= \frac{n_n}{4}\sqrt{\frac{8kT_n}{\pi m_i}} \simeq \frac{1}{2}n_n c_s \\ \Gamma_{ref} &= -R_r\frac{n_n}{4\sqrt{\alpha_n}}\sqrt{\frac{8kT_n\alpha_n}{\pi m_i}} = -R_r\Gamma_{inc} \\ \Gamma_{rec} &= -(1 - R_d)\frac{2}{3}n_{rec}v_{th}^{FC},\end{aligned} \tag{B.17}$$

where $c_s = \sqrt{kT_n/m_i}$ is the neutral sound speed and $\Gamma_{i,t}$ is the ion flux crossing the sheath. We can simplify $\Gamma_{n,t}$ by making use of the fact that

$$\Gamma_{rec} = -((1 - R_r)\Gamma_{inc} + \Gamma_{i,t})(1 - R_d) \tag{B.18}$$

from particle conservation (assuming 100% plasma recycling). Therefore,

$$\begin{aligned} \Gamma_{n,t} &= \Gamma_{inc} + \Gamma_{ref} + \Gamma_{rec} \\ &= R_d(1 - R_r)\Gamma_{inc} - (1 - R_d)\Gamma_{i,t}, \end{aligned} \tag{B.19}$$

where, for $R_d = 0$, we get

$$\Gamma_{n,t} = -\Gamma_{i,t} \tag{B.20}$$

as expected.

For non-zero redistribution, equation (B.19) allows us to define the redistribution flux,

$$\Gamma_{redist} = -R_d(1 - R_r)\Gamma_{inc} - R_d\Gamma_{i,t}, \tag{B.21}$$

such that $\Gamma_{n,t} + \Gamma_{redist} = -\Gamma_{i,t}$, confirming that redistribution conserves particles, assuming 100% plasma recycling.

Flow velocity

The boundary condition on the flow velocity is

$$u_{n,t} = \frac{\Gamma_{n,t}}{n_{n,t}} \simeq \frac{-(1 - R_d)\Gamma_{i,t}}{n_{n,t}}, \tag{B.22}$$

which always points into the simulation domain as expected. The boundary density, $n_{n,t}$ is

$$n_{n,t} = \int f_{n,t} d\mathbf{v} = \frac{1}{2} n_n(1 + R_r) + n_{rec}, \tag{B.23}$$

which requires us to evaluate n_{rec}. We can do this by finding the velocity moment of f_{rec},

$$u_{rec} = \frac{1}{n_{rec}} \int v_x f_{rec} d\mathbf{v} = -(1 - R_d)\frac{2}{3} v_{th}^{FC}, \tag{B.24}$$

and so

$$n_{rec} = \frac{\Gamma_{rec}}{u_{rec}} = \frac{3}{2v_{th}^{FC}} \left((1 - R_r)\Gamma_{inc} + \Gamma_{i,t} \right). \tag{B.25}$$

If both $u_{n\parallel}$ and $u_{n\perp}$ are evolved, this boundary condition on the flow velocity is applied to $u_{n,eff}$. The value of $u_{n\parallel}$ at the boundary is then free ($\frac{\partial u_{n\parallel}}{\partial x} = 0$) and $u_{n\perp}$ is constrained by $u_{n,eff} = u_{n\parallel} + u_{n\perp}/\tan\alpha$.

Energy flux

The energy flux across the boundary is

$$\begin{aligned} q_{n,t} &= \int \frac{1}{2} m_i v^2 v_x f_{n,t} d\mathbf{v} \\ &= \frac{1}{2} m_i \left(\underbrace{\int v^2 v_x f_{inc} d\mathbf{v}}_{q_{inc}} + \underbrace{\int v^2 v_x f_{ref} d\mathbf{v}}_{q_{ref}} + \underbrace{\int v^2 v_x f_{rec} d\mathbf{v}}_{q_{rec}} \right). \end{aligned} \tag{B.26}$$

These three terms are

$$\begin{aligned} q_{inc} &= \int \frac{1}{2} m_i v^2 v_x f_{inc} d\mathbf{v} = \frac{1}{2} n_n k T_n \sqrt{\frac{8kT_n}{\pi m_i}} = 2kT_n \Gamma_{inc} \\ q_{ref} &= \int \frac{1}{2} m_i v^2 v_x f_{ref} d\mathbf{v} = -2R_r \alpha_n k T_n \Gamma_{inc} \\ q_{rec} &= \int \frac{1}{2} m_i v^2 v_x f_{rec} d\mathbf{v} = -(1 - R_d)\frac{2}{3} n_{rec} k T_{FC} v_{th}^{FC} = kT_{FC}\Gamma_{rec}, \end{aligned} \tag{B.27}$$

so the net heat flux across the boundary can be written

$$q_{n,t} = \gamma_n k T_n n_n c_s - (1 - R_d) k T_{FC} \Gamma_{i,t}, \tag{B.28}$$

with a neutral sheath heat transmission coefficient defined as

$$\gamma_n = 1 - \alpha_n R_r - (1 - R_r)(1 - R_d)\frac{T_{FC}}{2T_n}. \tag{B.29}$$

The first term in (3.61) is the neutral heat loss to the walls, while the second term is the input from the recycled ions. The effect of the non-reflected neutrals is included in γ_n. Depending on the choice of R_r and α_n, as well as the plasma and neutral conditions at the wall, the net heat flux across the boundary for the neutrals may be positive or negative. Reasonable values for deuterium neutrals incident on a Tungsten wall can be obtained from the TRIM database (`http://www.eirene.de/html/surface_data.html`), and here we may use $\alpha_n = 0.75$ and $R_r = 0.8$. This results in $\gamma_n = 0.3$ at $T_n = T_{FC}$, assuming $R_d = 0$.

Appendix C

Mirror force in Legendre decomposition of kinetic electron equation

Expanding magnetic field lines produce a mirror force on electrons. We seek here to develop a form of this magnetic mirror force in the Legendre polynomial decomposition of the kinetic equation, which will enable a kinetic treatment of flux tube expansion in SOL simulations in codes such as SOL-KiT. We will treat only the mirror force here and not other effects due to flux tube expansion, which are relatively straightforward and involve modified spatial gradients in the parallel direction.

C.1 Mirror force

An electron moves with parallel and perpendicular velocity components,

$$\mathbf{v} = v_x \hat{x} + v_\perp \hat{\phi},$$

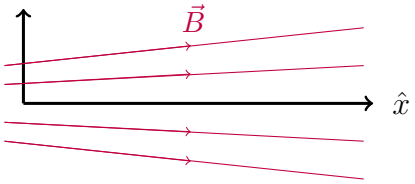

(a) Expanding field lines.

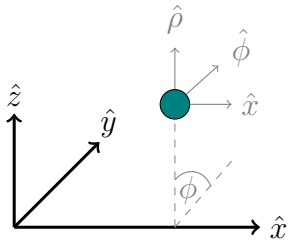

(b) Coordinate system for an electron orbiting about the x-axis.

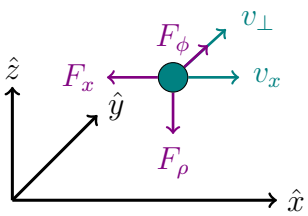

(c) Diagram of the velocity (cyan) and Lorentz force (purple) components acting on the electron.

Figure C.1: Geometry of an electron orbiting about the x-axis in an expanding flux tube.

in an expanding magnetic flux tube such that the magnetic field has radial and parallel components,

$$\mathbf{B} = B_\rho \hat{\rho} + B_x \hat{x},$$

where $\hat{\rho}$, $\hat{\phi}$ and $\hat{x}$ are the cylindrical coordinate unit vectors, i.e. $\hat{\rho} = \cos\phi\hat{y} + \sin\phi\hat{z}$, $\hat{\phi} = -\sin\phi\hat{y} + \cos\phi\hat{z}$, where ϕ is the azmithual angle in the yz-plane. The acceleration from the Lorentz force on the electron due to the magnetic field is

$$\mathbf{a} = -\frac{e}{m_e}\mathbf{v} \times \mathbf{B} = -\frac{e}{m_e}(v_\perp B_x \hat{\rho} + v_x B_\rho \hat{\phi} - v_\perp B_\rho \hat{x}) \tag{C.1}$$

This is shown in Figure C.1.

Assuming the magnetic field strength is approximately constant over a Larmor orbit (with radius r_L), and $B_\rho \ll B_x$, then we can write

$$B_\rho \simeq -\frac{1}{2} r_L \frac{\partial B_x}{\partial x} = \frac{m_e v_\perp}{2eB_x}\frac{\partial B_x}{\partial x}, \tag{C.2}$$

where e is the electric charge and m_e is the electron mass.

C.2 Derivation of the mirror force term in the kinetic equation

Starting from the kinetic equation,

$$\frac{\partial f(\mathbf{v})}{\partial t} + \mathbf{v} \cdot \nabla f(\mathbf{v}) + \mathbf{a} \cdot \nabla_v f(\mathbf{v}) = C, \tag{C.3}$$

we consider the consequences of the addition (compared to the SOL-KiT treatment of the kinetic equation, Section A.1) of a force due to the magnetic field. It can be shown, by rewriting the $\mathbf{a} \cdot \nabla_v f(\mathbf{v})$ term above in spherical coordinates, that the $\hat{\rho}$ and $\hat{\phi}$ components of $\mathbf{a}$ in (C.1) do not drive azimuthal asymmetries in f, and are non-zero only if f already has azimuthal asymmetries, i.e. if $\frac{\partial f}{\partial \phi} \neq 0$. As such, we can justify a 1D treatment along the x-axis, assuming symmetry of f about x, such that this becomes

$$\frac{\partial f(\mathbf{v})}{\partial t} + v_x \frac{\partial f(\mathbf{v})}{\partial x} + a_x \frac{\partial f(\mathbf{v})}{\partial v_x} = C. \tag{C.4}$$

This will enable a Legendre decomposition of the mirror force along similar lines to the treatment of the Vlasov terms outlined in Section A.1.

Focussing solely on the mirror force term, the x-component of $\mathbf{a}$ can be written

$$a_x = \frac{e}{m_e} v_\perp B_\rho = -\frac{v_\perp^2}{2B_x} \frac{\partial B_x}{\partial x} = -v^2 \sin^2\theta \frac{1}{2B} \frac{\partial B_x}{\partial x} \tag{C.5}$$

where θ is the polar angle between $\mathbf{v}$ and the x-axis. In spherical coordinates therefore,

$$a_x \frac{\partial f(\mathbf{v})}{\partial v_x} = -v^2 \sin^2\theta \frac{1}{2B} \frac{\partial B_x}{\partial x} \left(\cos\theta \frac{\partial f}{\partial v} - \frac{\sin\theta}{v} \frac{\partial f}{\partial \theta} \right). \tag{C.6}$$

Expanding $f(\mathbf{v})$ in Legendre polynomials,

$$f(\mathbf{v}) = \sum_{l=0}^{\infty} f(v) P_l(\cos\theta),$$

and writing $\xi = \cos\theta$, then (C.6) becomes

$$a_x \frac{\partial f(\mathbf{v})}{\partial v_x} = \frac{v^2}{2B_x}\frac{\partial B_x}{\partial x}\sum_{l=0}^{\infty}\left\{(\xi^2-1)\left(\xi P_l \frac{\partial f_l(v)}{\partial v} + f_l(v)\frac{1-\xi^2}{v}\frac{dP_l}{d\xi}\right)\right\}. \tag{C.7}$$

This can be dealt with in a similar way to the velocity space advection due to the electric field, as outlined in Section A.1. Using the Legendre polynomial recurrence relations,

$$\xi P_l = \frac{l+1}{2l+1}P_{l+1} + \frac{l}{2l+1}P_{l-1},$$

$$(\xi^2-1)\frac{dP_l}{d\xi} = \frac{l(l+1)}{2l+1}(P_{l+1} - P_{l-1}),$$

we can obtain

$$\xi^2 P_l = \underbrace{\frac{(l+1)(l+2)}{(2l+1)(2l+3)}}_{\equiv\alpha_l} P_{l+2} + \underbrace{\frac{2l^2+2l-1}{(2l-1)(2l+3)}}_{\equiv\beta_l} P_l + \underbrace{\frac{l(l-1)}{(2l-1)(2l+1)}}_{\equiv\gamma_l} P_{l-2}. \tag{C.9}$$

Using these relations (noting the definitions of the constants α_l, β_l and γ_l) and making use of the functions

$$F_l(v) \equiv \frac{l}{2l+1}\left(\frac{\partial f_l}{\partial v} + (l+1)\frac{f_l}{v}\right),$$

$$J_l(v) \equiv \frac{l+1}{2l+1}\left(\frac{\partial f_l}{\partial v} - l\frac{f_l}{v}\right),$$

equation (C.7) becomes

$$\begin{aligned} a_x \frac{\partial f(\mathbf{v})}{\partial v_x} = \frac{v^2}{2B_x}\frac{\partial B_x}{\partial x}\sum_{l=0}^{\infty}\{&P_{l-3}F_l\gamma_{l-1} + P_{l-1}\left[F_l(\beta_{l-1}-1) + J_l\gamma_{l+1}\right] \\ &+ P_{l+1}\left[F_l\alpha_{l-1} + J_l(\beta_{l+1}-1)\right] + P_{l+3}J_l\alpha_{l+1}\}. \end{aligned} \tag{C.11}$$

Now, we can group into factors of the same order polynomial by changing summation indices and exploiting vanishing terms, meaning the summation part of this can be written

$$\sum_{l=0}^{\infty}\{F_{l+3}\gamma_{l+2} + F_{l+1}(\beta_l - 1) + J_{l+1}\gamma_{l+2} + F_{l-1}\alpha_{l-2} + J_{l-1}(\beta_l - 1) + J_{l-3}\alpha_{l-2}\}P_l. \tag{C.12}$$

Finally, by using the orthogonality of Legendre polynomials we arrive at a set of coefficients B_l,

$$B_l = -\frac{v^2}{2B_x}\frac{\partial B_x}{\partial x}\left\{F_{l+3}\gamma_{l+2} + F_{l+1}(\beta_l - 1) + J_{l+1}\gamma_{l+2} \right. \\ \left. + F_{l-1}\alpha_{l-2} + J_{l-1}(\beta_l - 1) + J_{l-3}\alpha_{l-2}\right\}, \tag{C.13}$$

which are readily inserted into the evolution equation for each f_l,

$$\frac{\partial f_l}{\partial t} = B_l + A_l + E_l + C_l \tag{C.14}$$

where E_l, A_l and C_l are the usual electric field, spatial advection and collision terms respectively as defined in Section A.1.

Bibliography

[1] A. V. Chankin and D. P. Coster. Comparison of 2D models for the plasma edge with experimental measurements and assessment of deficiencies. *Journal of Nuclear Materials*, 390-391(1):319–324, 2009.

[2] D. Tskhakaya. On Recent Massively Parallelized PIC Simulations of the SOL. *Contributions to Plasma Physics*, 52(5-6):490–499, 2012.

[3] M. Zhao, A. V. Chankin, and D. P. Coster. Kinetic simulations of electron heat flux in the scrape-off layer. *Nuclear Materials and Energy*, 12:819–824, 2017.

[4] S. Mijin, A. Antony, F. Militello, and R. J. Kingham. SOL-KiT—Fully implicit code for kinetic simulation of parallel electron transport in the tokamak Scrape-Off Layer. *Computer Physics Communications*, 258:107600, 2021.

[5] Marina Fischer-Kowalski and Anke Schaffartzik. Energy availability and energy sources as determinants of societal development in a long-term perspective. *MRS Energy & Sustainability*, 2(1):1–14, 2015.

[6] International Energy Outlook 2021. Technical report, United States Energy Information Administration, 2021.

[7] Dan Welsby, James Price, Steve Pye, and Paul Ekins. Unextractable fossil fuels in a 1.5 °C world. *Nature*, 597(7875):230–234, 2021.

[8] Paul Warde. *Energy Consumption in England & Wales: 1560-2000*. Consiglio Nazionale delle Ricerche, 2007.

[9] David JC MacKay. *Sustainable energy without the hot air*. UIT Cambridge, 2008.

[10] Hannah Ritchie, Max Roser, and Pablo Rosado. Energy. *Our World in Data*, 2022.

[11] G. Giruzzi, J. F. Artaud, M. Baruzzo, T. Bolzonella, E. Fable, L. Garzotti, I. Ivanova-Stanik, R. Kemp, D. B. King, M. Schneider, R. Stankiewicz, W. Stępniewski, P. Vincenzi, D. Ward, and R. Zagórski. Modelling of pulsed and steady-state DEMO scenarios. *Nuclear Fusion*, 55(7), 2015.

[12] Sehila M. Gonzalez De Vicente, Nicholas A. Smith, Laila El-Guebaly, Sergio Ciattaglia, Luigi Di Pace, Mark Gilbert, Robert Mandoki, Sandrine Rosanvallon, Youji Someya, Kenji Tobita, and David Torcy. Overview on the management of radioactive waste from fusion facilities: ITER, demonstration machines and power plants. *Nuclear Fusion*, 62(8), 2022.

[13] H. et al. Abu-Shawareb. Lawson Criterion for Ignition Exceeded in an Inertial Fusion Experiment. *Physical Review Letters*, 129(7):75001, 2022.

[14] R. J. Buttery, J. M. Park, J. T. McClenaghan, D. B. Weisberg, J. Canik, J. Ferron, A. M. Garofalo, C. T. Holcomb, J. A. Leuer, and P. B. Snyder. The advanced tokamak path to a compact net electric fusion pilot plant. *Nuclear Fusion*, 61, 2021.

[15] Michel Claessens. *ITER: The Giant Fusion Reactor*. 2020.

[16] T Donné. European research roadmap to the realisation of fusion energy, 2018.

[17] A. Yu Dnestrovskij, J. W. Connor, and M. P. Gryaznevich. On the confinement modeling of a high field spherical tokamak ST40. *Plasma Physics and Controlled Fusion*, 61(5), 2019.

[18] A. J. Creely, M. J. Greenwald, S. B. Ballinger, D. Brunner, J. Canik, J. Doody, T. Fülöp, D. T. Garnier, R. Granetz, T. K. Gray, C. Holland, N. T. Howard, J. W. Hughes, J. H. Irby, V. A. Izzo, G. J. Kramer, A. Q. Kuang, B. Labombard, Y. Lin, B. Lipschultz, N. C. Logan, J. D. Lore, E. S. Marmar, K. Montes, R. T. Mumgaard, C. Paz-Soldan, C. Rea, M. L. Reinke, P. Rodriguez-Fernandez, K. Särkimäki, F. Sciortino, S. D. Scott, A. Snicker,

P. B. Snyder, B. N. Sorbom, R. Sweeney, R. A. Tinguely, E. A. Tolman, M. Umansky, O. Vallhagen, J. Varje, D. G. Whyte, J. C. Wright, S. J. Wukitch, and J. Zhu. Overview of the SPARC tokamak. *Journal of Plasma Physics*, pages 1–25, 2020.

[19] H. Han, S. J. Park, C. Sung, J. Kang, Y. H. Lee, J. Chung, T. S. Hahm, B. Kim, J. K. Park, J. G. Bak, M. S. Cha, G. J. Choi, M. J. Choi, J. Gwak, S. H. Hahn, J. Jang, K. C. Lee, J. H. Kim, S. K. Kim, W. C. Kim, J. Ko, W. H. Ko, C. Y. Lee, J. H. Lee, J. H. Lee, J. K. Lee, J. P. Lee, K. D. Lee, Y. S. Park, J. Seo, S. M. Yang, S. W. Yoon, and Y. S. Na. A sustained high-temperature fusion plasma regime facilitated by fast ions. *Nature*, 609(7926):269–275, 2022.

[20] M. E. Fenstermacher. DIII-D research advancing the physics basis for optimizing the tokamak approach. 2022.

[21] John Wesson. *Tokamaks*. Oxford University Press, 3rd edition, 2004.

[22] J. D. Lawson. Some criteria for a power producing thermonuclear reactor. *Proceedings of the Physical Society. Section B*, 70(1):6–10, 1957.

[23] Samuel E. Wurzel and Scott C. Hsu. Progress toward fusion energy breakeven and gain as measured against the Lawson criterion. *Submitted to arXiv: 2105.10954*, 2022.

[24] P. C. Stangeby. The Plasma Boundary of Magnetic Fusion Devices. *Plasma Physics and Controlled Fusion*, 43(2):223–224, 2001.

[25] Noah Mandell. Magnetic Fluctuations in Gyrokinetic Simulations of Tokamak Scrape-Off Layer Turbulence. (May), 2021.

[26] R. A. Pitts, X. Bonnin, F. Escourbiac, H. Frerichs, J. P. Gunn, T. Hirai, A. S. Kukushkin, E. Kaveeva, M. A. Miller, D. Moulton, V. Rozhansky, I. Senichenkov, E. Sytova, O. Schmitz, P. C. Stangeby, G. De Temmerman, I. Veselova, and S. Wiesen. Physics basis for the first ITER tungsten divertor. *Nuclear Materials and Energy*, 20(February):100696, 2019.

[27] A. Fasoli, S. Brunner, W. A. Cooper, J. P. Graves, P. Ricci, O. Sauter, and L. Villard. Computational challenges in magnetic-confinement fusion physics. *Nature Physics*, 12(5):411–423, 2016.

[28] T. D. Rognlien. Understanding of edge plasmas in magnetic fusion energy devices. *Plasma Physics and Controlled Fusion*, 47(5 A), 2005.

[29] A. W. Leonard, J. A. Boedo, M. Groth, B. L. Lipschultz, G. D. Porter, D. L. Rudakov, and D. G. Whyte. Particle flux and radial profiles in the SOL of DIII-D during ELMing H-mode. *Journal of Nuclear Materials*, 363-365(1-3):1066–1070, 2007.

[30] S. K. Erents and P. C. Stangeby. Heat transport in the JET scrape-off layer. *Nuclear Fusion*, 38(11):1637–1650, 1998.

[31] Giulio Rubino, R. Ambrosino, G. Calabrò, V. Pericoli Ridolfini, and B. Viola. Comparative analysis of the SOL plasma in DEMO using EDGE2D/EIRENE and TECXY codes. *Nuclear Materials and Energy*, 12:864–868, 2017.

[32] Michael R K Wigram. *Modelling tokamak power exhaust and scrape-off-layer thermal transport in high-power fusion devices*. PhD thesis, 2019.

[33] A. Q. Kuang, S. Ballinger, D. Brunner, J. Canik, A. J. Creely, T. Gray, M. Greenwald, J. W. Hughes, J. Irby, B. Labombard, B. Lipschultz, J. D. Lore, M. L. Reinke, J. L. Terry, M. Umansky, D. G. Whyte, and S. Wukitch. Divertor heat flux challenge and mitigation in SPARC. *Journal of Plasma Physics*, (2020), 2020.

[34] X. Bonnin, Wouter DEKEYSER, Richard PITTS, David COSTER, Serguey VOSKOBOYNIKOV, and Sven WIESEN. Presentation of the New SOLPS-ITER Code Package for Tokamak Plasma Edge Modelling. *Plasma and Fusion Research*, 11(0):1403102–1403102, 2016.

[35] A. V. Chankin, D. P. Coster, R. Dux, Ch Fuchs, G. Haas, A. Herrmann, L. D. Horton, A. Kallenbach, M. Kaufmann, Ch Konz, K. Lackner, C. Maggi, H. W. Müller, J. Neuhauser, R. Pugno, M. Reich, and W. Schneider. SOLPS modelling of ASDEX upgrade H-mode plasma. *Plasma Physics and Controlled Fusion*, 48(6):839–868, 2006.

[36] M. Wensing, H. Reimerdes, O. Février, C. Colandrea, L. Martinelli, K. Verhaegh, F. Bagnato, P. Blanchard, B. Vincent, A. Perek, S. Gorno, H. De Oliveira, C. Theiler, B. P. Duval, C. K. Tsui, M. Baquero-Ruiz, and M. Wischmeier. SOLPS-ITER validation with TCV L-mode discharges. *Physics of Plasmas*, 28(8), 2021.

[37] D. Tskhakaya, S. Jachmich, T. Eich, and W. Fundamenski. Interpretation of divertor Langmuir probe measurements during the ELMs at JET. *Journal of Nuclear Materials*, 415(1 SUPPL):S860–S864, 2011.

[38] D. Brunner and B. Labombard. Surface thermocouples for measurement of pulsed heat flux in the divertor of the Alcator C-Mod tokamak. *Review of Scientific Instruments*, 83(3), 2012.

[39] D. Power, S. Mijin, F. Militello, and R. J. Kingham. Ion–electron energy transfer in kinetic and fluid modelling of the tokamak scrape-off layer. *The European Physical Journal Plus*, 136(11):1–13, 2021.

[40] T J M Boyd and J J Sanderson. *The physics of plasmas*. Cambridge University Press, Cambridge, 2003.

[41] D. G. Swanson. *Plasma Kinetic Theory*. 2008.

[42] I. P. Shkarofsky, M. P. Bachynski, and T. W. Johnston. *The Particle Kinetics of Plasmas*. Reading, Mass.; Dordrecht printed, 1966.

[43] Paul M Bellan. *Fundamentals of Plasma Physics*. Cambridge University Press, 2006.

[44] Toshiaki Makabe and Kiyoichi Takatsu. *Plasma Electronics*. 2 edition, 2014.

[45] C. Cercignani. *The Boltzmann Equation and its Applications*. Springer New York, 1988.

[46] S. Chapman and T. G. Cowling. *The Mathematical Theory of Non-uniform Gases*. Cambridge University Press, 1952.

[47] A. S. Richardson. 2019 NRL Plasma Formulary. *Plasma Physics*, pages 1–71, 2019.

[48] S I Braginskii. *Transport Processes in Plasmas*. New York, 1965.

[49] Lyman Spitzer and Richard Härm. Transport phenomena in a completely ionized gas. *Physical Review*, 89(5):977–981, 1953.

[50] P. Helander, S. I. Krasheninnikov, and P. J. Catto. Fluid equations for a partially ionized plasma. *Physics of Plasmas*, 1(10):3174–3180, 1994.

[51] V. M. Zhdanov. *Transport Processes in Multicomponent Plasma*. CRC Press, 1st edition, 2002.

[52] D. R. Bates, A. E. Kingston, and W. P. McWhirter. Recombination between electrons and atomic ions, 1. Optically thin plasmas. *Proceedings of the Royal Society*, 267, 1962.

[53] H. P. Summers, W. J. Dickson, M. G. O'Mullane, N. R. Badnell, A. D. Whiteford, D. H. Brooks, J. Lang, S. D. Loch, and D. C. Griffin. Ionization state, excited populations and emission of impurities in dynamic finite density plasmas: I. The generalized collisional-radiative model for light elements. *Plasma Physics and Controlled Fusion*, 48(2):263–293, 2006.

[54] P. T. Greenland. Collisional-radiative models with molecules. pages 1821–1839, 2001.

[55] Y. Ohkouchi, S. Sasaki, S. Takamura, and T. Kato. Effective Emission and Ionization Rate Coefficients of Atomic Carbons in Plasmas. (June), 1993.

[56] Keiji Sawada and Takashi Fujimoto. Effective ionization and dissociation rate coefficients of molecular hydrogen in plasma. *Journal of Applied Physics*, 78(5):2913–2924, 1995.

[57] D. Reiter, M. Baelmans, and P. Börner. The eirene and B2-eirene codes. *Fusion Science and Technology*, 47(2):172–186, 2005.

[58] F. Sciortino, T. Odstrčil, A. Cavallaro, S. Smith, O. Meneghini, R. Reksoatmodjo, O. Linder, J. D. Lore, N. T. Howard, E. S. Marmar, and S. Mordijck. Modeling of Particle Transport, Neutrals and Radiation in Magnetically-Confined Plasmas with AURORA. pages 1–9, 2021.

[59] J. Ongena, R. Koch, R. Wolf, and H. Zohm. Magnetic-confinement fusion. *Nature Physics*, 12(5):398–410, 2016.

[60] F. Militello. *Boundary Plasma Physics*. 2020.

[61] M. Groth, V. Solokha, S. Aleiferis, S. Brezinsek, M. Brix, I. S. Carvalho, P. Carvalho, G. Corrigan, D. Harting, N. Horsten, I. Jepu, J. Karhunen, K. Kirov, B. Lomanowski, K. D. Lawson, C. Lowry, A. G. Meigs, S. Menmuir, E. Pawelec, T. Pereira, A. Shaw, S. Silburn, B. Thomas, S. Wiesen, P. Börner, D. Borodin, S. Jachmich, D. Reiter, G. Sergienko, Z. Stancar, B. Viola, P. Beaumont, J. Bernardo, I. Coffey, N. J. Conway, E. de la Luna, D. Douai, C. Giroud, J. Hillesheim, L. Horvath, A. Huber, P. Lomas, C. F. Maggi, M. Maslov, C. Perez von Thun, S. Scully, N. Vianello, and M. Wischmeier. Characterisation of divertor detachment onset in JET-ILW hydrogen, deuterium, tritium and deuterium–tritium low-confinement mode plasmas. *Nuclear Materials and Energy*, 34(November 2022), 2023.

[62] Bruce Lipschultz, Felix I. Parra, and Ian H. Hutchinson. Sensitivity of detachment extent to magnetic configuration and external parameters. *Nuclear Fusion*, 56(5), 2016.

[63] A. V. Chankin and D. P. Coster. On the locality of parallel transport of heat carrying electrons in the SOL. *Journal of Nuclear Materials*, 463:498–501, 2015.

[64] W. Fundamenski. Parallel heat flux limits in the tokamak scrape-off layer. *Plasma Physics and Controlled Fusion*, 47(11), 2005.

[65] A. A. Batishcheva, O. V. Batishchev, S. I. Krasheninnikov, D. J. Sigmar, A. E. Koniges, G. G. Craddock, and V. Djordjevic. Massively Parallel Fokker-Planck Code ALLAp. *Contributions to Plasma Physics*, 36(2-3):414–418, 1996.

[66] A. A. Batishcheva, O. V. Batishchev, S. I. Krasheninnikov, D. J. Sigmar, M. M. Shoucri, and I. P. Shkarofsky. Fokker-Planck Simulation of Electron Transport in SOL Plasmas with ALLA Code. *Contributions to Plasma Physics*, 36(2-3):235–239, 1996.

[67] O. V. Batishchev, S. I. Krasheninnikov, Peter J. Catto, A. A. Batishcheva, D. J. Sigmar, X. Q. Xu, J. A. Byers, T. D. Rognlien, R. H. Cohen, M. M. Shoucri, and I. P. Shkarofskii. Kinetic effects in tokamak scrape-off layer plasmas. *Physics of Plasmas*, 4(5 /2):1672–1680, 1997.

[68] O. V. Batishchev, M. M. Shoucri, A. A. Batishcheva, and I. P. Shkarofsky. Fully kinetic simulation of coupled plasma and neutral particles in scrape-off layer plasmas of fusion devices. *Journal of Plasma Physics*, 61(2):347–364, 1999.

[69] P. L. Bhatnagar, E. P. Gross, and M. Krook. A Model for Collision Processes in Gases. I. Small Amplitude Processes in Charged and Neutral One-Component Systems. *Physical Review*, 94(3):511–525, 1954.

[70] D. Tskhakaya and S. Kuhn. Particle simulations of magnetized hydrogen plasma-wall transition taking into account collisions with hydrogen atoms. *29th EPS conference on Plasma Physics and Controlled Fusion*, 26(June):2–5, 2002.

[71] D. Tskhakaya and S. Kuhn. The magnetised plasma-wall transition: Theory and PIC simulation. *Contributions to Plasma Physics*, 44(5-6):564–570, 2004.

[72] D. Tskhakaya. Kinetic Modelling of the Detached Divertor Plasma. (633053), 2015.

[73] D. Tskhakaya and M. Groth. 1D kinetic modelling of the JET SOL with tungsten divertor plates. *Journal of Nuclear Materials*, 438(SUPPL):S522–S525, 2013.

[74] D. Tskhakaya and M. Groth. Modelling of tungsten re-deposition coefficient. *Journal of Nuclear Materials*, 463:624–628, 2015.

[75] D. Tskhakaya, F. Subba, X. Bonnin, D. P. Coster, W. Fundamenski, and R. A. Pitts. On kinetic effects during parallel transport in the SOL. *Contributions to Plasma Physics*, 48(1-3):89–93, 2008.

[76] D. Tskhakaya, J. Adamek, M. Dimitrova, K. Hromasova, J. Seidl, M. Sos, and P. Vondracek. Kinetic model of the COMPASS tokamak SOL. *Nuclear Materials and Energy*, 26(November 2020):0–5, 2021.

[77] I. Vasileska and L. Kos. Time-Dependent Boundary Conditions During ELMs in ITER Plasma. *Journal of Fusion Energy*, 39(5):212–220, 2020.

[78] I. Vasileska and L. Kos. Kinetic-fluid coupling simulations of ITER Type I ELM. *Fusion Engineering and Design*, 168(December 2020):112407, 2021.

[79] A. V. Chankin, D. P. Coster, and G. Meisl. Development and Benchmarking of a New Kinetic Code for Plasma Periphery (KIPP). *Contributions to Plasma Physics*, 52(5-6):500–504, 2012.

[80] A. V. Chankin, Gerard Corrigan, and Aaro Einari Jaervinen. Kinetic modelling of parallel ion transport in the SOL and divertor of inter-ELM JET high radiative H-mode plasma. *Plasma Physics and Controlled Fusion*, pages 0–10, 2020.

[81] A. V. Chankin, G. Corrigan, and A. E. Jaervinen. Assessment of the strength of kinetic effects of parallel electron transport in the SOL and divertor of JET high radiative H-mode plasmas using EDGE2D-EIRENE and KIPP codes. *Plasma Physics and Controlled Fusion*, 60(11), 2018.

[82] Menglong Zhao, A. V. Chankin, and D. P. Coster. Implementation of an inelastic collision operator into KIPP-SOLPS coupling and its effects on electron parallel transport in the scrape-off layer plasmas. *Contributions to Plasma Physics*, 59(7):1–13, 2019.

[83] S. Mijin, F. Militello, S. Newton, J. Omotani, and R. J. Kingham. Kinetic and fluid simulations of parallel electron transport during equilibria and transients in the scrape-off layer. *Plasma Physics and Controlled Fusion*, 62(9):095004, 2020.

[84] S. Mijin, F. Militello, S. Newton, J. Omotani, and R. J. Kingham. Kinetic effects in parallel electron energy transport channels in the Scrape-Off Layer. Technical report, 2019.

[85] T. D. Rognlien, D. D. Ryutov, N. Mattor, and G. D. Porter. Two-dimensional electric fields and drifts near the magnetic separatrix in divertor tokamaks. *Physics of Plasmas*, 6(5 I):1851–1857, 1999.

[86] S. O. Makarov, D. P. Coster, E. G. Kaveeva, V. A. Rozhansky, I. Y. Senichenkov, I. Veselova, S. Voskoboynikov, A. A. Stepanenko, X. Bonnin, and R. A. Pitts. Implementation of SOLPS-ITER codewith new Grad-Zhdanov module for D-T mixture. *Nuclear Fusion*, (Accepted manuscript), 2022.

[87] P. Ricci, F. D. Halpern, S. Jolliet, J. Loizu, A. Mosetto, A. Fasoli, I. Furno, and C. Theiler. Simulation of plasma turbulence in scrape-off layer conditions: The GBS code, simulation results and code validation. *Plasma Physics and Controlled Fusion*, 54(12), 2012.

[88] B. Dudson, M. V. Umansky, X. Q. Xu, P. B. Snyder, and H. R. Wilson. BOUT++: A framework for parallel plasma fluid simulations. *Computer Physics Communications*, 180(9):1467–1480, 2009.

[89] E. Havlíčková, W. Fundamenski, F. Subba, D. Coster, M. Wischmeier, and G. Fishpool. Benchmarking of a 1D scrape-off layer code SOLF1D with SOLPS and its use in modelling long-legged divertors. *Plasma Physics and Controlled Fusion*, 55(6), 2013.

[90] B. Dudson, J. Allen, T. Body, B. Chapman, C. Lau, L. Townley, D. Moulton, J. Harrison, and B. Lipschultz. The role of particle, energy and momentum losses in 1D simulations of divertor detachment. *Plasma Physics and Controlled Fusion*, 61(6), 2019.

[91] G L Derks, J P K W Frankemölle, J T W Koenders, M van Berkel, H Reimerdes, M Wensing, and E Westerhof. Benchmark of a self-consistent dynamic 1D divertor model DIV1D using the 2D SOLPS-ITER code. *Plasma Physics and Controlled Fusion*, 64(12):125013, 2022.

[92] M. Kryjak, B. Dudson, D. Power, S. Mijin, and C. Ridgers. Sensitivity of scrape-off layer codes to modelling approaches. *48th EPS Conference on Plasma Physics, EPS 2022*, pages 4–7, 2022.

[93] G. P. Schurtz, P. D. Nicolaï, and M. Busquet. A nonlocal electron conduction model for multidimensional radiation hydrodynamics codes. *Physics of Plasmas*, 7(10):4238–4249, 2000.

[94] J. R. Albritton, E. A. Williams, I. B. Bernstein, and K. P. Swartz. Nonlocal electron heat transport by not quite maxwell-boltzmann distributions. *Physical Review Letters*, 57(15):1887–1890, 1986.

[95] M. D. Rosen, H. A. Scott, D. E. Hinkel, E. A. Williams, D. A. Callahan, R. P.J. Town, L. Divol, P. A. Michel, W. L. Kruer, L. J. Suter, R. A. London, J. A. Harte, and G. B.

Zimmerman. The role of a detailed configuration accounting (DCA) atomic physics package in explaining the energy balance in ignition-scale hohlraums. *High Energy Density Physics*, 7(3):180–190, 2011.

[96] A. Marocchino, M. Tzoufras, S. Atzeni, A. Schiavi, Ph. Nicolaï, J. Mallet, V. Tikhonchuk, and J. L. Feugeas. Comparison for non-local hydrodynamic thermal conduction models. *Physics of Plasmas*, 20(2), 2013.

[97] J. P. Brodrick, R. J. Kingham, M. M. Marinak, M. V. Patel, A. V. Chankin, J. T. Omotani, M. V. Umansky, D. Del Sorbo, B. Dudson, J. T. Parker, G. D. Kerbel, M. Sherlock, and C. P. Ridgers. Testing nonlocal models of electron thermal conduction for magnetic and inertial confinement fusion applications. *Physics of Plasmas*, 24(9), sep 2017.

[98] M Sherlock, J. P. Brodrick, and C. P. Ridgers. A comparison of non-local electron transport models for laser-plasmas relevant to inertial con?nement fusion. 2017.

[99] Jeong Young Ji, Eric D. Held, and Carl R. Sovinec. Moment approach to deriving parallel heat flow for general collisionality. *Physics of Plasmas*, 16(2), 2009.

[100] J. T. Omotani and B. D. Dudson. Non-local approach to kinetic effects on parallel transport in fluid models of the scrape-off layer. *Plasma Physics and Controlled Fusion*, 55(5), 2013.

[101] M. Wigram, C. P. Ridgers, B. Dudson, J. P. Brodrick, and J. T. Omotani. Incorporating nonlocal parallel thermal transport in 1D ITER SOL modelling. 2020.

[102] D. Del Sorbo, J. L. Feugeas, Ph. Nicolaï, M. Olazabal-Loumé, B. Dubroca, S. Guisset, M. Touati, and V. Tikhonchuk. Reduced entropic model for studies of multidimensional nonlocal transport in high-energy-density plasmas. *Physics of Plasmas*, 22(8), 2015.

[103] D. Del Sorbo, J. L. Feugeas, P. Nicolaï, M. Olazabal-Loumé, B. Dubroca, and V. Tikhonchuk. Extension of a reduced entropic model of electron transport to magnetized nonlocal regimes of high-energy-density plasmas. *Laser and Particle Beams*, 34(3):412–425, 2016.

[104] Wallace Manheimer, Denis Colombant, and Valeri Goncharov. The development of a Krook model for nonlocal transport in laser produced plasmas. I. Basic theory. *Physics of Plasmas*, 15(8), 2008.

[105] J. P. Brodrick, D. Del Sorbo, and C. P. Ridgers. An alternative justification for the stationary assumption made by many reduced models for nonlocal electron heat flow in plasmas. *Physics of Plasmas*, 30(5), 2023.

[106] L. Lengyel. Analysis of Radiating Plasma Boundary Layers. Technical report, IPP, 1981.

[107] D Moulton, P C Stangeby, X Bonnin, and R A Pitts. Comparison between SOLPS-4 . 3 and the Lengyel Model for ITER baseline neon-seeded plasmas. 2021.

[108] Yuki Homma. Assessment of the impact of the kinetic effect of ion parallel heat conduction on DEMO-relevant SOL plasma using integrated SOL-divertor code SONIC. *Plasma Physics and Controlled Fusion*, 64(4), 2022.

[109] S. Mijin. *Modelling of Kinetic Effects in Parallel Transport in the Tokamak Scrape-Off Layer*. PhD thesis, Imperial College London.

[110] A. R. Bell, A. P.L. Robinson, M. Sherlock, R. J. Kingham, and W. Rozmus. Fast electron transport in laser-produced plasmas and the KALOS code for solution of the Vlasov-Fokker-Planck equation. *Plasma Physics and Controlled Fusion*, 48(3), 2006.

[111] R. J. Kingham and A. R. Bell. *An implicit Vlasov-Fokker-Planck code to model non-local electron transport in 2-D with magnetic fields*, volume 194. 2004.

[112] M. Tzoufras, A. R. Bell, P. A. Norreys, and F. S. Tsung. A Vlasov-Fokker-Planck code for high energy density physics. *Journal of Computational Physics*, 230(17):6475–6494, 2011.

[113] R. K. Janev, D Reiter, and U Samm. *Collision Processes in Low-Temperature Hydrogen Plasmas*. 2003.

[114] D P Stotler and C Karney. Neutral Gas Transport Modeling with DEGAS 2. *Contributions to Plasma Physics*, 34(2/3):392–397, 1994.

[115] Maarten Blommaert, N. Horsten, Petra Börner, and W. Dekeyser. A spatially hybrid fluid-kinetic neutral model for SOLPS-ITER plasma edge simulations. *Nuclear Materials and Energy*, 19(August 2018):28–33, 2019.

[116] H. L. Pauls, G. P. Zank, and H. R. Müller. Interaction of the solar wind with the local interstellar medium. *Journal of Geophysical Research*, 100, 1995.

[117] Eric Todd Meier. Modeling Plasmas with Strong Anisotropy, Neutral Fluid Effects and Open Boundaries. (August 2011):213, 2011.

[118] S. Balay, S. Abhyankar, M. F. Adams, S. Benson, J. Brown, P. Brune, K. Buschel Man, E. M. Constantinescu, L. Dalcin, A. Dener, V. Eijkhout, J. Faibussowitsch, W. D. Gropp, V. Hapla, T. Isaac, P. Jolivet, D. Karpeev, D. Kaushik, M. G.Knepley, F. Kong, S. Kruger, D. A. May, L. Curfman McInnes, R. Tran Mills, L. Mitchell, T. Munson, J. E. Roman, K. Rupp, P. Sanan, J. Sarich, B. F. Smith, S. Zampini, H. Zhang, H. Zhang, and J. Zhang. PETSc / TAO Users Manual - Revision 3.18. Technical report, 2022.

[119] Ming Feng Gu. The flexible atomic code. *Canadian Journal of Physics*, 86(5):675–689, 2004.

[120] A. Kramida, Y. Ralchenko, and J. Reader. Nist atomic spectra database, 2020.

[121] Hiroya Suno and Takako Kato. Cross section database for carbon atoms and ions: Electron-impact ionization, excitation, and charge exchange in collisions with hydrogen atoms. *Atomic Data and Nuclear Data Tables*, 92(4):407–455, 2006.

[122] J. Adamek, D. Tskhakaya, A. Devitre, J. Cavalier, J. Horacek, M. Komm, M. Sos, P. Bilkova, P. Böhm, J. Seidl, V. Weinzettl, P. Vondracek, T. Markovic, M. Hron, and R. Panek. On the transport of edge localized mode filaments in the tokamak scrape-off layer. *Nuclear Fusion*, 60(9), 2020.

[123] S. Costea, J. Kovačič, D. Tskhakaya, R. Schrittwieser, T. Gyergyek, and Tsv K. Popov. Particle-in-cell simulations of parallel dynamics of a blob in the scrape-off-layer plasma of a generic medium-size tokamak. *Plasma Physics and Controlled Fusion*, 63(5), 2021.

[124] Z. Abou-Assaleh, M. Petravic, R. Vesey, J. P. Matte, and T. W. Johnston. Non-Local Transport in a Tokamak Plasma Divertor with Recycling. *Contributions to Plasma Physics*, 34(2-3):175–179, 1994.

[125] D. P. Coster. Detachment physics in SOLPS simulations. *Journal of Nuclear Materials*, 415(1 SUPPL):S545–S548, 2011.

[126] Irina Veselova, Elizaveta Kaveeva, Vladimir Rozhansky, Ilya Senichenkov, Anastasia Poletaeva, Richard A. Pitts, and Xavier Bonnin. SOLPS-ITER drift modelling of ITER burning plasmas with narrow near-SOL heat flux channels. *Nuclear Materials and Energy*, 26:100870, 2021.

[127] Giulio Rubino, R. Ambrosino, G. Calabrò, V. Pericoli Ridolfini, and B. Viola. Comparative analysis of the SOL plasma in DEMO using EDGE2D/EIRENE and TECXY codes. *Nuclear Materials and Energy*, 12:864–868, 2017.

[128] Xian Zhu Tang and Zehua Guo. Sheath energy transmission in a collisional plasma with collisionless sheath. *Physics of Plasmas*, 22(10), 2015.

[129] P. C. Stangeby. Basic physical processes and reduced models for plasma detachment. *Plasma Physics and Controlled Fusion*, 60(4), mar 2018.

[130] D. Tskhakaya, K. Matyash, R. Schneider, and F. Taccogna. The particle-in-cell method. *Contributions to Plasma Physics*, 47(8-9):563–594, 2007.

[131] C. A. Johnson, S. D. Loch, and D. A. Ennis. ColRadPy: A Python collisional radiative solver. *Nuclear Materials and Energy*, 20(August 2018), 2019.

[132] D. Reiter. The EIRENE Code User Manual Manual version : May 16, 2019. page 304, 2019.

[133] V. Kotov, D. Reiter, R. A. Pitts, S. Jachmich, A. Huber, and D. P. Coster. Numerical modelling of high density JET divertor plasma with the SOLPS4.2 (B2-EIRENE) code. *Plasma Physics and Controlled Fusion*, 50(10), 2008.

[134] Nathan A. Garland, Hyun Kyung Chung, Christopher J. Fontes, Mark C. Zammit, James Colgan, Todd Elder, Christopher J. McDevitt, Timothy M. Wildey, and Xian Zhu Tang. Impact of a minority relativistic electron tail interacting with a thermal plasma containing high-atomic-number impurities. *Physics of Plasmas*, 27(4), 2020.

[135] Nathan A. Garland, Hyun Kyung Chung, Mark C. Zammit, Christopher J. McDevitt, James Colgan, Christopher J. Fontes, and Xian Zhu Tang. Understanding how minority relativistic electron populations may dominate charge state balance and radiative cooling of a post-thermal quench tokamak plasma. *Physics of Plasmas*, 29(1), 2022.

[136] G. Fishpool, J. Canik, G. Cunningham, J. Harrison, I. Katramados, A. Kirk, M. Kovari, H. Meyer, and R. Scannell. MAST-upgrade divertor facility and assessing performance of long-legged divertors. *Journal of Nuclear Materials*, 438(SUPPL):S356–S359, 2013.

[137] A. I. Khrabry, V. A. Soukhanovskii, T. D. Rognlien, M. V. Umansky, D. Moulton, and J. R. Harrison. Modeling snowflake divertors in MAST-U tokamak using UEDGE code. *Nuclear Materials and Energy*, 26(July 2020):100896, 2021.

[138] N. Horsten, W. Dekeyser, G. Samaey, and M. Baelmans. Comparison of fluid neutral models for one-dimensional plasma edge modeling with a finite volume solution of the Boltzmann equation. *Physics of Plasmas*, 23(1), 2016.

[139] N. Horsten, W. Dekeyser, G. Samaey, and M. Baelmans. Assessment of fluid neutral models for a detached ITER case. *Nuclear Materials and Energy*, 12:869–875, 2017.